Protein Modulation of Ion Channels



Alexander M. Cloake
Magdalen College
University of Oxford

Supervisor: Professor Stephen J. Tucker

A thesis submitted for the degree of
Doctor of Philosophy
Hilary Term 2021

Acknowledgements

The work presented in this thesis would not have been possible without a number of people. First and foremost, I would like to express my gratitude to Stephen for his continued knowledge, support and patience throughout the last four years. In addition, the day-to-day assistance provided by all of my colleagues, especially at the beginning of my D.Phil by colleagues turned friends, Linus Conrad, Manuel Arcangeletti and Sam Usher, as well as students I have supervised, Jenna Elliott and Kathryn Smith, have been truly immeasurable. I am eternally grateful to my mentors at Genentech, Jian Payandeh, Thomas Clairefeuille and David Hackos who gave me such a comprehensive and intellectually stimulating internship and the opportunity to join such an exciting project. It would be remiss of me not to give a special expression of gratitude towards Dave who taught me how to patch and always went above and beyond to continue my ion channel education. I would also like to take the opportunity to thank the Medical Research Council for providing me with the funding to embark on my academic journey.

Outside of the lab I would like to thank my friends and family who supported me throughout the undertaking of this thesis; particularly unwavering love and support from my mum, dad, Samantha and Alex. Without their encouragement and support during the past few years, the completion of this body of work would have been impossible.

Abstract

Ion channels lie at the heart of electrical excitability. They represent attractive targets for treatments of a range of pathophysiological conditions, including pain, ischemia and epilepsy. To date, small molecule approaches have dominated ion channel drug discovery, but small molecules often lack the appropriate safety and specificity, ultimately leading to their rejection in the clinic. One way in which to overcome this is to use proteins which use large molecular scaffolds to very precisely place a few key residues in order to modulate ion channel function. To this end, we characterise α-scorpion toxin binding to Nav channels, showing α-scorpion toxin AahII binds to VSDIV and inhibits upward voltage sensor movement. We interrogate the pharmacology of these naturally occurring toxins and probe electrochemical coupling involved in the fast-inactivation process of Nav channels which was uncovered in our work, in order to gain insights into the gating cycle of the channels. Better understanding of this process may allow development of novel therapeutics targeting inactivated Nav channels. Additionally, we characterise VHH domain antibody binding to K2P channels, showing they are capable of both activation and inhibition of channel activity and show high selectivity towards their target. We postulate a mechanism of action through the external pH-sensing pathway and show their activity on rodent channels, uncovering analgesic potential. Additionally, we develop the VHH antibodies as tools to allow visualisation of TREK-2 in native cells, showing selective binding against their target over closely related channels and provide some preliminary data to show localisation of TREK-2 within neurons of rat sympathetic cervical ganglia but not in the glial cells, consistent with RNA-seq data.

List of Abbreviations

ADHD	=	Attention Deficit Hyperactivity Disorder
AP	=	Action Potential
BSA	=	Bovine Serum Albumin
CC	=	Current Clamp
VC	=	Voltage Clamp
CHS	=	Conserved Hydrophobic Surface
CIP	=	Chronic Insensitivity to Pain
CMV	=	Cytomegalovirus
MBP	=	Maltose Binding Protein
CNS	=	Central Nervous System
Cryo – EM	=	cryo- Electron Microscopy
CTD	=	C-terminal Domain
DAPI	=	4,6'-dimidino-2-phenylindole
DMSO	=	Dimethyl sulfoxide
DRG	=	Dorsal Root Ganglion
EC_{50}	=	Median Effective Concentration
EDTA	=	Ethylenediaminetetraacetic acid
EGFP	=	Enhanced Green Fluorescent Protein
ENC	=	Extracellular Negative Cluster
EPR	=	Electron Paramagnetic Resonance
ER	=	Endoplasmic Reticulum
eSrtA	=	evolved sortase A
Fab	=	Fragment Antigen Binding
FBS	=	Fetal Bovine Serum
FRET	=	Förster Resonance Energy Transfer
GOF	=	Gain of Function
GOI	=	Gene of Interest
GST	=	Glutathione-S-Transferase
HBC	=	Helix Bundle Crossing
HCS	=	Hydrophobic Constriction Site
HPLC	=	High Performance Liquid Chromatography
HRP	=	Horseradish Peroxidase
HRV	=	Human Rhinovirus
IC_{50}	=	Median Inhibitory Concentration
IEM	=	Inherited erythromelalgia

Ig	=	Immunoglobulin
IGNAR	=	Immunoglobulin New Antigen Receptor
IHC	=	Immunohisto(cyto)chemistry
IMAC	=	Immobilised Metal Affinity Chromatography
INC	=	Intracellular Negative Cluster
Kd	=	Dissociation Constant
Kv	=	Voltage-gated Potassium Channel
LOF	=	Loss of Function
MCS	=	Multiple Cloning Site
MD	=	Molecular Dynamics
MWCO	=	Molecular Weight Cut Off
Nav	=	Voltage-gated Sodium Channel
Ni – NTA	=	Nickel-nitrilotriacetic acid
NMR	=	Nuclear Magnetic Resonance
ORF	=	Open Reading Frame
PAGE	=	Polyacrylamide Gel Electrophoresis
PBS	=	Phosphate Buffered Saline
PCR	=	Polymerase Chain Reaction
PD	=	Pore Domain
PDB	=	Protein Data Bank
PelB	=	Pectate Lyase B
Pfu	=	*Pyrococcus furiosus*
PM	=	Pore Module
PNK	=	Polynucleotide Kinase
PNS	=	Peripheral Nervous System
rpm	=	Revolutions per minute
RTP	=	Room Temperature and Pressure
ScFc	=	Single Chain Fragment Constant
SCG	=	Superior Cervical Ganglion
SDM	=	Site-Directed Mutagenesis
SDS	=	Sodium Dodecyl Sulphate
SEC	=	Size Exclusion Chromatography
SF	=	Selectivity Filter
Shaker – IR	=	Inactivation Resistant Shaker

Sorttag	=	Sortase Tag
TAE	=	Tris-Acetate-EDTA
TEA	=	Tetraethyl ammonium
TEV	=	Tobacco Etch Virus
TEVC	=	Two Electrode Voltage Clamp
TGI	=	Trigeminal Ganglion
TM	=	Transmembrane
TMB	=	3,3,5,5-Tetramethylbenzidine
TRP	=	Transient Receptor Potential
TTX	=	Tetrodotoxin
UTR	=	Untranslated Region
UV	=	Ultraviolet
VHH	=	Variable Domain of Heavy chain of heavy chain only Antibodies
VNAR	=	Variable Domain of New Antigen Receptor Antibodies
VSD	=	Voltage-sensing Domain
WT	=	Wild Type

Contents

1 Introduction **1**

1.1 Background 1

1.1.1 'I would rather feel pain than nothing at all' 1

1.1.2 What is pain? 2

1.1.3 Action Potentials and Hodgkin-Huxley 4

1.1.4 Meet the Team 7

1.1.4.1 K2P and K_{ir} Channels Set the Resting Membrane Potential 9

1.1.4.2 Subthreshold Depolarisations are the Result of Stimuli-Induced Opening of Transient Receptor Potential Channels 9

1.1.4.3 Voltage-Gated Sodium Channels initiate and propagate action potentials 10

1.1.4.4 Voltage-Gated Potassium Channels terminate action potentials 11

1.1.5 Targeting the pain pathway 11

1.2 Introduction to Ion Channel Biophysics 14

1.2.1 Ionic Gradients 14

1.2.2 Properties of Ion Channels 15

1.2.2.1 Permeation 15

1.2.2.2 Gating 16

1.2.3 I-V curves 21

1.2.4 Selectivity 22

1.2.5 Electrical Properties of Membranes 23

1.2.6 Studying Ion Channels in Membranes 25

1.2.7 Voltage Clamp Techniques 27

1.2.7.1 Two Electrode voltage Clamp 27

1.2.7.2 Whole Cell Patch Clamp 28

1.3 Tetrameric Ion Channel Superfamily 30
1.3.1 Knowledge during the Classical era 32
1.3.1.1 Discovery of Gating Currents 33
1.3.1.2 Advent of Molecular Cloning 37
1.3.1.3 Gating Currents in Heterologously Expressed Channels 38
1.3.1.4 Mapping of the Potassium Channel Pore using toxins 39
1.3.1.5 Mapping of the Sodium Channel Pore using toxins 40
1.3.1.6 Identifying the voltage-sensor 41
1.3.1.7 Voltage-Sensor movement 42
1.3.1.8 Identification of the fast inactivation machinery in Nav Channels 44
1.3.2 The Structural Revolution 45
1.3.2.1 X-ray Crystallography of Membrane Proteins 45
1.3.2.2 Structural Basis of Potassium Channel Selectivity . 46
1.3.2.3 Potassium Channel Gating from KcsA, MthK and Shaker 48
1.3.2.4 Relative speeds of the voltage sensors 49
1.3.2.5 The first structure of a voltage sensor 50
1.3.2.6 Focusing of the electric field within the voltage sensor 51
1.3.2.7 A hydrophobic Plug is central to Voltage-Sensor Operation 54
1.3.2.8 Sodium channel structure 56
1.3.3 The Cryo-Electron Microscopy (Cryo-EM) Revolution 58
1.3.3.1 Structures of Proteins from native tissues 59
1.3.3.2 Structures from Recombinant Sources 62
1.3.4 Challenges and Unanswered Questions 63
1.4 Pharmacological Intervention to trap novel states 64
1.4.1 Theory of Ligand Binding 64
1.4.2 Trapping Pharmacologically and Mechanistically Relevant states 68

2 Materials and Methods **90**
2.1 Preface 90
2.2 Molecular Biology 90
2.2.1 Materials 90

2.2.2 Summary of Channel Constructs used in this study 92
2.2.3 Summary of Scorpion Toxin Constructs used in this Study . . 95
2.2.4 Summary of VHH Antibody Constructs used in this Study . 97
2.2.5 Subcloning by PCR 101
2.2.6 Site-Directed Mutagenesis 107
2.2.7 Subcloning by Restriction Digest 111
2.2.8 Cloning K2P-mCherry Channel fusions by Extension Overlap PCR 112
2.2.9 Cloning Sorttagged VHH antibodies by Inverse PCR 115
2.2.10 Nav1.7 Mutagenesis and Subcloning 116
2.2.11 Heat Shock Transformation 116
2.2.12 Culture and DNA extraction 117
2.2.13 Sequencing 117
2.2.14 Channel mRNA production 119
2.2.15 pScFcAC Vector creation 119
2.3 Mammalian Cell Culture 122
2.3.1 Materials: 122
2.3.2 Cell Maintenance 123
2.3.3 Thawing adherent Cells 124
2.3.4 Freezing adherent Cells 124
2.3.5 Splitting adherent Cells 125
2.3.6 Poly-L-Lysine Coated Coverslips 125
2.3.7 Seeding adherent Cells 125
2.3.8 Splitting non-adherent Cells 126
2.4 Heterologous Expression in Mammalian Cells 126
2.4.1 Induction of Nav1.2 in Freestyle ™ 293-F 126
2.4.2 Transfection of Nav1.7 mutants and K2P Channels 126
2.4.3 Transfection of VHH Antibody-mVenus for Immunohistocytochemisry Studies 128
2.4.4 Mammalian cell preparation for Dynaflow measurements (Nav and K2P electrophysiology) 128
2.4.5 Mammalian cell preparation for Immunohistocytochemistry experiments 128
2.5 Heterologous Expression in *Xenopus Laevis* Oocytes 129
2.5.1 Materials 129
2.5.2 Solutions and Buffers 129

2.5.3 Oocyte Preparation 131
2.5.4 mRNA injection 131
2.6 Protein Biochemistry 132
2.6.1 Materials 132
2.6.2 Solutions and Buffers 134
2.6.3 Making competent cells 135
2.6.4 Purification of Scorpion Toxins 135
2.6.5 Periplasmic expression of VHH antibodies 137
2.6.6 Small Scale Expression and Purification of VHH antibodies in different *E. coli* strains 138
2.6.7 Cytosolic expression of VHH antibodies 139
2.6.8 HRV3C and TEV Purification 142
2.6.9 Sortase Purification 144
2.6.10 C-terminal labelling of VHH Antibodies 145
2.6.11 Sortagging of VHH antibodies 146
2.6.12 VHH Antibody-mVenus harvesting from Mammalian cells . 146
2.6.13 Characterisation of mVenus-tagged VHH antibodies 147
2.7 Immunohistocytochemistry 149
2.7.1 Immunohistocytochemistry on *Xenopus laevis* Oocytes 149
2.7.2 Immunohistocytochemistry on HEK293T Cells 149
2.7.3 Immunohistocytochemistry on Rat Superior Cervical Ganglion 152
2.8 Electrophysiology 153
2.8.1 Materials 153
2.8.2 Whole Cell Patch Clamp Recordings of Nav Channels 153
2.8.2.1 AahII Dose Response Measurements on Nav1.7 and Nav1.2, Nav1.7 mutants, Nav1.2 mutants and Toxin Mutants 154
2.8.2.2 State-dependence Measurements of AahII on Nav1.7 156
2.8.2.3 Biophysical Characterisation of Nav1.7 Mutations . 158
2.8.2.4 Voltage-Dependence of Activation 158
2.8.2.5 Voltage-Dependence of Inactivation 160
2.8.2.6 Time-Dependence of Inactivation 162
2.8.2.7 Data Processing 163
2.8.3 Two Electrode Voltage Clamp Recordings of K2P Channels . 164
2.8.3.1 Steady-State Current-Voltage Relationships 165
2.8.3.2 Dose Response Curves 167

2.8.4 Whole Cell Patch Clamp Recordings of K2P Channels 169
2.8.4.1 Problems with Whole Cell Recordings 169
2.8.4.2 Dose-Response Measurements 170
2.9 Figures in This Thesis 172

3 Scorpion Toxin Action on Nav Channels 175
3.1 Disclaimer 175
3.2 Introduction to Sodium Channels, Fast Inactivation and Toxins . . . 177
3.2.1 Nav Channels iInitiate and Propagate APs 177
3.2.2 Nav Channels are highly glycosylated tetrameric channels . 178
3.2.3 Nav Channels are the target of natural toxins 181
3.2.4 α- scorpion toxins slow down fast inactivation 183
3.2.5 α- scorpion toxins bind to Neurotoxin Receptor Site 3 188
3.2.6 Rationale 190
3.2.7 A humanised NavPas Chimera structure sets the scene 190
3.3 Results 191
3.3.1 Native AahII is a potent modulator of Nav Channels 191
3.3.2 AahII activity is state-dependent 194
3.3.3 Interactions with Neurotoxin Receptor Site 3 196
3.3.4 Channel Determinants of Specificity 196
3.3.4.1 Summary 197
3.3.4.2 Glycan-PM and D1-PM 198
3.3.4.3 S1-S2 Loop 200
3.3.4.4 S3-S4 Loop 201
3.3.5 Toxin Determinants of Specificity 203
3.3.5.1 Summary 203
3.3.5.2 Recombinant AahII proves difficult to isolate 204
3.3.5.3 Recombinant OD1 proves unstable 207
3.3.5.4 Synthetic AahII mutants show the importance of charge in α- scorpion toxin action and explain the state-dependence 208
3.3.6 VSDI interaction Site 211
3.3.7 Mechanism of Fast Inactivation 213
3.4 Discussion 218
3.4.1 In Light of the Nav1.5-LqhIII structure 220
3.4.1.1 Interactions with Neurotoxin Receptor Site 3 221

3.4.1.2 VSDI Interaction Site . . . 221
3.4.1.3 Mechanism of Fast Inactivation . . . 222

4 VHH Antibody Action on K2P Channels 232
4.1 Disclaimer . . . 232
4.2 Introduction . . . 234
4.2.1 Antibody Structure and Derivatives . . . 234
4.2.2 Introduction to the Adaptive Immune Response . . . 238
4.2.3 Introduction to the K2P Channel Family . . . 243
4.2.3.1 A Selectivity Filter Gate . . . 244
4.2.3.2 External pH Sensitivity . . . 246
4.2.3.3 Mechanosensitivity, Temperature Gating and Intracellular pH gating via the TM helices (up/down transitions) . . . 248
4.2.3.4 Voltage-Gating . . . 252
4.2.3.5 Structural Changes in the Gate . . . 252
4.2.3.6 K2P Pharmacology . . . 254
4.2.4 Antibodies Targeting Ion Channels . . . 255
4.2.5 Why Target K2P Channels with VHH Antibodies? . . . 257
4.3 Results and Discussion . . . 258
4.3.1 Strategy . . . 258
4.3.2 Screening for Extracellular Modulators of TREK-2 . . . 259
4.3.3 Potency of modulation by VHH antibodies . . . 263
4.3.4 Specificity of Functional Binders . . . 265
4.3.5 Mechanism of Action . . . 269
4.3.6 Determinants of Efficacy . . . 276
4.4 Discussion . . . 280

5 VHH antibodies as Tools 291
5.1 Disclaimer . . . 291
5.2 Introduction . . . 293
5.2.1 The need for tools for localisation . . . 293
5.2.2 Currently Available Antibodies . . . 294
5.2.3 Advantages of VHH antibodies . . . 295
5.3 Results . . . 296
5.3.1 VHH antibody expression and purification in *E. coli* . . . 296
5.3.2 Optimisation of expression in *E. coli* . . . 299

5.3.2.1 Expression in different strains and whole cell purification . . . 299
5.3.2.2 Expression using a stronger Promoter . . . 300
5.3.3 Immunohistocytochemistry on *Xenopus* Oocytes . . . 302
5.3.4 Expression of Fluorescent VHH antibodies in *E. coli* . . . 303
5.3.4.1 Cytosolic Expression and Purification of VHH antibodies . . . 304
5.3.4.2 C-terminal Tagging of VHH antibodies . . . 307
5.3.5 Expression of VHH antibodies in Mammalian Cells . . . 312
5.3.5.1 Expression of C-terminal mVenus tagged VHH antibodies . . . 313
5.3.5.2 Creating a Modular Mammalian Expression System 314
5.3.6 IHC on Mammalian Cells . . . 317
5.3.6.1 Identification of VHH Domain Candidates for Use in Native Tissues . . . 317
5.3.6.2 Candidate Refinement for VHH Antibodies for Use in Native Tissues . . . 320
5.3.6.3 IHC on rat Superior Cervical Ganglion . . . 322
5.4 Discussion . . . 324

6 Discussion **330**
6.1 Toxins and Antibodies Targeting Ion Channels . . . 330
6.2 Concluding Remarks . . . 334

List of Figures

1.1 Pain signalling 3
1.2 Action Potential of the Squid Giant Axon 6
1.3 Contributors to the Mammalian Action Potential 8
1.4 CNS Disorders and Therapeutic Interventions 13
1.5 An Example of a Single Channel Recording 17
1.6 Gating Processes at the Microscopic and Macroscopic Levels 20
1.7 RC Circuit of a Channel in a Membrane Environment 26
1.8 Two Electrode voltage Clamp Experimental and Electrical Set-up . . 28
1.9 Patch Clamp Configurations 29
1.10 Topology of the Tetrameric Ion Superfamily 31
1.11 Hodgkin-Huxley Gating Model 33
1.12 Sodium Channel Gating Currents 34
1.13 Coupled Inactivation Gating Model of Sodium Channels 36
1.14 Sequence Alignment of S4 37
1.15 KcsA Structure and Potassium Selectivity 47
1.16 Asynchronous Gating Model 50
1.17 Kv1.2 Structure 53
1.18 High Resolution Voltage Sensor Structure from the Paddle Chimera 55
1.19 NavAb Structure and Sodium Selectivity 57
1.20 Eukaryotic Structures Reveal the C-terminal Domain (CTD) and IFM Motif Positioning 61
1.21 Stabilisation of Novel States Using Ligands 65
1.22 The Definitions of Affinity, Efficacy and Potency 67
1.23 Percentage of Antibody Involved in Binding to the Target 69

2.1 Summary and Structural Alignment of α- Scorpion Toxins used in this Study 96
2.2 Summary and Structural Alignment of VHH Antibodies Raised against TREK-2 99

2.3 Summary and Structural Alignment of VHH Antibodies Raised against TREK-1 . . . 100
2.4 Schematic of Subcloning by PCR . . . 101
2.5 Schematic of Site Directed Mutagenesis . . . 107
2.6 Schematic of Extension Overlap PCR . . . 113
2.7 Schematic of Sorttag Cloning Using Inverse PCR . . . 115
2.8 Summary of pScFcAC Vector . . . 121
2.9 Purification of α-scorpion Toxins . . . 136
2.10 Periplasmic Purification of VHH Antibodies . . . 137
2.11 Cytosolic Purification of VHH Antibodies . . . 140
2.12 Purification of HRV3C and TEV . . . 143
2.13 Purification of eSrtA . . . 145
2.14 Fluorescent Protein Spectra and Filter Cube Specifications . . . 151
2.15 AahII Dose Response Measurements . . . 155
2.16 State-dependence Measurements of AahII on Nav1.7 . . . 157
2.17 Voltage-Dependence of Activation . . . 159
2.18 Voltage-Dependence of Inactivation . . . 161
2.19 Time-Dependence of Inactivation . . . 162
2.20 Steady-State Current-Voltage Relationships . . . 166
2.21 Activator Dose-Response Measurements . . . 168
2.22 Patch Clamp Dose-Response Measurements . . . 171

3.1 Sodium Channels are the Target of Many Natural Toxins . . . 180
3.2 AahII Sequence and Structure . . . 186
3.3 AahII is a Potent α- Scorpion Toxin . . . 192
3.4 AahII activity is State-Dependent . . . 195
3.5 Interactions with the Domain I Pore Module and Glycan Pore Module 199
3.6 Interactions with the S1-S2 Loop . . . 201
3.7 Interactions with the S3-S4 Loop . . . 202
3.8 Scorpion Toxin Biochemistry and Glycosylation . . . 206
3.9 Instability of OD1 . . . 207
3.10 Biochemical Identity of Synthetic and Native AahII . . . 208
3.11 Synthetic Toxin Mutants and their Potency on WT Nav1.7 . . . 209
3.12 AahII Interaction with VSDI . . . 212
3.13 Mutations Probing the 'Switch 1' Interface . . . 215

4.1 Antibodies and Common Derivatives . . . 235

4.2 V(D)J Recombination of Heavy and Light Chain Antibodies 242
4.3 TWIK-1 Structure Showing General K2P Architecture 245
4.4 TREK-2 Up and Down Structures Highlighting TM Transitions . . . 250
4.5 Intrinsic Asymmetry of the Selectivity Filter Gate Showing Dynamics 253
4.6 K2P Pharmacology 255
4.7 Screening for Extracellular Modulators of TREK-2 261
4.8 Potency of VHH Antibody Modulators of TREK-2 264
4.9 Specificity of Functional Modulators of TREK-2 267
4.10 VHH Antibody-Mediated Functional Modulation of TREK-2 Gating Mutants 271
4.11 VHH Antibody Modulation Response to External pH 274
4.12 VHH67 Determinants of Efficacy on TREK-2 in HEK293 Cells 277
4.13 Inert and Functional VHH Antibody Binders 282

5.1 Periplasmic Expression and Purification of VHH Antibodies 298
5.2 VHH Antibody Expression in Different *E. coli* Strains 299
5.3 VHH antibody Expression in Different Vectors 301
5.4 Detection of VHH Antibody Binding to TREK-2 by IHC on *Xenopus* oocytes 302
5.5 Cytosolic Expression and Purification of VHH Antibodies 306
5.6 Sorttagging of VHH Antibodies 309
5.7 Expression of C-terminal mVenus Tagged VHH Antibodies 314
5.8 Creation of and Expression from a Modular Mammalian Expression Vector 316
5.9 Immunohistocytochemistry Using VHH antibody mVenus on HEK293T Cells Expressing hTREK-2 319
5.10 Immunohistocytochemistry using VHH Antibody mVenus on HEK293T cells Expressing a Number of K2P Channels 321
5.11 Immunohistocytochemistry using VHH Antibody mVenus Fusions on Rat Superior Cervical Ganglia 323

Chapter 1

Introduction

1.1 Background

1.1.1 'I would rather feel pain than nothing at all'

Pain sensation is important for protecting the body from further injury, however, when 'chronic', this unwanted pain confers a burden on the whole spectrum of society, putting stress on individuals and healthcare systems alike. According to the British Pain Society, 8 million Britons suffer from chronic pain (Fayaz et al., 2016) and back pain alone costs £10 billion for the UK economy (Maniadakis and Gray, 2000).

Currently, opioids lead the market for mild to severe pain (typified by codeine and morphine), but these come with significant side effects, not limited to addiction and dependency (Volkow and McLellan, 2016). Better control is therefore needed to attempt to reduce this monumental medical and economic burden.

1.1.2 What is pain?

Whenever tissue damage or noxious stimuli (e.g. hot or cold) are detected, this damage signal is relayed to the brain, which is what we perceive as pain. During this process, intense thermal, mechanical and chemical stimuli are sensed by the peripheral nerve endings of a sub-population of neurons called nociceptors which reside in the skin and other organs. This process is known as nociception and is the first step of pain signalling to the brain. Pain encompasses both the sensory and emotional aspects and thus the requirement for and involvement of the brain.

The cell bodies of these nociceptors reside either in the Trigeminal Ganglia (TGI) for neurons which innervate the head or Dorsal Root Ganglia (DRG) for neurons that innervate the rest of the body. Both of these neurons connect and signal from their target organ to the spinal cord. Neurons in the brain and spinal cord are broadly labelled the Central Nervous System (CNS), while those everywhere else are known as the Peripheral Nervous System (PNS). As such, DRG and TGI neurons connect the PNS and the CNS. An example of a DRG neuron is shown in Figure 1.1 below.

In response to stimulation, a transient depolarisation of membrane potential, termed an Action Potential (AP) is initiated in the peripheral nerve endings (green, Figure 1.1). This AP is then propagated down the axon (blue, Figure 1.1) towards the cell body where the signal is terminated (grey, Figure 1.1) causing the release of neurotransmitters. These neurotransmitters activate secondary neurons which signal to the brain. Persistent signalling by means of an AP down these nerve fibres to the brain is the molecular basis of pain.

Every step of this process occurs via changes in ionic gradients across the neu-

ronal membrane by the concerted action of many ion channels. Some major contributors are shown at the top of Figure 1.1.

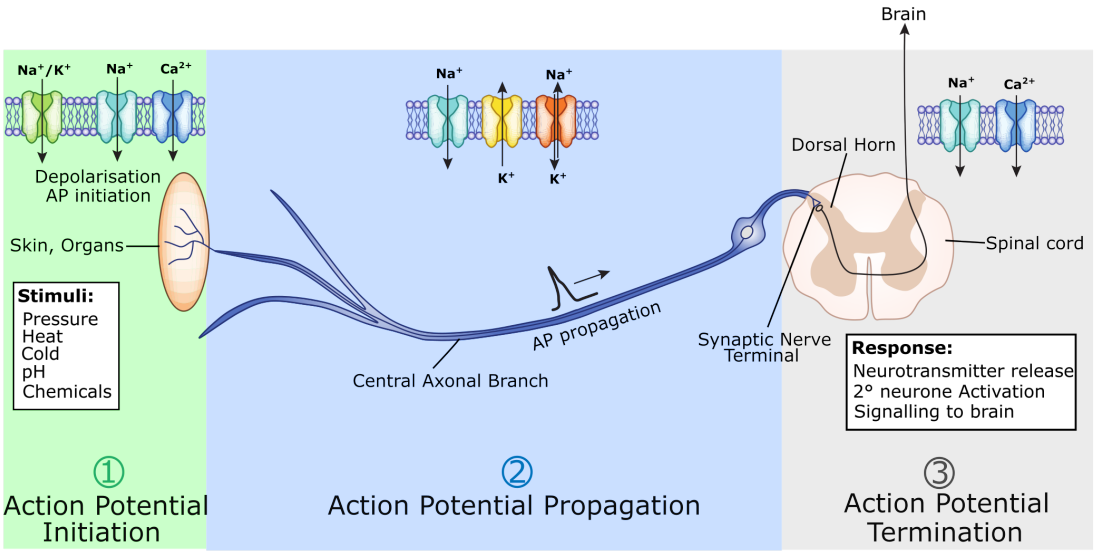


Figure 1.1: **Pain signalling**
In response to stimuli, in the form of pressure, heat, cold, pH and chemicals, an Action Potential (AP) is initiated in the peripheral nerve endings residing in the skin and other organs (green, ①). Depolarisation of the membrane occurs by inward flux of Na^+, K^+ and Ca^{2+} into the neurons. The AP is then propagated down the axon, a process that involves inward movement of Na^+, outward movement of K^+ and energetic Na^+/K^+ exchange across the membrane (blue, ②). The AP is terminated at the synaptic nerve terminal, here shown to reside in the Dorsal Horn, which causes neurotransmitter release, secondary neuron activation and signalling to the brain. These processes involve the inward movement of Na^+ and Ca^{2+} (grey, ③).
Figure adapted from Waxman and Zamponi (2014). Reproduced with permission of Springer Nature.

The best way of understanding the different ways of dampening pain signalling is to understand the principle components of the AP that goes from nerve endings of the nociceptor to the brain, and the nature of it. Our understanding of the AP came largely from pioneering studies by Hodgkin and Huxley in the mid 20th Century.

1.1.3 Action Potentials and Hodgkin-Huxley

Early mathematical modelling of the AP in the squid giant axon by Hodgkin and Huxley revolutionised the way the world viewed bioelectricity, long before the molecular machines that drive these processes were discovered, let alone mechanistically probed. In their revolutionary work, they derived non-linear equations describing each component of the giant squid axon conductance as electrical elements.

The current flowing through the membrane (I_m) upon changes in membrane voltage (dV_m/dt) was modelled as a capacitor of capacitance C_m in Equation 1.1

$$I_m = C_m \frac{dV_m}{dt} \tag{1.1}$$

The current of a single ion (I_i) was modelled as the product of the conductance (g_i) and the driving force defined as the difference between the membrane potential and reversal potential of the ion ($V_m - V_i$) in Equation 1.2.

$$I_i = g_i(V_m - V_i) \tag{1.2}$$

A more detailed description of the physical meanings of these parameters and where they are derived from can be found in Section 1.2. Hodgkin and Huxley used these basic equations and some empirically derived constants (n, m and h) from simple voltage-clamp experiments on the squid giant axon to derive their Nobel prize winning predictions about action potentials. (1.3).

$$I = C_m \frac{dV_m}{dt} + g_K n^4 (V_m - V_K) + g_{Na} m^3 h (V_m - V_{Na}) + g_l (V_m - V_l) \qquad (1.3)$$

Importantly, Hodgkin and Huxley predicted three principal conductances in the squid giant axon; a sodium conductance, a potassium conductance and a leak conductance. The overall shape of the action potential can be seen on the left of Figure 1.2, and the corresponding conductance changes on the right. The cell is maintained at a negative potential by the leak conductance. This is called the resting membrane potential. The action potential is all-or-nothing; depolarisations under threshold (dashed lines, Figure 1.2) do not result in action potential firing.

Hodgkin and Huxley correctly deduced that a voltage-dependent sodium conductance was responsible for the rising phase of the AP, where the membrane depolarises (green, Figure 1.2). In addition, they deduced that the voltage-dependent potassium conductance was responsible for the falling phase of the AP, where the membrane repolarises (blue, Figure 1.2) and then hyperpolarises (grey, Figure 1.2).

Decades later, the molecular identities of these conductances were discovered. The sodium conductance is carried by voltage-gated sodium channels (Nav), the potassium conductance by the voltage-gated potassium channels (Kv). The background leak conductances by contrast are carried by a number of different channels including Inwardly Rectifying Potassium Channels (K_{ir}) and members of the Potassium Two Pore Domain (K2P) family. As their names suggest, Nav and Kv open in response to changes in voltage.

By chance, the squid giant axon, from which Hodgkin and Huxley deduced the basis of the action potential, only contains one Nav channel and one Kv channel,

thus giving it a relatively simple shape. Many mammalian neurons (and some invertebrate neurons) contain a whole orchestra of distinct voltage-gated channels. As channel expression in each type of neuron is different, different combinations of these channels act in concert and give rise to distinct and complex firing patterns and afterpolarisations (one example is the hyperpolarisation shown in Figure 1.2). A comprehensive review of shaping of mammalian action potentials can be found in(Bean, 2007).

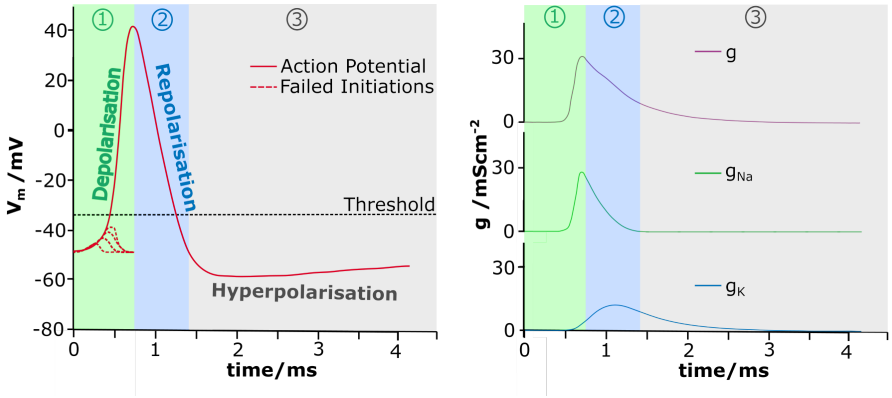


Figure 1.2: **Action Potential of the Squid Giant Axon**
A: Voltage Changes During an Action Potential. The Membrane potential (V_m is held at around -50 mV. Depolarisations beneath the threshold (horizontal dotted line) fail to initiate Action Potentials (red dashed lines). Depolarisations above threshold initiate an Action Potential (solid red line), which can be characterised by three distinct phases. Depolarisation (green, ①) results in the membrane potential rapidly moving to positive values, followed by repolarisation where the membrane potential rapidly returns to negative values (blue, ②). In the example shown here, the repolarisation overshoots and is termed hyperpolarisation (grey, ③).
B: Conductance changes during an Action Potential. The total conductance (g) of the AP spans the three distinct phases of the AP (purple line, top) . The sodium conductance (g_{Na}) is primarily involved in depolarising the membrane (green line, middle), while the potassium conductance (g_K) is primarily responsible for the repolarisation and hyperpolarisation of the AP (blue line, bottom).
Figure adapted from Rai et al. (2013).©IOP Publishing. Reproduced with permission of IOP.

1.1.4 Meet the Team

As previously mentioned, there are many voltage-gated channels that act in concert to produce mammalian action potentials. Channel expression patterns between neurons are variable, so defining the role of individual channels is difficult. It is the combination of expression patterns and biophysical properties of individual channels that shape the action potential in any given neuron. For now, we will largely ignore the biophysical properties of the channels until we have introduced them in detail in Section 1.2, except for one key property; the channels open at different thresholds. This dictates which part of the action potential they are involved in.

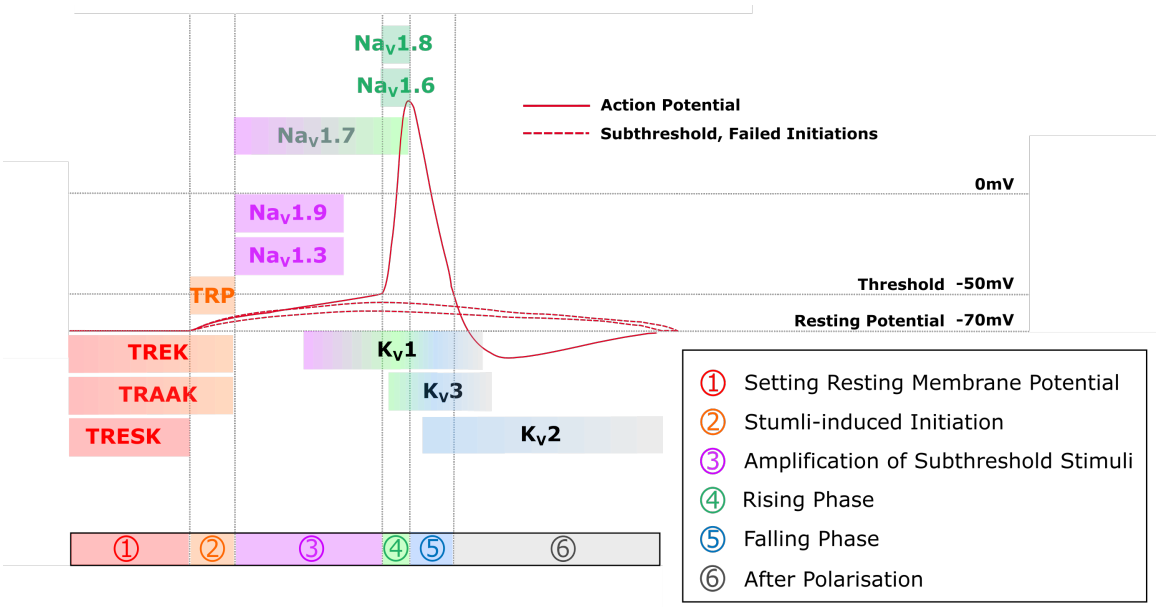


Figure 1.3: **Contributors to the Mammalian Action Potential**
The Mammalian AP is much more complicated than in the Squid Giant axon. The resting membrane potential is set at -70 mV by the contribution of K2P channels of the TREK, TRAAK and TRESK subfamilies, (red, ①). In response to stimuli, the AP is initiated through the Transient Receptor Potential (TRP) family of channels with other contributions from some K2P subfamilies (orange, ②). These subthreshold stimuli are amplified by members of the Nav family, primarily Nav1.3, Nav1.9 and Nav1.7 (purple, ③) which in turn initiates the rising phase of the action potential again involving Nav1.7 but also other contributions from Nav1.8 and Nav1.6. (green ④). Kv channel members from the Kv1, Kv2 and Kv3 subfamilies are responsible for the falling phase of the action potential (blue, ④) and the subsequent afterpolarisation (grey, ⑥). Figure adapted from (Bennett et al., 2019). Reprinted with permission of APS.

1.1.4.1 K2P and K_{ir} Channels Set the Resting Membrane Potential

The so called leak channels are responsible for setting the resting membrane potential (red, Figure 1.3). The leak channels comprise a number of different families, including the K2P and (K_{ir}) potassium channels. There are 15 K2P members in humans encoded by KCNK genes, with complicated nomenclature. Of these, family members TASK-1-3, TREK 1-2, TRAAK, TWIK-1-2 and TRESK are expressed in adult sensory neurons (Talley et al., 2001; Marsh et al., 2012; Plant, 2012), with TREK-2 and TRESK most likely being the predominant background potassium conductance in nociceptors (Kang and Kim, 2006). There are also 15 K_{ir} members in humans encoded by KCNJ genes. One family member, K_{ATP} is expressed in adult sensory neurons (Zoga et al., 2010) where it helps set the resting membrane potential and possibly protects the neuron under ischemic conditions (Yamada and Inagaki, 2005). There are also additional non selective inward Na^+ leak currents that oppose the K^+ efflux through a number of channels exemplified by the sodium selective NALCN channel (Cochet-Bissuel et al., 2014).

1.1.4.2 Subthreshold Depolarisations are the Result of Stimuli-Induced Opening of Transient Receptor Potential Channels

Members of the Transient Receptor Potential (TRP) family are responsible for initiating subthreshold depolarisations in response to stimuli (orange, Figure 1.3). They are calcium-permeant cation channels which respond to a wide variety of signals including, but not limited to, temperature, pressure, small molecules and intracellular signals. Although these won't be discussed further as they are beyond the remit of this thesis, there are a number of comprehensive reviews available Ramsey et al. (2006).

1.1.4.3 Voltage-Gated Sodium Channels initiate and propagate action potentials

Voltage-gated sodium channels initiate and propagate action potentials down nerve and muscle fibres by opening in response to small sub- and super-threshold depolarisations (purple and green, Figure 1.3) . In humans there are nine functional isoforms Nav1.1-1.9 encoded by SCNxA genes (x = 1–5 corresponding to Nav1.1–Nav1.5, and x = 8–11 for Nav1.6–Nav1.9, respectively, (Catterall et al., 2003)). While it is impossible to exhaustively characterise expression of each isoform, as there is tremendous cross-over, Nav1.1, Nav1.6, Nav1.7, Nav1.8, and Nav1.9 are all expressed by adult sensory neurons (Akopian et al., 1996; Black et al., 1996; Dib-Hajj et al., 1998; Fukuoka et al., 2008; Bennett et al., 2019). Nav1.3, one of the isoforms expressed during development and subsequently down-regulated (Felts et al., 1997) can be up-regulated in adulthood in response to peripheral nerve injury (Black et al., 1995).

Nav1.9, Nav1.3 and Nav1.7 have low activation thresholds, and as such help amplify subthreshold stimuli (purple, Figure 1.3). The rising phase of the action Potential is predominantly caused by Nav1.8, which has a higher activation threshold, with additional contributions from Nav1.7 and Nav1.6. Nav1.6 is also responsible for the resurgent sodium current (not shown).

Point mutants in these channels, particularly Nav1.7, Nav1.8, and Nav1.9 are involved in inherited Pain disorders typified by Inherited Erythromelalgia (IEM) (Waxman and Dib-Hajj, 2005) and Chronic Insensitivity to Pain (CIP)(Manfredi et al., 1981). These Gain of Function (GOF) and Loss of Function (LOF) mutations manifest in constant pain signalling and the sensation of being on fire or being unable to feel any pain respectively. IEM is often colloquially called 'man on fire'

syndrome owing to the unpleasant sensation of constant heat felt by sufferers.

1.1.4.4 Voltage-Gated Potassium Channels terminate action potentials

Voltage-gated Potassium Channels are responsible for terminating action potentials down nerve and muscle fibres by opening in response to large depolarisations caused by the voltage-gated sodium channels and repolarising back to a resting membrane potential, (blue, Figure 1.3). In addition, they also help set the threshold for action potential firing and the resting potential. In humans there are forty isoforms grouped into twelve subfamilies Kv1-12. (Gutman et al., 2003). Kv1, Kv2, Kv3, Kv4, Kv7, Kv8, Kv9 are all expressed in adult sensory neurons, (reviewed in Du and Gamper (2013)), but of these, Kv8 and Kv9 are thought to be electrically silent.

Members of subfamilies Kv1, Kv4 and Kv7 have low activation thresholds and as such are involved in setting the threshold potential for action potential initiation and influence the number of action potentials that fire. Members of subfamilies Kv2 and Kv3, with higher activation thresholds are predominantly responsible for repolarisation helping to shape the action potential.

1.1.5 Targeting the pain pathway

There are two main approaches one could take to target the pain pathway; either by targeting signal transduction in the neuron itself or by targeting signal transmission from the neuron into the effector. One such class of channels involved in the latter process are voltage-gated Calcium channels, the trafficking of which can be regulated via targeting their $\alpha 2\delta$- auxiliary subunits with gabapentins, but

beyond the scope of this thesis.

We want to target the channels in the neurons themselves. Fine-tuning of the electrical excitability of neurons involved in pain by targeting some of the key components should be possible. As previously mentioned, chronic pain stems from persistent signalling in DRG and TGI neurons, resulting in increased neuronal firing (red, figure 1.4) and termed hyperexcitability. Therapeutically, we could reduce this back to normal firing by targeting the three aforementioned families of channels.

The proof of principle for these therapeutic interventions come from naturally occurring GOF and LOF mutations within Nav, Kv and leak channels which effect normal AP firing and the associated disorders. This is summarised in Figure 1.4). Black arrows represent naturally occurring mutations within the respective channel classes, and grey arrows represent therapeutic interventions which could restore normal AP firing. Interestingly, Nav channel GOF mutations can result in hypoexcitability if the repetitive firing causes Nav channel inactivation (discussed more thoroughly in Introduction to Ion Channel Biophysics)

The ion channels within this pathway therefore represent very good analgesic targets, and indeed a large amount of time and money is being spent developing drugs against key channels (Yaksh et al., 2015). Either by selectively inhibiting Nav1.7 (Chapter 3) or by activating one of the background channels (Chapters 4-5), in theory it is possible to electrically silence cells by preventing action potential initiation and propagation. Before going into detail about the channels in question, it is first important to understand key biophysical properties of ion channels and the electrical properties that they exert on cells.

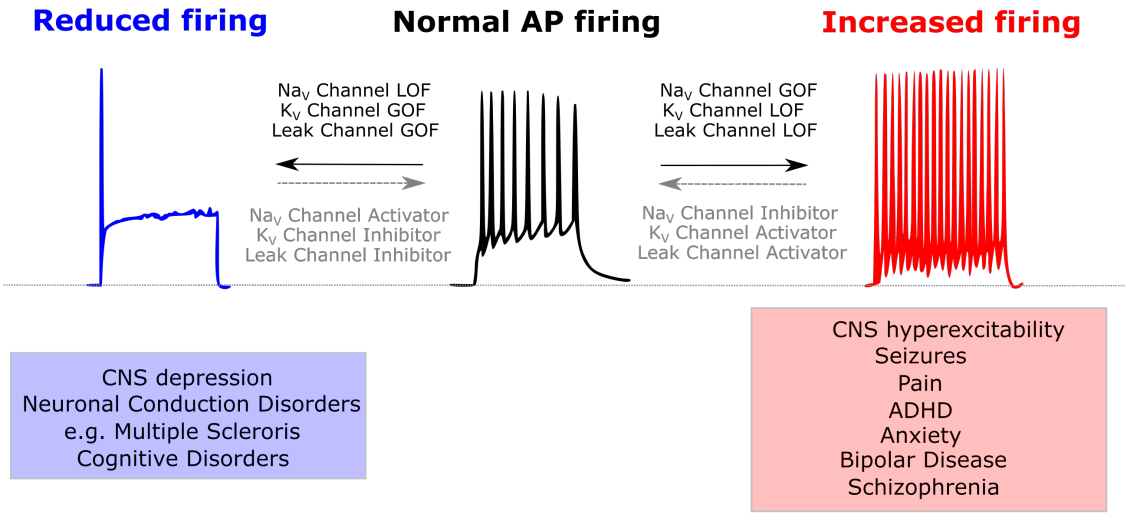


Figure 1.4: **CNS Disorders and Therapeutic Interventions**
Reduced firing or hypoexcitability of neurons which can be caused by Nav channel LOF or Nav, Kv and Leak channel GOF manifests in a number of pathophysiological conditions such as CNS depression, neuronal conduction disorders and Cognitive disorders, blue. Normal AP firing can be therapeutically restored by use of Nav channel activators or Kv and Leak channel inhibitors. Conversely, Nav channel GOF and Kv and Leak Channel LOF can result in increased firing or hyperexcitability, manifesting in a number of pathophysiological disorders such as seizures, pain, Attention deficit hyperactivity disorder (ADHD), anxiety and schizophrenia. Normal AP firing can be therapeutically restored by use of Nav channel inhibitors or Kv and Leak channel activators.
Figure adapted from Wulff et al. (2009). Reproduced with permission of Springer Nature.

1.2 Introduction to Ion Channel Biophysics

1.2.1 Ionic Gradients

Biological cells are surrounded by membranes; a phospholipid bilayer which physically separates the inside of the cell from the outside world. This bilayer serves many structural purposes such as providing shape via anchoring the cell to the cytoskeleton, as well as attaching the cell to the extracellular matrix which in turn provides the physical and biochemical support to allow cell adhesion and the build-up of tissues. As well as these crucial structural roles, the membrane is *partially permeable* and prevents free diffusion of all substances across it.

Gases (e.g. O_2, CO_2), hydrophobic molecules (e.g. benzene) and small polar molecules (e.g. H_2O, EtOH) can freely cross the membrane down their concentration gradient via passive osmosis or diffusion. However, large polar molecules (e.g. glucose), and charged molecules (e.g. amino acids and ions) are unable to cross and gain entry to the cell. Specialised proteins; channels, transporters and pumps have evolved to provide a pathway for these substances to move across the membrane in a regulated way.

Ionic gradients are set up across the membrane at the expense of energy harnessed from chemical processes by the action of ion pumps and transporters. This uneven distribution of charge results in a transmembrane voltage (V_m). Typical concentrations of such ionic gradients are shown in Table 1.1 below. Set up and maintenance of these gradients are crucial for ion channel function.

Ion	[Extracellular]/mM	[Intracellular]/mM	E_x /mV
Sodium	135-145	12	+66
Potassium	3.5-5	140	-93
Calcium	2.25-2.52	10^{-7}	+135
Chloride	115	2.5-50	-42
pH	7.37-7.42	7.1-7.2	-15

Table 1.1: **Typical Ion Concentrations and Equilibrium Potentials**

1.2.2 Properties of Ion Channels

1.2.2.1 Permeation

These uneven charge distributions across the membrane result in an *electrochemical gradient*. If the membrane contains open ion channels, then ions can flow across the membrane through these channels, down this essential gradient. The process of ions flowing through a channel is called *permeation*. As the name suggests, the electrochemical gradient has two components, an 'electrical' and a 'chemical' one. Analogous to non-charged atoms, when separated by a permeable membrane, the concentration gradient creates a force on the ion to move down their concentration gradient. However, there is also an electric field across the membrane as the ions are charged and unevenly distributed across it, producing an electrical force on the ions. The movement of the ion is therefore governed by both of these phenomena.

Ions move down their electrochemical gradient until the electrical force on the ion balances the opposing force of the concentration gradient. The voltage at which this occurs is called the equilibrium potential of the ion (E_x) and is given by the Nernst Equation (Equation 1.4). This potential is calculated for each of the common ionic species and shown in the final column of Table 1.1.

$$E_x = \frac{RT}{zF} ln \frac{[X]_o}{[X]_i} \tag{1.4}$$

where:

E_x = Equilibrium Potential of ion x (V)

R = Universal Gas Constant (8.3145 $Jmol^{-1}K^{-1}$)

T = Temperature (K)

z = Charge on ion x

F = Faraday Constant (96485.332 $Cmol^{-1}$)

$[X]_o$ = Concentration of ion x outside the cell (M)

$[X]_i$ = Concentration of ion x inside the cell (M)

If a channel is permeant to more than one species of ion, then the equilibrium potential is calculated by the electrochemical gradients of the individuals ions capable of permeating as well as the relative permeability of the ion (p_x) and is known as the Goldman-Hodgkin-Katz flux equation.

$$E_x = \frac{RT}{F} ln\left(\frac{p_{Na}[Na]_o + p_K[K]_o + p_{Cl}[Cl]_i}{p_{Na}[Na]_i + p_K[K]_i + p_{Cl}[Cl]_o}\right) \tag{1.5}$$

where the additional parameter:

p_x = The relative permeability of ion x

The difference between the membrane voltage (V_m) and the equilibrium potential of the ion (E_x) is typically termed the *driving force*, and it is this driving force that governs ion permeation through open channels.

$$Driving\ Force = V_m - E_x \tag{1.6}$$

1.2.2.2 Gating

Ions can only permeate through open channels, however, in order to meet the changing needs of the cell, ion channels are dynamic molecules; they open and

close in a process known as *gating*. Gating at its simplest level can be shown by means of a single channel recording held at a single voltage as shown in Figure 1.5 below. Here we see step-wise transitions between an open (blue, Figure 1.5) and closed (red, Figure 1.5) state of a channel. When closed, no current passes, and upon opening, current is then able to flow through the channel. Upward deflections represent channel opening while downward reflections indicate channel closing. From a trace such as this we can introduce a few other concepts.

Single channel opening and closing is stochastic, and so we can define a *mean open time* and *mean closed time* by measuring a large number of these openings and closings. The *Open Probability*, P_o can then be defined as the time the channel spends in the open states (c_{open}) divided by the total recording time. The size of the deflection represents the single channel conductance, γ. In this simple example, there is only a single conductance state, but many channels are more complex; having one or more different *subconductances*.

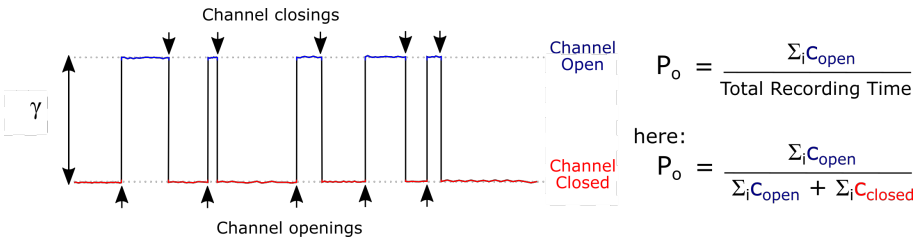


Figure 1.5: **An Example of a Single Channel recording**
When a channel is closed it does not pass current (red, lower line). Single channel activity is stochastic, the channel opens (upward deflections, upward arrows) randomly and can then pass current (blue), and then closes randomly (downward deflections, downward arrows). The Open probability may be defined as the fraction of the time that the channel spends in the open state.

At this point, it is worth noting a further complexity; just because a channel doesn't pass ions does not mean that it is closed. A third state, known as an inactivated state is where ion permeation through the channel is prevented despite the

channel not being gated closed. Some channels exhibit this type of gating termed *inactivation gating*. On a trace such as the one shown in Figure 1.5, if the channel exhibits inactivation gating, then the lower current level represents a combination of closed and inactivated as both states do not pass current; a timecourse at a single voltage, such as Figure 1.5 is not capable of distinguishing between the two.

Channels are *gated* by stimuli; for example, voltage-gated channels open and close in response to changes in voltage, ligand-gated channels open and close in response to ligand binding. The physical (structural) part of the channel which controls the opening and closing is known as the *gate*. With this new complexity, and with the help of two types of channel, the voltage-gated sodium channel and a potassium channel, we can now add a few further definitions which are commonly used incorrectly.

Activation refers to the opening of a channel in response to a stimulus as shown in the grey shaded area in Figure 1.6. *Deactivation* refers to the closing of a channel in response to a removal of stimulus as shown in the green shaded area in Figure 1.6. Deactivation is therefore the opposite of Activation.

By contrast, *inactivation* refers to the cessation of ion flow by a mechanism other than channel closing while still in the presence of a stimulus. When inactivated, a channel cannot be opened by their usual stimulus. This is represented by the red shaded area in Figure 1.6 The opposite of inactivation is referred to as *recovery*, where the channel is returned to a state where it is able to activate/deactivate by its usual stimulus. This is not shown in Figure 1.6 as there is no current through both inactivated and closed channels so one cannot see this transition on a simple voltage-step.

These processes can be seen both at the microscopic level (middle Figure 1.6), and the macroscopic level, (bottom Figure 1.6). The process is perhaps easier to see for the macroscopic recordings where the stochastic process of single channels opening and closing averaged out, such that the gating by the stimulus can be clearly seen. On the macroscopic level, we can define open probability (P_o) in a slightly different way, as a fraction of open channels at any given time.

$$P_o = \frac{N_{Open}}{N_{Total}} \tag{1.7}$$

For completeness, there are a number of other processes that ion channels can exhibit. Many ligand-gated channels exhibit *desensitisation*, where sustained agonist binding causes channels to enter a state which is refractory to activation. Ligand-gated channels that undergo this process must recover in order to be available for response by ligand binding. For simplicity, this is not shown in Figure 1.6, but is similar to inactivation in voltage-gated channels, but the stimulus is ligand-binding not changes in voltage.

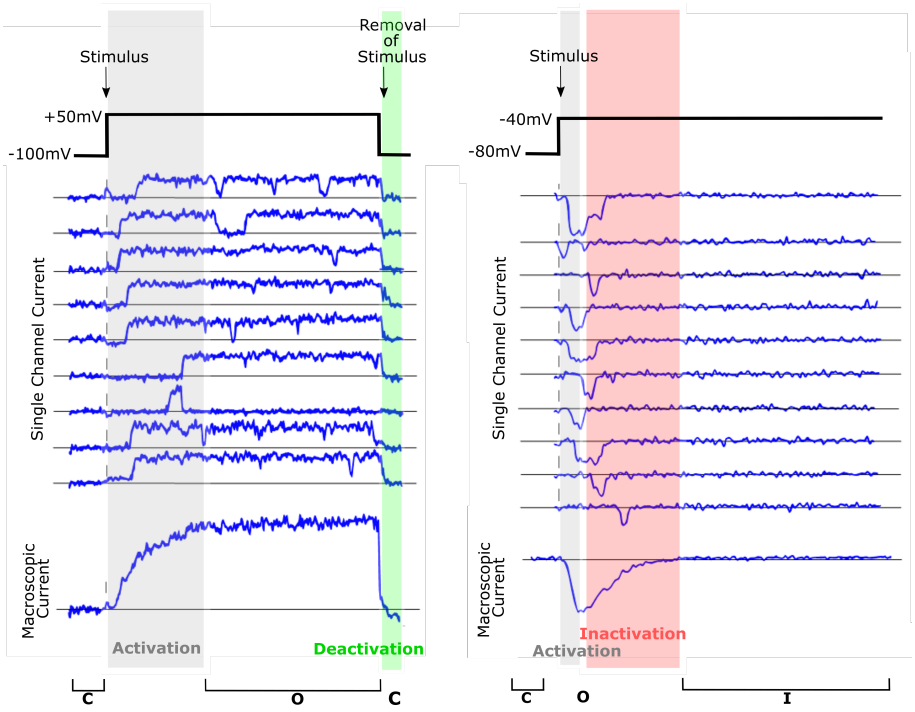


Figure 1.6: **Gating Processes at the Microscopic and Macroscopic levels**
Left: A typical K channel trace. Upon application of a stimulus (here, a voltage pulse from -100mV to +50mV (black line and arrow)), individual K conductances can be seen after opening (single upward deflections) as an increase in current (middle panels). Channels can open at any point in the presence of a stimulus. Upon the removal of a stimulus (green), channels deactivate (downward reflections). The sum of all of the single conductances can be used to generate a macroscopic current trace where a slow time-dependent activation upon application of a stimulus (grey) and fast time-dependent deactivation after the removal of the stimulus (green).
Right: A typical Na channel trace. Upon application of a stimulus (here, a voltage pulse from -80mV to +40mV, black line and arrow), individual Na conductances can be seen immediately after opening (single upward deflections) as an increase in current (middle panels). Current can only be seen immediately after stimulation. While still in the presence of the stimulus, channels inactivate (downward reflections). The sum of all of the single conductances can be used to generate a macroscopic current trace where a fast time-dependent activation upon application of a stimulus (grey) and slow time-dependent inactivation in the presence of a stimulus (red).
Figure adapted from Hille (1992) with permission of PLS.

1.2.3 I-V curves

Now we know that ion channels are not simply pores, but are gated, it is important to consider how an ion channel behaves in response to changing voltage. In symmetrical ionic conditions, the current-voltage relationship can be described by Ohms law as in Equation 1.8, the slope of which is the conductance (G), the reciprocal of resistance (R).

$$I = \frac{V}{R} = GV = G(V_m - E_x) \tag{1.8}$$

where:

I	=	Current (A)
V	=	Voltage (V)
R	=	Resistance (Ω)
G	=	Conductance (S)
$V_m - E_x$	=	Driving Force (V)

However, in reality, I-V curves are rarely linear; they often show *rectification*; asymmetric current flow in opposite directions. This is due to the fact that the the conductance of the channel is a non-linear function of a number of variables including voltage, ion concentrations and temperature. For example, if a channel is gated by voltage, then in addition to changing the driving force, the current will also change due to the voltage changing the Open Probability (P_o). The current also depends on the single channel conductance (γ) and the number of channels present (n). In reality, unless the ionic conditions are very asymmetric, or there is a voltage-dependent block, the single channel conductance is very unlikely to change when changing voltage. Taking this all together, the I-V relationship of a channel can be better described by the non-linear Equation 1.9, where the G term from Equation 1.8 is expanded to include the Open Probability, the number of

channels and the single channel conductance.

$$I = n\gamma P_o(V_m - E_x) \tag{1.9}$$

where:

I	=	Current (A)
n	=	Number of channels (V)
γ	=	Single Channel Conductance (S)
P_o	=	Open Probability
V_m	=	Membrane voltage
E_x	=	Equilibrium Potential for ion x
$V_m - E_x$	=	Driving Force

1.2.4 Selectivity

Ions will not simply move through any channel if a driving force exists; the channel through which it is going through needs to be permeable to it. Selectivity is a relative term, so for clarity we will use the definition from Roux (2017):

> "At the simplest level, the word "selective" indicates that ions of the "correct" type can permeate through these channels more easily (i.e. at a faster rate) than ions of the "wrong" type."

It is generally accepted that selectivity occurs at the narrowest constriction of the ion permeation pathway, a region called the selectivity filter (SF). Immediately this indicates that the size of the ions compared to the pore is important. One can clearly see how a channel is able to physically occlude all ions larger than its SF. However, this 'molecular sieve' mechanism (Hille, 1992) is too crude to account for the astonishing selectivity that some ion channels can exhibit. Take

for example a potassium channel which is about 100x more permeable to potassium than sodium, despite the fact that the ionic radius of a sodium ion is actually smaller than that of a potassium ion. In reality channels use a combination of steric, coulombic and chemical mechanisms to favour permeation of the "correct" ion, even in a mixture of ions where the concentration of the "wrong" ion dominates. Specific details of how this is achieved in sodium and potassium channels is discussed later.

The selectivity of a single species of ion channel can be deciphered from the I-V curves from the reversal potential, that is, the voltage at which the channel current reverses direction- i.e. zero amperes (Equation 1.9 explains why). Assuming that γ is non-zero, that is, the channel is permeable to the ion, **only** when the membrane potential V_m is equal to the Reversal potential E_x for the permeant ion, the current (I) will be zero. For a perfectly selective channel (a channel through which only a single type of ion can pass) the Reversal Potential (E_{Rev}) will equal the Equilibrium Potential (E_x) for that ion. Often the selectivity of a channel is expressed as a *permeability ratio* between two ions (p_x/p_y). By conducting experiments in the presence of only those two ions, this permeability ratio can be calculated from the Reversal Potential by rearrangement of Equation 1.5.

1.2.5 Electrical Properties of Membranes

In order to understand structure-function relationships as well as the pharmacology of channels, we need to be able to record their function in real time. Fortunately, as their major function is to conduct ions, we can measure the movement of the ions across the membrane. However, because we require the channels to be in a membrane environment, there is another important electrical element we need to consider.

The lipid bilayer itself has a thickness of 30-40Åand there is an electric field across it. As such, it makes a capacitor of capacitance (C), meaning it is able to store charge (Q) when a transmembrane voltage (ΔV) is applied across it, as shown in Equation 1.10.

$$Q = C\Delta V \tag{1.10}$$

where:

Q = Stored Charge (C)

C = Capacitance (F)

ΔV = Transmembrane voltage (V)

The capacitance C is proportional to the area and inversely proportional to the membrane thickness. Given that the membrane area is large, the capacitance is large and scales with cell size. Charge is only stored in a capacitor (the membrane) when there is a change in voltage across it, as shown in Equation 1.11.

$$I = C\frac{dV}{dt} \tag{1.11}$$

where:

I = Current (A)

C = Capacitance (F)

dV/dt = Change in transmembrane voltage over time (Vs^{-1})

1.2.6 Studying Ion Channels in Membranes

The current flowing across the membrane (I_M) is therefore the summation of currents flowing through ion channels (I_i) and the capacative current of the membrane (I_C), as shown in 1.12 below. Any current we record from the membrane will therefore represent both of these entities. It is for this reason that membranes containing ion channels are modelled as Resistor-Capacitor (RC) circuits, as shown in Figure 1.7. These are the basis of Hodgkin and Huxley's equations which we introduced in Equations 1.1-1.3). One important thing to notice in Equation 1.12 is that the capacative current is only present when the voltage changes. This needs to be taken into account during voltage changes (see later) but means that while the voltage is being held at a constant voltage, i.e. $dV/dt = 0$, then the recorded membrane current (I_M, Equation 1.12) is given solely by the ionic current (I_i, Equation 1.12), which is exactly what we are interested in.

$$I_M = I_i + I_C = I_i + C_M \frac{dV}{dt} \tag{1.12}$$

where:

I_M	=	Membrane Current (A)
I_i	=	Ionic Current (A)
I_C	=	Capacative Current
C_M	=	Membrane Capacitance (F)
dV/dt	=	Change in transmembrane voltage over time (Vs^{-1})

Now we understand what we are measuring, it is important to explain how the measurements are performed. The set up involves gaining access to the inside of the cell with a recording electrode. When the recording electrode has electrical contact with the cell interior, there are two major modes of experiment that one can use to measure ion channel activity; namely Current-Clamp (CC) and voltage-

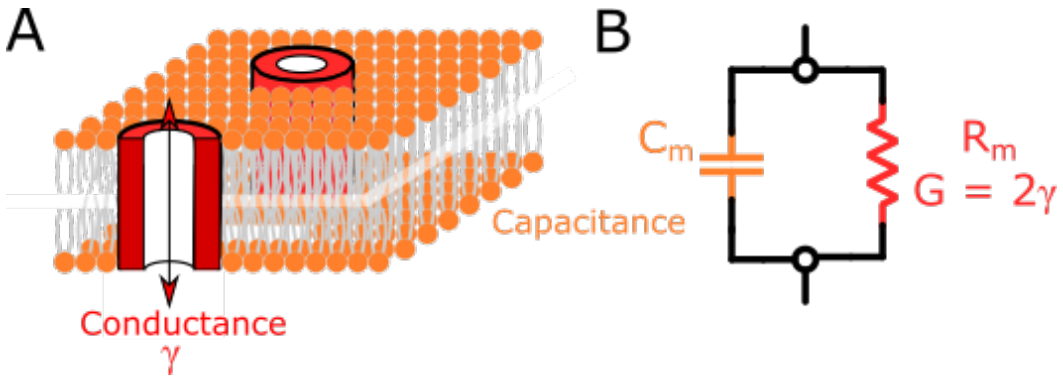


Figure 1.7: **RC Circuit of a Channel in a Membrane Environment**
A: Cartoon representation of two ion channels (red cylinders) in a lipid bilayer membrane (orange and grey). The physical separation of charge on the membrane results in a capacitance across the membrane (orange), while the ability of ions to flow through open channels (red) results in a conductance across the membrane.
B: Electrical equivalence RC Circuit. The channel in a membrane environment may be modelled as a parallel circuit consisting of a resistor (red) of resistance R_m representing the channel and a capacitor (orange) of capacitance C_m representing the membrane. As the resistors are in parallel, the conductances sum such that for the two channels here, the membrane conductance (G) is equal to the sum of the two single channel conductances.

clamp (VC) modes.

Current-clamp techniques involve injecting a defined amount of current (i.e. not true 'clamping') and allowing the transmembrane voltage to freely change. The transmembrane voltage (V_m) changes by virtue of changes in permeability of the membrane over time through the concerted action of many different ion channels. The experimenter records the transmembrane voltage. This is the set-up typically used to measure Action Potentials.

By contrast, voltage-Clamp involves controlling the voltage across the cell membrane and recording the current injection required to keep the transmembrane voltage at the level given by the experimenter (i.e. true 'clamping'). Generally voltage-clamp set-ups are used to record the currents flowing through channels

of single type, and by extension can be used to monitor the effects of mutations, drugs and other stimuli. As this is the major electrophysiological technique used in this thesis, we shall expand further on these types of experiments.

1.2.7 Voltage Clamp Techniques

The injected current flows locally across the membrane (as an ionic current through open channels) and as a capacitive transient (as the membrane charges and decharges) as shown in Equation 1.12. Ionic permeability changes can be rapid and so a feedback amplifier is required to continually readjust the current injection and keep the voltage clamped at a level defined by the experimenter.

This type of experiment can take a number of arrangements, many of them not relevant to this thesis. Here I will summarise two key setups; namely the two microelectrode and the patch clamp sets ups.

1.2.7.1 Two Electrode voltage Clamp

Two Electrode voltage Clamp (TEVC) involves placing two low-resistance pipettes into a cell. The microelectrodes are filled with a conductive solution and are used to control the membrane potential. The experimental set-up of this configuration is shown in Figure 1.8A, while the electrical equivalent circuit is shown in Figure 1.8. One of the electrodes, the *voltage electrode* measures the voltage across the membrane (V_m), comparing it to the bath electrode (left, Figure 1.8) using a unity-gain buffer amplifier. This transmembrane voltage is then signalled into an operational amplifier which compares the voltage to a command voltage (V_{Cmd}) set by a computer. The difference between the two is then injected as a current by

the other electrode, the *current electrode* (right, Figure 1.8). The current injected then has to go to ground in order to complete the circuit. The voltage is recorded relative to ground, so whenever current is injected, the cell will pass current across its membrane in an attempt to return to its natural resting potential. This is opposed by the clamp amplifier passing current to maintain the holding potential.

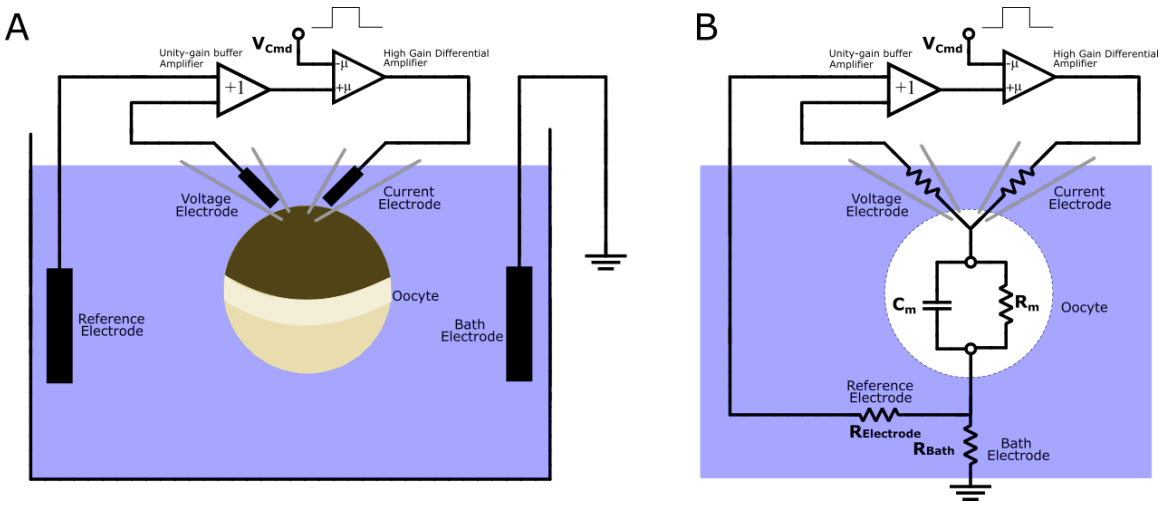


Figure 1.8: **Two Electrode voltage Clamp Experimental and Electrical Set-up**
A: Experimental Set Up for Two Electrode Voltage Clamp. The oocyte is impaled by two microelectrodes. The voltage electrode measures the voltage across the membrane (V_m) and is compared to the reference electrode which is defined as 0 by the experimenter using a unity-gain amplifier.A high gain differential amplifier then compares the membrane voltage to a command voltage (V_{cmd}) set by the computer and injects the amount of current into the oocyte to offset this voltage. This current will then flow to ground in order to complete the circuit.
B: Electrical Equivalence circuit for Two Electrode Voltage Clamp. The oocyte is modelled as an RC circuit as described in Figure 1.7 in series with the voltage and current microelectrodes.

1.2.7.2 Whole Cell Patch Clamp

There are a number of different patch clamp configurations, but all start with sealing a blunt low-resistance pipette onto the surface of a membrane using suction. This configuration is called the cell-attached mode, left, Figure 1.9A. In this mode,

there is a pipette resistance (R_p) in parallel with the resistance of the patch (R_{patch}) and the seal resistance (R_{Seal}), right, Figure 1.9A.

For the whole cell-configuration, which we will focus on, the membrane enclosed within the tip of the pipette is ruptured allowing the pipette solution to form an electrical continuity with the interior of the cell, left Figure 1.9B. In this configuration, the Seal Resistance is in parallel with the cell, again represented by a RC circuit.

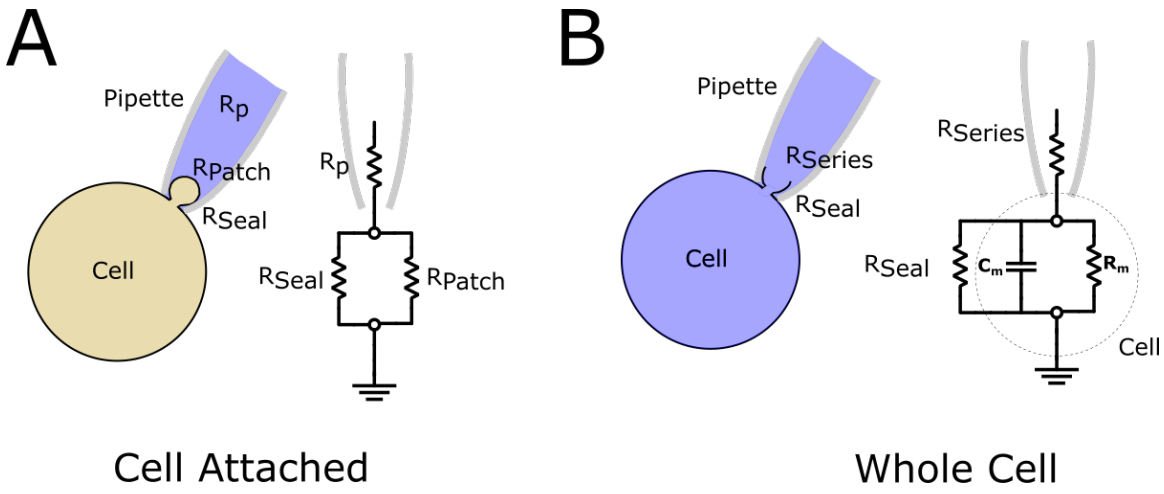


Figure 1.9: **Patch Clamp Configurations**
A: Cell-Attached Configuration. A small region of the membrane is enclosed within the tip of the recording pipette (left). The pipette resistance (R_p) is in series with the parallel patch resistance (Rp) and seal resistance (R_s) shown as an electrical equivalence circuit (right).
B: Whole Cell Configuration. The small region of the membrane enclosed within the tip of the recording pipette is burst so that the pipette solution is in electrical continuity with the whole cell (left). In this configuration, the Seal resistance is again in parallel with the cell which is represented by a RC circuit as described in 1.7, and every resistance in series with this is encompassed by the series resistance (R_{Series})

.

Here, the same electrode is used simultaneously for voltage recording and current injection. The voltage recorded at the top of the pipette is a sum of the membrane potential (V_m) and the current induced voltage-drop across the pipette,

called the series Resistance (R_{Series}), which can be compensated to some extent. The set up relies on a very high resistance amplifier which measures the voltage without drawing current.

1.3 Tetrameric Ion Channel Superfamily

The tetrameric ion channel superfamily is the largest related-group of ion channels, thought to have evolved from a common ancestral gene. The family show high sequence homology but have specialised in terms of obtaining different selectivity and different gating mechanisms. All channels have a pore domain (PD) consisting of two transmembrane helices with a membrane re-entrant loop between them which contains the SF, seen as the simplest case in the Kir channel (top left, Figure 1.10). As suggested by the name of the family, functional channels are formed by the coming together of four pore domains. A presumed gene duplication event whereby a second pore domain was added in tandem results with the membrane topology of the K2P channels (top right, Figure 1.10), from where they get their name, and means that they function as dimers rather than tetramers. Additional functionality also evolved, such as the addition of a voltage sensing domain (VSD), a four transmembrane helix bundle that associates with the pore domain and operates it, as seen in the Kv channel (bottom left, Figure 1.10). The larger mammalian Nav and Cav channels are analogous to simple 4 Kv channels in tandem and thus function as monomers (bottom right, Figure 1.10).

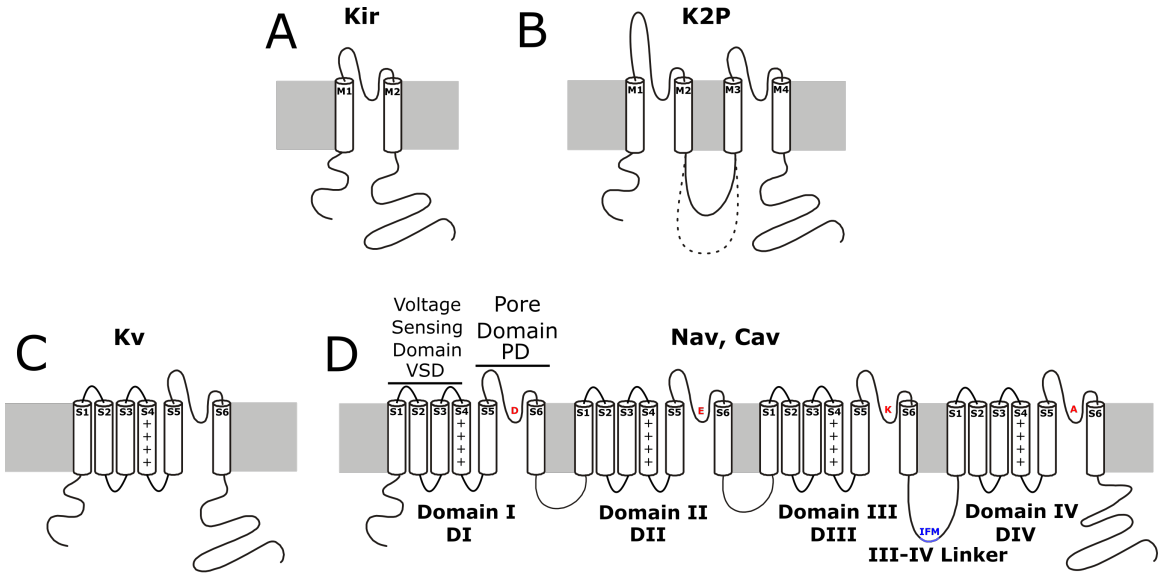


Figure 1.10: **Topology of the Tetrameric Ion Superfamily**
A: Topology of the Kir Family. The Kir subfamily consist of two membrane spanning helices M1 and M2 and membrane re-entrant loop between them. They therefore function as tetramers.
B: Topology of the K2P Family. The K2P family consist of four membrane spanning helices (M1-M4) and membrane re-entrant loops between M1 and M2 and between M3 and M4. They therefore function as dimers.
C: Topology of the Kv Family. The Kv channels consist of 6 membrane spanning helices S1-S6, the first four of which S1-S4 constitute the voltage sensing domain (VSD) while S5 and S6 and the membrane re-entrant loop between them constitute the pore domain (PD). They therefore function as tetramers.
D: Topology of Nav and Cav Families. The Nav and Cav families consist of 24 transmembrane helices split into four domains. Each domain contains 4 membrane spanning helices (S1-S4) which constitute a (VSD) and a pore domain comprising of S5 and S6 and the membrane re-entrant loop between them. They therefore function as momomers.

1.3.1 Knowledge during the Classical era

Thanks to the development of voltage-clamp techniques and later the advent of molecular cloning, these channels could be interrogated, eventually in isolation, long before visualising their three-dimensional structure was possible. During this so called 'classical era' functional data from wild-type and mutant channels were used to map the structure and provide mechanistic insights about channel gating.

Hodgkin and Huxley's work showed that the basis of the generation of an action potential in the squid giant axon was through two specialised pathways and that the conductance was voltage dependent (Hodgkin and Huxley, 1952a,b,c). They also noticed that there was no detectable outward current preceding the inward sodium current. This led to the hypothesis that they were gated only by position of a few charged particles whose distribution is modified by the membrane potential.

Hodgkin and Huxley empirical constants could be extrapolated to conclude that potassium channel opening occurs via cooperative movement of four activating '*n*' gating particles to the up-state, while sodium channel opening occurs via movement of three activating '*m*' gating particles to the up-state (transition 1, Figure 1.11), followed by a slower movement of a single inactivating '*h*' gating particle to produce inactivation (transition 2, Figure 1.11). This model, termed the Hodgkin-Huxley model, was inferred by mathematical descriptions of conductance and empirically derived constants (*n*, *m* and *h*) and provides a good baseline for mechanistic understanding of voltage gated channels (Hodgkin et al., 1952).

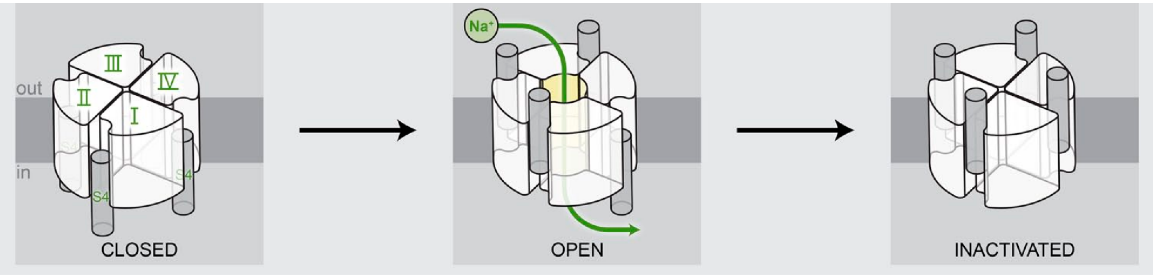


Figure 1.11: **Hodgkin-Huxley Gating Model**
For the voltage gated sodium channels, channel opening involves the movement of three activating '*m*' gating particles to the up state (transition 1). Channel inactivation occurs by a slower movement of a single inactivating '*h*' gating particle to produce inactivation where conductance through the channel is terminated.
Figure adapted from Ahern et al. (2016). Reproduced and adapted within the remit of the creative commons public license.

1.3.1.1 Discovery of Gating Currents

It took until 1973 and the discovery of gating currents for their model to be experimentally tested. Gating currents are transient currents generated by movement of voltage-sensing charges or dipoles (the gating charges) within the electric field even when the channel is closed or inactivated and directly predicted from Hodgkin and Huxleys model.

Gating currents were recorded from Skeletal Muscle (Schneider and Chandler, 1973) and Squid Axon (Armstrong and Bezanilla, 1973; Keynes and Rojas, 1973) in the absence of permeant ions and presence of channel blockers. Minute gating currents were extracted by subtraction of the linear capacity transient using voltage pulses in the region of voltage where the gating charge is not moving. The gating currents from the squid axon were rapid enough to be compatible with changes leading to the opening of the sodium channels, while the gating currents from skeletal muscle were significantly slower, but not related to K channel opening. It was not until 1982 that any gating currents were detected with similar kinetics to K+ channel activation. Using an increased temperature, a new component could

be detected which showed kinetics and voltage similar to those of K+ activation at the same temperature (Bezanilla et al., 1982).

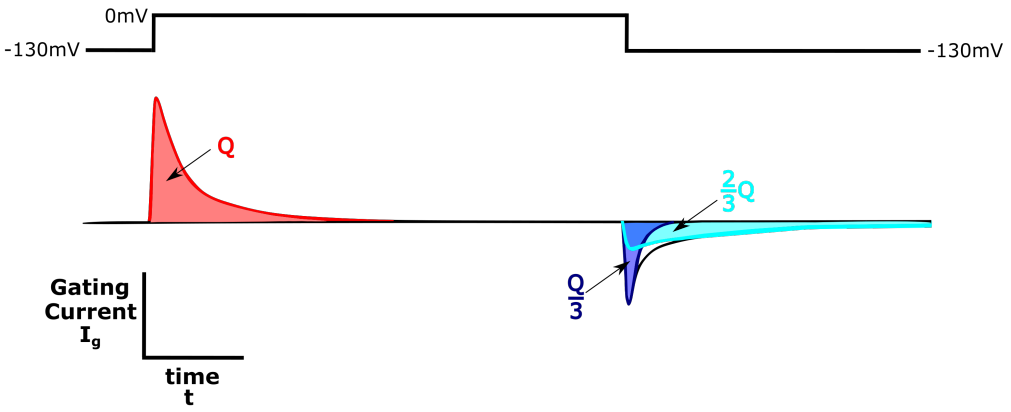


Figure 1.12: **Sodium Channel Gating Currents**
Upon depolarisation, a 'on' gating current corresponding to activation can be recorded if the channel current is prevented by either removing permeant ions and/or in the presence of channel blockers. The area under the gating current (red) is the gating charge. This matches the time course of activation. In response to repolarisation, a 'off' gating current opposite in direction could be recorded. For short depolarisations, this was the same magnitude as the on gating charge, however, for long depolarisations, the off gating charge was only about 1/3 of the on charge. This apparent violation of displacement current conservation can be rationalised by a biphasic response. The fast component carrying q/3 (blue) can readily be seen but the slow component, carrying 2/3 of charge can only be seen during short depolarisations and matches the time course of recovery from inactivation.
Figure from Bezanilla (2000) (Figure 7, p589). Reprinted with permission of APS.

Follow-up experiments of gating currents showed that the 'off' gating currents from sodium channels were greatly affected by the duration of the pulse; for short depolarisations, the 'on' charge (red, Figure 1.12) equalled the 'off' charge but for long depolarisations, the off charge was only about one-third of the 'on' charge (Armstrong and Bezanilla, 1973), Figure 1.12. This apparent violation of displace-

ment current conservation was rationalised by the involvement of two components in the 'off' gating currents. The fast component, carrying one-third of the charge is readily seen (blue, Figure 1.12), and a slow component carrying two-thirds of the charge can only be seen during short depolarisations (cyan, Figure 1.12), and matches the time course of recovery from inactivation.

Other experiments on the squid axon showed that sodium channel inactivation could be enzymatically removed by the internal perfusion of pronase, without affecting the activation, voltage-dependence or off kinetics (Armstrong et al., 1973), suggesting that inactivation was not directly caused by the inactivation particle as proposed by Hodgkin and Huxley.

To rationalise these observations, Armstrong and Bezanilla proposed a coupled inactivation model of sodium channels (Bezanilla and Armstrong, 1977; Armstrong and Bezanilla, 1977) as shown in Figure 1.13. During a depolarisation, the voltage sensor repositions the activation charge to open the channel (transition 1, Figure 1.13). Then a second conformational change in the channel prevents conduction and at the same time prevents movements of up to two-thirds of the activation charge that moved to open the channel. This second conformational change they suggested to involve a ball and chain like mechanism which hinders downward gating charge movement (transition 2, Figure 1.13). Upon repolarisation, the other two thirds of the charge returns as the inactivation is recovered.

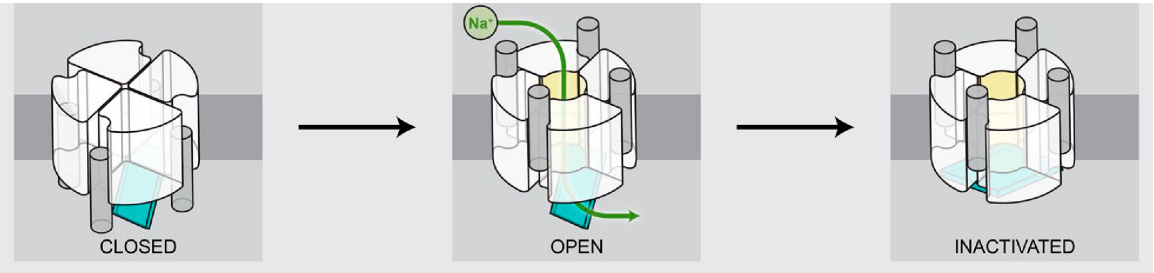


Figure 1.13: **Coupled Inactivation Gating Model of Sodium Channels**
For the voltage gated sodium channels, channel opening involves the movement of four gating particles (m^3h) to the up state (transition 1). When all four gating particles are in the up position, the closing of an inactivation lid (blue) is triggered (transition 2) and ion flow through the channel is terminated.
Figure adapted from Ahern et al. (2016). Reproduced and adapted within the remit of the creative commons public license.

1.3.1.2 Advent of Molecular Cloning

The sodium channel was shown to be composed of a principal alpha subunit of 260kDa and one or more beta subunits using Ultraviolet (UV)-induced covalent labelling of total protein extracted from synaptosomes using a specific scorpion toxin (Beneski and Catterall, 1980). With the arrival of molecular cloning, the primary structure elucidiation of the electric eel (*Electrophorus electricus*) EeNav1.4 followed (Noda et al., 1984). Using hydropathy analysis, they correctly predicted that the single polypeptide chain contained 24 helices arranged as 6 repeats. One putative helix within each repeat (S4) contained a large number of positive charges which they tentatively suggested as a candidate for the gating particle first postulated by Hodgkin and Huxley some 32 years before. This membrane topology and highly charged S4 was confirmed to be typical of the group when the first shaker K^+ channel from Drosophila was cloned (Tempel et al., 1987), as shown in Figure 1.14.

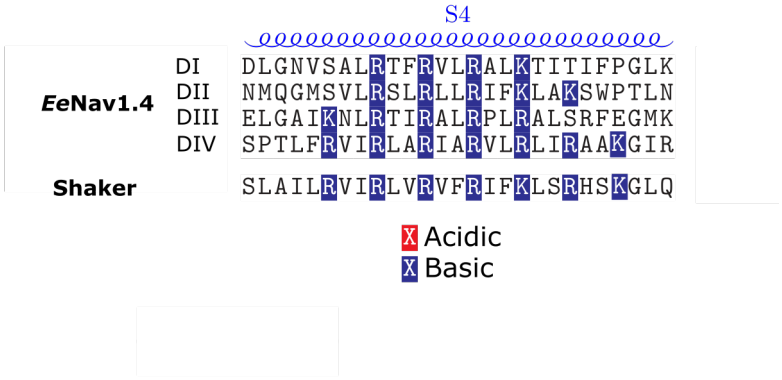


Figure 1.14: **Sequence Alignment of S4**
Cloning of the eel Nav1.4 sodium channel revealed that the putative transmembrane helix S4 in all four domains contained a large number of Basic residues separated by two amino acids (Rxx). Cloning of the shaker channel also revealed a high number of basic amino acids in the putative S4, also separated by two other amino acids.

The ability to clone channel DNA and study overexpressed channels in heterol-

ogous expression systems set the scene for an era where isolated channels could be mapped using toxins and critical residues could be assigned to parts of the protein by mutagenesis studies.

1.3.1.3 Gating Currents in Heterologously Expressed Channels

Gating currents could not be measured at the single channel level and so their properties were probed using analysis of the fluctuations of the ensemble gating currents. To work out whether the movement of the gating charge was continuous or discrete, gating currents were measured from *X. laevis* oocytes injected with sodium channel mRNA and were found to be similar to the gating current recorded from native nerve preparations and showed a shot-like (i.e. instantaneous) character of individual gating current contributions. Most of the gating charge movement that accompanies sodium channel activation occurs in 2 to 3 brief packets each carrying 2.3 electron charges (e0). This shot-like process was later confirmed in a shaker K^+ channel with slower kinetics (Stefani et al., 1994; Bezanilla et al., 1994)

The first gating current recorded from the shaker K^+ channel showed that the charge on the voltage sensor was progressively immobilised by prolonged depolarisations, but this charge was not immobilised in a channel mutant where the inactivation particle is removed (hereby named shaker-IR) (Bezanilla et al., 1991). The total charge moved per channel was measured to be 13e0 in both wild type shaker and shaker-IR(Schoppa et al., 1992), roughly 6 orders of magnitude smaller than the ionic currents flowing through the channels. This result was confirmed by a number of other studies in the shaker channel (Noceti et al., 1996; Seoh et al., 1996) and a sodium channel (Hirschberg et al., 1995).

The conclusive proof that the currents that had been measured in the last decade were indeed movements of the gating charges came from the heterologous expression of a non-conducting shaker in *X. Laevis* oocytes, where a mutation in the putative pore region completely abolished ion conduction without affecting gating charge. The non-conducting mutant could still undergo the closed-open transitions (Perozo et al., 1993).

1.3.1.4 Mapping of the Potassium Channel Pore using toxins

A combination of scorpion toxins, small molecule inhibitors and non-physiological ions were used to map the potassium channel pore in the absence of an overall appreciation for the three dimensional structure.

Mutations affecting affinity of charybdotoxin defined a binding site for the toxin on the outer mouth of the pore between the putative S5 and S6 helices, and containing a highly conserved stretch of eight amino acids termed the K+ signature sequence (MacKinnon and Miller, 1989; MacKinnon et al., 1990; MacKinnon and Yellen, 1990). A similar approach using the quarternary ammonium TEA (MacKinnon and Yellen, 1990; Yellen et al., 1991; Kavanaugh et al., 1991, 1992) also implicated this region as the pore.

Movement of a 21 amino acid segment from a voltage-activated potassium channel NGK2 to another potassium channel DRK1 with very different pore properties conferred the biophysical properties of the donor channel suggesting that this region may form the conduction pathway (Hartmann et al., 1991). Channel properties could also be transferred from channel to channel via relatively subtle changes in this conserved region (Heginbotham et al., 1992; Kirsch et al., 1992).

Mutations in S5 were able to enhance passage of ammonium and rubidium ions which are larger than sodium, without compromising the ability to exclude the smaller sodium cation (Yool and Schwarz, 1991). The potassium channel SF was defined as TXGYG by recording mutant channels in bi-ionic conditions (Heginbotham et al., 1994). As well as its crucial role in ion selectivity, the SF was implicated in C-type inactivation by mutagenesis and effects of external cations ((López-Barneo et al., 1993; Liu et al., 1996; Starkus et al., 1997).

1.3.1.5 Mapping of the Sodium Channel Pore using toxins

In an analogous fashion, a combination of toxins/ drugs and mutagenesis were used to map the sodium channel pore. Tetrodoxin (TTX), a pore-blocking toxin from the puffer fish fugu and local anaesthetics respectively mapped the inner and outer mouth of the pore to the loop between transmembrane helices S5 and S6.

Neutralisation of a conserved glutamate residue in each of the repeats prevented TTX block of a TTX-sensitive brain channel, identifying the pore as a negatively charged ring on the outer side of the channel (Noda et al., 1989). Cardiac and denervated skeletal muscle sensitivity to TTX could be introduced by replacement of an adjacent cysteine to a tyrosine (naturally found in the brain variant), further confirming the importance of this region in the outer mouth of the pore (Satin et al., 1992). Such mutations that alter TTX sensitivity also had effects on single channel conductance and selectivity. Neutralisation of a conserved aspartate almost completely abolished the sodium current but not the gating current showing that these channels were present in the membrane and had normal voltage-dependence and further reinforcing the role of this region in the pore (Pusch et al., 1991).

The sodium channel SF sequence was ultimately determined to be DEKA; whilst the corresponding calcium channel sequence was EEEE. These signature motifs refer to the contribution of one residue from each domain (DEKA = Domain I D, Domain II E, Domain III K, Domain IV A) (Favre et al., 1996). Mutation of sodium channel K or A to EE allowed a sodium channel to resemble a calcium channel in its selectivity properties, such as divalent block and permeation of monovalent cations (Heinemann et al., 1992). This provided evidence that these residues constituted part of the SF and lie within the permeation pathway.

1.3.1.6 Identifying the voltage-sensor

A number of studies provided evidence that suggested but could not prove that the S4 helix was the voltage sensor. Mutations in the S4 sequence were shown to alter the voltage-dependence of the channels (Papazian et al., 1991) and the gating charge (Liman et al., 1991; Logothetis et al., 1992). The total gating charge per channel was measured in shaker channels containing neutralisation mutations of conserved charged amino acids in putative S2, S3 and S4 helices. Of the eight residues tested, four contributed significantly to the gating charge: the innermost acidic residue in S2 (but not the outermost) and 3 basic residues in S4. The maximal *Po* was unchanged by the neutralisation mutations suggesting that the open position in the voltage sensor was unperturbed (Seoh et al., 1996).

A simultaneous study tested six of the seven charges in S4 using a K^+channel-specific radioligand to determine the origin of the gating charges within the shaker channel. Charge-neutralisation of the outermost positive charges led to large decreases of about 4e0 in the gating charge, while a mutant where 10 non-basic

residues in S4 were mutated was identical to Wild type (Aggarwal and MacKinnon, 1996).

Although the estimates in each study gave slightly different contributions of individual charge, mainly stemming from the differential expression systems and ways of estimating charge and number of channels, the consensus emerged that the most extracellular 4 charges were the most important, each contributing about 1e0 to the total gating current. The fifth charge has a smaller contribution, while the sixth charge does not participate. It follows that the charged residues on the extracellular side seem to be more important, and those on the intracellular side may be involved in stability of the overall fold (Tiwari-Woodruff et al., 1997). That being said, it is impossible to define clearly the contribution of each gating charge in such a way, as charge neutralisation not only removes the gating charge from the presumed movement but also alters the apparent electric field felt by the other gating charges.

Based on this data, Papazian and Bezanilla proposed that the first four charges in S4 lie in a narrow aqueous crevice continuous with the intracellular medium in the closed state and the extracellular medium in the open state. Importantly, translocation between these two states upon depolarisation involves limited movement of the S4 and requires a focused electric field (Papazian and Bezanilla, 1997).

1.3.1.7 Voltage-Sensor movement

The voltage-sensor was shown to move in response to changes in voltage by a number of experiments. The first evidence came from state-dependent modification of a cysteine-mutated S4 arginine in the skeletal muscle Na channel. The rate of modification by an MTS reagent was dependent on the applied voltage suggest-

ing different arginine exposure at different voltages (Yang and Horn, 1995). A more detailed study of other charged residues was used to define the roles of the individual arginine residues within S4, which was consistent with similar experiments conducted in the shaker potassium channel by cysteine-scanning mutagenesis (Larsson et al., 1996), preserving charge (Yusaf et al., 1996) and using a fluorescent reporter (Baker et al., 1998).

Taken together, the experiments showed that R1 was outside, independent of the voltage. R2 and R3 were inside at hyperpolarised potentials and outside at depolarised potentials and R4 and R5 were inside independent of the voltage. Taken together it suggested that R2 and R3 move from inside to outside upon depolarisation.

Similar studies in the shaker-IR channel using histidine-scanning mutagenesis allowed charge on the S4 to be changed within a single experiment based on the solvent accessibility of the histidine and the resultant gating charge to be measured (Starace and Bezanilla, 2001). These elegant experiments showed the same results as the state-dependent cysteine modification but also implicated the first gating charge in moving upon changes in voltage. These results were echoed by fluorescent labelling of two positions in the S3-S4 linker and three positions in the putative S4 helix of the shaker-IR channel which revealed that charged residues in S4 are preferentially labelled in depolarised conditions whereas residues in the S3-S4 linker equally labelled in hyper- and de-polarising conditions (Mannuzzu et al., 1996).

In order to measure molecular distances, lanthanide based Förster resonance energy transfer (FRET) was used to measure lifetimes of mutated cysteine attached to lanthanide chelators and fluorescein in oocytes (Cha et al., 1999b). They mea-

sured energy transfer from several sites across the VSD. The tested site in S4 did not show changes in distance with voltage, but three sites in the S3-S4 linker showed distance changes: the first measurement of an actual distance change in response to voltage. This suggested that the S4 moved perpendicularly to the channel pore by means of a rotation as the technique was only capable of measuring radial distance.

1.3.1.8 Identification of the fast inactivation machinery in Nav Channels

The ability to prevent fast-inactivation by intracellular perfusion of pronase was the original evidence that suggested that inactivation might work by an intracellular particle (Armstrong et al., 1973). Channels with a clipped Domain III and Domain IV linker had impaired inactivation (Stühmer et al., 1989), while antibodies directed against the III-IV linker disrupted inactivation (Vassilev et al., 1989), suggesting a role of the DIII-IV linker in inactivation.

Site directed mutagenesis of the domain III-IV linker showed that mutation of charged residues or internal deletions of the domain III-IV linker are tolerated (Moorman et al., 1990; Patton et al., 1992), but mutation of the highly conserved putative intracellular particle residues IFM to QQQ (the Q^3 mutation) abolished fast inactivation (West et al., 1992). The structure of the ~53 residue linker was revealed to be largely disordered, aside from a short α- helical segment, by solution Nuclear Magnetic Resonance (NMR) (Rohl et al., 1999).

The receptor for the IFM motif proved to be elusive but was thought to involve the domain III S4-S5 linker (Smith and Goldin, 1997), domain IV S4 (Chen et al., 1996) and domain IV S4-S5 loop (McPhee et al., 1998).

Owing to the fact that the sodium channel is a single polypeptide chain, individual domains could be probed more readily than the tetrameric shaker channel. Using site-directed fluorescence labelling, the contribution of each voltage sensor to the the $\frac{2}{3}$ of immobilised charge caused by inactivation was tested. The fluorescence kinetics matched the time course of activation and deactivation when the fluorophore was attached to the S4 of domain I or II, and inactivation had no influence on the movements detected (Cha et al., 1999a). By contrast, in domain III, a component of the fluorescent signal followed the superposition of the activation time course and the inactivation time course. This result was more pronounced in domain IV. Taken together, it suggested that the non-immobilisable components are domains I and II and domains III and IV are the gating charges that are immobilised by the inactivation particle (Cha et al., 1999a). This result agreed with the electrophysiology studies outlined above.

1.3.2 The Structural Revolution

1.3.2.1 X-ray Crystallography of Membrane Proteins

The requirement of X-ray crystallography for high resolution structures hindered structural progress in the membrane protein field. Researchers turned towards simpler channels cloned from bacteria, particularly extremophiles to aid their crystallisation attempts in lieu of their eukaryotic counterparts. Eukaryotic channels are extensively glycosylated, have much longer loops and express poorly and are thus not usually tractable for X-ray crystallography. In their stead, bacterial channels were and continue to be used as structural surrogates; their immense value demonstrated through their high conservation and modularity, allowing design of a Nav1.7-selective small-molecule antagonist against a human Nav1.7-NavAb chimera (Ahuja et al., 2015).

1.3.2.2 Structural Basis of Potassium Channel Selectivity

The molecular determinants of potassium channel selectivity were solved by the seminal publication by Mackinnon and colleagues who solved the structure of the K channel from *Streptomyces Lividans* (KcsA, PDB: 1BL8, (Doyle et al., 1998)), a bacterial homolog of a potassium channel which became the workhorse of the field for decades. The four-fold symmetric structure (Figure 1.15A) was reminiscent of an inverted teepee and showed that the ion conduction pathway was formed by two regions, a filter and a water-filled cavity, and is physically occluded at the intracellular side by a gate, termed a helix-bundle crossing (HBC) gate based on the structural features (Figure 1.15B).

This structure, along with Fab-stabilised higher resolution structures in high and low potassium (PDB: 1K4C, (Zhou et al., 2001)) elegantly explained the ability of potassium channels to be highly selective for potassium over sodium. The pore helices (P, Figure 1.15) place the carbonyls of a membrane re-entrant loop containing the highly conserved TXGYG motif into a narrow constriction which acts as a water-mimetic pore; mimicking the hydration of potassium ions in bulk solution. Potassium ions are coordinated by the carbonyl backbone of GYGV and the side-chain hydroxyl group of the threonine (Figure 1.15C). In addition, the hydrophobic residues which form the water-filled cavity ensure that the potassium only interacts with the channel sparingly; ensuring fast conduction. Computational modelling of the SF showed that potassium is only able to move through the pore when it is dehydrated (Bernèche and Roux, 2001). This process is far too energetically expensive to do for sodium ions (Morais-Cabral et al., 2001). In the higher resolution structures, the hydration shell could easily be seen.

The ability of both small molecule and protein toxins evolved against mammalian channels to bind to and modulate bacterial homologs emphasised the conservation of the channels between prokaryotes and eukaryotes (MacKinnon et al., 1998). The SF and basic architecture was shown to be typical of the potassium channels upon the elucidation of the structure of the calcium-gated potassium channel from *Methanobacterium thermoautotrophicum* (MthK, PDB: 1LNQ, (Jiang et al., 2002)), voltage-gated Potassium Channel from *Aeropyrum Pernix* (KvAP, PDB:1ORQ, (Jiang et al., 2003) and an inwardly rectifying potassium channel (KirBac3.1, PDB: 2QKS, (Nishida et al., 2007)).

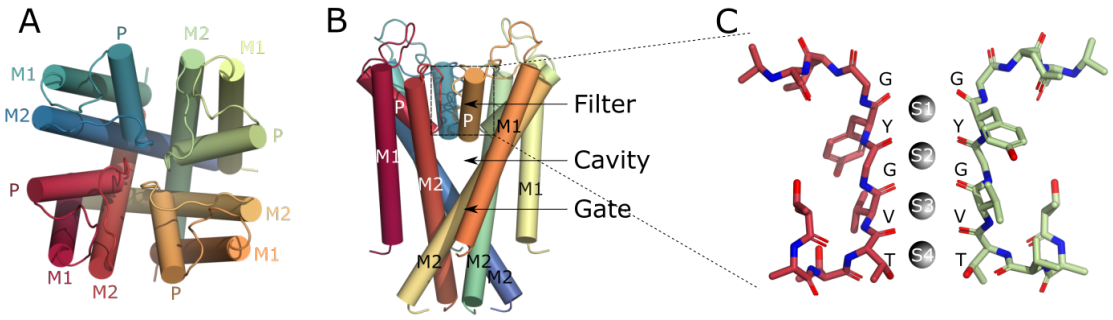


Figure 1.15: **KcsA Structure and Potassium Selectivity**
A: KcsA structure (PDB: 1K4C) as viewed from the extracellular side showing the transmembrane helices M1 and M2 and pore helix (P) from each subunit of the tetramer forming a ion conducting pore down the centre.
B: KcsA structure as viewed from within the membrane plane showing the SF, a water filled cavity and an intracellular gate formed by the bundle-crossing of the M2 helices.
C: Close up of the SF showing that the S1, S2, S3 and S4 K+ sites are formed by the carbonyls of the GYGVT SF sequence while the S4 site additionally involves the side chain hydroxyl of the threonine (T). Oxygen atoms are coloured red and nitrogen atoms are coloured blue.

1.3.2.3 Potassium Channel Gating from KcsA, MthK and Shaker

In terms of gating, the classical inverted teepee structure of KcsA clearly showed a constriction at the intracellular side formed by the HBC which would prevent ion flow and assumed to be the gate. In the second solved Potassium structure of the Ca^{2+}-gated potassium channel MthK, the bundle crossing was splayed open. This basic structural unit was assumed to be gate in potassium channels, operated by pH in pH-gated channels such as KcsA, by calcium in MthK, by ligand binding in Kir channels and by voltage (operated by the VSD) in voltage-gated channels, thus unifying the potassium channels by a single gate. The inner helices in this structure were bent at a highly conserved glycine, herein referred to as the 'hinge' glycine.

However, this idealised picture became clouded shortly after by free energy molecular dynamics (MD) simulations, where they showed reorientation of two peptide bonds (herein called the 'carbonyl flip') in the SF of KcsA leading to stable non-conducting states, for the first time suggesting the SF as a gate in addition to its critical role in potassium selectivity (Bernèche and Roux, 2005). They suggested that the SF could be the molecular determinant of C-type inactivation amongst other gating events. Accordingly, the original KcsA and KcsA-Fab structures was annotated as closed—open (C—O) a highly adopted nomenclature signifying that the HBC gate is closed and the SF gate is open. Ion conduction can only occur when both gates are open.

In a seminal publication, proton-dependent activation in KcsA was shown to be followed by an inactivation process with the hallmarks of C-type inactivation. Using site-directed mutagenesis, they discovered a mutation (E71A) in the pore helix which was capable of abolishing inactivation (Cordero-Morales et al., 2006). Crys-

tal structures of the E71A mutant allowed both conformations of the carbonyl flip to be captured. In one conformation, E71A was flipped outwards (PDB: 2ATK) and in the other conformation E71A was non-flipped (PDB: 1ZWI), for the first time showing a range of conformations of the SF. In the same study, they used electron paramagnetic resonance (EPR) spectroscopy to show that the HBC gate opens maximally at low pH (i.e. is the activation gate) irrespective of the single channel open probability, suggesting that the SF is the major gate (Cordero-Morales et al., 2006).

The first Open—Inactivated (O—I) structure was fortuitously captured by a series of open KcsA structures in which TM2 was captured with different degrees of splaying of the TM2 helices in the same conditions (PDB: 3HPL and 3FB7, Cuello et al. (2010)). The structures showed reduced K occupancy in both the S2 and S3 sites caused by backbone conformation rearrangements at or near Gly77, suggesting a non-conductive state. These structures show the first structures of a C-type inactivated K channel. In the same issue, the same authors suggested a structural basis for coupling between the activation gate and the SF. They suggested that the TM splaying causes a steric clash at channel mouth, affecting a conserved network of Hydrogen bonds behind the pore loop and SF (Cuello et al., 2010).

Although these series of structures started to provide a mechanistic understanding of gating, selectivity and permeation in K channels, KcsA does not have a voltage sensor so the mechanism of voltage-gating remained enigmatic from a structural point of view.

1.3.2.4 Relative speeds of the voltage sensors

An important contribution to our mechanistic understanding of Nav channel function came from measurements of voltage-sensor kinetics by tagging them with

fluorescent reporters. The results showed that VSDIV moves five-fold slower than those in the first three domains (Chanda and Bezanilla, 2002). This fourth voltage sensor was correlated with the onset of inactivation and the slow ON gating charge movement.

These observations helped to develop the asynchronous gating model, where activation of VSDI-III causes channel opening (transition 1, Figure 1.16) followed by the upwards movement of VSDIV which leads to a second open state (transition 2, Figure 1.16). The upwards movement of VSDIV uncovers the binding site for the inactivation particle, allowing it to plug the pore (transition 3, 1.16).

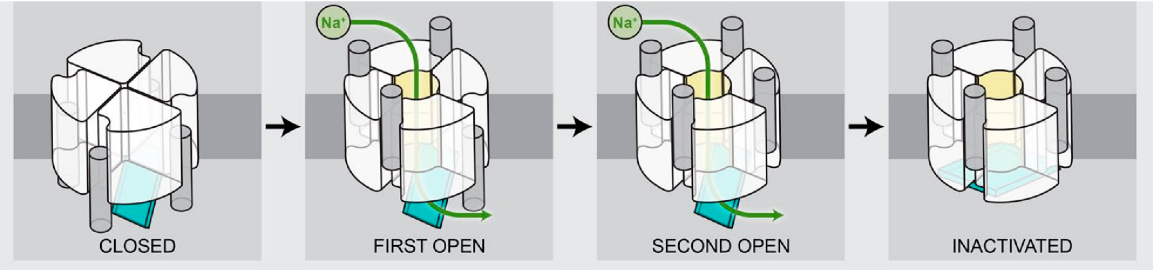


Figure 1.16: **Asynchronous Gating Model**
For the voltage gated sodium channels, channel opening involves the movement of three activating '*m*' gating particles to the up state (transition 1) to form the first open state. Upwards movement of the inactivating '*m*' gating particle to the up state then occurs to form the second open state (transition 2). Upwards movement of the inactivating '*m*' gating particle triggers the closing of an inactivation lid (blue, transition 3) and termination of ion flow through the channel. **Figure adapted from Ahern et al. (2016). Reproduced and adapted within the remit of the creative commons public license.**

1.3.2.5 The first structure of a voltage sensor

The first structure of a voltage-gated Potassium channel from Aeropyrum Pernix (KvAP) only clouded the mechanism of voltage-sensing by a modular VSD; the structure was eventually revealed to be caught in a non-native conformation caused

by the lack of lipid stabilising the protein (Lee et al., 2005), but formed the basis of studies and apparent contradictions for some years. KvAP showed all of the electrophysiological properties of the eukaryotic Kv channels and the SF was identical to KcsA, despite their different gating mechanisms. Both in KcsA and KvAP the S5 and S6 helices were anti-parallel suggesting that they move as a single unit; Li et al. postulated that this might be responsible for opening the pore by pulling the S5 and S6 helices away from the central pore axis.

The structure of the voltage sensors caused a stir and was inconsistent with previous studies. Helices S1 and S2 lay closest to S5 and helix S3, expected to be a complete helix, actually formed a broken helix, the two segments named S3a and S3b. They coined the term 'voltage-sensor paddle' to describe the unexpected S3b-S4 helix turn helix structure which was hydrophobic in nature except for the gating charges. Surprisingly, this was on its side, nearly parallel to the inner membrane surface and has since been suggested to be an artefact of crystallisation conditions (Lee et al., 2005).

1.3.2.6 Focusing of the electric field within the voltage sensor

A number of biophysics studies reinforced the idea that the electric field was focused within the voltage-sensor; inconsistent with the KvAP structure and the paddle mechanism. Electrochromic probes (Asamoah et al., 2003) showed that the electric field was concentrated more in the voltage-sensor than in the bilayer, and different side-chain length substitutions in the outermost gating charge showed that this field was focused on the position of the first gating charge in the closed state (Ahern and Horn, 2005).

Mutation of the outermost voltage-sensing arginine residues to hisitidine resulted in a proton pore (Starace and Bezanilla, 2004) which could be made into a cation pore by mutation to a small residue such as cysteine suggesting that the S4 ratchets between conformations in which successive arginine residues occupy and occlude ions in the narrowest constriction.

The first eukaryotic structure of a voltage-gated ion channel was a lot easier to digest for the ion channel community. The structure of *rattus norvegicus* Kv1.2 (shaker, PDB: 2A79, (Long et al., 2005)) showed all six transmembrane helices in the transmembrane position (Figure 1.17A and C). The S6 segments were again bent at the hinge glycine, and the pore was open. However, this time, the S4 helix traversed the membrane and placed the innermost gating charges centrally within the voltage-sensor, consistent with an activated 'up' state with an open pore (Figure 1.17C).

Although side-chain density was particularly poorly resolved in the voltage-sensor, the position of the first gating charge could be seen within a computed electric field profile which was focused as suggested by previous studies. The structure showed each voltage sensor decorating the channel pore on the periphery in a domain-swapped orientation such that each VSD is most closely associated with the PD of its neighbour, seen most clearly in 1.17B. This suggested a molecular mechanism by which conformational changes in the voltage sensor can be relayed to an adjacent subunit allowing concerted opening to a full conductance site by interaction of all four subunits (Long et al., 2005). The structure showed the voltage-sensor connected to the pore by the S4-S5 linker. Functionally the structure most likely corresponds to the open and slow-inactivation state of the channel due to the absence of an electric field.

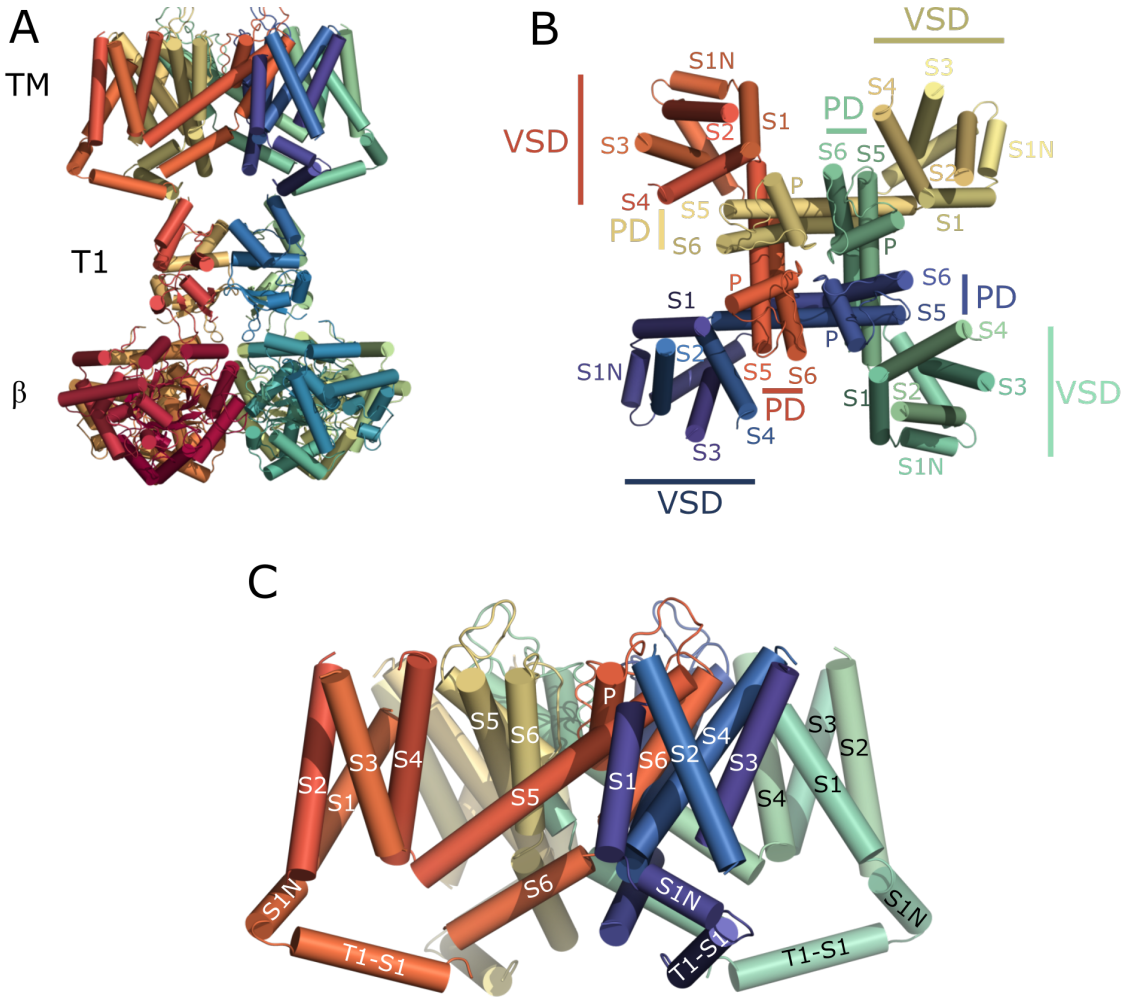


Figure 1.17: **Kv1.2 Structure**
A: Kv1.2 structure (PDB: 2A79) as viewed from within the membrane plane showing the transmembrane region (TM), the tetramerisation domain (T1) and the auxiliary beta subunits (β).
B:Kv1.2 structure as viewed from the extracellular side showing the transmembrane helices S1 to S4 of each tetramer forming the VSD (VSD) while S5 and S6 of each subunit of the tetramer form the pore domain (PD) akin to M1 and M2 in KcsA. The PD of each monomer most closely associates with the VSD of the adjacent subunit in a domain-swapped orientation.
C: Kv1.2 structure as viewed from within the membrane plane showing just the transmembrane helices, with the central pore domain being decorated by the surrounding VSDs.

The Kv1.2 structure was simulated using Molecular Dynamics and showed the two most extracellular arginine residues in contact with lipid and water on the extracellular side of the membrane. Water deeply penetrates the protein, concentrating the electric field in the extracellular half of the protein (Jogini and Roux, 2007). In light of this new structure, and increasing evidence against a paddle motion, the shaker structure was generally accepted as a typical voltage-gated ion channel structure.

1.3.2.7 A hydrophobic Plug is central to Voltage-Sensor Operation

The portability of voltage sensors (Alabi et al., 2007) allowed a higher resolution structure of the so-called 'paddle chimera' (PDB: 2R9R) where a voltage sensor from Kv2.1 was transferred onto Kv1.2 to be captured in the presence of lipid (Long et al., 2007). The chimeric structure showed a remarkable similarity to the Kv1.2 structure despite the formation of different crystal lattices.

Importantly, higher resolution of the voltage sensors allowed molecular details to be seen and understood. Helices S1, S2 and S3 (red, orange, beige respectively, Figure 1.18A) contained large regions of negative charge which could be grouped into two clusters, one on the extracellular side (the Extracellular Negative Cluster, ENC) and one on the intracellular side (the Intracellular Negative Cluster, INC). The ENC was water-accessible while the INC was buried 10Åfrom the intracellular membrane surface. A phenylalanine 2 residues below the isoleucines predicted by cysteine cross-linking separated the ENC and INC and was suggested to be the hydrophobic plug/ hydrophobic constriction site (HCS) (Long et al., 2007). These negative clusters are highly conserved channels containing voltage sensing domains. A schematic view of a typical voltage sensor is shown in Figure 1.18B to emphasise the water-filled cavities and importance of the ENC, HCS and INC).

The INC interacted with gating charges K5 and R6 by means of ionised hydrogen bonds, while the ENC interacted with gating charges R3 and R4. Gating charges R0, R1, R2, R3 and R4 were able to access the external media, as would be expected of an 'up' state voltage sensor. The lower half of the S4 helix unwound into a 3_{10} helix, placing the charged residues directly above each other.

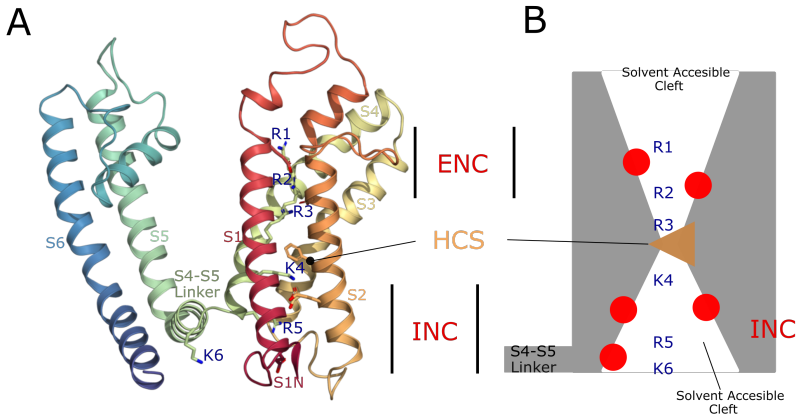


Figure 1.18: **High Resolution Voltage Sensor Structure from the Paddle Chimera**
A: Structure of a single subunit of the paddle chimera (PDB: 2R9R) as viewed from the transmembrane plane, showing all transmembrane helices. The S4 of the voltage sensor has adopted a 3_{10} helix such that the gating charges lie directly above each other. The gating charges are shown as sticks and positively-charged groups are shown in blue. The gating charges are labelled numerically from the N-terminus of S4 from R1-K6. The voltage sensor forms two solvent-accessible clefts which are cut off by the Hydrophobic Constriction Site (HCS) and the phenylalanine responsible is shown as sticks. On the extracellular accessible site, gating charges R1, R2 and R3 interact with a conserved patch of negative residues, the Extracellular Negative Cluster (ENC) which are shown as sticks and their negatively charged groups are highlighted in red. On the intracellular side, gating charges K4, R5 and K6 interact with another conserved patch of negative residues, the Intracellular Negative Cluster (INC) which are shown as sticks and their negatively charged groups are highlighted in red.
B: Schematic of a voltage-sensor as in A. Gating charges are represented by their residue and number (R1-K6) and their positions relative to the HCS is clearly shown. Likewise, residues from the ENC and INC are shown as red circles and their relative positions clearly shown. Also shown are the solvent accessible clefts which concentrate the electric field.

As well as allowing a higher resolution structure, portability of voltage-sensors allowed swapping of Nav channel VSDs into a Kv channel background. This showed that Domain IV VSDs are intrinsically slower (Bosmans et al., 2008), adding weight to the asynchronous gating model.

1.3.2.8 Sodium channel structure

The structure of sodium channels remained unknown until 2012 when the first voltage-gated sodium channel was crystallised from the halophile bacterium Arcobacter butzleri (NavAb, PDB: 3RVY, (Payandeh et al., 2011)). The structure showed a domain-swapped orientation analogous to Kv1.2 (Figure 1.19A) and a similar domain architecture of the voltage sensor and its connections to the pore (Figure 1.19B, D). It also captured interactions of gating charge arginines on the S4 helix with a conserved ENC and INC. These two charged clusters were separated by a HCS which focuses the electric field, analogous to the paddle chimera voltage sensor. The gating charges were separated by two hydrophobic residues and form a 3_{10} helix such that the arginines lie directly above each other and allow vertical translocation of the charge. The authors concluded that this was an activated voltage-sensor, since two arginines, R2 and R3 interact with the ENC. Despite all four voltage sensors being activated, the activation gate was closed, leading the authors to conclude it was a 'pre-open state'. Comparison of their structure with the solved Kv1.2 structure led to the first structural mechanism of activation gating in Nav channels. They proposed that upward movement of the first 3 voltage sensors pulls on the S4-S5 linker to dilate the pore in an iris-like movement.

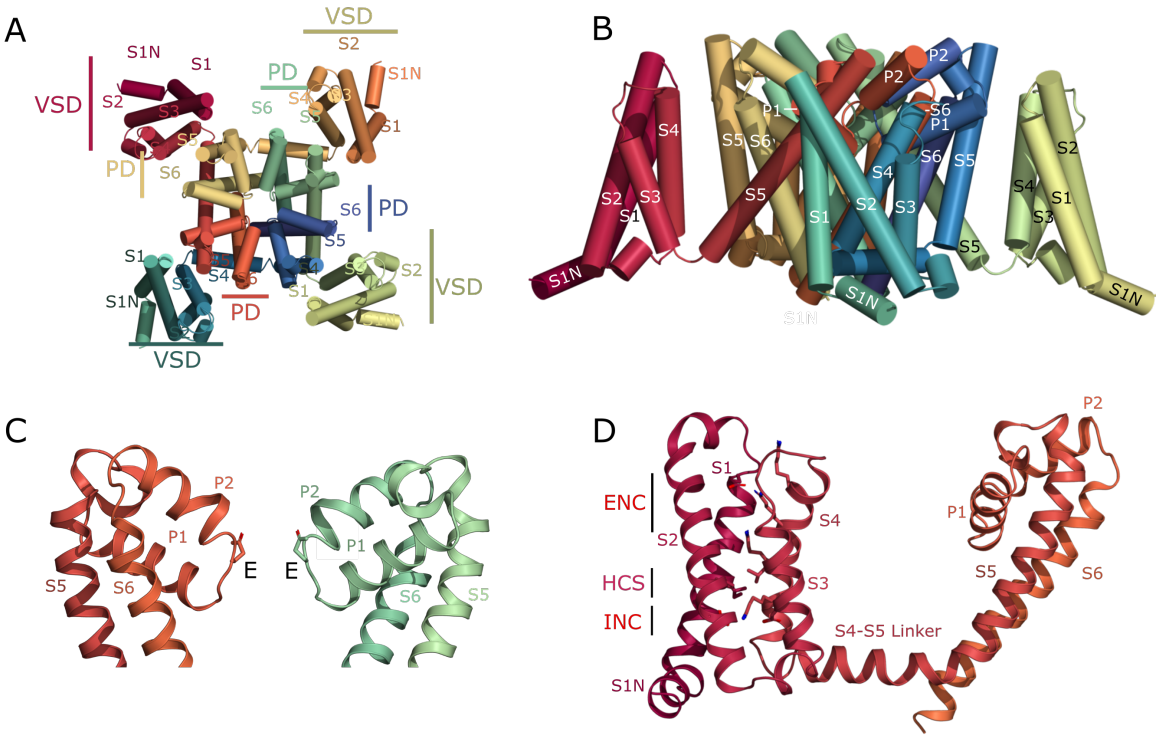


Figure 1.19: **NavAb Structure and Sodium Selectivity**
A: NavAb structure (PDB: 3RVY) as viewed from the extracellular side showing the transmembrane helices S1 to S4 of each tetramer forming the VSD while S5 and S6 of each subunit of the tetramer form the PD akin to M1 and M2 in KcsA. The PD of each monomer most closely associates with the VSD of the adjacent subunit in a domain-swapped orientation.
B: NavAb structure as viewed from within the membrane plane showing the transmembrane region.
C: Close up of the SF showing that the conserved glutamate residues held on a loop between P1 and P2 form the narrowest constriction.
D: Structure of a single subunit as viewed from the transmembrane plane, showing all transmembrane helices. The high conservation of the ENC, INC and HCS are highlighted to show their high conservation between voltage-gated sodium channels and potassium channels, which differ mostly in their pore region.

As well as providing the first structural insights into the mechanism of voltage sensing, the structure also showed a route for ion permeation, composed of a large external vestibule followed by a narrow ion SF followed by a central cavity and an intracellular activation gate. The SF is made up of one acidic glutamate residue emanating from a loop connecting P1 and P2 from each domain to create an opening large enough to conduct partially hydrated sodium, and this narrow constriction confers sodium selectivity (Figure 1.19C). However, the filter is more like Cav channels (EEEE) than Nav channels (DEKA)

This landmark structure was followed by other bacterial sodium channels from other groups, reviewed in Clairfeuille et al. (2017). However, these structures had a number of limitations. The bacterial homologs were all homotetramers compared to the monomeric mammalian channels. Not only did this prevent them from having an asymmetric SF, which was known to exist in mammalian channels from the early toxin mapping studies, but also, by definition, this meant that they lacked linkers between the domains. Of particular relevance was the lack of the III-IV linker which had long been known to be involved in fast-inactivation.

1.3.3 The Cryo-Electron Microscopy (Cryo-EM) Revolution

The movement of cryo-electron microscopy (cryo-EM) into the forefront of structural biology greatly facilitated structural progress in the membrane protein field. The resolution of cryo-EM has been dramatically improved by technological advances, particularly in direct electron detection methods (Rivera-Calzada and Carroni, 2019), and opened the door for obtaining eukaryotic structures of ion channels. This presented a great opportunity to study mammalian channels. Suddenly, bigger was better and structures sought after for decades were solved in very quick

succession, including members of previously unsolved families.

1.3.3.1 Structures of Proteins from native tissues

Nieng Yan's group obtained the first structure of a eukaryotic Cav channel by purifying Cav1.1 (PDB: 3JBR) from rabbit skeletal muscle membranes using glutathione-S-transferase (GST)- fused β1a, an exclusive auxiliary subunit of Cav1.1 (Cav1, Wu et al. (2015). Although at low resolution, the clockwise domain-swapped architecture typical of voltage-gated channels was clearly seen, with a cytosolic C-terminal domain. The SF was formed of 4 glutamate residues and the carbonyls of 2 preceding residues in each repeat. The transmembrane γ- subunit, a 4 helix bundle, interacts with VSDIV while the cytosolic β- subunit interacts with the bottom of VSDII. By contrast, the α2δsubunit binds to the loops protruding from repeats I to III. Although a pioneering structure, the low resolution only allowed assignment of one quarter of the molecular mass; in particular the α2δsubunit and importantly VSDII and III were nearly invisible (Wu et al., 2015).

Using carbon-film-coated grids and optimisation of freezing conditions, the authors improved contrast in the images and allowed resolution of all four VSDs in a follow up study two years later (PDB: 5GJV, Wu et al. (2016)).

However, it was not until 2017 until the first eukaryotic sodium channel structure (NavPas, PDB: 5X0M) from the American cockroach (*Periplaneta Americana*) was solved, again by Nieng Yan and her colleagues (Shen et al., 2017). This structure shares between 36 and 43% sequence identity to the nine human isoforms but has shorter loops than other insect and mammalian homologs. The structure showed the asymmetric SF with clear definition of the signature SF residues

(DEKA), as well as seven glycosylation sites for the first time.

With respect to gating, the NavPas pore was closed at the activation gate. The 4 VSDs were tilted relative to each other and were in distinct conformations. Comparison with the similar, but more activated Cav1.1 structure reinforced the idea that upwards movement of the S4 helix results in opening of the activation gate via pulling of the S3-S4 linker, but added the idea that the VSDs tilt during this process. The structure also showed complete resolution of the III-IV linker (pink, Figure 1.20A and B); known to be important in fast-inactivation, showing interactions with the C-terminal domain (CTD, blue, Figure 1.20A and B) . Although NavPas does not have an IFM motif, the DIII-DIV linker consists of an α-helix followed by an unwound segment with residues ATD in place of the IFM motif (Figure 1.20B). However, NavPas current failed to be recorded in a number of expression systems and with a number of βsubunits, and as such it is not known whether it undergoes fast inactivation.

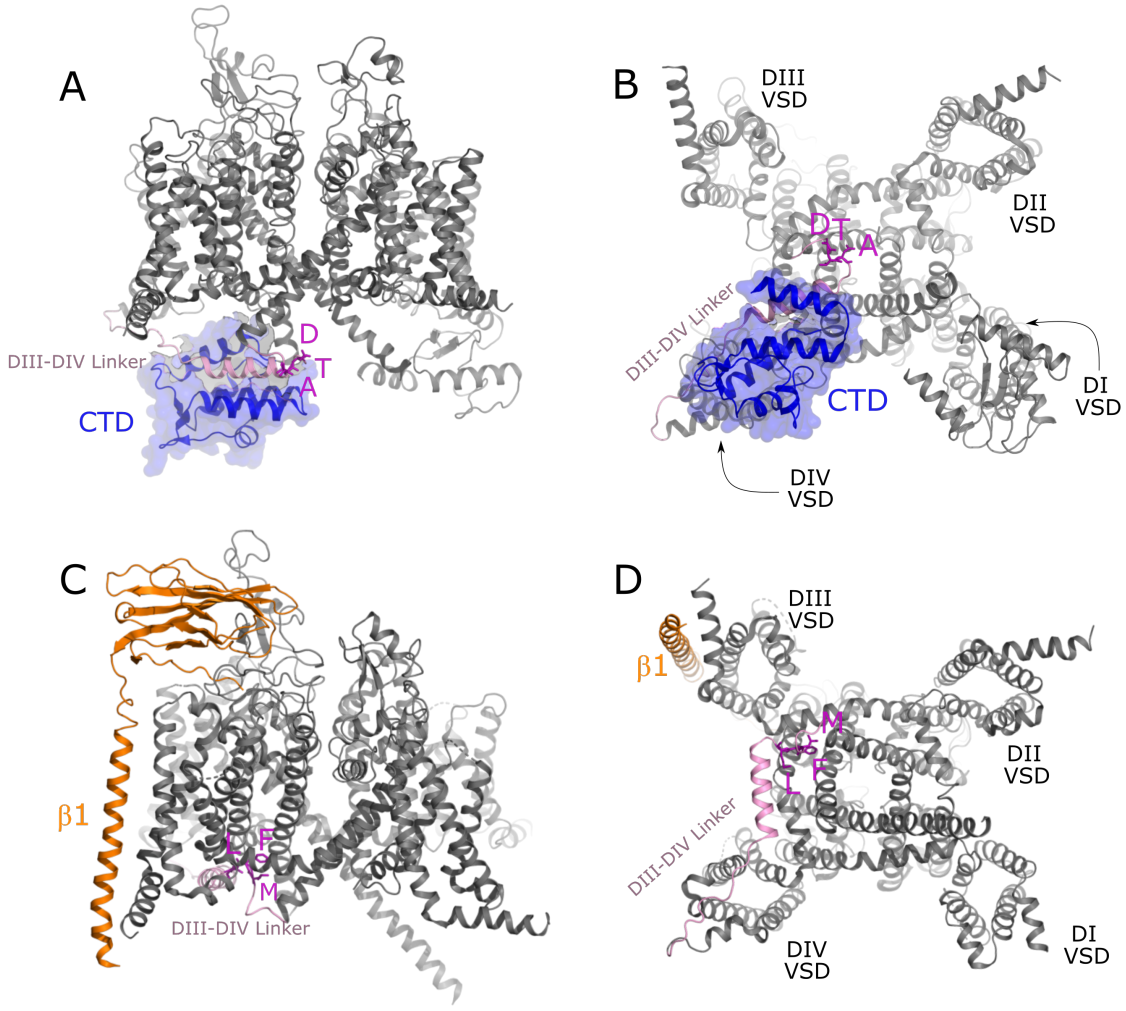


Figure 1.20: **Eukaryotic Structures Reveal the C-terminal Domain (CTD) and IFM Motif Positioning**
A: NavPas structure (PDB: 5X0M) as viewed from within the membrane plane showing the transmembrane region. The C-terminal domain (blue) is clearly visible and ordered and interacts with the Domain III-IV linker (pink), which contains the fast-inactivation peptide ATD shown as purple sticks.
B: NavPas structure as viewed from the intracellular side showing the positioning of the ATD motif compared to the pore.
C: Eel Nav1.4 structure (PDB: 5XSY) as viewed from within the membrane plane showing the transmembrane region. The C-terminal domain is not visible suggesting it is disordered. As a result, the Domain III-IV linker (pink) which contains the fast-inactivation peptide LFM (purple sticks) is in a markedly different position to the NavPas structure. Additionally shown is the axe-like β1 subunit (orange) which associates via its Immunoglobulin domain (axe-head) with the sodium channel pore.
D: Eel Nav1.4 structure as viewed from the intracellular side showing the drastic re-positioning of the LFM motif to interact with the S4-S5 segments and S6 in domains III and IV.

Yan's group subsequently solved a Nav1.4 structure in complex with β1 (EeNav-β1, PDB:5XSY) working with native protein from the electric organ (electroplax) of the eel (*Electrophorus electricus*) (Yan et al., 2017). Their EM structure captured eeNav1.4 in complex with an axe-like β1 subunit (orange, Figure 1.20C), the head of which interacts with the extracellular loops of VSDIII. Comparison with their NavPas structure revealed a drastic repositioning of the III-IV linker (pink Figure 1.20C) which appears to be freed from the non-detectable CTD. The III-IV linker places the IFM motif into the corner enclosed by the S4-S5 segments and S6 in domains III and IV thus showing the fast-inactivation lid for the first time. They proposed a potential allosteric blocking mechanism for fast inactivation, although the IFM does not physically occlude the pore, so details of this process remain unknown.

Of the four voltage sensors, VSDI and VSDII were too poorly resolved to see individual side chains, however, VSDIII and VSDIV are both in the up conformation. Comparison with NavAb and NavPas led to similar conclusions about channel activation. The structure could potentially be open, since the narrowest constriction point is the SF.

1.3.3.2 Structures from Recombinant Sources

Yan's group followed up with a human Nav1.4-β1 structure (PDB: 6AGF, Pan et al. (2018)), essentially identical in structure to its eel counterpart, although this time obtaining the protein using a recombinant strategy and achieving high resolution in all four activated VSDs. The interactions of the IFM motif were also better resolved, but their conclusions identical to the ones drawn from the eel structure. This overwhelming similarity between eel and human Nav1.4 demonstrates the

high value sodium channel ortholog structures.

Another flurry of structures in the presence of toxins saw a series of NavPas structures (NavPas-Dc1a, PDB: 6A90, NavPas-Dc1a-TTX, PDB: 6A95 and NavPas-Dc1a-STX, PDB: 6A91, Shen et al. (2018)), a Nav1.2-β2-μ-conotoxin structure (PDB: 6J8E, Pan et al. (2019)), two Nav1.7 structures (Nav1.7-β1-β2-HWTX-IV, PDB: 6J8I, Nav1.7-β1-β2-ProTx-II, PDB: 6J8J, (Shen et al., 2019)) and finally two rat Nav1.5 structures (rNav1.5, PDB: 6UZ3, rNav1.5-flecainide, PDB: 6UZ0,Jiang et al. (2020)) and most recently, a Nav1.1–β4 structure (PDB: 7DTD, (Pan et al., 2021)) and a human Nav1.5 structure (PDB: 7DTC, Li et al. (2021)). These structures provided valuable insights into β-subunit association and animal toxin modulation of Nav channels; particularly pore blockade through TTX, STX and μ-conotoxin. However, they provided more snapshots of up state voltage sensors even in the presence of ProTx-II and HWTX-IV and fast-inactivation machinery in a similar conformation to the one solved in Nav1.4, suggesting fast-inactivated structures, consistent with the structures being solved in the absence of an electric field.

1.3.4 Challenges and Unanswered Questions

Comparison of the known structures serves as an important framework for understanding gating mechanisms in ion channels, but sequence variations and lack of electrophysiological characterisation make them difficult to interpret functionally. Channels such as NavAb do not have loops connecting the domains so do not contain the III-IV linker long known to be involved in fast-inactivation, whilst other channels such as NavPas cannot be functionally probed. In addition, voltage-gated channels are opened and closed upon changes in voltage, yet in both crystals (X-

ray crystallography) and in vitreous ice (cryo-EM), the protein is in the absence of an electric field, i.e. at 0 mV, so one would expect that in all structures, all four VSDs are activated.

The biggest challenge however is that structures are static and often represent the lowest energy conformational state in the absence of a stimulus. However, gating is dynamic and we need to not only capture novel states by stabilising otherwise higher energy states, but functionally interpret what these mean. This stabilisation can be achieved in one of two ways: either using mutagenesis or ligands to stabilise the higher energy state. The latter, using ligands to stabilise novel conformations is the overriding theme of this thesis. In chapter 3, we use scorpion toxins to mimic a depolarised voltage and trap Nav1.7 with a down state voltage sensor in order to better understand fast-inactivation. In chapters 4 and 5 we attempt to use VHH antibodies to trap novel conformations of the TREK-2 K2P channels and attempt to functionally annotate these novel conformations.

1.4 Pharmacological Intervention to trap novel states

1.4.1 Theory of Ligand Binding

Channels, like all proteins, are dynamic molecules. A population of channels will adopt a heterogeneous mixture of different conformations that are capable of interconverting. A simple energy profile for a protein with two states, P and P*, is shown in teal in Figure 1.21. In the absence of ligand, the protein will exist mostly in the P state as this is the lowest energy state. The difference in energy between the two states is given by $\Delta G_{Convert}$. In order to convert to the second conformational state, P*, a barrier energy, $\Delta G_{Barrier}$, needs to be overcome. When a ligand

(L) binds to the protein, it is capable of binding both the P and P* states, it changes the local energy landscape (purple, Figure 1.21) but now, the protein will preferentially exist in the P*L state as this is the lowest energy state. The ligand binding therefore stabilises the P* state by $\Delta G_{Intrinsic}$ and the observed stabilisation is given by $\Delta G_{Observed}$.

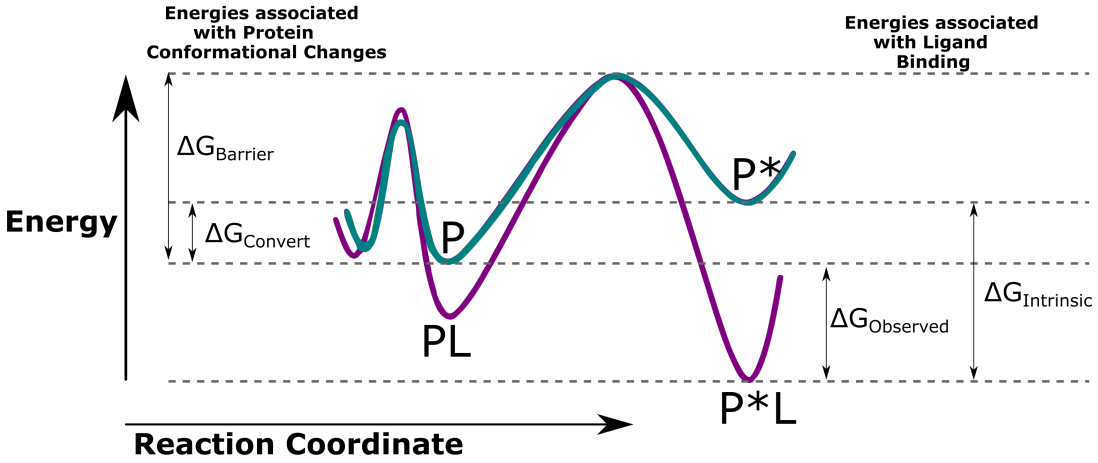


Figure 1.21: **Stabilisation of Novel states using Ligands**
A hypothetical energy profile for a protein with two states, P and P* in the absence (teal) and presence (purple) of a ligand (L). In the absence of a ligand, the two states can inter-convert so long as the barrier energy, $\Delta G_{Barrier}$ is overcome and the energy difference between the two states is given by $\Delta G_{Convert}$. When a ligand is added, the lowest energy state becomes the P*L state which is stabilised from P* without the ligand by $\Delta G_{Intrinsic}$, but in reality, the observed stabilisation is given by the difference between the lowest energy state without a ligand (P) and the lowest energy state with a ligand (P*L) given by $\Delta G_{Observed}$.
Figure adapted from Teague (2003). Reproduced with permission of Springer Nature.

To add relevance to this simple system, we can use an analogy of voltage-gated channels. If P represents the open state which is more stable than the P* state which represents the closed state, then the transmembrane electric field will have to do work (provide $\Delta G_{Convert}$) to close the gate. An example of this is HCN channels. If the closed state is more stable than the open state, then the transmembrane

electric field will have to do work to open the gate. This is utilised by Nav and Kv channels. We can extend the analogy further with mechanosensitive channels. In all known examples, the closed state (P) is more stable than the open state (P*) in the absence of membrane tension. Therefore the tension does work on the channel to open the gate. We can use ligands to stabilise otherwise unstable states.

In order to achieve our therapeutic and academic aim, we need to use a ligand that binds to its target and produces a functional effect. For clarity, we will first go through some definitions which are often used incorrectly, and are important to understand in terms of what is measured in the functional data in this thesis. For a much more detailed (and also ion channel focused) review see Colquhoun (1998) and references within, particularly the del Castillo Katz model (Del Castillo and Katz, 1957).

The first step of functional modulation involves a protein (P) binding to a ligand (L). The ability of a ligand to bind to a protein is called the **affinity**, (purple, Figure 1.22) and is often expressed numerically as a dissociation constant (K_D). The K_D is given by the ratio of the off and on rate constants (k_{off}, k_{on}) or the ratio of the concentration of free protein [P] and free ligand [L] to the concentration of the complex [PL].

The ability of the ligand binding to cause a functional response is called the **efficacy**, here it represents the conversion from a closed channel complex (PL) to an open channel complex (P*L) (blue, Figure 1.22). Efficacy can be expressed numerically in an identical fashion to affinity; a ratio of the opening and closing rate constants (k_{open}, k_{closed}) or the ratio of closed complex to open complex. Often for simplicity, efficacy is given as the maximal response to a saturating ligand concen-

tration, (R_{max}).

Potency is the measure of the effect of the ligand on the response, and therefore is determined by both the affinity and the efficacy (green, Figure 1.22). The potency is given numerically as the EC_{50} (Median Effective Concentration), the concentration of ligand that produces a half maximal response. For a ligand which is an inhibitor, the EC_{50} has a more specific name: an IC_{50} (Median Inhibitory Concentration 50). When recording the current response as a function of ligand concentration, we are therefore measuring the potency of the ligand, a combination of the affinity and efficacy.

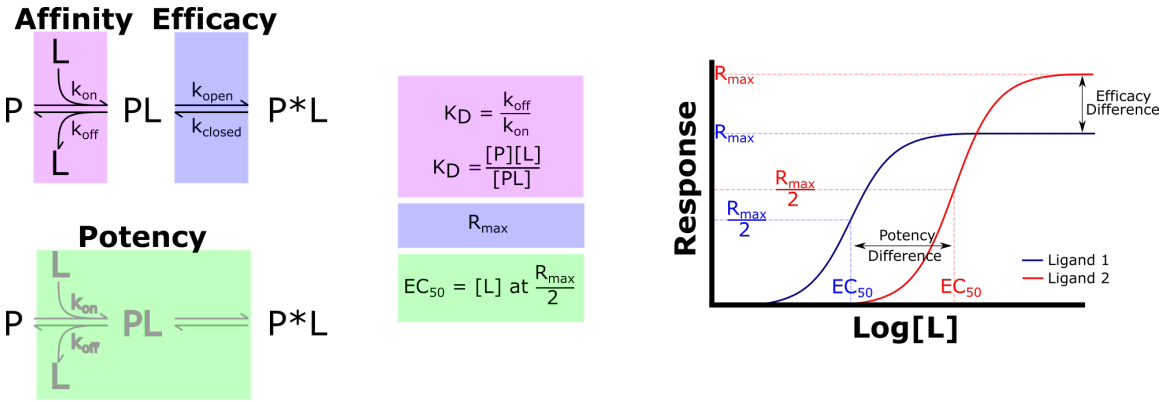


Figure 1.22: **The Definitions of Affinity, Efficacy and Potency**
Left: A simple model of ligand binding showing which parts the terms affinity, efficacy and potency refer to (purple, blue and green respectively).
Middle: These processes can be quantified and summarised by the equations shown in the boxes in the middle, and colour matched to the term they refer to.
Right: Typical sigmoidal dose-response curves of two different ligands (red and blue), highlighting the difference in efficacy and potency that can be obtained from such graphs.

Two final definitions which are often confused are **selectivity** and **specificity** which are thoroughly discussed and defined in Mencher and Wang (2005). Selectivity refers to the ability of a ligand to affect a particular population e.g. gene, protein, signalling pathway or cell, while not affecting other populations. In the context of antibodies, specificity refers to the selectivity towards an epitope se-

quence, which may not translate to e.g. channel subtype selectivity if the epitope is present in several (e.g. channel) subtypes.

1.4.2 Trapping Pharmacologically and Mechanistically Relevant states

The idea of trapping the channel in novel states is common to both the mechanistic and structural goals outlined above. Through understanding the gating cycle of a channel, we can work out which states within the cycle we want to stabilise. As an example, if we want to inhibit sodium current, we could either stabilise the inactivated or closed states, as neither pass current. By contrast, if we wanted to increase the sodium conductance, we would need to stabilise the open state where current is passed. More knowledge of the gating cycle, and particularly the structures of each state is desirable for drug discovery.

To date, small molecule approaches have dominated drug discovery efforts against ion channels. However, structural similarities between closely related channels means that often such approaches lack the appropriate selectivity to be safe and effective drugs, and consequently lead to their rejection in the clinic. The use of more selective, protein-based biologics to target such channels is one promising way to overcome this limitation, and combined with the possibility of high affinity, it is unsurprising that these approaches have attracted significant interest from both academia and industry. For review see Wilkinson et al. (2015).

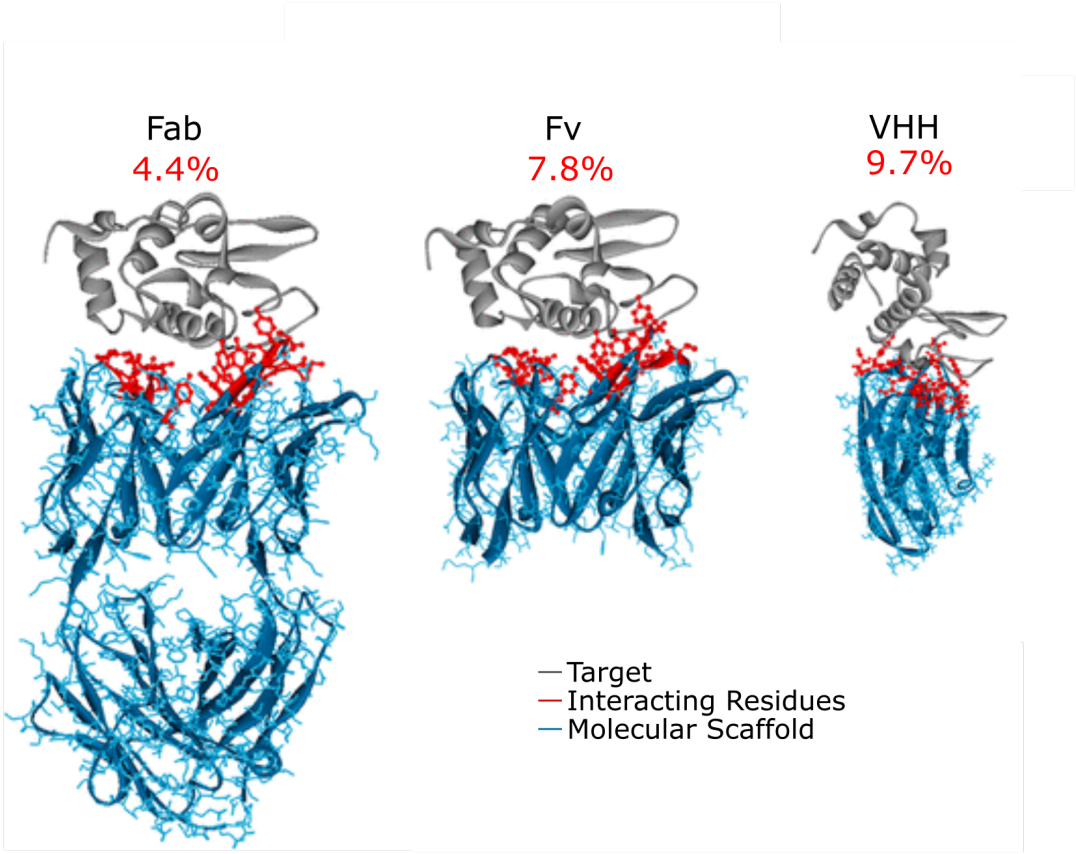


Figure 1.23: **Percentage of Antibody Involved in Binding to the Target**
Structures of Fab, Fv and VHH antibody fragments engaging with their target (grey). In all three cases, a huge molecular scaffold (blue) is used to place a very small number of residues which interact with the target (red) in a favourable position for binding.
Figure from Lawson et al. (2017). Reproduced with permission of A. Lawson under the ACS author choice designation

While the pharmaceutical industry is starting to see the potential of using proteins, mother nature has been exploiting proteins to specifically target other proteins since the beginning of life. A great example of this is antibodies: immune recognition molecules tasked with specifically binding to their target. They use a huge molecular scaffold to place only a few amino acids in the correct 3 dimensional space to specifically and potently bind to their molecular targets. A diagram showing the percentage of residues involved in binding lysozyme in three truncated antibody scaffolds is shown in Figure 1.23 and taken from (Lawson et al., 2017). A conventional tetrameric antibody devotes only 4.4% of its antigen binding domain to actually bind the target (left, Figure 1.23). Even when this region is enzymatically cleaved to leave only the Fv region, only 7.8% is involved in binding. Even one of the smallest known antibody based binding fragments, a VHH antibody or nanobody only engages its target with 9.7% of its sequence (right, Figure 1.23). The fact that nature uses the large molecular scaffolds to very accurately place so few residues, suggests both its importance for specificity purposes, but also that smaller molecules may be unable to target with such high specificity.

In this thesis we attempt to make use of naturally occurring α-scorpion toxins to target Nav channels as well as VHH antibodies to target K2P channels. A more comprehensive review of these classes of molecules are given at the start of Chapter 3 and Chapter 4 respectively, but it is pertinent to note that no natural protein toxin is known to bind to K2P channels meaning we had to raise a panel of VHH antibodies against the channels in hope of obtaining some which were capable of functional modulation.

In Chapter 3 we use scorpion toxins to mimic a depolarised voltage and trap Nav1.7 with a down state voltage sensor in order to better understand the fast-

inactivation process of Nav channels. Owing to experimental constraints, and as discussed, all previously solved structures are likely to represent activated voltage sensors due to the absence of an electric field. α-scorpion toxins are known to bind specifically to VSDIV and slow down the fast inactivation process of sodium channels and for this reason, we captured two structures in both an apo- and scorpion toxin bound state to better understand likely transitions between the up and down states of VSDIV and the electrochemical coupling to the pore. In order to do this, we made use of a humanised Nav1.7-NavPas chimera to ensure structural resolution was possible but recapitulated the human Nav1.7 VSDIV scorpion toxin binding site. This not only allowed mechanistic insight into electrochemical coupling to be obtained, but also allowed us to electrophysiologically characterise the α-scorpion toxin binding site in full length human Nav1.7 from both the channel and the toxin side.

In chapter 4 we use VHH antibodies to trap new conformations of K2P channels in order to better understand structure-function relationships. Unlike the potassium channels discussed in this chapter, most K2P channels (e.g. TREK-2 and TREK-1 which are used in this study) do not have a lower gate, and as such they are thought to gate primarily at the SF which is often referred to as a C-type gate, due to the similar nature it bears to C-type inactivation in e.g. KcsA which was discussed previously. Central to this idea is that (de-)stabilisation of the SF is known to affect K2P function. Indeed, extracellular modulation of K2P channels by external pH is thought to influence channel activity and this is one such place that we hoped VHH antibodies raised against K2Ps might bind. Using electrophysiology, we show that of our panel of about 30 VHH antibodies, three are capable of functional modulation of the channel, two of which appear to activate and one which appears to inhibit TREK-2 activity. We show that they selectively modu-

late both human and mouse TREK-2 and are mostly unable to modulate other K2P channels, suggesting their potential in rodent pain models. We attempt to show that they work through the external pH sensing pathway by use of pH-dependent experiments and known gating mutants.

In Chapter 5, we engineer our VHH antibody library to optimise expression and enhance their functionality for use in localisation studies. We adopted a number of orthogonal approaches in order to fluorescently tag VHH antibodies and used them to show that a large number of the VHH domain antibodies bind specifically to TREK-2 over all other K2P channels. Rather excitingly, we have also shown that some VHH antibodies within our library can bind to native tissue making use of a rat Superior Cervical Ganglia which is known from RNAseq data to express TREK-2, making them promising tools for future localisation studies.

Bibliography

Aggarwal, S. and MacKinnon, R. (1996). Contribution of the s4 segment to gating charge in the shaker k+ channel. *Neuron*, 16(6):1169–77. 42

Ahern, C. A. and Horn, R. (2005). Focused electric field across the voltage sensor of potassium channels. *Neuron*, 48(1):25–9. 51

Ahern, C. A., Payandeh, J., Bosmans, F., and Chanda, B. (2016). The hitchhiker's guide to the voltage-gated sodium channel galaxy. *J Gen Physiol*, 147(1):1–24. 33, 36, 50

Ahuja, S., Mukund, S., Deng, L., Khakh, K., Chang, E., Ho, H., Shriver, S., Young,

C., Lin, S., Johnson, J., et al. (2015). Structural basis of nav1. 7 inhibition by an isoform-selective small-molecule antagonist. *Science*, 350(6267). 45

Akopian, A., Sivilotti, L., and Wood, J. (1996). A tetrodotoxin-resistant voltage-gated sodium channel expressed by sensory neurons. *Nature*, 379(6562):257–62. 10

Alabi, A. A., Bahamonde, M. I., Jung, H. J., Kim, J. I., and Swartz, K. J. (2007). Portability of paddle motif function and pharmacology in voltage sensors. *Nature*, 450(7168):370–5. 54

Armstrong, C. and Bezanilla, F. (1977). Inactivation of the sodium channel. ii. gating current experiments. *J Gen Physiol*, 70(5):567–90. 35

Armstrong, C., Bezanilla, F., and Rojas, E. (1973). Destruction of sodium conductance inactivation in squid axons perfused with pronase. *J Gen Physiol*, 62(4):375–91. 35, 44

Armstrong, C. M. and Bezanilla, F. (1973). Currents related to movement of the gating particles of the sodium channels. *Nature*, 242(5398):459–461. 33, 34

Asamoah, O. K., Wuskell, J. P., Loew, L. M., and Bezanilla, F. (2003). A fluorometric approach to local electric field measurements in a voltage-gated ion channel. *Neuron*, 37(1):85–97. 51

Baker, O., Larsson, H. P., Mannuzzu, L., and Isacoff, E. (1998). Three transmembrane conformations and sequence-dependent displacement of the s4 domain in shaker k+ channel gating. *Neuron*, 20(6):1283–1294. 43

Bean, B. P. (2007). The action potential in mammalian central neurons. *Nature Reviews Neuroscience*, 8(6):451–465. 6

Beneski, D. and Catterall, W. (1980). Covalent labeling of protein components of the sodium channel with a photoactivable derivative of scorpion toxin. *Proc Natl Acad Sci U S A*, 77(1):639–43. 37

Bennett, D. L., Clark, A. J., Huang, J., Waxman, S. G., and Dib-Hajj, S. (2019). The role of voltage-gated sodium channels in pain signaling. *Physiol Rev*, 99(2):1079–1151. 8, 10

Bernèche, S. and Roux, B. (2001). Energetics of ion conduction through the k+ channel. *Nature*, 414(6859):73–7. 46

Bernèche, S. and Roux, B. (2005). A gate in the selectivity filter of potassium channels. *Structure*, 13(4):591–600. 48

Bezanilla, F. (2000). The voltage sensor in voltage-dependent ion channels. *Physiol Rev*, 80(2):555–592. 34

Bezanilla, F. and Armstrong, C. (1977). Inactivation of the sodium channel. i. sodium current experiments. *J Gen Physiol*, 70(5):549–66. 35

Bezanilla, F., Perozo, E., Papazian, D., and Stefani, E. (1991). Molecular basis of gating charge immobilization in shaker potassium channels. *Science*, 254(5032):679–83. 38

Bezanilla, F., Perozo, E., and Stefani, E. (1994). Gating of shaker k+ channels: II. the components of gating currents and a model of channel activation. *Biophys J*, 66(4):1011–21. 38

Bezanilla, F., White, M., and Taylor, R. (1982). Gating currents associated with potassium channel activation. *Nature*, 296(5858):657–9. 34

Black, J., Dib-Hajj, S., McNabola, K., Jeste, S., Rizzo, M., Kocsis, J., and Waxman, S.

(1996). Spinal sensory neurons express multiple sodium channel alpha-subunit mrnas. *Brain Res Mol Brain Res*, 43(1-2):117–31. 10

Black, J., Westenbroek, R., Catterall, W., and Waxman, S. (1995). Type ii brain sodium channel expression in non-neuronal cells: embryonic rat osteoblasts. *Brain Res Mol Brain Res*, 34(1):89–98. 10

Bosmans, F., Martin-Eauclaire, M.-F., and Swartz, K. J. (2008). Deconstructing voltage sensor function and pharmacology in sodium channels. *Nature*, 456(7219):202–208. 56

Catterall, W. A., Goldin, A. L., and Waxman, S. G. a. (2003). International union of pharmacology. xxxix.compendium of voltage-gated ion channels: sodium channels. *Pharmacol Rev*, 55(4):575–8. 10

Cha, A., Ruben, P., George, A., Fujimoto, E., and Bezanilla, F. (1999a). Voltage sensors in domains iii and iv, but not i and ii, are immobilized by na+ channel fast inactivation. *Neuron*, 22(1):73–87. 45

Cha, A., Snyder, G., Selvin, P., and Bezanilla, F. (1999b). Atomic scale movement of the voltage-sensing region in a potassium channel measured via spectroscopy. *Nature*, 402(6763):809–13. 43

Chanda, B. and Bezanilla, F. (2002). Tracking voltage-dependent conformational changes in skeletal muscle sodium channel during activation. *The Journal of general physiology*, 120(5):629–645. 50

Chen, L., Santarelli, V., Horn, R., and Kallen, R. (1996). A unique role for the s4 segment of domain 4 in the inactivation of sodium channels. *J Gen Physiol*, 108(6):549–56. 44

Clairfeuille, T., Xu, H., Koth, C. M., and Payandeh, J. (2017). Voltage-gated sodium channels viewed through a structural biology lens. *Curr Opin Struct Biol*, 45:74–84. 58

Cochet-Bissuel, M., Lory, P., and Monteil, A. (2014). The sodium leak channel, nalcn, in health and disease. *Front Cell Neurosci*, 8:132. 9

Colquhoun, D. (1998). Binding, gating, affinity and efficacy: the interpretation of structure-activity relationships for agonists and of the effects of mutating receptors. *Br J Pharmacol*, 125(5):924–47. 66

Cordero-Morales, J. F., Cuello, L. G., Zhao, Y., Jogini, V., Cortes, D., Roux, B., and Perozo, E. (2006). Molecular determinants of gating at the potassium-channel selectivity filter. *Nat Struct Mol Biol*, 13(4):311–8. 48, 49

Cuello, L. G., Jogini, V., Cortes, D., Pan, A. C., Gagnon, D. G., Dalmas, O., Cordero-Morales, J. F., Chakrapani, S., Roux, B., and Perozo, E. (2010). Structural basis for the coupling between activation and inactivation gates in k(+) channels. *Nature*, 466(7303):272–5. 49

Del Castillo, J. and Katz, B. (1957). Interaction at end-plate receptors between different choline derivatives. *Proc R Soc Lond B Biol Sci*, 146(924):369–81. 66

Dib-Hajj, S., Tyrrell, L., Black, J., and Waxman, S. (1998). Nan, a novel voltage-gated na channel, is expressed preferentially in peripheral sensory neurons and down-regulated after axotomy. *Proc Natl Acad Sci U S A*, 95(15):8963–8. 10

Doyle, D., Morais Cabral, J., Pfuetzner, R., Kuo, A., Gulbis, J., Cohen, S., Chait, B., and MacKinnon, R. (1998). The structure of the potassium channel: molecular basis of k+ conduction and selectivity. *Science*, 280(5360):69–77. 46

Du, X. and Gamper, N. (2013). Potassium channels in peripheral pain pathways: expression, function and therapeutic potential. *Curr Neuropharmacol*, 11(6):621–40. 11

Favre, I., Moczydlowski, E., and Schild, L. (1996). On the structural basis for ionic selectivity among na+, k+, and ca2+ in the voltage-gated sodium channel. *Biophys J*, 71(6):3110–25. 41

Fayaz, A., Croft, P., Langford, R., Donaldson, L., and Jones, G. (2016). Prevalence of chronic pain in the uk: a systematic review and meta-analysis of population studies. *BMJ Open*, 6(6):e010364. 1

Felts, P., Yokoyama, S., Dib-Hajj, S., Black, J., and Waxman, S. (1997). Sodium channel alpha-subunit mrnas i, ii, iii, nag, na6 and hne (pn1): different expression patterns in developing rat nervous system. *Brain Res Mol Brain Res*, 45(1):71–82. 10

Fukuoka, T., Kobayashi, K., Yamanaka, H., Obata, K., Dai, Y., and Noguchi, K. (2008). Comparative study of the distribution of the alpha-subunits of voltage-gated sodium channels in normal and axotomized rat dorsal root ganglion neurons. *J Comp Neurol*, 510(2):188–206. 10

Gutman, G. A., Chandy, K., Adelman, J. P., Aiyar, J., Bayliss, D. A., Clapham, D. E., Covarriubias, M., Desir, G. V., Furuichi, K., Ganetzky, B., Garcia, M. L., Grissmer, S., Jan, L. Y., Karschin, A., Kim, D., Kuperschmidt, S., Kurachi, Y., Lazdunski, M., Lesage, F., Lester, H. A., McKinnon, D., Nichols, C. G., O'Kelly, I., Robbins, J., Robertson, G. A., Rudy, B., Sanguinetti, M., Seino, S., Stuehmer, W., Tamkun, M. M., Vandenberg, C. A., Wei, A., Wulff, H., and Wymore, R. S. (2003). International union of pharmacology. xli. compendium of voltage-gated ion channels: potassium channels. *Pharmacol Rev*, 55(4):583–6. 11

Hartmann, H., Kirsch, G., Drewe, J., Taglialatela, M., Joho, R., and Brown, A. (1991). Exchange of conduction pathways between two related k+ channels. *Science*, 251(4996):942–4. 39

Heginbotham, L., Abramson, T., and MacKinnon, R. (1992). A functional connection between the pores of distantly related ion channels as revealed by mutant k+ channels. *Science*, 258(5085):1152–5. 39

Heginbotham, L., Lu, Z., Abramson, T., and MacKinnon, R. (1994). Mutations in the k+ channel signature sequence. *Biophys J*, 66(4):1061–7. 40

Heinemann, S., Terlau, H., Stühmer, W., Imoto, K., and Numa, S. (1992). Calcium channel characteristics conferred on the sodium channel by single mutations. *Nature*, 356(6368):441–3. 41

Hille, B. (1992). *Ionic Channels of Excitable Membranes*. Oxford University Press, Incorporated. 20, 22

Hirschberg, B., Rovner, A., Lieberman, M., and Patlak, J. (1995). Transfer of twelve charges is needed to open skeletal muscle na+ channels. *J Gen Physiol*, 106(6):1053–68. 38

Hodgkin, A. and Huxley, A. (1952a). The components of membrane conductance in the giant axon of loligo. *The Journal of physiology*, 116(4):473–496. 32

Hodgkin, A. and Huxley, A. (1952b). Currents carried by sodium and potassium ions through the membrane of the giant axon of loligo. *J Physiol*, 116(4):449–72. 32

Hodgkin, A., Huxley, A., and Katz, B. (1952). Measurement of current-voltage relations in the membrane of the giant axon of loligo. *The Journal of physiology*. 32

Hodgkin, Allan, L. and Huxley, A. F. (1952c). The dual effect of membrane potential on sodium conductance in the giant axon of loligo. *The Journal of physiology*, 116(4):497–506. 32

Jiang, D., Shi, H., Tonggu, L., Gamal El-Din, T. M., Lenaeus, M. J., Zhao, Y., Yoshioka, C., Zheng, N., and Catterall, W. A. (2020). Structure of the cardiac sodium channel. *Cell*, 180(1):122–134.e10. 63

Jiang, Y., Lee, A., Chen, J., Cadene, M., Chait, B. T., and MacKinnon, R. (2002). Crystal structure and mechanism of a calcium-gated potassium channel. *Nature*, 417(6888):515–22. 47

Jiang, Y., Lee, A., Chen, J., Ruta, V., Cadene, M., Chait, B. T., and MacKinnon, R. (2003). X-ray structure of a voltage-dependent k+ channel. *Nature*, 423(6935):33–41. 47

Jogini, V. and Roux, B. (2007). Dynamics of the kv1.2 voltage-gated k+ channel in a membrane environment. *Biophys J*, 93(9):3070–82. 54

Kang, D. and Kim, D. (2006). Trek-2 (k2p10.1) and tresk (k2p18.1) are major background k+ channels in dorsal root ganglion neurons. *Am J Physiol Cell Physiol*, 291(1):C138–46. 9

Kavanaugh, M., Hurst, R., Yakel, J., Varnum, M., Adelman, J., and North, R. (1992). Multiple subunits of a voltage-dependent potassium channel contribute to the binding site for tetraethylammonium. *Neuron*, 8(3):493–7. 39

Kavanaugh, M., Varnum, M., Osborne, P., Christie, M., Busch, A., Adelman, J., and North, R. (1991). Interaction between tetraethylammonium and amino acid residues in the pore of cloned voltage-dependent potassium channels. *J Biol Chem*, 266(12):7583–7. 39

Keynes, R. and Rojas, E. (1973). Characteristics of the sodium gating current in the squid giant axon. *J Physiol*, 233(1):28P–30P. 33

Kirsch, G., Drewe, J., Taglialatela, M., Joho, R., DeBiasi, M., Hartmann, H., and Brown, A. (1992). A single nonpolar residue in the deep pore of related k+ channels acts as a k+: Rb+ conductance switch. *Biophysical journal*, 62(1):136–144. 39

Larsson, H. P., Baker, O. S., Dhillon, D. S., and Isacoff, E. Y. (1996). Transmembrane movement of the shaker k+ channel s4. *Neuron*, 16(2):387–397. 43

Lawson, A. D., MacCoss, M., and Heer, J. P. (2017). Importance of rigidity in designing small molecule drugs to tackle protein–protein interactions (ppis) through stabilization of desired conformers: Miniperspective. *Journal of medicinal chemistry*, 61(10):4283–4289. 69, 70

Lee, S.-Y. Y., Lee, A., Chen, J., and MacKinnon, R. (2005). Structure of the kvap voltage-dependent k+ channel and its dependence on the lipid membrane. *Proc Natl Acad Sci U S A*, 102(43):15441–6. 51

Li, Z., Jin, X., Wu, T., Zhao, X., Wang, W., Lei, J., Pan, X., and Yan, N. (2021). Structure of human nav1. 5 reveals the fast inactivation-related segments as a mutational hotspot for the long qt syndrome. *Proceedings of the National Academy of Sciences*, 118(11). 63

Liman, E., Hess, P., Weaver, F., and Koren, G. (1991). Voltage-sensing residues in the s4 region of a mammalian k+ channel. *Nature*, 353(6346):752–6. 41

Liu, Y., Jurman, M., and Yellen, G. (1996). Dynamic rearrangement of the outer mouth of a k+ channel during gating. *Neuron*, 16(4):859–67. 40

Logothetis, D., Movahedi, S., Satler, C., Lindpaintner, K., and Nadal-Ginard, B. (1992). Incremental reductions of positive charge within the s4 region of a voltage-gated k+ channel result in corresponding decreases in gating charge. *Neuron*, 8(3):531–40. 41

Long, S. B., Campbell, E. B., and Mackinnon, R. (2005). Crystal structure of a mammalian voltage-dependent shaker family k+ channel. *Science*, 309(5736):897–903. 52

Long, S. B., Tao, X., Campbell, E. B., and MacKinnon, R. (2007). Atomic structure of a voltage-dependent k+ channel in a lipid membrane-like environment. *Nature*, 450(7168):376–82. 54

López-Barneo, J., Hoshi, T., Heinemann, S., and Aldrich, R. (1993). Effects of external cations and mutations in the pore region on c-type inactivation of shaker potassium channels. *Recept Channels*, 1(1):61–71. 40

MacKinnon, R., Cohen, S., Kuo, A., Lee, A., and Chait, B. (1998). Structural conservation in prokaryotic and eukaryotic potassium channels. *Science*, 280(5360):106–9. 47

MacKinnon, R., Heginbotham, L., and Abramson, T. (1990). Mapping the receptor site for charybdotoxin, a pore-blocking potassium channel inhibitor. *Neuron*, 5(6):767–71. 39

MacKinnon, R. and Miller, C. (1989). Mutant potassium channels with altered binding of charybdotoxin, a pore-blocking peptide inhibitor. *Science*, 245(4924):1382–5. 39

MacKinnon, R. and Yellen, G. (1990). Mutations affecting tea blockade and ion permeation in voltage-activated k+ channels. *Science*, 250(4978):276–9. 39

Manfredi, M., Bini, G., Cruccu, G., Accornero, N., Berardelli, A., and Medolago, L. (1981). Congenital absence of pain. *Arch Neurol*, 38(8):507–11. 10

Maniadakis, N. and Gray, A. (2000). The economic burden of back pain in the uk. *Pain*, 84(1):95–103. 1

Mannuzzu, L. M., Moronne, M. M., and Isacoff, E. Y. (1996). Direct physical measure of conformational rearrangement underlying potassium channel gating. *Science*, 271(5246):213–216. 43

Marsh, B., Acosta, C., Djouhri, L., and Lawson, S. N. (2012). Leak k channel mrnas in dorsal root ganglia: relation to inflammation and spontaneous pain behaviour. *Mol Cell Neurosci*, 49(3):375–86. 9

McPhee, J., Ragsdale, D., Scheuer, T., and Catterall, W. (1998). A critical role for the s4-s5 intracellular loop in domain iv of the sodium channel alpha-subunit in fast inactivation. *J Biol Chem*, 273(2):1121–9. 44

Mencher, S. K. and Wang, L. G. (2005). Promiscuous drugs compared to selective drugs (promiscuity can be a virtue). *BMC clinical pharmacology*, 5(1):1–7. 67

Moorman, J., Kirsch, G., Brown, A., and Joho, R. (1990). Changes in sodium channel gating produced by point mutations in a cytoplasmic linker. *Science*, 250(4981):688–91. 44

Morais-Cabral, J., Zhou, Y., and MacKinnon, R. (2001). Energetic optimization of ion conduction rate by the k+ selectivity filter. *Nature*, 414(6859):37–42. 46

Nishida, M., Cadene, M., Chait, B. T., and MacKinnon, R. (2007). Crystal structure of a kir3.1-prokaryotic kir channel chimera. *EMBO J*, 26(17):4005–15. 47

Noceti, F., Baldelli, P., Wei, X., Qin, N., Toro, L., Birnbaumer, L., and Stefani, E.

(1996). Effective gating charges per channel in voltage-dependent k+ and ca2+ channels. *J Gen Physiol*, 108(3):143–55. 38

Noda, M., Shimizu, S., Tanabe, T., Takai, T., Kayano, T., Ikeda, T., Takahashi, H., Nakayama, H., Kanaoka, Y., and Minamino, N. (1984). Primary structure of electrophorus electricus sodium channel deduced from cdna sequence. *Nature*, 312(5990):121–7. 37

Noda, M., Suzuki, H., Numa, S., and Stühmer, W. (1989). A single point mutation confers tetrodotoxin and saxitoxin insensitivity on the sodium channel ii. *FEBS Lett*, 259(1):213–6. 40

Pan, X., Li, Z., Huang, X., Huang, G., Gao, S., Shen, H., Liu, L., Lei, J., and Yan, N. (2019). Molecular basis for pore blockade of human na+ channel nav1.2 by the μ-conotoxin kiiia. *Science*, 363(6433):1309–1313. 63

Pan, X., Li, Z., Jin, X., Zhao, Y., Huang, G., Huang, X., Shen, Z., Cao, Y., Dong, M., Lei, J., et al. (2021). Comparative structural analysis of human nav1. 1 and nav1. 5 reveals mutational hotspots for sodium channelopathies. *Proceedings of the National Academy of Sciences*, 118(11). 63

Pan, X., Li, Z., Zhou, Q., Shen, H., Wu, K., Huang, X., Chen, J., Zhang, J., Zhu, X., Lei, J., Xiong, W., Gong, H., Xiao, B., and Yan, N. (2018). Structure of the human voltage-gated sodium channel nav1.4 in complex with β1. *Science*, 362(6412):eaau2486. 62

Papazian, D., Timpe, L., Jan, Y., and Jan, L. (1991). Alteration of voltage-dependence of shaker potassium channel by mutations in the s4 sequence. *Nature*, 349(6307):305–10. 41

Papazian, D. M. and Bezanilla, F. (1997). How does an ion channel sense voltage? *Physiology*, 12(5):203–210. 42

Patton, D., West, J., Catterall, W., and Goldin, A. (1992). Amino acid residues required for fast na(+)-channel inactivation: charge neutralizations and deletions in the iii-iv linker. *Proc Natl Acad Sci U S A*, 89(22):10905–9. 44

Payandeh, J., Scheuer, T., Zheng, N., and Catterall, W. A. (2011). The crystal structure of a voltage-gated sodium channel. *Nature*, 475(7356):353–8. 56

Perozo, E., R, M., Bezanilla, F., and Stefani, E. (1993). Gating currents from a nonconducting mutant reveal open-closed conformations in shaker k+ channels. *Neuron*, 11(2):353–8. 39

Plant, L. D. (2012). A role for k2p channels in the operation of somatosensory nociceptors. *Frontiers in molecular neuroscience*, 5:21. 9

Pusch, M., Noda, M., Stühmer, W., Numa, S., and Conti, F. (1991). Single point mutations of the sodium channel drastically reduce the pore permeability without preventing its gating. *Eur Biophys J*, 20(3):127–33. 40

Rai, P., Oh, S., Shyamkumar, P., Ramasamy, M., Harbaugh, R. E., and Varadan, V. K. (2013). Nano-bio-textile sensors with mobile wireless platform for wearable health monitoring of neurological and cardiovascular disorders. *Journal of The Electrochemical Society*, 161(2):B3116. 6

Ramsey, I., Delling, M., and Clapham, D. E. (2006). An introduction to trp channels. *Annu Rev Physiol*, 68:619–47. 9

Rivera-Calzada, A. and Carroni, M. (2019). Technical advances in cryo-electron microscopy. *Frontiers in molecular biosciences*, 6:72. 58

Rohl, C., Boeckman, F., Baker, C., Scheuer, T., Catterall, W., and Klevit, R. (1999). Solution structure of the sodium channel inactivation gate. *Biochemistry*, 38(3):855–61. 44

Roux, B. (2017). Ion channels and ion selectivity. *Essays Biochem*, 61(2):201–209. 22

Satin, J., Kyle, J., Chen, M., Bell, P., Cribbs, L., Fozzard, H., and Rogart, R. (1992). A mutant of ttx-resistant cardiac sodium channels with ttx-sensitive properties. *Science*, 256(5060):1202–5. 40

Schneider, M. and Chandler, W. (1973). Voltage dependent charge movement of skeletal muscle: a possible step in excitation-contraction coupling. *Nature*, 242(5395):244–6. 33

Schoppa, N., McCormack, K., Tanouye, M., and Sigworth, F. (1992). The size of gating charge in wild-type and mutant shaker potassium channels. *Science*, 255(5052):1712–5. 38

Seoh, S., Sigg, D., Papazian, D., and Bezanilla, F. (1996). Voltage-sensing residues in the s2 and s4 segments of the shaker k+ channel. *Neuron*, 16(6):1159–67. 38, 41

Shen, H., Li, Z., Jiang, Y., Pan, X., Wu, J., Cristofori-Armstrong, B., Smith, J. J., Chin, Y. K. Y. K., Lei, J., Zhou, Q., King, G. F., and Yan, N. (2018). Structural basis for the modulation of voltage-gated sodium channels by animal toxins. *Science*, 362(6412). 63

Shen, H., Liu, D., Wu, K., Lei, J., and Yan, N. (2019). Structures of human nav1.7 channel in complex with auxiliary subunits and animal toxins. *Science*, 363(6433):1303–1308. 63

Shen, H., Zhou, Q., Pan, X., Li, Z., Wu, J., and Yan, N. (2017). Structure of a eukaryotic voltage-gated sodium channel at near-atomic resolution. *Science*, 355(6328). 59

Smith, M. and Goldin, A. (1997). Interaction between the sodium channel inactivation linker and domain iii s4-s5. *Biophys J*, 73(4):1885–95. 44

Starace, D. M. and Bezanilla, F. (2001). Histidine scanning mutagenesis of basic residues of the s4 segment of the shaker k+ channel. *The Journal of general physiology*, 117(5):469–490. 43

Starace, D. M. and Bezanilla, F. (2004). A proton pore in a potassium channel voltage sensor reveals a focused electric field. *Nature*, 427(6974):548–53. 52

Starkus, J., Kuschel, L., Rayner, M., and Heinemann, S. (1997). Ion conduction through c-type inactivated shaker channels. *J Gen Physiol*, 110(5):539–50. 40

Stefani, E., Toro, L., Perozo, E., and Bezanilla, F. (1994). Gating of shaker k+ channels: I. ionic and gating currents. *Biophys J*, 66(4):996–1010. 38

Stühmer, W., Conti, F., Suzuki, H., Wang, X., Noda, M., Yahagi, N., Kubo, H., and Numa, S. (1989). Structural parts involved in activation and inactivation of the sodium channel. *Nature*, 339(6226):597–603. 44

Talley, E., Solorzano, G., Lei, Q., Kim, D., and Bayliss, D. (2001). Cns distribution of members of the two-pore-domain (kcnk) potassium channel family. *J Neurosci*, 21(19):7491–505. 9

Teague, S. J. (2003). Implications of protein flexibility for drug discovery. *Nature reviews Drug discovery*, 2(7):527–541. 65

Tempel, B., Papazian, D., Schwarz, T., Jan, Y., and Jan, L. (1987). Sequence of a probable potassium channel component encoded at shaker locus of drosophila. *Science*, 237(4816):770–5. 37

Tiwari-Woodruff, S., Schulteis, C., Mock, A., and Papazian, D. (1997). Electrostatic interactions between transmembrane segments mediate folding of shaker k+ channel subunits. *Biophys J*, 72(4):1489–500. 42

Vassilev, P., Scheuer, T., and Catterall, W. (1989). Inhibition of inactivation of single sodium channels by a site-directed antibody. *Proc Natl Acad Sci U S A*, 86(20):8147–51. 44

Volkow, N. D. and McLellan, A. (2016). Opioid abuse in chronic pain-misconceptions and mitigation strategies. *N Engl J Med*, 374(13):1253–63. 1

Waxman, S. G. and Dib-Hajj, S. D. (2005). Erythromelalgia: a hereditary pain syndrome enters the molecular era. *Ann Neurol*, 57(6):785–8. 10

Waxman, S. G. and Zamponi, G. W. (2014). Regulating excitability of peripheral afferents: emerging ion channel targets. *Nature neuroscience*, 17(2):153. 3

West, J., Patton, D., Scheuer, T., Wang, Y., Goldin, A., and Catterall, W. (1992). A cluster of hydrophobic amino acid residues required for fast na(+)-channel inactivation. *Proc Natl Acad Sci U S A*, 89(22):10910–4. 44

Wilkinson, T. C., Gardener, M. J., and Williams, W. A. (2015). Discovery of functional antibodies targeting ion channels. *J Biomol Screen*, 20(4):454–67. 68

Wu, J., Yan, Z., Li, Z., Qian, X., Lu, S., Dong, M., Zhou, Q., and Yan, N. (2016). Structure of the voltage-gated calcium channel ca(v)1.1 at 3.6 åresolution. *Nature*, 537(7619):191–196. 59

Wu, J., Yan, Z., Li, Z., Yan, C., Lu, S., Dong, M., and Yan, N. (2015). Structure of the voltage-gated calcium channel cav1.1 complex. *Science*, 350(6267):aad2395. 59

Wulff, H., Castle, N. A., and Pardo, L. A. (2009). Voltage-gated potassium channels as therapeutic targets. *Nat Rev Drug Discov*, 8(12):982–1001. 13

Yaksh, T. L., Woller, S. A., Ramachandran, R., and Sorkin, L. S. (2015). The search for novel analgesics: targets and mechanisms. *F1000prime reports*, 7. 12

Yamada, K. and Inagaki, N. (2005). Neuroprotection by katp channels. *J Mol Cell Cardiol*, 38(6):945–9. 9

Yan, Z., Zhou, Q., Wang, L., Wu, J., Zhao, Y., Huang, G., Peng, W., Shen, H., Lei, J., and Yan, N. (2017). Structure of the nav1.4-β1 complex from electric eel. *Cell*, 170(3):470–482.e11. 62

Yang, N. and Horn, R. (1995). Evidence for voltage-dependent s4 movement in sodium channels. *Neuron*, 15(1):213–218. 43

Yellen, G., Jurman, M., Abramson, T., and MacKinnon, R. (1991). Mutations affecting internal TEA blockade identify the probable pore-forming region of a k+ channel. *Science*, 251(4996):939–42. 39

Yool, A. and Schwarz, T. (1991). Alteration of ionic selectivity of a k+ channel by mutation of the h5 region. *Nature*, 349(6311):700–4. 40

Yusaf, S. P., Wray, D., and Sivaprasadarao, A. (1996). Measurement of the movement of the s4 segment during the activation of a voltage-gated potassium channel. *Pflügers Archiv*, 433(1):91–97. 43

Zhou, Y., Morais-Cabral, J., Kaufman, A., and MacKinnon, R. (2001). Chemistry of ion coordination and hydration revealed by a k+ channel-Fab complex at 2.0 åresolution. *Nature*, 414(6859):43–8. 46

Zoga, V., Kawano, T., Liang, M.-Y., Bienengraeber, M., Weihrauch, D., McCallum, B., Gemes, G., Hogan, Q., and Sarantopoulos, C. (2010). Katp channel sub-

units in rat dorsal root ganglia: alterations by painful axotomy. *Molecular pain*, 6:1744–8069. 9

Chapter 2

Materials and Methods

2.1 Preface

This chapter constitutes the materials and methods section for the entire thesis aims to verbosely detail all protocols used in order to complete the experiments outlined in the thesis. Product codes and manufacturers are given where appropriate. All chemicals were purchased from Sigma-Aldrich and can be found in their catalogue.

2.2 Molecular Biology

2.2.1 Materials

Category	Reagent	Source	Product Code
Kits	QIAX II Gel Extraction	Qiagen	20021
	QIAprep Spin Miniprep Kit	Qiagen	27106
	PureYield Plasmid Midiprep System	Promega	A2495
	Qiaquick PCR Purification Kit	Qiagen	28106
	RNEasy Mini Kit	Qiagen	74106
	SP6 High Yield Message Kit	Cellscript	C-AC0706
Gel Electro-phoresis	Agarose	Sigma	A9539
	50X TAE Buffer	AppliChem	A1691
	Ethidium Bromide	Promega	H5041
	6X Gel Loading dye	NEB	B7025S
	1kb DNA ladder	NEB	N3232L
Restriction Enzymes	AgeI	Promega	R752A
	Acc65I	NEB	R0599S
	BamHI	Promega	R602A
	HindIII	Promega	R604A
	MluI	Promega	R638A
	PstI	Promega	R611A
	XbaI	Promega	R618A
Enzymes	DNA Pol I, Klenow Fragment	NEB	M0210S
	T4 Polynucleotide Kinase (PNK)	NEB	M0201S
PCR	Pfu Ultra HF DNA Polymerase	Agilent	600380-51
	Pfu DNA Polymerase	Promega	M774A
	Q5 Hot Start polymerase	NEB	M0493
	dNTP Mix	NEB	N0447S
	ddH_2O	Fischer Scientific	231-791-2
	DpnI	Promega	R623A
	T4 DNA Ligase	Promega	M180A
Media	Luria Broth	Sigma	L3522
	Select Agar	Sigma	A5054
	S.O.C. Medium	Invitrogen	15544-034
Anti-biotics	Carbenicillin Disodium	Apollo Sci. Ltd.	BIC0109
	Kanamycin monosulphate	Apollo Sci. Ltd.	D0610079
Plastic-ware	Sterilin ^{TM} 90mm Petri Dishes	Thermo Fisher	101VR20
	Spreaders	VWR	612-1561
	Coli rollers	Millipore	71013
	14ml Round Bottom Tubes	Falcon	352059
	Pyrex ^{TM} 250ml Erlenmeyer Flask	Fisher Scientific	12039012
	PCR Tubes	Sci. Spec. Inc.	3 240-00
Cells	Subcloning Efficiency ^{TM} DH5-α	Thermo Fisher	18265017

Table 2.1: **List of materials for Molecular Biology**
NEB = New England Biolabs, Apollo Sci. Ltd = Apollo Scientific Limited, VWR = VWR International, Sci. Spec. Inc = Scientific Specialties Incorporated

2.2.2 Summary of Channel Constructs used in this study

A summary of the channel, isoform, abbreviation and uniprotKB identifier are provided in Table 2.2 along with the vectors in which they were expressed. All sequences used in this study were human unless explicitly stated with a lower case prefix (h = human, m = mouse, r = rat).

The pUC19 vector (addgene: 50005 (Norrander et al., 1983)) is a cloning vector used to make mutations within indiviudal Nav1.7 (SCN9A) gene fragments.

The pBi vector (Clontech: 6152-1) is a mammalian expression vector which allows bi-directional expression of two proteins in the same vector using two minimal cytomegalovirus (CMV) promoters and was used to co-express either Nav1.2 or Nav1.7 with the β1 or β2 subunit in mammalian cells.

The pBF vector is an oocyte expression vector, containing an SP6 promoter, the 5' and 3' untranslated region (UTR) of the *Xenopus* globin gene and a poly(A) signal for mRNA stabilisation (Krieg and Melton, 1984; Liman et al., 1992; Shih et al., 1998) and allows synthesis of mature RNA using an appropriate kit that recognises the SP6 promoter. This vector was used to produce K2P channel mRNA for oocyte injection.

The pFAW vector is in house dual mammalian and oocyte expression vector derived from pCDNA6 and containing a T7 promoter and the 5' and 3' UTR of the *Xenopus* globin gene for mRNA stabilisation (Krieg and Melton, 1984; Liman et al., 1992; Shih et al., 1998) and allows synthesis of mature RNA using an appropriate kit that recognises the T7 promoter. The vector contains this between a CMV enhancer/promoter and the Bovine Growth Hormone Polyadenylation Signal so that

it may also be transfected into cells for mammalian expression of the same channel. This vector was used to express K2P channels and K2P-mcherry fusions

The pEXO vector is an oocyte expression vector derived from pSK and containing the 5' and 3' UTR of the *Xenopus* β-globin mRNA sequences for mRNA stabilization (Krieg and Melton, 1984; Liman et al., 1992; Shih et al., 1998). mTREK-2 in the pEXO vector was kindly provided by P. Enyedi; the procedure for cloning the mouse channel into the pEXO vector is described here (Czirják and Enyedi, 2006). This vector was used to produce mouse TREK-2 mRNA for oocyte injection.

Channel	Isoform	Vector(s)	Abbreviation	Uniprot
Nav1.7	*Homo Sapiens* Isoform 1	pBi with β2	Nav1.7 β2	Q15858-1 O60939
Nav1.2	*Homo Sapiens* Isoform 6A/ Adult	pBi with β1	Nav1.2 β1	Q99250-1 Q07699-1
TREK-2	*Homo sapiens* Isoform B	pBF pFAW	hTREK-2b	P57789-4
TREK-1	*Homo sapiens* Isoform 1	pBF PFAW	hTREK-1b	O95069-1
TREK-2	*Mus musculus* Isoform c	pEXO	mTREK-2b	Q3LS20
TRAAK	*Homo sapiens* Isoform 2	pFAW	hTRAAK Iso2	Q9NYG8-2
TRESK	*Homo sapiens*	pFAW	hTRESK	Q7Z418
TASK-1	*Homo sapiens*	pFAW	hTASK-1	O14649
TASK-2	*Homo sapiens*	pFAW	hTASK-2	O95279
TASK-3	*Homo sapiens*	pBF pFAW	hTASK-3	Q9NPC2-1
THIK-1	*Homo sapiens* Δ6-23	pFAW	hTHIK-1*	Q9HB14
THIK-2	*Homo sapiens*	pFAW	hTHIK-2	Q9HB15
TALK-1	*Homo sapiens*	pFAW	hTALK-1	Q96T55
TALK-2	*Homo sapiens*	pFAW	hTALK-2	Q96T54
TWIK-1	*Homo sapiens* II293/294AA	pFAW	hTWIK-1*	O00180
TWIK-2	*Homo sapiens*	pFAW	hTWIK-2	Q9Y257

Table 2.2: **Channels Used in this Study**

2.2.3 Summary of Scorpion Toxin Constructs used in this Study

The α-scorpion toxins were expressed as C-terminal His- Maltose Binding Protein (MBP) fusions in Sf9 insect cells. The MBP tag was cleaved using Tobacco Etch Virus (TEV) protease for which a cleavage site resides in the linker. Details of the purification can be found in Purification of Scorpion Toxins.

5 α-scorpion toxins were used in this study, and full sequences of the fusion protein can be found in Figure 2.1. The structural features used in this alignemnt are based on PDB accession 1PTX, a published structure of AahII which was the workhorse for this study. The topology of AahII and an annotated structure is also given in Figure 2.1.

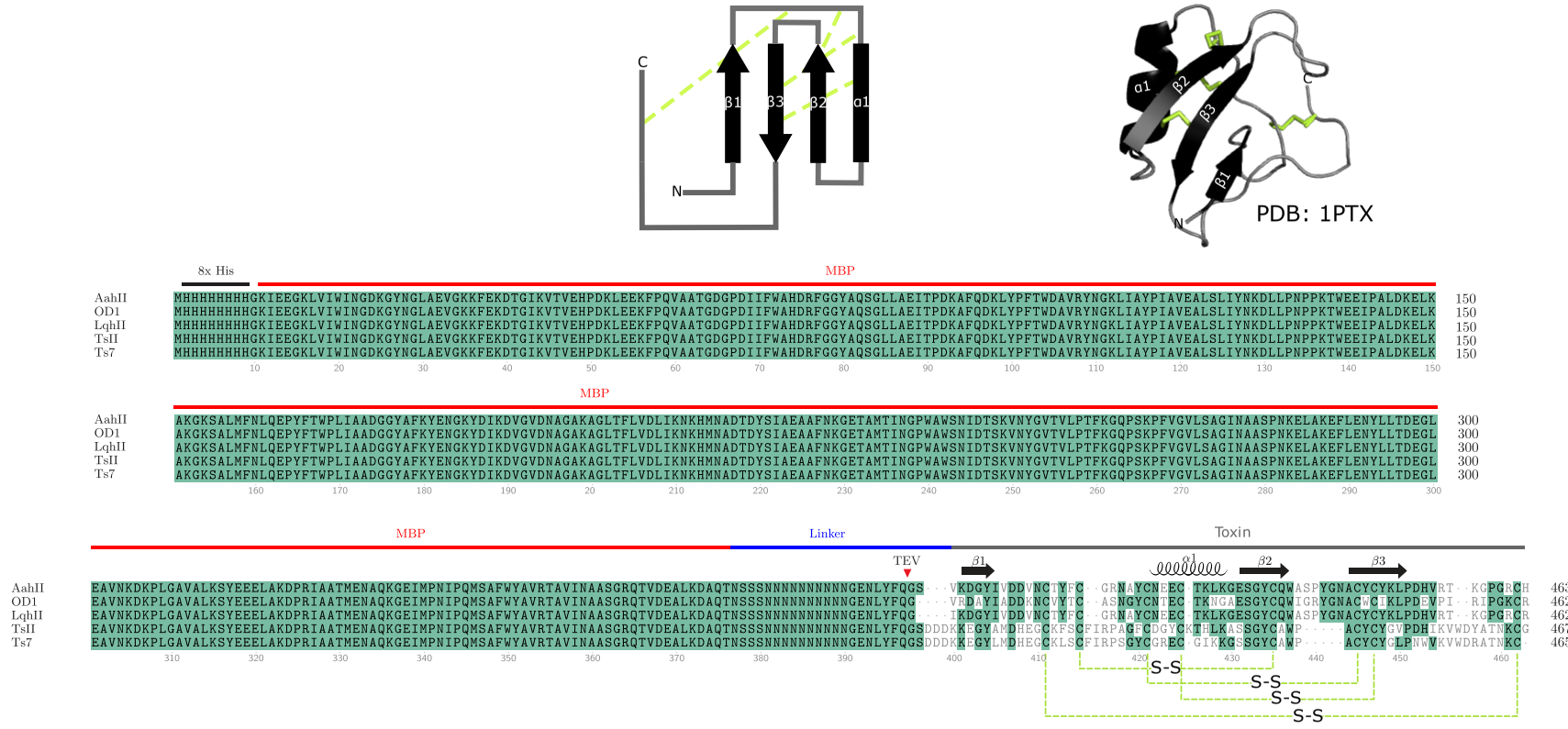


Figure 2.1: **Summary and Structural Alignment of α- Scorpion Toxins used in this Study**

2.2.4 Summary of VHH Antibody Constructs used in this Study

All VHH Antibodies were provided in the pMESy4 vector (GenBank KF415192). The pMESy4 vector is a phage display vector but places the VHH Antibody sequence downstream of a lactose (lac) promoter/operator and a pectate lyase B (pelB) signal secretion sequence and in frame with a C-terminal His-tag and Capture Select^{TM} tag, allowing bacterial induction, periplasmic expression and subsequent purification. Details of the purification can be found in Periplasmic expression of VHH antibodies.

pET-22b (MilliporeSigma (Novagen) is a bacterial expression vector containing a T7 promoter upstream of the Lac operator. The MCS allows cloning of genes upstream of the pelB signal secretion sequence and in frame with a C-terminal His tag, allowing bacterial induction, periplasmic expression and subsequent purification. Details of cloning can be found in Subcloning by PCR and details of the purification can be found in Periplasmic expression of VHH antibodies.

pET-28a (EMD Biosciences) is a bacterial expression vector containing a T7 promoter upstream of the Lac operator. The multiple cloning site (MCS) allows cloning of genes downstream of a His_6- thrombin- leader peptide from bacteriophage T7 gene 10 and upstream of a C-terminal His tag. Details of cloning can be found in Subcloning by PCR and details of the purification can be found in Cytosolic expression of VHH antibodies.

pHLSec is a mammalian expression and secretion vector (Aricescu et al., 2006) containing a CMV enhancer, chicken β-actin promoter and a chimeric intron (Hermening et al., 2004) upstream of a Signal secretion sequence. It allows cloning of a gene upstream of a C-terminal His tag, which will subsequently allow expression

and secretion of the protein product. Details of cloning can be found in Subcloning by PCR and details of the expression and characterisation/quantification can be found in VHH Antibody-mVenus harvesting from Mammalian cells and Characterisation of mVenus-tagged VHH antibodies respectively.

pScFcAC is a novel in house vector which uses the pHLSec vector backbone features but places a His-tagged C-terminal Single Chain Fragment Constant (ScFc) (Newnham et al., 2015) downstream of two genes of interest separated by a human rhinovirus 3C (HRV3C) protease and TEV protease sites. Full details of creation of this vector can be found in pScFcAC Vector creation.

A total of 32 unique VHH Antibodies labelled numerically from CA10752-CA10783 were raised against a truncated hTREK-2c construct (G66-E340 Ct 10x His FLAG, top left, Figure 2.2). All of the translated open reading frames (ORFs) matched the protein sequences given by Nanobodies4INSTRUCT. The full alignment is given at the bottom of Figure 2.2. The structural features used in this alignment are based on PDB: 5OVW, a published structure with the highest sequence identity to CA10752 Figure 2.2.

A total of 18 unique VHH Antibodies labelled numerically from CA11343-CA1160 were raised against a truncated hTREK-1b construct (P26-S30 Ct 10x His FLAG top left, Figure 2.3). 12 of the 18 translated ORFs matched the protein sequences given by Nanobodies4INSTRUCT. Only these 12 are included in the alignment which is given at the bottom of Figure 2.3 for clarity. The structural features used in this alignment are based on PDB: 5NBD published structure with the highest sequence identity to CA11343 Figure 2.3.

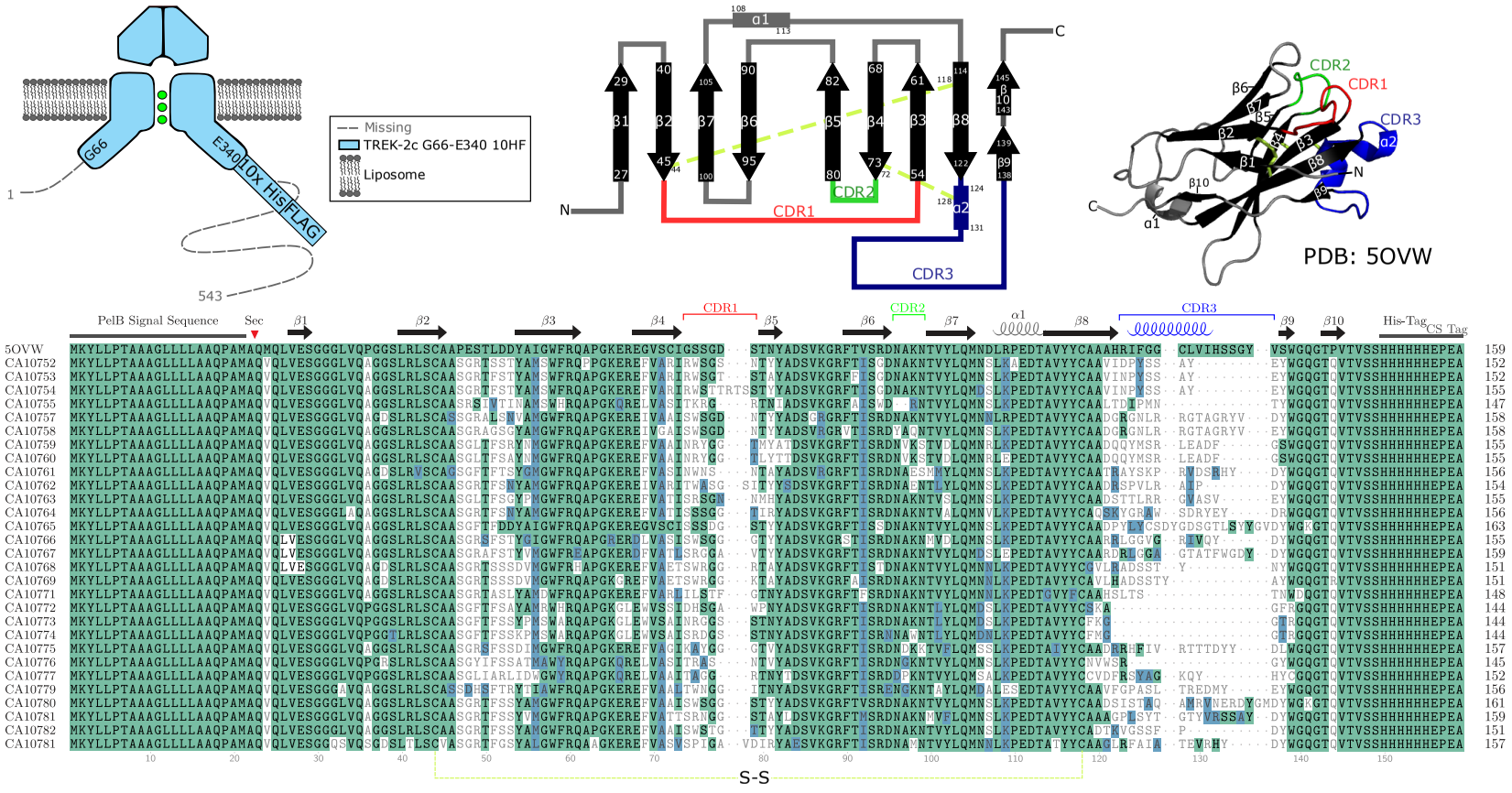


Figure 2.2: **Summary and Structural Alignment of VHH Antibodies Raised against TREK-2**

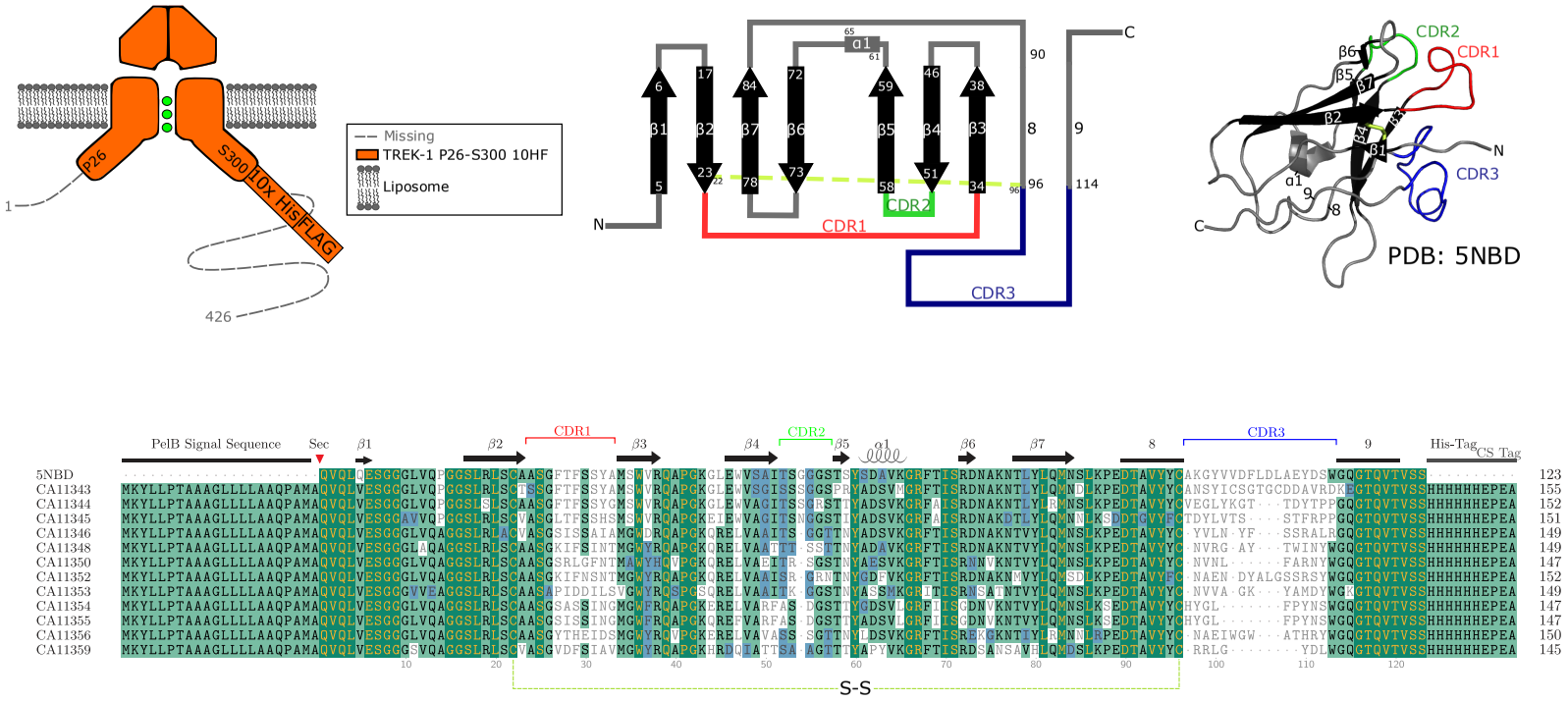


Figure 2.3: **Summary and Structural Alignment of VHH Antibodies Raised against TREK-1**

2.2.5 Subcloning by PCR

If there were no appropriate restriction sites to move genes of interest (GOI) between vectors, or if extra functionality required (e.g. kozak sequence, start codon, stop codon), then they were subcloned using polymerae chain reaction (PCR). Forward and reverse primers were designed as shown in Figure 2.4, and the specific sequence details for each gene subcloned are shown in Table 2.3 below. The colours in Table 2.3 are matched to the ones in Figure 2.4 for clarity.

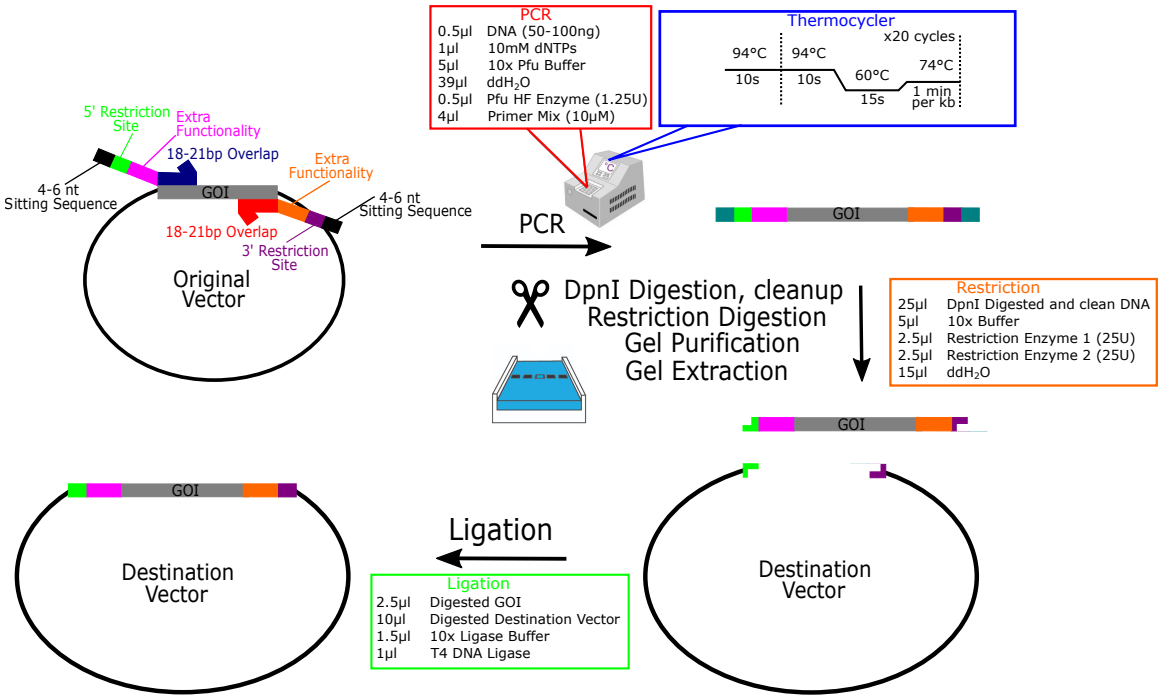


Figure 2.4: **Schematic of Subcloning by PCR**

Briefly, the DNA fragments were amplified by PCR using Pfu (*Pyrococcus furiosus*) polymerase using the reaction mixture detailed in the red box in Figure 2.4, followed by thermocycling using the general protocol shown in the blue box in Figure 2.4. Following amplification by PCR, the methylated DNA was digested by addition of 1 µl of DpnI (10U) to the 50 µl PCR product, incubated at 37°C for at least one hour and then cleaned using the PCR cleanup kit (Qiagen) accord-

ing to manufacturers instructions (diluted 5:1 with Buffer PB) and eluted in 25 µl ddH_2O. The cleaned PCR product and the destination vector were then digested with an appropriate pair of restriction enzymes in a suitable buffer (detailed in Table 2.3) and separated by size using agarose gel electrophoressis on a 1% agarose gel (w:v in Tris-acetate-EDTA (TAE), 100V, 35mins). Following separation by size, the digested vector backbone and digested insert were cut out and extracted from the gel using the Gel extraction kit (Qiagen) according to manufacturers instructions and eluted in 30µl of ddH_2O. The purified GOI and destination vector were mixed 1:4 by volume and ligated in a 15 µl reaction as detailed in the green box in Figure 2.4 and left to ligate overnight at 4 °C. The full ligation reaction was then transformed using the standard protocol detailed in Heat Shock Transformation.

Gene	Original Vector	New Vector	Forward Primer	Reverse Primer
CA10751 CA10752 CA10753 CA10754 CA10755 CA10757 CA10758 CA10761 CA10762 CA10763 CA10767	pMESy4	pHLSec Ct mVenus	**pHLSec Clone Ct F** GCCTTAACC GGTCAGGTG CAGCTGGTG GAG AgeI	**pHLSec Clone R** CTAGTCGGT ACCACTGGA GACGGTGAC CT Acc65I
CA10761 CA10767	pMESy4	pET-28a(+)	**Clone pET28a F** ATCTGGGAT CCCAGGTGC AGCTGGTGG AG BamHI	**Clone pET28a R** ATGCAAGCT TACTGGAGA CGGTGACCT GG HindIII

Continued on next page

Gene	Original Vector	New Vector	Forward Primer	Reverse Primer
CA10761 CA10767	pMESy4	pET-22b(+)	**Clone pET22b For** TACCTATTG CCTACGGCA GCC	**Clone pET22b Rev** CATGGAAGC TTACTAGGC TTCAGGTTC GTG HindIII
mCherry	pHAF	pCDNA3	**mCherry Clone F** CATGGGTAC CGCCCCCAC CATGGTGAG CAAGGGCGA G Acc65I Kozak	**mCherry Clone R** ACGTTCTAG ACTACTTGT ACAGCTCGT CCATGCC XbaI
hTALK-1d	pFB-CT10HF LIC	pFAW	**TALK1 CloneF** ATTGCGGAA TTCGCCCCC ACCATGCCC AGTGCTGGG CTCTGC EcoRI Kozak	**TALK1 CloneR** ATGTAA GGT ACCTCAGCT TCCCAGTCC TTTCTTGGA TATGGGGAA Acc65I
hTHIK-2	pFB-CT10HF LIC	pFAW	GCCCAGTCT AGAGCCACC ATGTCCTCC CGCAGCCCC XbaI Kozak	**THIK-2 R** CTGGGCGGT ACCCTACCT GGAGGCGCT GGTCTC Acc65I

Continued on next page

Gene	Original Vector	New Vector	Forward Primer	Reverse Primer
EGFP	pEGFP-N1	pScFcAc	**GFP BamHI F** ATCGACGGATCCATGGTGAGCAAGGGCGAGGAG BamHI	**GFP Acc65I R** CTGACGGTACCCTTGTACAGCTCGTCCATGCC Acc65I
hTWIK-1* I293A / I294A	pFAW	hTREK-1-mCherry-BamHI*	**T7F** TAATACGACTCACTATAGGG	**TWIK-1 R** ATCGACGGATCCATGGTTTGCAGGGCCATC Acc65I
hTWIK-2	pFAW	hTREK-1-mCherry-BamHI*	**T7F** TAATACGACTCACTATAGGG	**TWIK-2 R** ATCGACGGATCCCCTGGGGATGGAAGCGTA Acc65I
hTASK-1	pFAW	hTREK-1-mCherry-BamHI*	**T7F** TAATACGACTCACTATAGGG	**TASK-1 R** ATCGACGGATCCCACGGAGCTCCTGCGCTT Acc65I

Continued on next page

Gene	Original Vector	New Vector	Forward Primer	Reverse Primer
hTRESK	pFAW	hTASK-1-mCherry-BamHI*	**T7F** TAATACGACTCACTATAGGG	**TRESK R** ATCGACGGATCCCTTTTTAACAAGGTGGTA Acc65I
hTASK-2	pFAW	hTASK-1-mCherry-BamHI*	**T7F** TAATACGACTCACTATAGGG	**TASK-2 R** ATCGACGGATCCTGTGCCCTTGGGGCTGTT Acc65I
hTASK-3	pFAW	hTASK-1-mCherry-BamHI*	**T7F** TAATACGACTCACTATAGGG	**TASK-3 R** ATCGACGGATCCAACGGACTTCCGGCGTTT Acc65I
hTHIK-2	pFAW	hTASK-1-mCherry-BamHI*	**THIK-2 Δ 6-23** AAAAAATCTAGAGCCACCATGTCCTCCCGCAGCTGCTGCTGCTGCCGCCGTTCGCACCTCAACG XbaI Kozak, MSSRS (1-5)	**THIK-2 R** ATCGACGGATCCCCTGGAGGCGCTGGTCTC Acc65I

Continued on next page

Gene	Original Vector	New Vector	Forward Primer	Reverse Primer
			pHLSec Clone Ct F	**Clone pET28a R**
CA10752				
CA10757			GCCTTAACC	
CA10758	pHLSec	pScFcAC	GGTCAGGTG	ATGCAA
CA10761			CAGCTGGTG	GCTTACTGG
CA10762			GAG	AGACGGTGA
CA10763				CCTGG
			AgeI	HindIII

Table 2.3: **Summary of Constructs Cloned by PCR**

2.2.6 Site-Directed Mutagenesis

Point mutations were made in genes of interest using site-directed mutagenesis (SDM). Forward and reverse primers were designed to include overlap with the GOI upstream and downstream of the desired mutation and including the desired mutation as shown in Figure 2.5. The primers used for each point mutant made are shown in Table 2.4 below, where the triplet containing the mutation is highlighted for clarity, and match the colours in Figure 2.5.

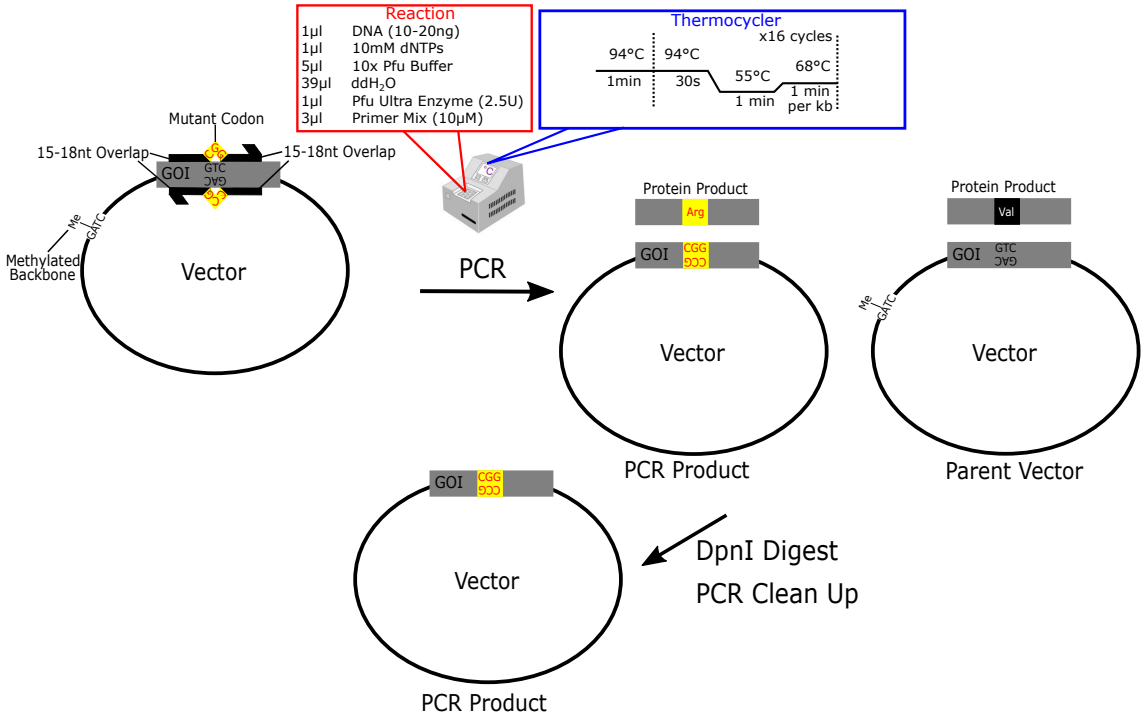


Figure 2.5: **Schematic of Site Directed Mutagenesis**

Briefly, the DNA fragments were amplified by PCR using Phusion HF polymerase using the reaction mixture detailed in the red box in Figure 2.5, followed by thermocycling using the general protocol shown in the blue box in Figure 2.5. The primers for each point mutant are shown in Table 2.4 below, and the amplification time was altered to be 1 min per kb of the plasmid to be mutated. Following amplification by PCR, the methylated template was digested by addition of DpnI

for 1 hour at 37 °C. The mutated DNA was purified using the QiaQuick spin-column kit according to manufacturers instructions and eluted in 30 µl ddH_2O. The full eluate was then transformed using the standard protocol detailed in Heat Shock Transformation.

Mutation	**Gene Vector**	**Forward Primer**	**Reverse Primer**
E113A	hTREK-2b pFAW	GAATACCATCGCCTTG GCG AAGGCGGAATTCC	GGAATTCCGCCTT CGC CAAGGCGATGGTATTC
E116A		GCCTTGGAGAAGGCG GCA TTCCTGCGGGATC	GATCCCGCAGGAA TGC CGCCTTCTCCAAGGC
F117A		TTGGAGAAGGCGGAA GCC CTGCGGGATCATGTC	GACATGATCCCGCAG GGC TTCCGCCTTCTCCAA
D120A		GCGGAATTCCTGCGG GCT CATGTCTGTGTGAG	CTCACACAGACATG AGC CCGCAGGAATTCCGC
Q127A		GTCTGTGTGAGCCCC GCG GAGCTGGAGACGTTG	CAACGTCTCCAGCTC CGC GGGGCTCACACAGAC
E128A		TGTGTGAGCCCCCAG GCG CTGGAGACGTTGATC	GATCAACGTCTCCAG CGC CTGGGGGCTCACACA
T131A		CCCCAGGAGCTGGAG GCG TTGATCCAGCATGCT	AGCATGCTGGATCAA CGC CTCCAGCTCCTGGGG
H135A		GAGACGTTGATCCAG GCT GCTCTTGATGCTGAC	GTCAGCATCAAGAGC AGC CTGGATCAACGTCTC
D138A		ATCCAGCATGCTCTT GCT GCTGACAATGCGGGA	TCCCGCATTGTCAGC AGC AAGAGCATGCTGGAT
N292A		TTTGTGGCAGGGGGA GCC GCTGGCATCAATTATC	GATAATTGATGCCAGC GGC TCCCCCTGCCACAAA
S321A		CTTTGCAGCTGTCCTC GCT ATGATCGGAGATTG	CAATCTCCGATCAT AGCG AGGACAGCTGCAAAG

Continued on next page

Mutation	Gene Vector	Forward Primer	Reverse Primer
D325A	hTREK-2b pFAW	CCTCAGTATGATCGGA GCT TGGCTACGGGTTC	GAACCCGTAGCCA AGC TCCGATCATACTGAGG
R328A		GATCGGAGATTGGCTA GCG GTTCTGTCCAAAAAG	CTTTTTGGACAGAAC CGC TAGCCAATCTCCGATC
K335A		GTTCTGTCCAAAAAG ACAGCA GAAGAGGTGGGTG	CACCCACCTCTTC TGCTGT CTTTTTGGACAGAAC
S30A	CA10767 pMESy4	CTGGACGCGCCTTC GCT ACCTATGTCATGGGC	GCCCATGACATAGGT AGC GAAGGCGCGTCCAG
S52A		CTTTGTGGCAACTCTT GCT CGGGGTGGTGCTG	CAGCACCACCCCG AGC AAGAGTTGCCACAAAG
R53A		TGTGGCAACTCTTAGT GCG GGTGGTGCTGTGAC	GTCACAGCACCACC CGC ACTAAGAGTTGCCACA
G54A		GGCAACTCTTAGTCGG GCT GGTGCTGTGACATAC	GTATGTCACAGCACC AGC CCGACTAAGAGTTGCC
A56V		TCTTAGTCGGGGTGGT GTT GTGACATACTATG	CATAGTATGTCAC AAC ACCACCCCGACTAAGA
Y59A		GGTGGTGCTGTGACA GCC TATGCAGACTCCGTG	CACGGAGTCTGCATA GGC TGTCACAGCACCACC
G103A		CAGCACGTGATAGACT TGCG GGCGCCGGTACG	CGTACCGGCGCC CGCA AGTCTATCACGTGCTG
G106A		AGACTTGGGGGCGCC GCT ACGGCCACCTTTTG	CAAAAGGTGGCCGT AGC GGCGCCCCCAAGTCT
L47A	CA10776 pMESy4	GGGAAGCAGCGCGAG GCG GTCGCAAGTATTACT	AGTAATACTTGCGAC CGC CTCGCGCTGCTTCCC
T52A		GTTGGTCGCAAGTATT GCT AGGGCTAGTAACACAG	CTGTGTTACTAGCCCT AGC AATACTTGCGACCAAC

Continued on next page

Mutation	Gene Vector	Forward Primer	Reverse Primer
R53A	CA10776 pMESy4	GTCGCAAGTATTACT GCG GCTAGTAACACAGTC	GACTGTGTTACTAGC CGC AGTAATACTTGCGAC
A54V		GCAAGTATTACTAGG GTT AGTAACACAGTCTATG	CATAGACTGTGTTACT AAC CCTAGTAATACTTGC
S99A		TACTGTAATGTCTGG GCT CGCGGGTACTGGGGC	GCCCCAGTACCCGCG AGC CCAGACATTACAGTA
R100A		CTGTAATGTCTGGAGT GCC GGGTACTGGGGCCAG	CTGGCCCCAGTACCC GGC ACTCCAGACATTACAG
S164P	hTREK-1c pFAW	GGATTTGGAAACATC CCA CCACGCACAGAAGGC	GCCTTCTGTGCGTGG TGG GATGTTTCCAAATCC
R14A	hTHIK-2 pFAW	CCGCCCCGCCGTAGC GCC CGCCGCCTGCCGCGC	GCGCGGCAGGC GGCGGGC GCTACGGCGGGGCGG
RR14/ 15AA		CCCCCGCCCCGCCGT AGCGCCGCCCG CCTGCCGCGCCCCTCC	GGAGGGGCGCGGCAG GCGGGCGGCGCTACG GCGGGGCGGGGGCCG
BamHI Removal	hTREK-1c mCherry pFAW	GCTCAACTTTGGCAG GCA TCCGGGCCCCGGGTT	AACCCGGGGCCCGGA TGC CTGCCAAAGTTGAGC

Table 2.4: **Summary of Site Directed Mutagenesis Mutants Made during this study**

2.2.7 Subcloning by Restriction Digest

If the gene of interest had appropriate restriction enzyme sites and did not require extra functionality, then it was subcloned by restriction digest, as summarised in Table 2.5 below.

Briefly, the gene of interest and the destination vector were digested with a pair of restriction enzymes (detailed in Table 2.5) and cloned as described in Subcloning by PCR, but without the need for the initial PCR amplification step.

Gene	Original Vector	Destination Vector	5′ Restriction Site	3′ Restriction Site
hTASK-2 hTWIK-2 Iso1 hTRAAK Iso2 hTHIK-1 hTREK-1c P2Ct TREK2b hTREK-2b P2Ct TREK1c	pBF	pFAW	XbaI	Acc65I
ScFc	pCDNA3.1	pLexm*	EcoRI	XbaI

Table 2.5: **Summary of Genes Subcloned by Restriction Digest**

2.2.8 Cloning K2P-mCherry Channel fusions by Extension Overlap PCR

Fluorescent K2P channels containing internal BamHI sites were cloned using extension overlap PCR. Primers were designed to ensure that the Reverse primer for the channel construct and the forward primer for mCherry contained the full G-S-G-S-G linker and elements of the cognate channel and mCherry, as demonstrated in Figure 2.6. A summary of channels cloned by this method can be found in Table 2.6 and the colour is matched to Figure 2.6 for clarity. The forward primer used for TREK-2 was EO-PCR-F (5' GGTGCGTCCGAGGACAAC 3') and for all other channels was T7F (5' TAATACGACTCACTATAGGG 3'). The reverse primer for all mCherry PCRs was EO-PCR-R (5' ATGTCAGGTACCCTACTTGTACAGCTCGTCCA 3') which contains the Acc65I restriction site. Primer names are coloured green in Figure 2.6. Both K2P and mCherry were amplified by PCR using Phusion HF polymerase using the reaction mixture detailed in the red box in Figure 2.6, followed by thermocycling using the general protocol shown in the blue box in Figure 2.6. Following amplification by PCR, the methylated template was digested by addition of DpnI for 1 hour at 37 °C. The mutated DNA was purified using the QiaQuick spin-column kit according to manufacturers instructions and eluted in 30 µl ddH_2O.

A second round of Extension Overlap PCR using the forward primer from the channel PCR (EO PCR F or T7F)) and the reverse primer from the mCherry PCR (EO PCR R) along with the cleaned PCR products from reaction 1 and reaction 2 were then set up using the thermocycling conditions shown in the blue box 'Extension Overlap PCR' in Figure 2.6 to create K2P-mCherry fusions. TREK-2-mCherry fusion was subcloned back into hTREK-2-pFAW using the BspHI and Acc65I restriction sites, while all other channels used XbaI and Acc65I and were cloned into

the empty pFAW vector using an analogous protocol to the one described in Subcloning by PCR and detailed in orange in Figure 2.6.

Following successful production of K2P channels with internal BamHI sites, the BamHI site in the MCS of the pFAW vector of the TREK-1-mCherry construct was removed by SDM as detailed in Site-Directed Mutagenesis, and other channels cloned into either this construct (TREK-1*-mCherry) or a resultant BamHI removed construct (TASK-1*-mCherry) making use of the G-S-G-S-G linker BamHI, as detailed in Schematic of Subcloning by PCR.

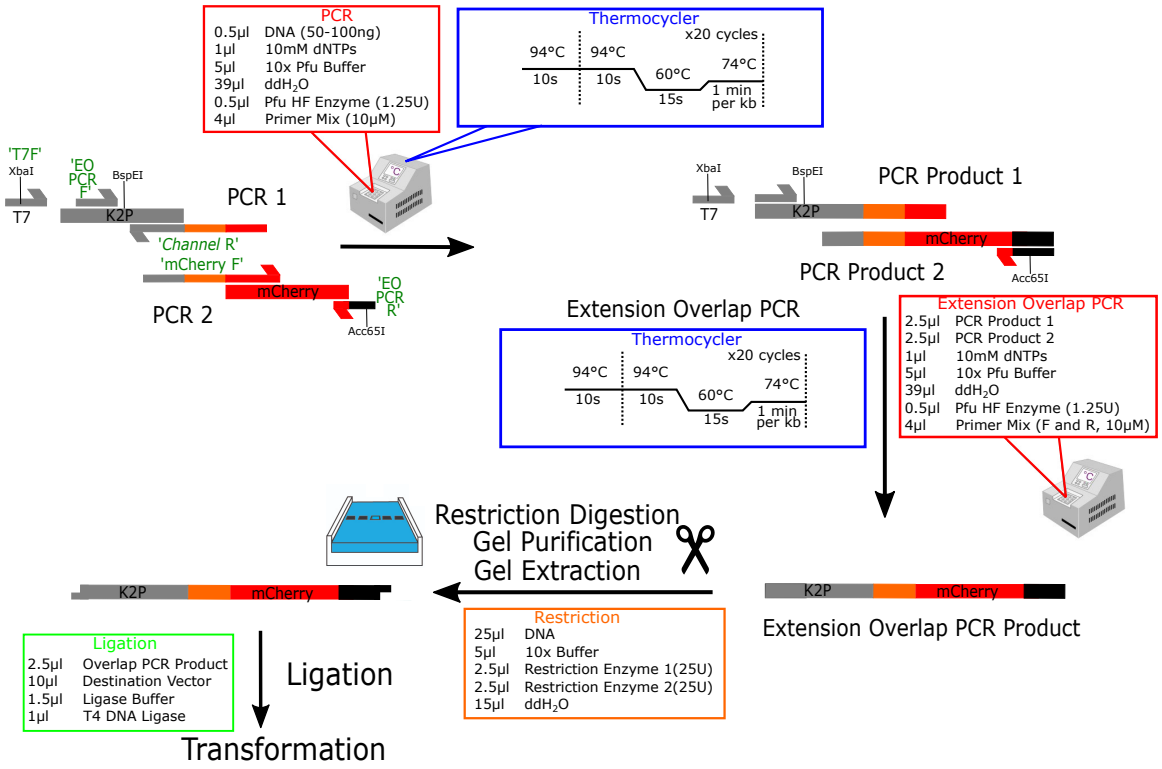


Figure 2.6: **Schematic of Extension Overlap PCR**

Gene	Overlap Extension R (Top, 5'-3') and F (Bottom), 3'-5'
hTREK-2	AGTAATGAACTTCTGTCTTTGCCTAGGCCCTCACCTTACCACTCGTTCCCGCTC
mCherry	3' TTACTTGAAGACAGAAACGGATCCGGGAGTGGAATGGTGAGCAAGGGCGAGGAG
hTREK-1	CGACACTAACTCTTGTAGTTTCCTAGGCCCTCACCTTACCACTCGTTCCCGCTC
mCherry	3' GTGATTGAGAACATCAAAGGATCCGGGAGTGGAATGGTGAGCAAGGGCGAGGAG
hTRAAK	GCTCTGTTTCCGCACGGCCACCCTAGGCCCTCACCTTACCACTCGTTCCCGCTC
mCherry	3' GACAAAGGCGTGCCGGTGGGATCCGGGAGTGGAATGGTGAGCAAGGGCGAGGAG
hTALK-1	AGGTTCTTTCCTGACCCTTCGCCTAGGCCCTCACCTTACCACTCGTTCCCGCTC
mCherry	3' AAGAAAGGACTGGGAAGCGGATCCGGGAGTGGAATGGTGAGCAAGGGCGAGGAG
hTHIK-1	CGTCTCTGGTCACCCCTGTCC CCTAGGCCCTCACCTTACCACTCGTTCCCGCTC
mCherry	3' GAGACCAGTGGGGACAGGGGATCCGGGAGTGGAATGGTGAGCAAGGGCGAGGAG

Table 2.6: **Summary of genes and primers used for cloning by Extension Overlap PCR**

2.2.9 Cloning Sorttagged VHH antibodies by Inverse PCR

VHH antibodies in the pMESy4 vector were amplified using Q5 hot Start Polymerase in a 50 µl reaction with SortagF (5' GGGGGGCCACCACCATCACCATCACG 3') and SortagR (5' GTCTCAGGCAGTGAGGAGACGGTGACCTGG 3'). Following amplification by PCR, the methylated template was digested by addition of DpnI for 1 hour at 37 °C. The linear sorttagged DNA was purified using the QiaQuick spin-column kit according to manufacturers instructions and eluted in 45 µl ddH_2O. The linear sortagged DNA was then phosphorylated by addition of 1 µl of T4 Polynucleotide Kinase (PNK) and 5 µl of 10x T4 DNA ligase buffer for 30 minutes at 37 °C. The PNK reaction was then heat inactivated by incubation at 65 °C for 20 minutes. The linear phosphorylated PCR product was then be intramolecularly ligated by addition of 1 µl of T4 DNA ligase (the reaction already contains T4 ligase buffer and ATP) overnight at 4°C. The ligation product was then transformed using the standard protocol detailed in Heat Shock Transformation.

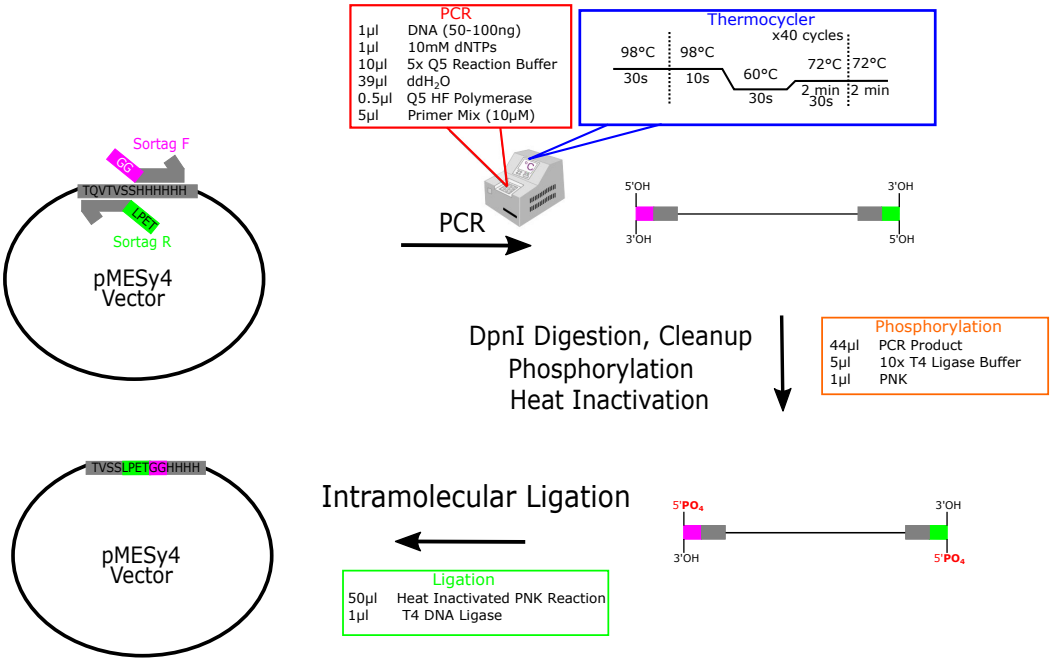


Figure 2.7: **Schematic of Sorttag Cloning Using Inverse PCR**

2.2.10 Nav1.7 Mutagenesis and Subcloning

Owing to the large size and difficulty in cloning of the SCN9A gene, point mutations were made to SCN9A gene fragments each in the pUC19 vector and then subcloned into the pBi vector after the mutation had been verified. Briefly, point mutations were made in the relevant SCN9A gene fragment in pUC19 using the Quickchage II (Agilent) kit according to manufacturers instructions and mutation confirmed by sequencing. The fragment was then subcloned into a full length Nav1.7 construct (in the pBi vector) by restriction cloning as described above. The ligation was transformed to 100µl NEB Turbo (NEB) cells and used to inoculate a 5ml overnight culture (shaking 37 °C, 200 revolutions per minue (rpm.)) The 5ml culture was used to inoculate a 500ml master culture (shaking 37 °C, 200rpm) from which DNA was purified using a Maxiprep kit (ThermoFischer) according to manufacturers instructions. The whole vector was subsequently sequenced to verify the correct mutation and no rearrangements had occurred.

2.2.11 Heat Shock Transformation

Cleaned PCR products (SDM) or ligated DNA products (subcloning) were mixed with 100 µl competent DH5-αcells on ice for 30 mins. This mixture was then heat shocked at 42°C for 45 seconds before being left to recover on ice for 2 mins. If plating on kanamycin supplemented plates, the cells were mixed with 500 µl of unsupplemented S.O.C. media and grown for 1 hour at 37 °C, shaking at 180rpm to allow antibiotic resistance to develop prior to plating. Otherwise, the whole cell-DNA mixture was then immediately plated on Lysogeny Broth (LB)-Agar plates supplemented with an appropriate antibiotic 100 $\mu g ml^{-1}$ Carbenicillin or 50 $\mu g ml^{-1}$ kanamycin). Plates were incubated overnight at 37 °C and were subsequently stored sealed from air at 4 °C.

2.2.12 Culture and DNA extraction

For general cloning purposes, 5ml overnight cultures of LB supplemented with an appropriate antibiotic (100 µgml-1 Carbenicillin or 50 µgml-1 kanamycin) were inoculated from an agar plate with a sterile pipette tip and grown in 15ml round-bottom tubes at 37 °C, shaking at 180rpm. DNA was extracted with the Qiaprep Spin Miniprep Kit according to manufacturers instructions. Purified DNA was eluted in 50 µl of ddH_2O before being sent for sequencing. DNA concentration was measured and purity assessed using a NanoDrop 1000 Spectrophotometer (ThermoScientific).

For DNA constructs which were to be transiently transfected into mammalian cells, 50-100ml overnight cultures of LB supplemented with an appropriate antibiotic (100 μgml^{-1} Carbenicillin or 50 μgml^{-1} kanamycin) were inoculated from an agar plate with a sterile pipette tip and grown in 250ml erlenmeyer flasks at 37 °C, shaking at 180rpm. DNA was extracted with the PureYield Plasmid Midiprep Kit according to manufacturers instructions. Purified DNA was eluted in 500 µl of ddH_2O before being sent for sequencing. Generating DNA using this method not only produces a higher quantity of DNA, but also involves an endotoxin wash making it more suitable for mammalian applications. DNA concentration was measured and purity assessed using a NanoDrop 1000 Spectrophotometer (ThermoScientific).

2.2.13 Sequencing

Correct sequences of cloned constructs were confirmed by forward and reverse sequencing the construct using the automated Sanger sequencing service provided by Source Bioscience. Forward and Reverse Primers were provided at 3.2 pmol/µl, 5 µl per reaction as well as 5 µl per reaction of plasmid DNA at 100ng/µl. A

summary of sequencing primers for each vector is provided in Table 2.7 below.

Vector	Forward Primer	Reverse Primer
pBF pEXO	**SP6** (Source Bioscience) ATTTAGGTGACACTATAG	**R8** GCTACATTTTGGGGGACAAC
pFAW	**T7 Promoter F**(Source Bioscience) TAATACGACTCACTATAGGG	**R8** GCTACATTTTGGGGGACAAC
pCDNA3	**T7 Promoter F**(Source Bioscience) TAATACGACTCACTATAGGG	**pCDNA3.1Rev** GGCTGGCAACTAGAAGGCACAG
pET-22b(+) pET-28a(+)	**T7 Promoter F**(Source Bioscience) TAATACGACTCACTATAGGG	**T7 Terminator R** (Source Bioscience) GCTAGTTATTGCTCAGCGG
pHLSec pScFcAC	**pHLSecSeqFor** GCTCTAGAGCCTCTGCTAACC	**pHLSecRev** CACCAGCCACCACCTTCTGAT
pMESy4	**pMESy4seq** TTATGCTTCCGGCTCGTATG	**pMESy4SeqRev** CCACAGACAGCCCTCATAG

Table 2.7: **Sequencing Primers for Vectors Used in this Study**

2.2.14 Channel mRNA production

Plasmid channel DNA was purified by using a standard miniprep protocol as described in Culture and DNA extraction. DNA was linearised as described in the restriction digestion step in Subcloning by PCR, but the second restriction enzyme replaced with ddH_2O. Following linearisation using MluI (for channels in the pBF vector) or XbaI (for channels in the pEXO vector), channel mRNA was synthesised using AmpliCap-Max SP6 High Yield Message Maker Kit (CellScript) acccording to manufacturers instructions. mRNA concentration was measured using a NanoDrop 1000 Spectrophotometer (ThermoScientific) and purity assessed using agarose gel electrophoresis.

2.2.15 pScFcAC Vector creation

The ScFc insert was designed using the amino acid sequence of human IgG1 (Uniprot Kb: PO1857) for the CH2 and CH3 domains, and using the 59 amino acid linker described in (Newnham et al., 2015). The amino acid sequence codon optimised for human expression using the GenSmart^{TM} Codon Optimisation tool (Genscript) and HRV3C and TEV cleavage sites as well as a number of restriction sites to allow modular cloning into this new construct. The insert was synthesised by GenScript and provided in the pCDNA3.1(+) mammalian expression vector.

In order to allow modular cloning into this vector, the pLexm vector was cut sequentially with HindIII followed by PstI and the two sites removed by blunting with the Klenow fragment of DNA Polymerase I which carries out 3' end resection and fill in of 3' recessed (5' overhang) DNA. Briefly, 5 µg of double digested pLexm DNA was added to T4 DNA ligase buffer, supplemented with 33 µM of each dNTP and 5U of Klenow were added and incubated for 15 mins at 25 °C. The reaction was stopped by addition of Ethylenediaminetetraacetic acid (EDTA) to a

final concentration of 10mM and heating at 75 for 20 minutes. The DNA product from the reaction was then purified using the QiaQuick spin-column kit according to manufacturers instructions and eluted in 25 µl ddH_2O which was transformed into 100 µl of DH5-αas described in Heat Shock Transformation. Single colonies were inoculated into liquid culture and DNA purified by a standard miniprep as described in Culture and DNA extraction. Clones were then sequenced using a primer which binds to the Lac Promoter (LacP, 5'CACTTTATGCTTCCGGCTCG-TATGTTG') to confirm the successful deletion of both HindIII and PstI restriction sites. This new vector was named pLexm*.

The ScFc region was subcloned from pCDNA3.1(+) into this modified pLexm* vector using the EcoRI and XbaI restriction sites to make the final vector termed pScFcAc (for details see Subcloning by Restriction Digest). The DNA sequence for enhanced green fluorescent protein (EGFP) containing 5' BamHI and 3' Acc65I sites were amplified by PCR without stop codons from pEGFP-N1. The PCR product containing EGFP was then subcloned using the BamHI and Acc65I sites into the pScFcAc vector to create a parent vector termed -EGFP-pScFcAc as detailed in Subcloning by PCR). 5' AgeI and 3' HindIII restriction sites were added onto VHH antibody genes by PCR and subcloned into the -EGFP-pScFcAc vector for study as detailed in Subcloning by PCR.

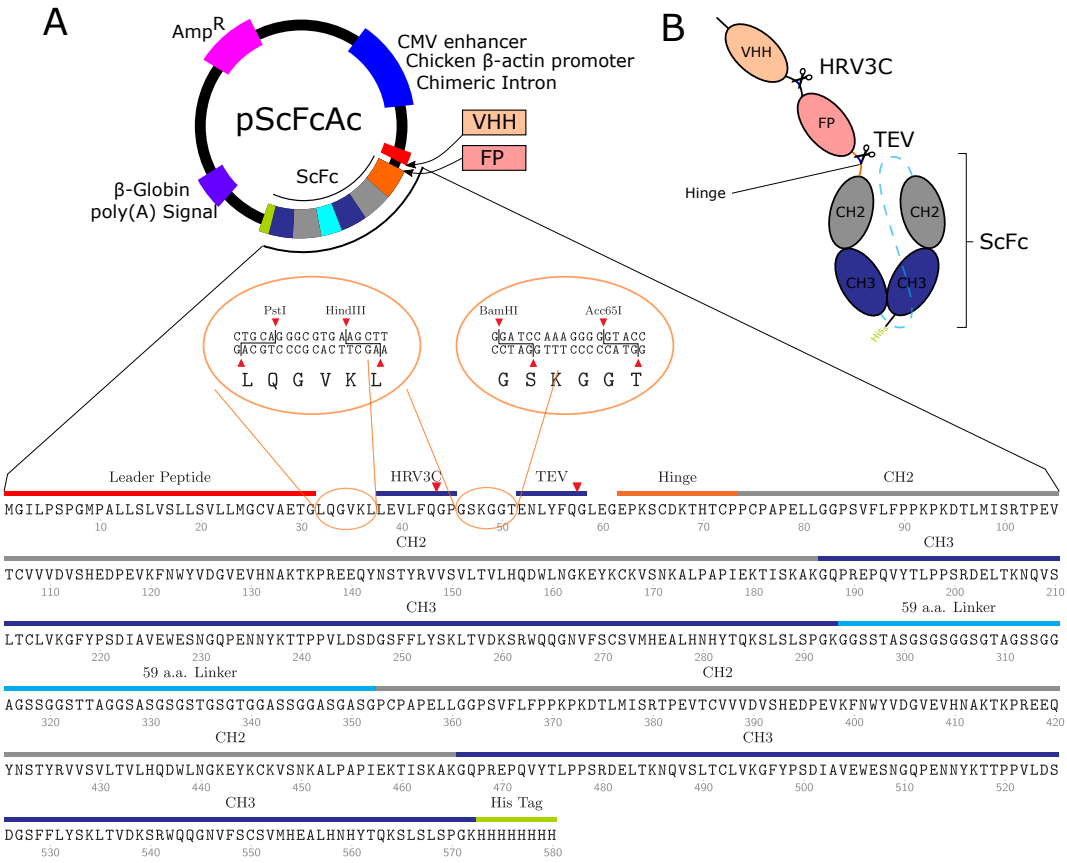


Figure 2.8: **Summary of pScFcAC Vector**

2.3 Mammalian Cell Culture

2.3.1 Materials:

Category	Reagent	Source	Product Code
Media	DMEM* F-12 Ham	Sigma	D6421
	DMEM* High Glucose	Gibco	41965039
	DMEM*	Sigma	D5030
	OPTI-MEM	Gibco	31985
	Dulbeccos PBS	Sigma	D8537
Supplement	GlutaMAX	Gibco	35050061
	Fetal Bovine Serum (FBS)	Gibco	16000044
	Tet System Approved FBS	Takaro	631106
	MEM NEAA^{+}	Gibco	11140050
	Geneticin^{TM} (G418 Sulfate)	Gibco	10131035
	Hygromycin B	Gibco	10687010
	Zeocin	Gibco	R25005
	Blasticidin-S	Gibco	A1113902
	DMSO	Sigma	D2650
	Poly-L-Lysine	Sigma	P8920
	Triton-X-100	Sigma	T9284l
Enzyme	Detachin	Gelantis	T100100
	Trypsin-EDTA Solution	Sigma	P8920
Reagent	FuGene HD Transfection Reagent	Promega	E2311
	Lipofectamine^{TM} LTX	ThermoFisher	15338100
	Doxycycline	Clontech	631311
Disposables	T75	Sci. Lab. Supplies	430725U
	T25	Sci.Lab. Supplies	1583099-1
	6 Well Plates	Sarstedt	83.3920.005
	250ml Erlenmeyer Flasks	Corning	38012
	35x 10mm Petri Dishes	Sci. Lab. Supplies	353001
	35mm Glass Coverslips	Cyto-One	7682-3340
	2ml Aspirators	Falcon	357558

Table 2.8: **List of materials for Mammalian Cell Culture and Heterologous Expression in Mammalian Cells**
*DMEM = Dulbecco's Modified Eagle's Medium, $^{+}$NEAA = Non Essential Amino Acids, Sci. Lab. Supplies = Scientific Laboratory Supplies.

2.3.2 Cell Maintenance

Numerous cell types were used during this study and required constant maintenance. Table 2.9 below summarises the cell types, base media and supplementation required for cell survival. In the following sections, for a given cell type, 'appropriate supplemented media' refers to the combination of the second and third columns.

Cell Line	Media	Supplementation	Use
HEK293-TetOn 3G (Clontech: 631182)	DMEM High Glucose	10% FBS (Takara) 1X GlutaMAX 1x NEAA 300 µg/ml G418	EPhys. Studies of Nav Channel Mutants
Nav1.7 HEK293-TetOn 3G (Clontech: 631182)	DMEM High Glucose	10% FBS (Takara) 1X GlutaMAX 1x NEAA 300 µg/ml G418 50 µg/ml Hygromycin	Ephys. Studies of WT Nav1.7
Nav1.2 FreeStyle™ 293-F (ThermoFisher: R79007)	Freestyle™	600 µg/ml G418 5 µg/ml zeomycin 5 µg/ml blasticidin-S	Ephys. Studies of WT Nav1.2
HEK293T	DMEM-F12	10% FBS (Sigma) 1X GlutaMAX	Fluorescent VHH Antibody Expression
HEK293 (Sigma: 85120602-1VL)	DMEM-F12	10% FBS (Sigma) 1X GlutaMAX	VHH Antibody Ephys and Localisation Studies

Table 2.9: **List of Mammalian Cell Lines carried along with the media and supplementation.**

2.3.3 Thawing adherent Cells

Cells were removed from liquid nitrogen and quickly thawed using a 37 °C water bath. 1ml cell suspension was pipetted into 5ml of appropriate supplemented media in a T25 flask, and left to recover in a humidified 37°C, 5% CO_2 incubator. When the cells reached 70-80% confluency, the media was aspirated, the cells were washed with 2ml divalent-free PBS and subsequently digested with 0.3ml Trypsin-EDTA for 2 mins at 37°C. Trypsin was inhibited by addition of 2ml of appropriate supplemented media, the cells were triturated by gentle pipetting and then the whole solution was equally split between 2 T75 flasks, each containing 12ml of appropriate supplemented media.

2.3.4 Freezing adherent Cells

When the cells reached 70-80% confluency, media was aspirated, the cells were washed with 5ml divalent-free PBS and subsequently digested with 1ml Trypsin-EDTA for 2 mins at 37 °C. Tryspin was then inhibited with 5ml of appropriate supplemented media and the cells were triturated by gentle pipetting and transferred into a 15ml conical tube. Cells were pelleted by spinning at 200rpm for 5 minutes. The Supernatant was then carefully removed and the cells were resuspended in freezing solution (FBS +10% DMSO). The cell suspension- freezing solution mix was then aliquoted into 1ml fractions inside cryogenic tubes and cooled at 1 °C /min to ensure cryopreservation of cells using the Nalgene Mr. Frosty freezing chamber (Sigma: C1562-1EA) containing fresh acetone. After 1-2 days, the frozen cryogenic vials were moved to liquid Nitrogen for long term storage.

2.3.5 Splitting adherent Cells

When the cells reached 70-80% confluency, media was aspirated, the cells were washed with 5ml divalent-free PBS and subsequently digested with 1ml Trypsin-EDTA for 2 mins at 37 °C. Tryspin was then inhibited with 5ml of appropriate supplemented media and the cells were triturated by gentle pipetting. 1ml and 0.5ml of this cell solution were pipetted into a T75 flask containing 12ml appropriate supplemented media to create a 1:6 and 1:12 split respectively. These cells were recovered in a humidified 37 °C 5% CO_2 incubator. Cells from the 1:6 splits were preferentially maintained and the 1:12 split used only if a backup was required, otherwise were discarded.

2.3.6 Poly-L-Lysine Coated Coverslips

Poly-L-Lysine was diluted 1:10 with sterile water and used to incubate autoclaved petri dishes containing 8mm cover glass for 20-30 mins at room temperature and pressure (RTP). Each dish was then washed with 5ml sterile water, and then left to dry for 3-4 hours or overnight if possible.

2.3.7 Seeding adherent Cells

HEK293-TetOn and HEK293 cells used for electrophysiology studies of Nav channels and K2P channels respectively were seeded during splitting into an untreated 6 well tissue culture plate, each well containing 2ml appropriate supplemented media.

HEK293T cells used for expressing fluorescent VHH Antibodies were seeded during splitting into an untreated 6 well tissue culture, each well containing 1X DMEM 10% FBS, media which does not contain phenol red to limit background

fluorescence.

HEK293T cells used to express K2P-mCherry fusions for VHH Antibody localisation studies were seeded during splitting (250 µl per well) into 6-well plates containing poly-L-Lysine coated coverslips, and 2ml 1X DMEM 10% FBS, media which does not contain phenol red to limit background fluorescence.

2.3.8 Splitting non-adherent Cells

Freestyle^{TM} 293-F cells were maintained in 125ml polycarbonate sterile Erlenmeyer flasks containing 30ml cell suspension in appropriate supplemented media in a humidified 37 °C, 5% CO2 incubator shaking at 120rpm. When at high density, the cells were split by aspiration of 25ml of cell suspension followed by addition of 25ml fresh appropriate supplemented media into the same flask.

2.4 Heterologous Expression in Mammalian Cells

2.4.1 Induction of Nav1.2 in Freestyle ^{TM} 293-F

1ml of Freestyle^{TM} 293-F cells were diluted by a factor of 10 into appropriate supplemented media in a 125ml polycarbonate sterile Erlenmeyer flask in a humidified 37 °C, 5% CO_2 incubator. Expression of Nav1.2 and β1 was induced by addition of 50ng/ml Doxycline. The induced cells were left to shake at 120rpm for 16-20 hours (overnight) prior to preparation for experiments.

2.4.2 Transfection of Nav1.7 mutants and K2P Channels

For electrophysiology studies of Mutant Nav channels, 2 µg of Nav1.7 mutant DNA in the pBi vector (Clontech: 6152-1) containing the β2 subunit (Unipro-

tKb: O60939-1) was co-transfected with 200ng/ µl CAGS-GFP (addgene: Plasmid 16664) in order to visualise succesfully transfected cells. The DNA was pipetted into 300 µl OPTI-MEM in an eppendorff tube and mixed with 2.5 µl of PLUS reagent. 10 µl of LTX reagent was then pipetted into the centre of the eppendorff tube and mixed by vortex. This transfection solution was then incubated at RTP for 30 mins before being added dropwise to adherent cells at 50% confluency in a 6 well plate. The transfected cells were left in the humidified 37 °C, 5% CO_2 incubator for 16-20 hours (overnight) prior to preparation for experiments.

For electrophysiology studies of WT and mutants K2P Channels, 250ng of K2P DNA in the pFAW vector(in house) was co-transfected with 100 ng/µl pEGFP-N1 (Clontech: 6085-1) in order to visualise succesfully transfected cells. The DNA was pipetted into 300 µl OPTI-MEM in an eppendorff tube and mixed with 2.25 µl of FuGene HD Transfection Reagent. This transfection solution was then incubated at RTP for 15 mins before being added dropwise to adherent cells at 50% confluency in a 6 well plate. The transfected cells were left in the humidified 37 °C, 5% CO_2 incubator for 16-20 hours (overnight) prior to preparation for experiments.

For immunohistocytochemistry studies, 1 µg of K2P-mCherry DNA in the pFAW vector (in house) was transfected. The DNA was pipetted into 250 µl OPTI-MEM in an eppendorff tube and mixed with 3 µl of FuGene HD Transfection Reagent. This transfection solution was then incubated at RTP for 15 mins before being added dropwise to adherent cells in a 6 well plate. The transfected cells were left in the humidified 37 °C, 5% CO_2 incubator for 30 hours prior to preparation for experiments.

2.4.3 Transfection of VHH Antibody-mVenus for Immunohistocytochemisry Studies

To produce secreted VHH antibody-mvenus protein, 2 µg of VHH Antibody-mVenus fusions in the pHLSec Vector was transfected. The DNA was pipetted into 300 µl OPTI-MEM in an eppendorff tube and mixed with 6 µl of FuGene HD Transfection Reagent. This transfection solution was then incubated at RTP for 15 mins before being added dropwise to adherent cells in a 6 well plate. The transfected cells were left in the humidified 37 °C, 5% CO_2 incubator for 72-96 hours prior to harvesting.

2.4.4 Mammalian cell preparation for Dynaflow measurements (Nav and K2P electrophysiology)

Prior to experiments, media was aspirated and the cells were carefully washed with 1ml divalent-free PBS and subsequently digested with 1ml Detachin at 37 °C. Detachin is more gentle than trypsin and thus is better for downstream electrophysiology applications. Detachin was then inhibited with 1ml of appropriate supplemented media and the cells were triturated by gentle pipetting. The whole cell solution was put into an eppendorff tube which was then shaken during experiments on a table top rotator, and cells were taken as needed.

2.4.5 Mammalian cell preparation for Immunohistocytochemistry experiments

Prior to experiments, the media was aspirated and the cells were carefully washed with 1ml divalent-free PBS. The cells were fixed by incubation in 500 µl of 4% formaldehyde solution for 10 mins and washed three times with 500 µl of divalent-free PBS. Cells were permeabilised (if appropriate) via addition of 500 µl of Triton-

X100 (0.2% in PBS) for 5 mins before again washing three times with PBS.

2.5 Heterologous Expression in *Xenopus Laevis* Oocytes

2.5.1 Materials

Category	Reagent	Source	Product Code
Enzyme	Collagenase A	Roche Diagnostics	11088793001
Plasticware	6 well plate	Cellstar	M9062-100EA
	24 well plate	Cellstar	662160
	35x10mm Petri dishes	Falcon	351008
Injection Glass	10 µL Microdispenser	Drummond Scientific	3-000-210-G

Table 2.10: **List of materials for Heterologous Expression in *Xenopus laevis* oocytes**

2.5.2 Solutions and Buffers

Solution/ Buffer	Composition
Ca^{2+} free Barth's solution (Low $[K^+]$)	88mM NaCl 1mM KCl 2.4mM $NaHCO_3$ 10mM HEPES 1.68mM $MgSO_4$ pH 7.2
Barth's solution (Low $[K^+]$)	88mM NaCl 1mM KCl 2.4mM $NaHCO_3$ 10mM HEPES 1.68mM $MgSO_4$ 0.41mM $CaCl_2$ 0.47mM $Ca(NO_3)_2$ pH 7.2
Barth's solution (High $[K^+]$)	10mM NaCl 80mM KCl 10mM HEPES 2.4mM $NaHCO_3$ 1.68mM $MgSO_4$ 0.41mM $CaCl_2$ 0.47mM $Ca(NO_3)_2$ pH 7.2

Table 2.11: **Oocyte preparation Solutions and Buffers**

2.5.3 Oocyte Preparation

Oocytes were surgically removed from adult female *Xenopus laevis*, washed with Ca^{2+}-free Barth's solution and digested by gentle agitation with 2 $mgml^{-1}$ collagenase A for 1 hour at 21 °C, 90 rpm. Digestion was stopped by washing three times with Barth's solution (which contains calcium and inhibits collagenase.) Following washing, oocytes were manually defolliculated using calipers and stored in Low potassium Barth's solution at 16.5 °C.

2.5.4 mRNA injection

50nl of 5ngμl^{-1} K2P channel mRNA was injected into the animal pole of each oocyte 48 to 60 hours before currents were measured. After injection, oocytes were incubated at 16.5 °C in high [K^+] Barth's solution.

2.6 Protein Biochemistry

2.6.1 Materials

Category	Reagent	Source	Product Code
Media	Sf-900^{TM} III SFM	Gibco	12658019
	Terrific Broth (TB)	Merck	1.01629.0500
	Luria Broth (LB)	Sigma	L3522-1KG
	2xYT	Sigma	Y2627
Antibiotic	Carbenicillin Disodium	Apollo Sci. Ltd.	BIC0109
	Kanamycin monosulphate	Apollo Sci. Ltd.	D0610079
	Chloramphenicol	Apollo Sci. Ltd.	BIC0113
Purification/ Induction	Ni-NTA	Thermo Fisher	88222
	TALON Metal Affinity Resin	TaKara	635503
	IPTG	Apollo Sci. Ltd.	BIMB1008
	L-(+)-Arabinose	Sigma	A3256
	DNAse I	Sigma	11284932001
	PD10 columns	GE Healthcare	17-0851-01
	3kDa MWCO Concentrators	Millipore	UFC900324
	3kDa Concentrators (0.5ml)	Millipore	UFC5003BK
	10kDa MWCO Concentrators	Millipore	UFC901096
	Micro Bio-Spin^{TM} 6	BioRad	7326221
	Vivaspin 500 3kDa MWCO	Viva Products	VS0192
Gels	NuPAGE LDS Sample buffer 4x	Invitrogen	NP0007
	NuPAGE sample reducing agent	Invitrogen	NP0004
	SeeBlue Pre-Stained Standard	Novex	LC5625
	Instant Blue (Coomassie)	Expedeon	ISB1L
	NuPAGE SDS Running Buffer	Invitrogen	NP0002
	NuPAGE 4-12% Bis-Tris Gel	Invitrogen	NP0335Box
	Native PAGE^{TM} Running Buffer	Invitrogen	BN2001
	Native PAGE^{TM} Cathode Buffer	Invitrogen	BN2002
	Native PAGE 4-16% Bis Tris Gel	Invitrogen	BN1002Box
	iBlot Transfer Stacks	Invitrogen	IB301002
Antibodies	ab1187 Rb pAb to 6His (HRP)	Abcam	GR300288-1
Assay	1 step TMB Blotting	Thermo Fischer	34018
Dyes	Amersham Cy^{TM}3b NHS ester	Sigma	GEPA13101
	GGG-[C(AF488)]-amide	Discovery Peptides	crb1110801h
Cells	Wk6-su	SGC (Oxford)	
	BL21(DE3)-R3-pRARE2	SGC (Oxford)	
	BL21(DE3)pLysS	Promega	L1195
	BL21(DE3)	Thermo Fischer	EC0114

Table 2.12: **List of materials for Protein Biochemistry**
Apollo Sci. Ltd. = Apollo Scientific Limited

2.6.2 Solutions and Buffers

Solutions and buffers used for Protein Biochemistry are listed in Table 2.12 in order of appearance in the methods section. In all cases, the desired pH was obtained via addition of the acid/base of the most abundant salt and was filtered after preparation using a bottle top vacuum filter.

Protein	Media	Resuspension	Wash 1	Wash 2	Elution
Scorpion Toxins	SFM Media		50 mM Tris 30mM Imi* pH8.0		50mM Tris 300mM Imi* pH8.0
VHH	TB	200mM Tris 0.5mM EDTA 0.5M Sucrose	50mM Na P 1M NaCl pH7.0	50mM Na P 1M NaCl pH6.0	50mM Na P 150mM NaCl 300mM Imi* pH7.0
HRV 3C	2xYT	50mM HEPES 0.5M NaCl 5% glycerol 5mM β-ME pH 7.5	+50mM Imi*	+100mM Imi*	+500mM Imi*
TEV	2xYT	20mM Tris 125mM NaCl	+20mM Imi*	+100mM Imi*	+500mM Imi*
eSrtA Pent	LB	50mM Tris 300mM NaCl 1mM MgCl2 pH8.0	25mM Tris 150mM NaCl 15mM Imi* pH7.5	25mM Tris 150mM NaCl 30mM Imi* pH7.5	25mM Tris 150mM NaCl 250mM Imi* pH7.5

Table 2.13: **List of Solutions and Buffers used for Protein Biochemistry**
* Imi = imidazole

2.6.3 Making competent cells

Frozen glycerol stocks of non-competent bacterial cells were streaked onto unsupplemented agar plates, a single colony was picked and grown in unsupplemented LB overnight 37 °C, shaking at 180rpm, using standard sterile technique. 1ml of this overnight culture was used to inoculate a 100ml master culture with 99ml unsupplemented LB. This was grown, shaking at 37 °C, 180rpm until the OD_{600} was measured to be between 0.2 and 0.4. The cells were then placed on ice for 15 mins and kept on ice during the subsequent steps. The cells were pelleted by centrifugation at 4000g, 4 °C, 5mins in a JS5.3 rotor (Beckman), the supernatant was discarded and the pellet was resuspended in 100ml sterile 100mM $CaCl_2$. The cell suspension was centrifuged as above, the supernatant discarded and the pellet resupsended in 50ml sterile 100mM $CaCl_2$. This process was repeated a further two times, resusepending in 25ml and then 10ml sterile $CaCl_2$ in each round. The 10ml was then aliquoted into twenty 500µl aliquots and placed into the -80 °C freezer for long term storage.

2.6.4 Purification of Scorpion Toxins

2L of culture media containing MBP-Scorpion toxin-His tag fusions was mixed with 2ml of Nickel-nitrilotriacetic acid (Ni-NTA) resin for 1 hour rotating at 4 °C. The scorpion toxins were washed with 10 column volumes (CV, 20ml) of wash buffer and eluted with 5CV (10ml) elution buffer. The MBP tag was cleaved by addition of TEV protease 1:100 (w/w) from stock overnight in the presence of 1 mM TCEP. The following day, the cleaved toxin was concentrated using a 3kDa molecular weight cut off (MWCO) concentrator. 500 µl of protein was injected into a S200 column (GE Healthcare) and purified protein was eluted into PBS + 150mM NaCl. The fractions were run on a Sodium Dodecyl Sulphate Polyacrylamide Gel Electrophoresis (SDS-PAGE) gel and pure fractions were pooled and once again

concentrated using a 3KDa MWCO concentrator and concentrated protein was flash frozen in liquid N_2 for long term storage.

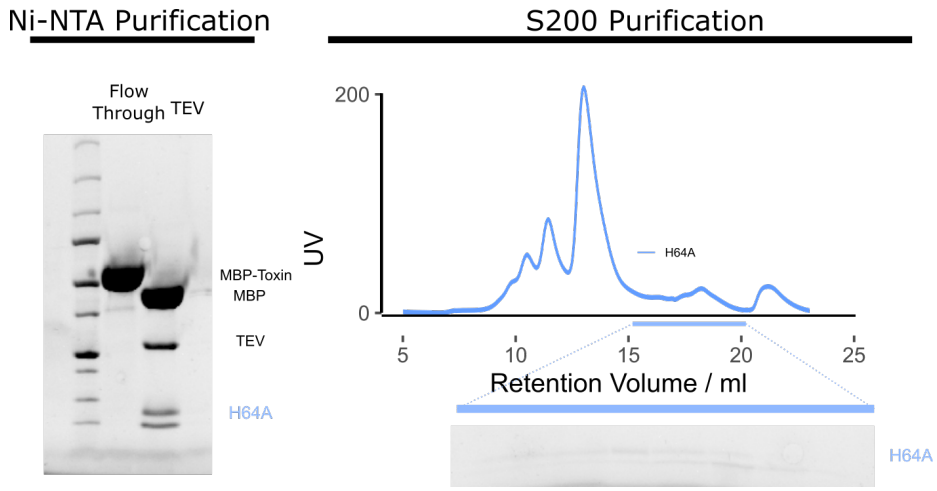


Figure 2.9: **Purification of α-scorpion Toxins**

2.6.5 Periplasmic expression of VHH antibodies

Periplasmic expression and purification of VHH antibodies was modified from the protocol published in (Pardon et al., 2014). Purified miniprepped DNA of VHH antibody in the pMESy4 or the pET-22b vector were freshly transformed into competent wk6su (*E. coli*, SGC) and grown overnight on agar plates supplemented with 100 $\mu g \mu l^{-1}$ carbenicillin at 37 °C. LB supplemented with 100 $\mu g \mu l^{-1}$ carbenicillin was inoculated with single colonies from the plates and grown overnight at 37 °C shaking at 200rpm. 10ml overnight cultures were then used to inoculate 1 litre Master cultures (1L TB + 4ml Glycerol + 0.1 % w:v glucose + 100 $\mu g \mu l^{-1}$ carbenicillin). These cultures were then grown at 37 °C shaking at 180rpm. VHH antibody production was induced by addition of 0.5mM IPTG when OD_{600} reached 0.8 and were then grown at 28 °C, shaking at 180rpm overnight.

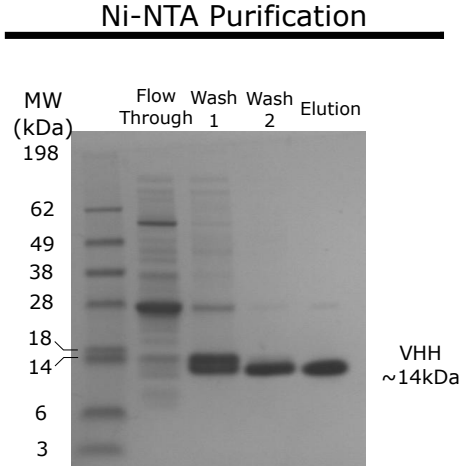


Figure 2.10: **Periplasmic Purification of VHH Antibodies**

Cells were harvested by spinning at 5000g for 20 mins. at 4 °C in a JLA8.1 rotor (Beckman) and the pellets resuspended in ice-cold resuspension buffer containing Tris, EDTA and Sucrose (hereby termed TES). To disrupt the periplasm, cells were kept on ice and shaken for 1 hour in TES and then for a further hour after addition of 5mM $MgCl_2$ to a final volume of 35ml. The periplasm was then extracted

by spinning the cells at 15000g, for 15 mins at 4 °C in a JA25.5 rotor (Beckman). His-tagged VHH antibodies were then purified by addition of Ni-NTA resin to the supernatant and rotating at 4 °C for 2.5 hours. Following washing with Wash Buffer 1 and Wash Buffer 2, VHH Antibodies were eluted in Elution buffer, and the imidazole rich solution exchanged into either Gel Filtration Buffer (200mM KCl 20mM HEPES pH7.5, for screening experiments), ND96 (in mM: 96 NaCl, 2 KCl, 1.8 $CaCl_2$, 1 $MgCl_2$, 20 HEPES, 2.5 Na Pyruvate, for other oocyte experiments), or EC buffer (in mM: 140 NaCl, 10 TEA-Cl, 5 KCl, 3 $MgCl_2$, 1 $CaCl_2$,10 HEPES, pH7.4, for Patch clamp electrophysiology) using PD10 columns. Purity was assesed by SDS-PAGE as shown in Figure 2.10

2.6.6 Small Scale Expression and Purification of VHH antibodies in different *E. coli* strains

Purified miniprepped DNA of VHH antibody in the pMESy4 vector were freshly transformed into competent wk6su (SGC), BL21(DE3)-R3-pRARE2 (addgene:26242) and BL21(DE3)-pLysS (promega: L1195) and grown overnight on LB-agar plates supplemented with 100 $\mu g \mu l^{-1}$ carbenicillin at 37 °C. LB supplemented with 100 $\mu g \mu l^{-1}$ carbenicillin was inoculated with single colonies from the plates and grown overnight at 37 °C shaking at 200rpm. 1ml of overnight cultures were then used to inoculate 50ml Master cultures (50ml TB + 100 $\mu g \mu l^{-1}$ carbenicillin). These cultures were then grown at 37 °C shaking at 180rpm. VHH antibody production was induced by addition of 0.5mM IPTG when OD_{600} reached 0.8 and were then grown at 28 °C, shaking at 180rpm overnight.

Cells were harvested by spinning at 5000g for 20 mins at 4 °C in a JLA8.1 rotor (Beckman) and the pellets resuspended in 5ml ice-cold TES buffer. To disrupt the periplasm, cells were kept on ice and shaken for 1 hour this buffer (Table 2.13)

and then for a further hour after addition of TES/4 to a final volume of 20ml. The periplasm was then extracted by spinning the cells at 15000g, for 15 mins at 4 °C in a JA25.5 rotor (Beckman). His-tagged VHH antibodies were then purified by addition of TALON resin to the supernatant and rotating at 4 °C for 2.5 hours. Following washing with Wash Buffer 1 and Wash Buffer 2, VHH Antibodies were eluted in Elution buffer, and the imidazole rich solution exchanged into Gel Filtration Buffer (200mM KCl, 20mM HEPES pH7.5) using PD10 columns. Relative concentration was determined using a photospectrometer (1Abs = 1mg/ml) and purity asessed by SDS-PAGE.

2.6.7 Cytosolic expression of VHH antibodies

Cytosolic expression and purification of VHH antibodies was modified from the protocol published in Veggiani et al. (2016). VHH antibodies in the pET-28a vector were transformed into competent BL21(DE3) RIPL + Erv1p + DsbC cells (kind gift of M. Howarth) using the standard protocol detailed in Heat Shock Transformation and plated onto agar plates supplemented with 50 $\mu g \mu l^{-1}$ kanamycin and 35 $\mu g \mu l^{-1}$ chloramphenicol and grown overnight at 37°C. A single colony of each was used to a inoculate a 10ml starter cultures of LB supplemented with 50 $\mu g\ l^{-1}$ kanamycin and 35 $\mu g \mu l^{-1}$ chloramphenicol and grown overnight at 37 °C, shaking at 180rpm. The 10ml starter cultures were used to inoculate 1L master cultures each consisting of 1L LB media supplemented with 50 $\mu g\ l^{-1}$ kanamycin and 35 $\mu g \mu l^{-1}$ chloramphenicol, and grown at 37 °C shaking at 180rpm. Erv1p and DsbC expression was induced when OD_{600} reached 0.6 with 0.1 % (w:v) arabinose one hour prior to induction of VHH antibody expression with 0.5 mM IPTG and the temperature was reduced to 28 °C to allow correct folding of the VHH antibodies

The cells were harvested by centrifugation at 5000g, 4 °C in a JLA8.1 rotor

(Beckman) and the pelleted cells resuspended in 35ml tris-buffered saline TBS (150mM NaCl, 20mM Tris, pH7.5). The resuspended cells were homogenised using a hand held homogeniser and a few crystals of DNAse I were added to digest DNA. The sample was then processed through a french press (Stansted), and the cell debris removed by centrifugation at 15000g, for 15 mins at 4 °C in a JA25.5 rotor (Beckman). The supernatants were transferred to ultracentrifuge tubes and spun at 100,000g in a F50L-8X39 rotor (Piramoon) for 1 hour to pellet cells membranes. The supernatant was collected and 4ml 50 % of pre-equilibrated Ni-NTA resin was added and incubated gently shaking for 1 hour at RT. The resin was transferred to a column and allowed to flow through. The column was washed with 10CV Wash buffer 1 and 10CV Wash buffer 2 and eluted in 5CV Elution buffer.

IMAC

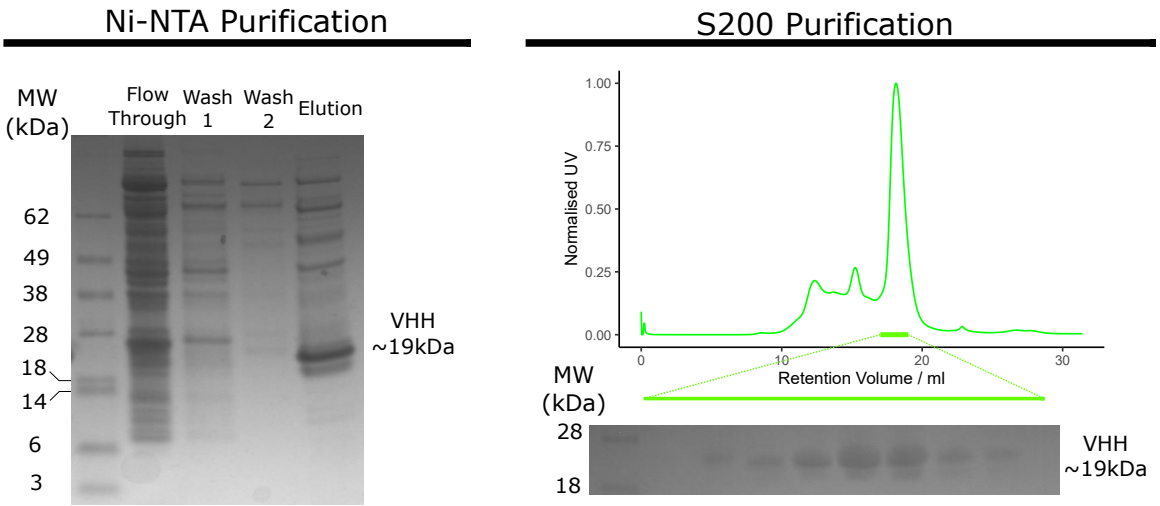


Figure 2.11: **Cytosolic Purification of VHH Antibodies**

The elution was concentrated using 10kDa MWCO concentrators, and loaded onto an S200 column attached to an ÄKTA purifier and eluted in 200mM KCl, 20mM HEPES pH7.5. Eluted fractions from the S200 were checked for purity by

SDS-PAGE, pooled, concentrated and flash frozen in liquid N_2. A summary of both the Ni-NTA purification and the S200 elution profile and corresponding protein bands are shown in Figure 2.11.

2.6.8 HRV3C and TEV Purification

TEV in the pMHTDelta vector (kind gift of C. Kelly, Biochemistry) and HRV3C in the pNIC-6H vector (kind gift of E. Carpenter, SGC) were transformed into competent BL21(DE3) cells using the standard protocol detailed in Heat Shock Transformation and plated onto agar plates supplemented with 50 µg $µl^{-1}$ kanamycin and grown overnight at 37°C. A single colony of each was used to a inoculate 10ml starter cultures of LB supplemented with $µl^{-1}$ kanamycin and grown overnight at 37 °C, shaking at 180rpm. The 10ml starter cultures were used to inoculate 1L master cultures each consisting of 1L 2xYT media supplemented with 50 µg l^{-1} kanamycin, and grown at 37 °C shaking at 180rpm. TEV and HRV3C expression was induced when OD_{600} reached 0.8-1.2 and the temperature was reduced to 28 °C to allow correct folding of HRV3C and TEV.

The cells were harvested by centrifugation at 5000g, 4 °C in a JLA8.1 rotor (Beckman) and the pelleted cells resuspended in 30ml Resuspension buffer. The resuspended cells were homogenised using a hand held homogeniser and a few crystals of DNAse I were added to digest DNA. The sample was then processed through a french press (Stansted), and the cell debris removed by centrifugation at 15000g, for 15 mins at 4 °C in a JA25.5 rotor (Beckman). The supernatants were transferred to ultracentrifuge tubes and spun at 100,000g in an F50L-8X39 rotor (Piramoon) for 1 hour to pellet cells membranes. 4ml of 50% pre-equilibrated Ni-NTA resin was added to the supernatant which was subsequently diluted to a final volume of 100ml with Resuspension buffer containing 5mM imidazole. This mixture was incubated, gently shaking for 1 hour at RT. After 1 hour, the resin was transferred to a column and allowed to flow through and subsequently washed with 20CV Wash buffer 1 and 2CV Wash buffer 2 and eluted in Elution buffer and 8 x 0.5ml fractions were collected.

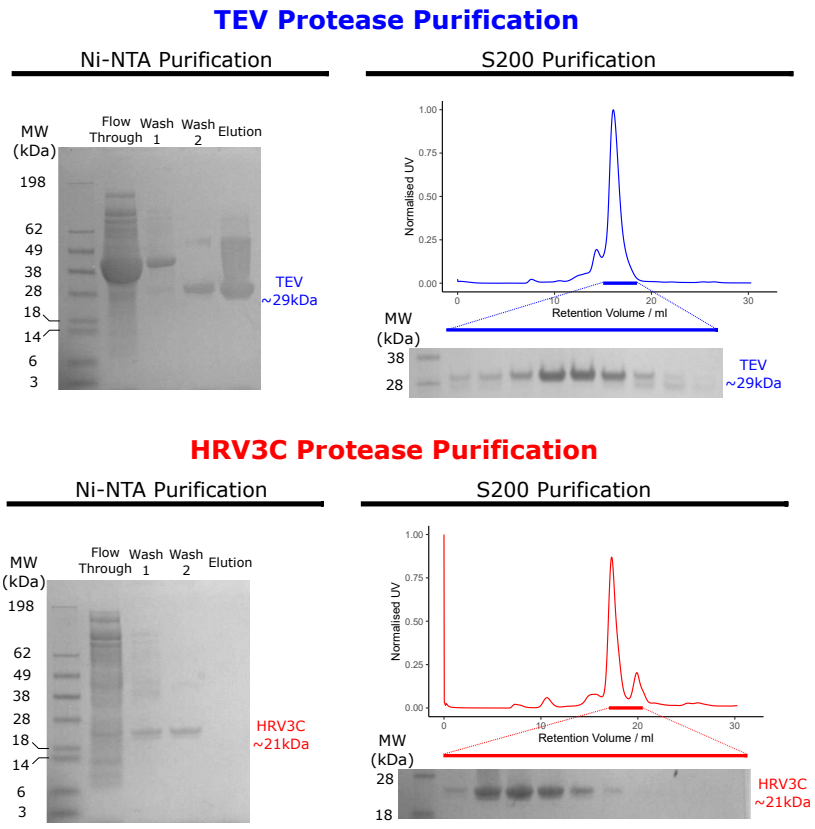


Figure 2.12: **Purification of HRV3C and TEV**

The protein concentration of the fractions was measured by A_{280} and the highest concentration fractions were pooled and buffer exchanged into Tris-TEV (20mM Tris, pH2.5, 125mM NaCl) or 3C Gel filtration buffer (20 mM HEPES pH 7.5, 150 mM KCl, 5% v:v glycerol, 1mM EDTA, 5mM β-ME) respectively using pre-equilibrated PD10 columns. The samples were then concentrated using 10kDa MWCO concentrators, and loaded onto an S200 column attached to an ÄKTA purifier. Eluted fractions from the S200 were checked for purity by SDS-PAGE, pooled, concentrated and flash frozen in liquid N_2. A summary of both the Ni-NTA purification and the S200 elution profile and corresponding protein bands are shown in Figure 2.12.

2.6.9 Sortase Purification

Cytosolic expression and purification of the evolved sortase A (eSrtA) pentamutant was modified from the protocol published in (Chen et al., 2011). esrtA Pentamutant in the pET-28a vector (kind gift of A. Kapanidis, Physics, addgene: 75144) were transformed into competent BL21(DE3) cells using the standard protocol detailed in Heat Shock Transformation and plated onto agar plates supplemented with 50ngµl^{-1} kanamycin and grown overnight at 37°C. A single colony of each was used to a inoculate a 10ml starter cultures of LB supplemented with 50 µg l^{-1} kanamycin and grown overnight at 37 °C, shaking at 180rpm. The 10ml starter cultures were used to inoculate 1L master cultures each consisting of 1L LB media supplemented with 50 µg l^{-1} kanamycin, and grown at 37 °C shaking at 180rpm. Sortase expression was induced when OD_{600} reached 0.5-0.8 and the temperature was reduced to 28 °C to allow correct folding of the eSrtA.

The cells were harvested by centrifugation at 5000g, 4 °C in a JLA8.1 rotor (Beckman) and the pelleted cells resuspended in 30ml Resuspension buffer. The resuspended cells were homogenised using a hand held homogeniser and a few crystals of DNAse I were added to digest DNA. The sample was then processed through a french press (Stansted), and the cell debris removed by centrifugation at 15000g, for 15 mins at 4 °C in a JA25.5 rotor (Beckman). The supernatants were transferred to ultracentrifuge tubes and spun at 100,000g in a F50L-8X39 rotor (Piramoon) for 1 hour to pellet cells membranes. The supernatant was collected and 4ml 50 % of pre-equilibrated Ni-NTA slurry was added and incubated gently shaking for 1 hour at RT. The resin was transferred to a column and allowed to flow through. The column was washed with 10CV Wash buffer 1 and 15CV Wash buffer 2 and eluted in 5CV Elution buffer.

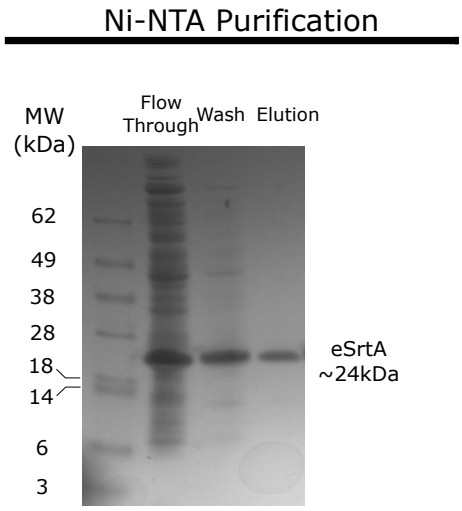


Figure 2.13: **Purification of eSrtA**

The protein concentration of the fractions was measured by A_{280} and the highest concentration fractions were pooled and buffer exchanged into TBS (25mM Tris, pH7.5, 150mM NaCl) using pre-equilibrated PD10 columns. The sample was then concentrated using a 10kDa MWCO concentrator and flash frozen in liquid N_2. A summary of the Ni-NTA purification is shown in Figure 2.13.

2.6.10 C-terminal labelling of VHH Antibodies

The C-terminal labelling reaction was modified from a N-terminal labelling reaction published in (Sélo et al., 1996). 0.5ml Amicon Ultra Columns with a 3kDa MWCO filter were passivated by incubation with 5% Tween-20 for 1 hour. The Tween-20 was then removed by pipetting and the columns washed three times with H_2O. 100µl of 1mg/ml purified protein to be labelled was then diluted 1 in 5 in 0.1M $NaPO_4$, pH6.5 to achieve a final volume of 0.5ml at 0.2mg/ml. The sample was then applied to a micro Bio-Spin^{TM} 6 column, and spun at 15000 rpm for 15 mins at 20 °C. The protein concentration was the calculated using a nanodrop spectrophotometer and 100 µl of a 5 time molar excess of Amersham Cy^{TM}3b mono NHS ester (dissolved in dimethyl sulfoxide, DMSO) was added to

each labelling reaction. Labelling reactions were then shaken at 4°C overnight at 600rpm in a thermomixer comfort (Eppendorff). Free dye was removed using Sephadex G-25 in PD10 desalting columns, eluting in a desired final buffer for downstream applications.

2.6.11 Sortagging of VHH antibodies

The Sortagging reaction was based on the optimised reaction published in (Massa et al., 2016). A VHH antibody containing a C-terminal sorttag was buffer exchanged into 150mM NaCl, 50mM Tris-HCl (pH7.9) using a PD10 colmumn. GGG-linked C-terminal AlexaFluor-488-amide (hereby named Alexa488) was dissolved in 150mM NaCl, 50mM Tris-HCl (pH7.9) to a final concentration of 10mM. A 100 µl sorttagging reaction was set up overnight at 37 °C as a 1:3:30 (50 µM VHH: 150 µM eSrtA: 1.5mM Alexa488) reaction in Reaction Buffer (150mM NaCl, 10mM $CaCl_2$, Tris-HCl, pH7.9).

The overnight reaction was applied to Ni-NTA (pre-equilibrated with reaction buffer) and the flow through collected which should contain both free dye as well as VHH antibody conjugated Alexa488. The flow through was incubated with 15mM EDTA for 30 mins at 37 to stop the Ca^{2+}-dependent sorttagging reaction. In order to separate the free and VHH-conjugated dye, the whole reaction was applied to a Superdex 75 (S75) column attached to an ÄKTA purification system at a flow rate of 0.4 ml/min. An SDS-PAGE gel was used to identify the substrates, products, intermediates in various stages of the reaction and purification.

2.6.12 VHH Antibody-mVenus harvesting from Mammalian cells

After 72-96 hours, the media containing secreted VHH antibody-mVenus fusion protein was carefully transferred to a 15ml conical tube and spun at 200rpm for

5 minutes to pellet any remaining cells. The supernatant was then carefully removed and stored at 4 °C.

2.6.13 Characterisation of mVenus-tagged VHH antibodies

The concentration of mVenus tagged antibodies was assesed either using a UV-Vis spectrometer or a plate-reader. For the UV-Vis Spectrometer, 1ml of harvested media was placed into a cuvette and an absoprtion spectrum was taken from 800-350nm using a Varian 50 bio UV-Vis Spectrophotometer (Agilent). The absorbance peak at 515nm (A_{515}) for the untransfected control was subtracted from the A_{515} from the sample, and the concentration calculated using the Beer-Lambert law (Equation 2.6.13). A_{515} was used opposed to the usual A_{280} to uniquely measure the mVenus absorbance as the media contains a large number of other proteins (including bovine serum albumin, BSA). To increase throughput when many VHH antibodies were expressed in parallel, A_{515} was measured using a CLARIOstar plus microplate reader (BMG Biotech) for both the VHH antibodies and the untransfected controls using 100µl in a 96-well plate in an analogous fashion.

$$A_{515(\text{Sample})} - A_{515(\text{Control})} = \text{"}cl \tag{2.1}$$

where:

$\epsilon =$ 104,000 $M^{-1}cm^{-1}$

mVenus-tagged VHH antibodies were detected specifically by both western Blotting and Native PAGE.

For Western blotting, SDS-PAGE gels were run as usual with a pre-stained ladder, but rather than visualising with Coomassie, the protein was transferred to a

polyvinylidene difluoride (PVDF) membrane using nitrocellulose transfer stacks using the iBlot Dry Blotting System (invitrogen) using the manufacturers default settings (P2, 7 mins). Following transfer, the membrane was blocked with 5ml TBST (150mM NaCl, 20mM Tris, pH 7.5 + 0.1 % Tween20) + 5 % BSA for one hour rotating at room temperature. The blocking solution was replaced with 5ml TBST and anti-hexa his antibody conjugated to HRP was added 1:1000 and rotated overnight at room temperature. Blots were washed three times with TBST then developed using a one-step TMB blotting kit according to manufacturers instructions.

For Native PAGE, the sample was not heated and was run using the NativePAGE ™ Novex Bis-Tris Gel System according to manufacturers instructions and the resultant gel was visualised using the Cy2 525BP20 filter (515nm to 535 nM) to visualise mVenus in an Amersham Typhoon (GE Healthcare).

2.7 Immunohistocytochemistry

Category	Reagent	Source	Product Code
Solutions & Chemicals	PBS	Sigma	P5119
	FBS	Sigma	A9418
	DAPI Hydrochloride	Sigma	D1306
Antibodies	ab1187 Rb pAb to 6His (HRP)	Abcam	GR300288-1
Reagents	TMB Substrate kit	Thermo Fischer	34021
Disposables	24-well plate	Thermo Fischer	142475
	Microscope Coverslips	Menzel	15707592

Table 2.14: **List of materials for Immunohistocytochemistry**

2.7.1 Immunohistocytochemistry on *Xenopus laevis* Oocytes

Oocytes were prepared and injected as described in Oocyte Preparation and mRNA injection. Five mock injected oocytes or oocytes expressing hTREK-2 were placed in a 96 well plate (5 per well) plate and blocked by incubation with ND96 + 1% BSA for 30 mins on ice to limit channel trafficking. After 30 mins, 1 µ g of VHH antibody was added and incubated for 1 hour. The oocytes were then washed 5 times with 200 µl of ND96, before being incubated with secondary Anti-HexaHis antibody conjugated to horseradish peroxidase (HRP) (1:1000 in ND96 + 1% BSA). The oocytes were then washed twice for 1 hour each with ND96 and ND96 + 1% BSA respectively and a colometric assay using tetramethylbenzidine (TMB) substrate to detect bound Antibody.

2.7.2 Immunohistocytochemistry on HEK293T Cells

Cells were prepared and transfected as described in Seeding adherent Cells and Transfection of Nav1.7 mutants and K2P Channels. Following cell preparation, seeded coverslips were manually picked up with callipers and moved into a 24 well plate (2 per plate containing 200 µl of VHH Antibody of interest, concen-

tration range 100nM-1 µM) and incubated for 2 hours at 37 °C to allow binding to occur. The coverslips were then carefully washed four times with divalent-free PBS to remove unbound VHH Antibody. On the final wash PBS was carefully removed and the coverslips were moved to a Nikon Eclipse TE200U microscope with appropriate filter cubes for imaging using a 10x objective.

Images were collected using a MDF-GFP filter cube (to detect GFP/mVenus) and either a MDF-TRITC or a MDF-MCHC filter cube (to detect mCherry), the specifications of which can be seen in Figure 2.14. The best combination of fluorphore and filter cubes to minimise spectral overlap are GFP and mCherry visualised with MDF-GFP and MDF-MCHC filter cubes. For this reason, after promising data from the preliminary experiments, a MDF-MCHC filter cube was purchased for the selectivity panel.

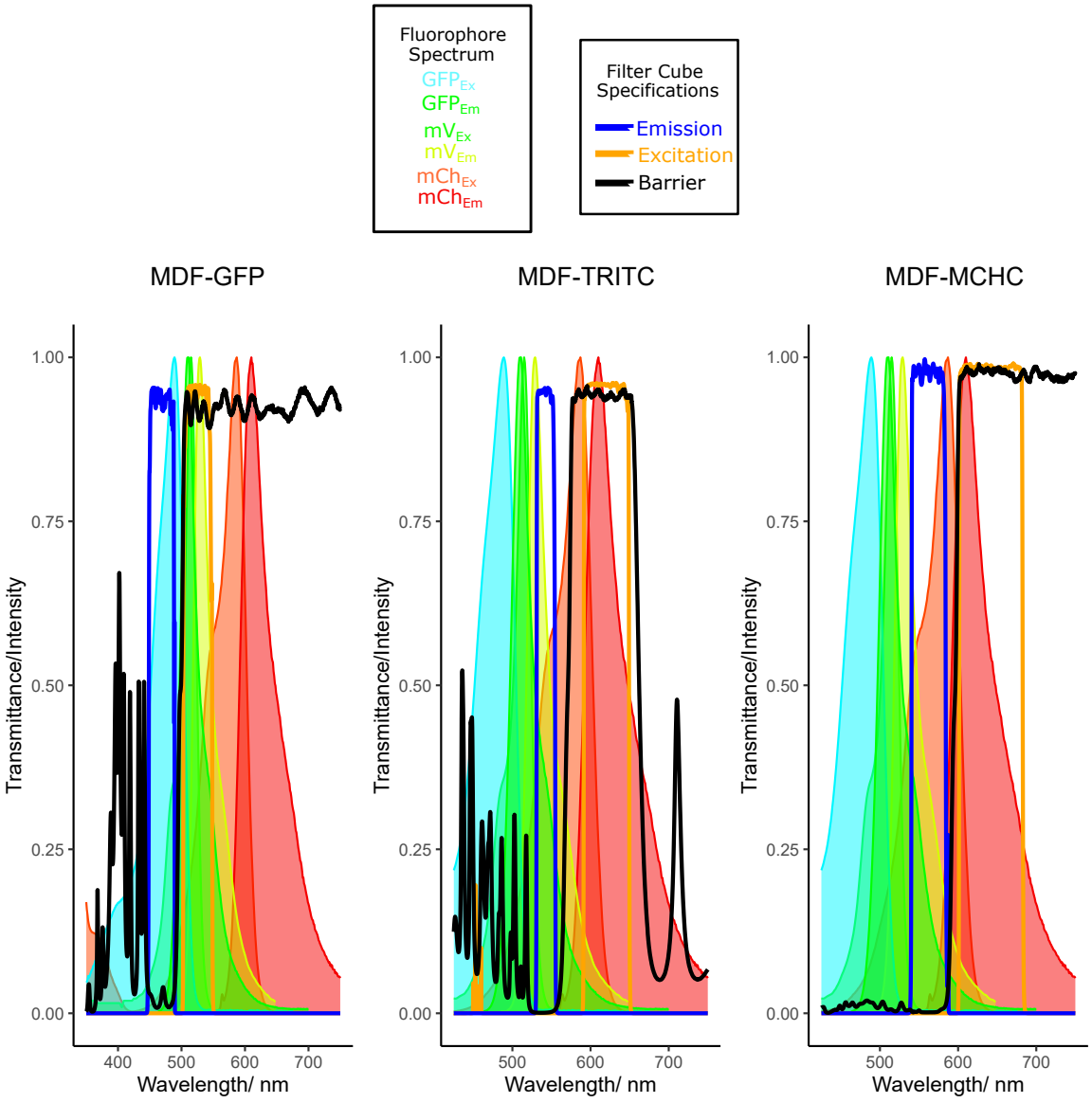


Figure 2.14: **Fluorescent Protein Spectra and Filter Cube Specifications**

For the original experiments, images were collected using the HCImage software (Hammatsu) with a C11440-50B CMOS camera (Hamamatsu) at 10x and 40x magnifications. Offline processing was conducted manually by J. Elliott using ImageJ. Briefly, pixel intensities of each cell and the background were calculated using the measure function using the shape outline of the cell as an area. Using the stack function this was carried out on the image obtained using the MDF-GFP and MDF-TRITC filter cubes in parallel. The background was subtracted for each to obtain the fluorescence intensity from the florophore for each cell. The fluorescence intensity in the green and red channels was then plotted against for the figure.

For the selectivity panel, images were collected using the ASICAP software (ZWO) with a ASI 120MC-S USB 3.0 Colour Camera (ZWO) with gain 100, red exposure time 100ms, green exposure time 300ms. Offline processing was conducted using a custom Python script written by Kathryn Smith. Briefly, the script opens the GFP and mCherry image pair, increases the Green value of both two-fold to account for the suboptimal mVenus excitation. Additionally for overlays, both images were converted to RGBα images, blended at 50% and and the RG values were scaled two-fold to account for the transparency. Scale bars were added by additionally taking images of a 0.01mm Stage Micrometer Microscope Camera Calibration Slide, calculating the distance: pixel ratio in ImageJ and manually adding them to the images.

2.7.3 Immunohistocytochemistry on Rat Superior Cervical Ganglion

Rat Superior Cervical Ganglion (SCG) tissue slices were received as fixed preparations from 5 week old mice on thick glass slides from H. Davis. 100µl of VHH

antibody at low µM concentration was incubated with the tissue preparation for 2 hours at 37 °C, followed by careful washing four times with PBS. Following washing, 100 µl of DAPI (final concentration 300nM) was incubated with the samples at room temperature, and protected from light by covering with foil for 5 mins. The tissue samples were then three times with PBS. After the final wash step, the PBS was carefully removed and a glass coverslip placed over the top of the sample to decrease the slide thickness if imaged upside down.

The sample was inverted and imaged on a nanoimager (ONI) with a 100x objective and using the 405nM laser at 10 % maximal intensity for DAPI imaging and the 473nm laser at 5 % maximal intensity for mVenus imaging and images collected with the onboard camera. Scale bars were added offline using ImageJ using the known distance to pixel ratio of 117nm per pixel.

2.8 Electrophysiology

2.8.1 Materials

Dimensions	Source	Product Code	Application
1.05x1.50x10	Science Products	GB150TF-10	TEVC
4 in, OD 1.5 mm	World Precision Instruments	1B150F-4	Nav1.7 Ephys
0.86x1.50x80mm	World Precision Instruments	GB150F-8P	K2P Ephys

Table 2.15: List of Glass Used to Pull Pipettes

2.8.2 Whole Cell Patch Clamp Recordings of Nav Channels

Whole-cell patch clamp recordings were obtained using a Molecular Devices Axopatch 200B patch clamp amplifier. The recording pipette intracellular solution contained (in mM): 140 CsF, 10 NaCl, 1.5 MgCl2, 10 HEPES, 5 EGTA adjusted

to pH 7.3 with CsOH, Osmolarity 300. The extracellular recording solution contained (in mM): 155 NaCl, 3 KCl, 1 MgCl2, 1.5 CaCl2, 10 HEPES, adjusted to pH 7.4 with NaOH. Currents were recorded at 20 kHz sampling frequency and filtered at 5 kHz. Series resistance compensation was applied at ¿80 %.

For all experiments involving toxin dose-response measurements, lyophilized powder of both native (purified by Marie-France Martin-Eauclaire and Pierre E. Bougis) and synthetic toxins (synthesised by Smartox Biotechnology) were resuspended in extracellular recording solution, and the concentration checked with A_{280} using a nanodrop photospectrometer. A stable baseline was established prior to toxin perfusion, after which increasing concentrations of toxin were perfused using the Dynaflow Resolve System (Fluicell) and resulting currents were measured after equilibrium reached.

2.8.2.1 AahII Dose Response Measurements on Nav1.7 and Nav1.2, Nav1.7 mutants, Nav1.2 mutants and Toxin Mutants

Dose-response measurements on Nav1.2, Nav1.7 and Nav1.7 mutants were made while holding the membrane voltage at -100 mV. A 100 ms pulse to 0 mV was used to open the channel (Figure 2.15). Using this protocol at a 0.5 Hz pulse rate, the membrane voltage is maintained at -100mV 95 % of the time. The voltage protocol and resultant timecourse is shown in Figure 2.15. A 15ms time series during the 0mV test pulse was used to quantify the proportion of inactivated channels (25-40 ms, grey box, Figure 2.15) while increasing doses of AahII were continuously perfused. The steady state values for each dose of AahII were then used to construct a dose-response curve as demonstrated pictorially in Figure 2.15, by normalising the current to the peak, subtracting the normalised current without

toxin and normalising to the maximal effect of the toxin. The normalised current was then fitted with a non-parametric version of the Hill Equation (Equation 2.3) to obtain an estimate for the EC_{50}.

$$I_{Normalised} = \frac{1}{1 + exp^{((EC_{50} - [Toxin])/h)}} \tag{2.2}$$

where:

$I_{Normalised}$	=	Normalised Current
EC_{50}	=	Median effective Concentration (M)
[Toxin]	=	Toxin Concentration (M)
h	=	Hill Coefficient

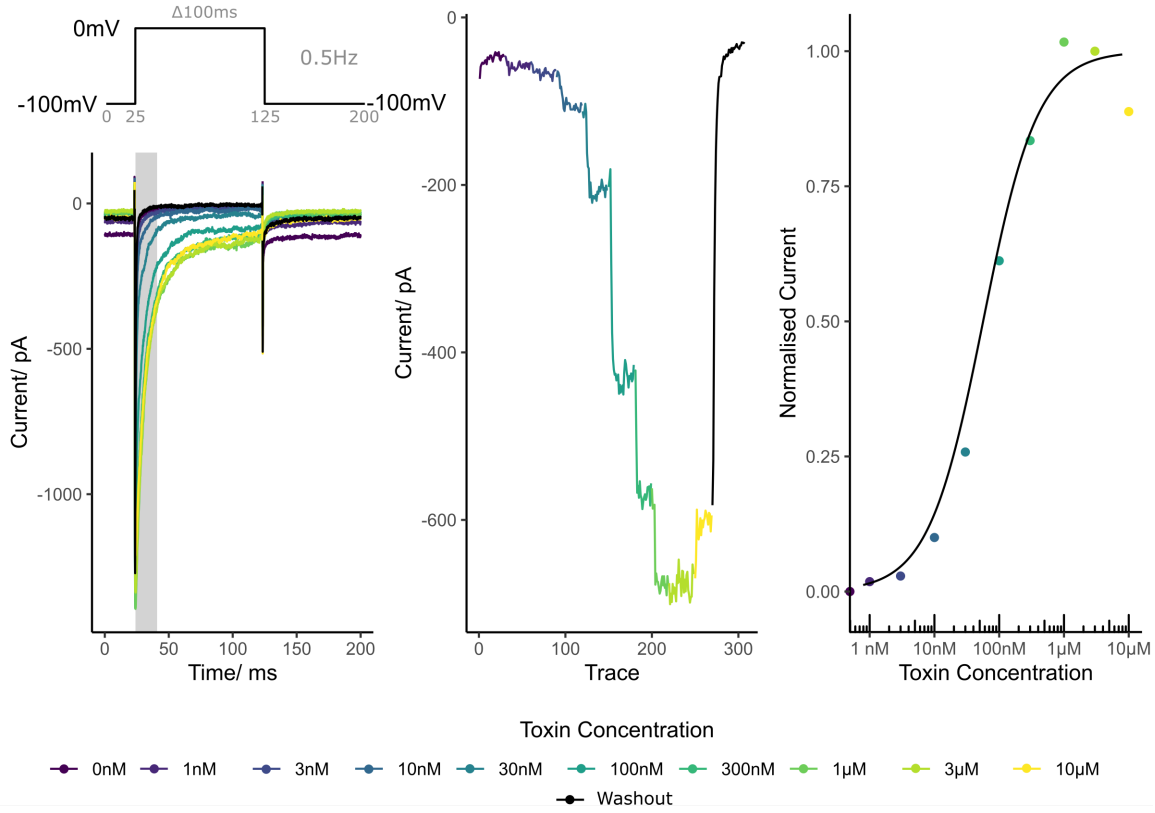


Figure 2.15: **AahII Dose Response Measurements**

2.8.2.2 State-dependence Measurements of AahII on Nav1.7

For state-dependence experiments, the membrane voltage was held either at -40 mV or -120 mV. A 20 ms prepulse to -150 mV was used to partially recover channels from inactivation, followed by a 20 ms pulse to 0 mV to open the channel Figure 2.16. Using this protocol at a 0.2 Hz pulse rate, the membrane voltage is maintained at -40 mV or -120 mV 99.2 % of the time. The Voltage protocols and resultant timecourses are shown in Figure 2.16. In both cases, the average of a 15ms time series during the 0mV test pulse was used to quantify the proportion of inactivated channels (47.5 ms-62.5 ms, grey box, Figure 2.16) while increasing doses of AahII were continuously perfused. The steady state values for each dose of AahII were then used to construct a dose-response curve as demonstrated pictorially in Figure 2.16, by normalising the current to the peak, subtracting the normalised current without toxin and normalised to the maximal effect of the toxin. The normalised current was then fitted with a non-parametric version of the Hill Equation (Equation 2.3) to obtain an estimate for the EC_{50}.

$$I_{Normalised} = \frac{1}{1 + exp^{((EC_{50} - [Toxin])/h)}} \tag{2.3}$$

where:

$I_{Normalised}$	=	Normalised Current
EC_{50}	=	Median effective Concentration (M)
[Toxin]	=	Toxin Concentration (M)
h	=	Hill Coefficient

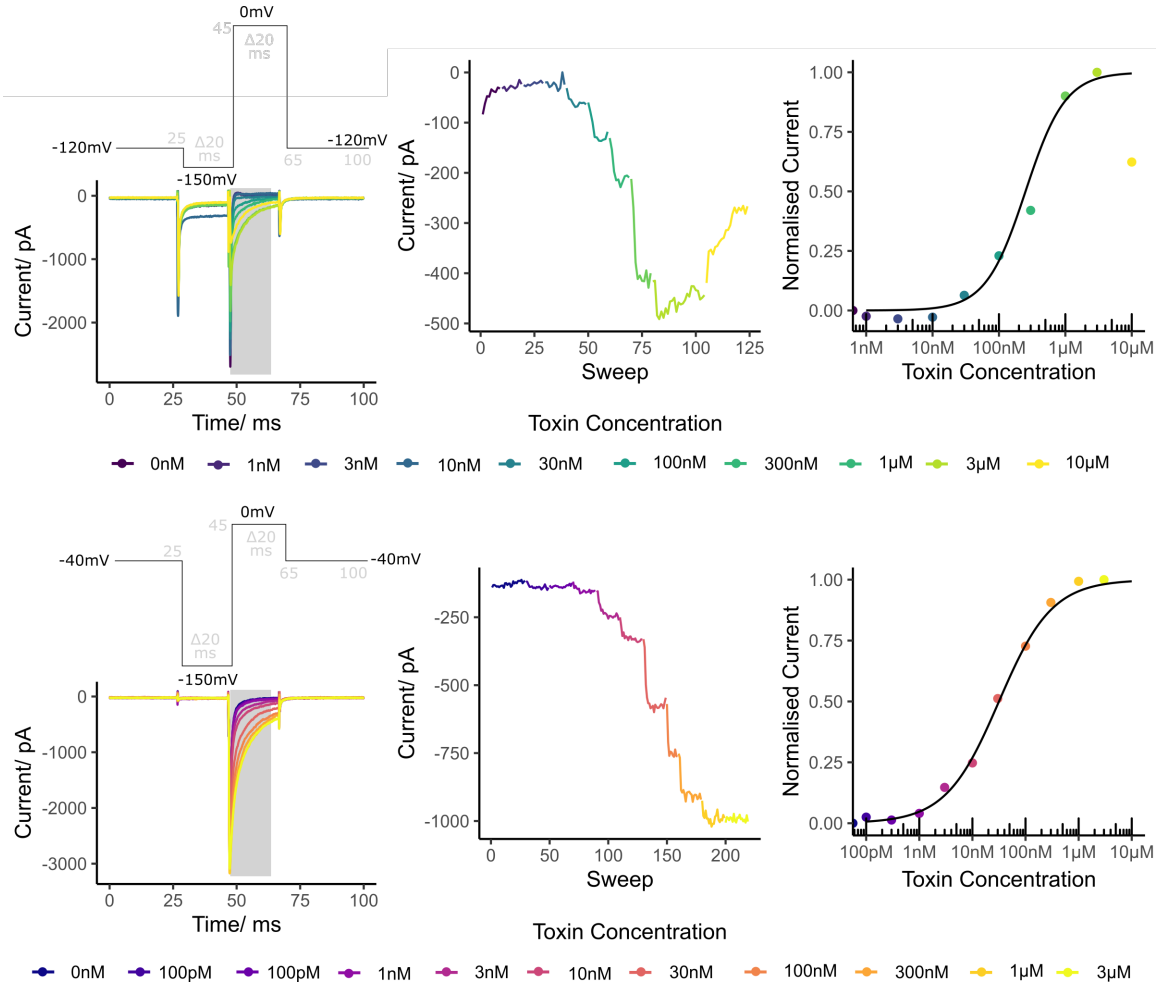


Figure 2.16: **State-dependence Measurements of AahII on Nav1.7**

2.8.2.3 Biophysical Characterisation of Nav1.7 Mutations

2.8.2.4 Voltage-Dependence of Activation

For voltage-dependence of activation measurements, the membrane voltage was held at -100 mV and channel activation evoked by a 20 ms test pulse to test voltages ranging from -80 mV to +40 mV in 5 mV increments Figure 2.17. P/4 subtraction as use to reduce leak currents. The Voltage protocols and resultant time-courses are shown in Figure 2.17. The peak current during the test pulse was used to quantify the proportion of activated channels at each test voltage. This was used to construct an m-infinity curve by normalising to the driving force as shown in Equation 2.4 to calculate the conductance.

$$\frac{G}{G_{Max}} = 1 - \frac{1}{1 + exp^{((V - V_{1/2})/SF)}} \tag{2.4}$$

where:

G	=	Conductance (S)
G_{max}	=	Maximal Conductance (S)
V	=	Test Voltage (mV)
$V_{1/2}$	=	Voltage of half-maximal activation (mV)
SF	=	Slope Factor

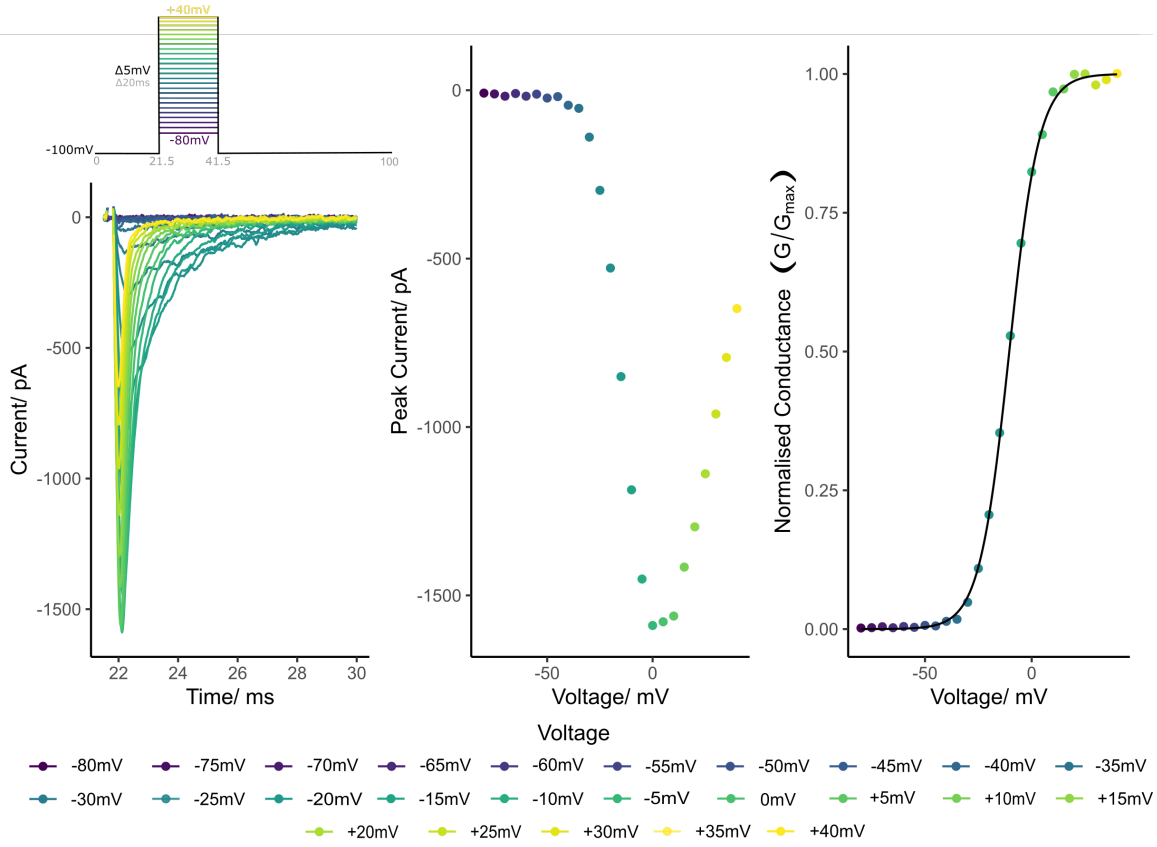


Figure 2.17: **Voltage-Dependence of Activation**

2.8.2.5 Voltage-Dependence of Inactivation

For voltage-dependence of inactivation measurements the membrane was held at -100 mV to stabilise the closed state of the channel. A 20 ms test pulse to 0mV was used to open the channels after a 50 ms pre-pulse ranging from -120 mV to 0 mV in 5 mV increments Figure 2.18. The voltage protocols and resultant timecourses are shown in Figure 2.18.The peak current during the test pulse was used to quantify the proportion of inactivation channels at each pre-pulse voltage. This was used to construct an h-infinity curve by fitting with a the Boltzmann Equation 2.5.

$$\frac{G}{G_{Max}} = \frac{1}{1 + exp^{((V - V_{1/2})/SF)}} \tag{2.5}$$

where:

G	=	Conductance (S)
G_{max}	=	Maximal Conductance (S)
V	=	Test Voltage (mV)
$V_{1/2}$	=	Voltage of half-maximal inactivation (mV)
SF	=	Slope Factor

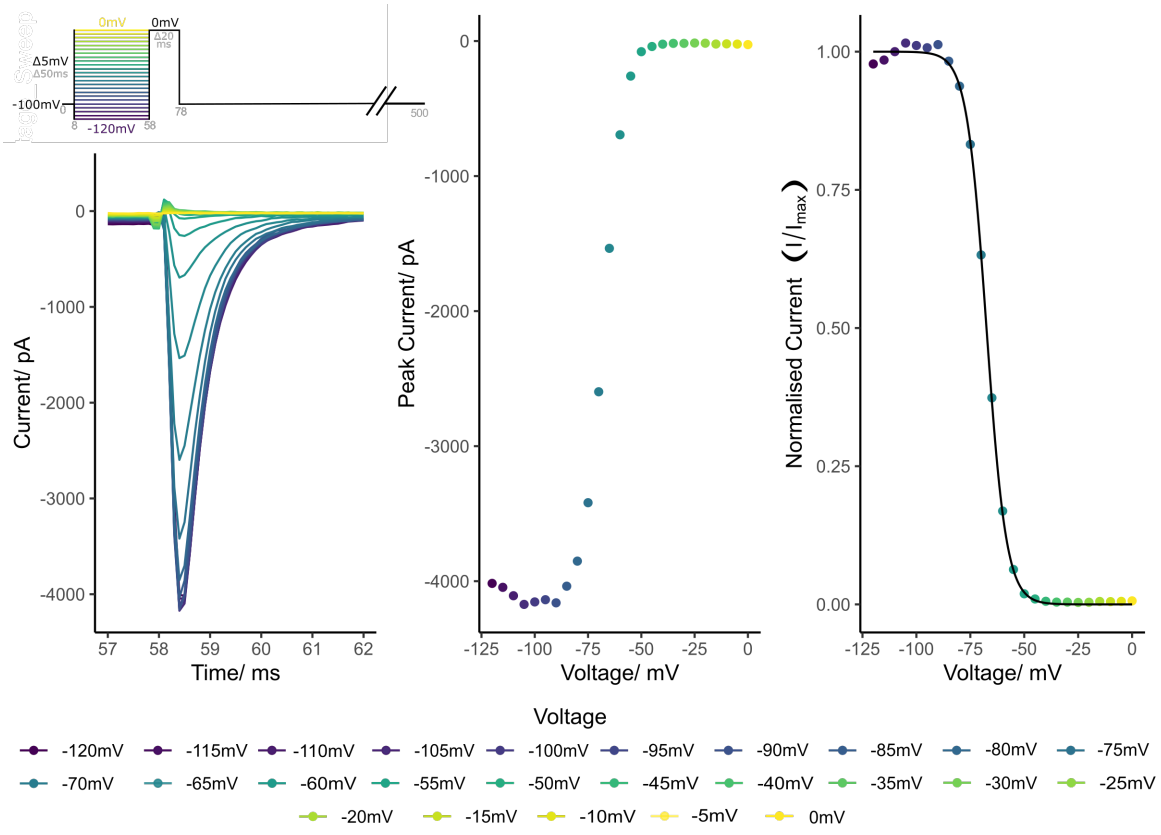


Figure 2.18: **Voltage-Dependence of Inactivation**

2.8.2.6 Time-Dependence of Inactivation

.

To calculate the time-dependence of inactivation, the data used from the voltage-dependence of activation was used. For each voltage, a single summary 'τ' value was obtained by fitting the timecourse of inactivation with a single exponential (Equation 2.6) and this value was subsequently plotted as a function of test voltage as shown in Figure 2.19.

$$I = Aexp^{(-t/\tau)} + C \tag{2.6}$$

where:

I = Current (A)

A = Initial Current (A)

t = time s

τ = time constant of inactivation

C = Arbitrary vertical offset

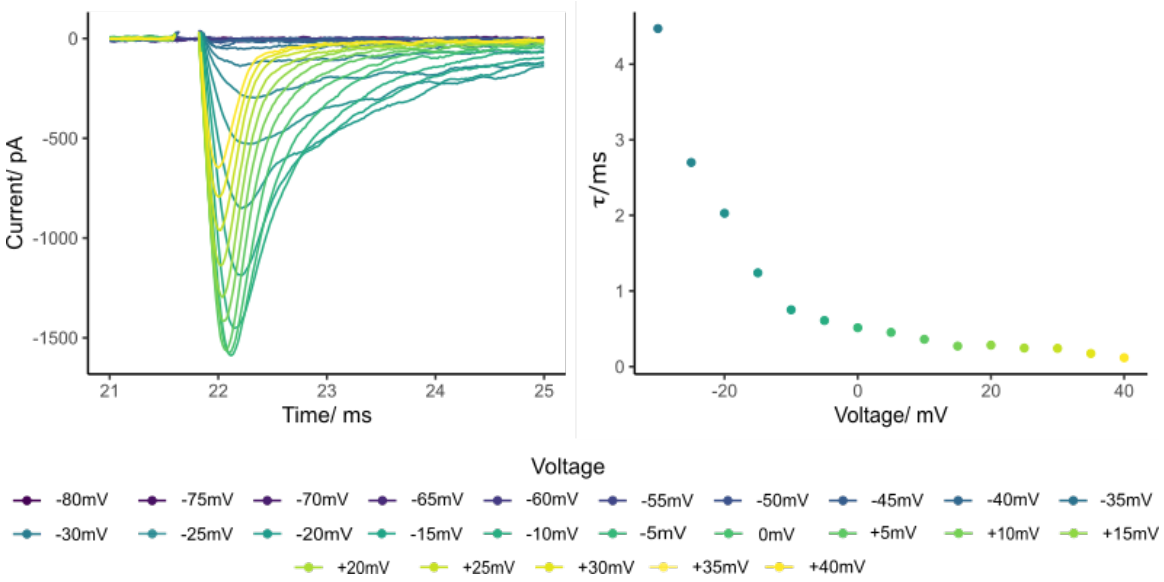


Figure 2.19: **Time-Dependence of Inactivation**

2.8.2.7 Data Processing

To account for drift in biophysical properties of channels, channel mutant activation and steady-state inactivation were recorded in each recording session alongside WT channels. Recordings from each cell for both mutant and WT channels were fitted using an appropriate Boltzmann equation as above to obtain a $V_{1/2}$ estimate. The mean $V_{1/2}$ for each mutant and WT was then calculated, and the difference ($\Delta V_{1/2}$) calculated by subtracting the WT mean to give an accurate $V_{1/2}$ shift on each recording day. Data was then combined using weighted means and the standard error was propagated as the root of the sum of square errors across the days to get the best possible estimate for the effect of the mutation of the biophysical properties of the channel.

$$\frac{G}{G_{Max}} = 1 - \frac{1}{1 + exp^{((V - V_{1/2})/SF)}} \quad \text{(Boltzmann Activation)}$$

$$\frac{I}{I_{Max}} = \frac{1}{1 + exp^{((V - V_{1/2})/SF)}} \quad \text{(Boltzmann Inactivation)}$$

$$V_{1/2(WT,i)} = \frac{\sum_1^n V_{1/2(WT,i)}}{n_{(WT,i)}} \quad \text{(WT mean on day i)}$$

$$\Delta V_{1/2(i)} = V_{1/2(i)} - \overline{V}_{1/2(WT,i)} \quad (V_{1/2} \text{ Shift on day i})$$

$$\Delta \overline{V}_{1/2(i)} = \frac{\sum_1^n \Delta V_{1/2}}{n_i} \quad (\text{Mean } V_{1/2} \text{ Shift on day i})$$

$$SEM_i = \sqrt{(\frac{\sigma_{i(Delta)}}{\sqrt{n_{i(Delta)}}})^2 + (\frac{\sigma_{i(WT)}}{\sqrt{n_{i(WT)}}})^2} \quad \text{(Standard Error on day i)}$$

$$\Delta \overline{V}_{1/2} = \frac{n_i \Delta \overline{V}_{1/2(i)} + n_j \Delta \overline{V}_{1/2(j)} + .. n_z \Delta \overline{V}_{1/2(z)}}{n_i + n_j + .. + n_z} \quad (\text{Weighted Mean } V_{1/2} \text{ Shift})$$

$$S.E.M_{ij..z} = \sqrt{(\frac{\sigma_i}{\sqrt{n_i}})^2 + (\frac{\sigma_j}{\sqrt{n_j}})^2 + .. + (\frac{\sigma_z}{\sqrt{n_z}})^2} \quad \text{(Propagated Standard Error)}$$

where:

G/I	=	Conductance (S)/ Current (A)
G_{Max}/ I_{Max}	=	Maximal Conductance (S)/ Maximal Current (A)
V	=	Voltage (mV)
$V_{1/2}$	=	Voltage of half Maximal Conductance (mV)
SF	=	Slope Factor
$_{i,j,z}$	=	Day i,j z
$_{WT}$	=	Wild-Type recording
$_{i,WT}$	=	Wild-Type recording on day i
n	=	number of recordings
SEM	=	Standard error of the mean
σ	=	Standard deviation

2.8.3 Two Electrode Voltage Clamp Recordings of K2P Channels

Whole cell currents were recorded at room temperature using the two-electrode voltage clamp method with an OC-725C amplifier (Warner Instruments). Borosilicate glass pipettes (Harvard Apparatus) were pulled to a resistance of 0.3-0.5 MΩ using a PC-10 puller (Narishige) and backfilled with 3M KCl.

For screening, oocytes were placed in a small chamber containing GFB (200mM KCl, 20mM HEPES, pH 7.5) and 1µg VHH Antibody (in GFB) was pipetted carefully into the bath without perfusion. For the dose-response measurements, oocytes were placed in the chamber containing ND96 (in mM): 96 NaCl, 2 KCl, 1.8 $CaCl_2$, 1 $MgCl_2$, 20 HEPES, 2.5 Na Pyruvate and constantly perfused with increasing concentrations of VHH Antibody (in ND96) using a peristaltic pump (Ismatec). For the specificity and gating experiments, VHH Antibodies were constantly perfused and measurements carried out in ND96.

All measurements were sampled at 2 kHz and filtered at 1 kHz, digitised with a Digidata 1440A (Molecular Devices) and recorded with WinWCP software (John Dempster, University of Strathclyde).

2.8.3.1 Steady-State Current-Voltage Relationships

For steady-sate current-voltage (I-V) relationships, currents were measured continuously during a 800 ms ramp from a holding potential of -50 mV (screening) or -120 mV (all other measurements) to +80 mV or +50 mV respectively Figure 2.20. The voltage-protocol and resultant I-V curves are shown in Figure 2.20. I-V curves were normalised to the the highest current in the absence of VHH antibody. A summary value of modulation for each VHH antibody was calculated at +50 mV (dotted lines, screening) or 0mV for all other measurements and this was use to plot the summary bar graphs for each VHH antibody modulator. 0 mV was used for experiments recorded in ND96 because it removes voltage-dependent effects, while +50 mV was used for the extracellular binders screen which was measured in high $[K^+]$. Data was plotted on a logarithmic scale so that 50 % activation and 50 % inhibition are the same size. To calculate voltage-dependence of modulation, the fractional current was calculated by dividing each current value at each voltage in the presence of VHH antibody to the current at the corresponding voltage in the absence of VHH antibody. The values between 0 mV and +30 mV as division by small numbers causes unreliable estimates in this region Figure 2.20.

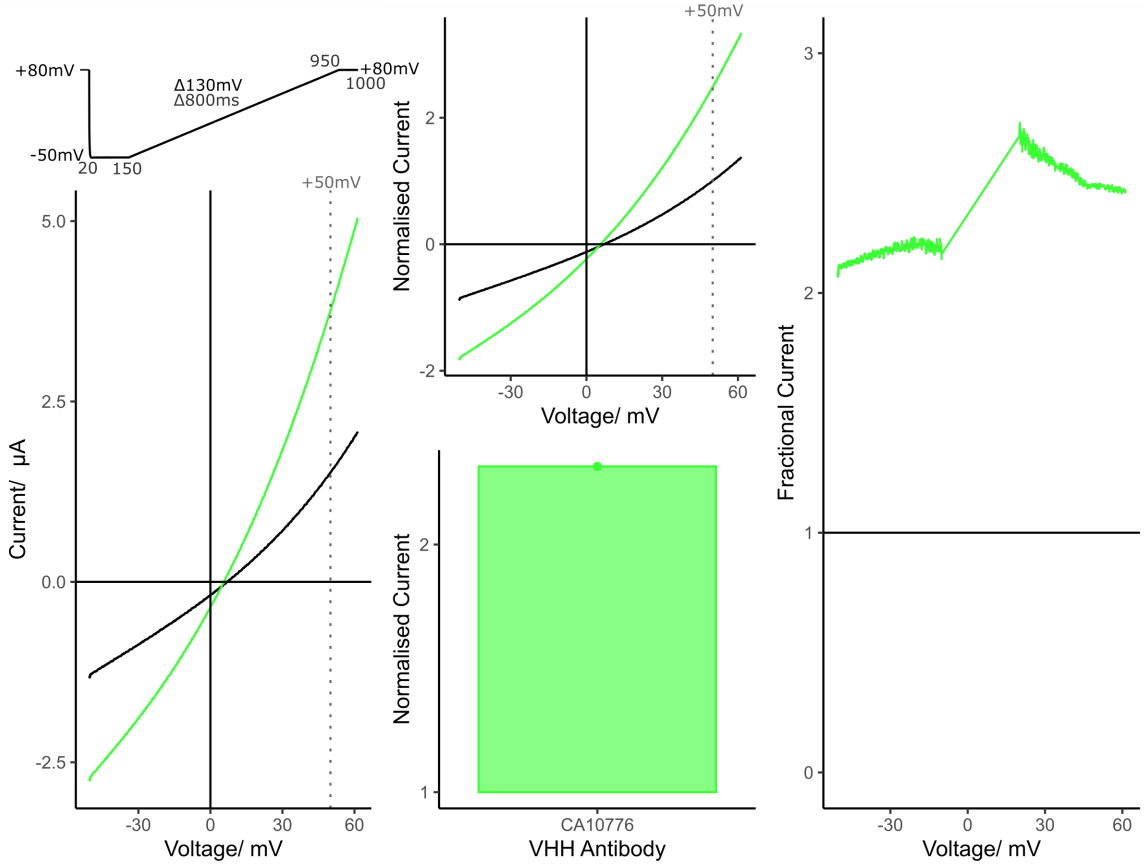


Figure 2.20: **Steady-State Current-Voltage Relationships**

2.8.3.2 Dose Response Curves

Dose-response measurements were carried out using steady-state current-voltage relationships as described above. For the inhibitor CA10761, individual dose-response measurements were fit using Equation (2.7), and the individual values averaged to get an estimate for the IC_{50}.

$$I_{Normalised} = \frac{1}{1 + exp^{(([VHH] - IC_{50})/h)}} \tag{2.7}$$

where:

I	=	Current (A)
IC_{50}	=	Median inhibitory Concentration (M)
[VHH]	=	VHH Antibody Concentration (M)
h	=	Hill Coefficient

Owing to the large disparity in the normalised current of modulation of the activators (Figure 2.21), each measurement was normalised to the maximal normalised current (dotted lines) and then fit using Equation 2.8. Individual estimates were then averaged in order to obtain an estimate for EC_{50}, as demonstrated for CA10767 2.21.

$$I_{Normalised} = \frac{Asym}{1 + exp^{((EC_{50} - [VHH])/h)}} \tag{2.8}$$

where:

I	=	Current (A)
Asym	=	Asymptote (A)
EC_{50}	=	Median effective Concentration (M)
[VHH]	=	VHH Antibody Concentration (M)
h	=	Hill Coefficient

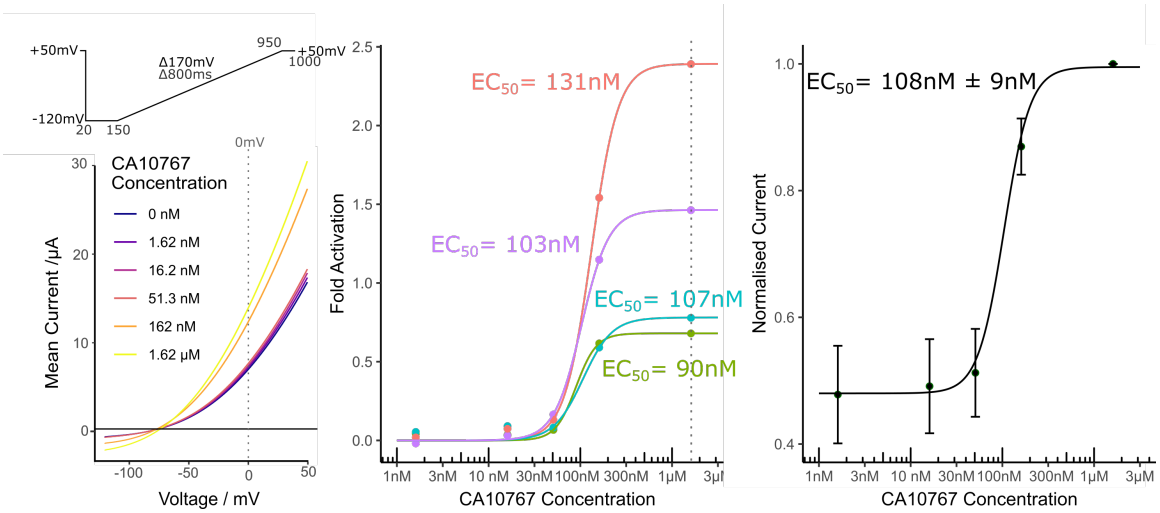


Figure 2.21: **Activator Dose-Response Measurements**

2.8.4 Whole Cell Patch Clamp Recordings of K2P Channels

Whole-cell patch clamp recordings were obtained using a Molecular Devices Axopatch200B patch clamp amplifier. The recording pipette intracellular solution contained (in mM): 155 KCl, 3 $MgCl_2$, 5 EGTA, 0.5 $CaCl_2$,10 HEPES adjusted to pH 7.2 with KOH, Osmolarity 300. The extracellular recording solution contained (in mM): 140 NaCl, 10 TEA-Cl, 5 KCl, 3 $MgCl_2$, 1 $CaCl_2$,10 HEPES, adjusted to pH 7.4 with NaOH. Currents were recorded at 20 kHz sampling frequency and filtered at 5 kHz.

For BL-1249 dose-response measurements, lyophilized powder of BL-1249 was resuspended in DMSO to a final concentration of 10mM. For measurements, this was diluted in extracellular recording solution. For VHH antibody dose-response measurements, purified VHH antibody was buffer exchanged using PD10 columns into extracellular recording solution and concentrated to approximately the highest concentration used. This stoch was serially diluted to make working concentrations. A stable baseline was established prior to perfusion, after which increasing concentrations of agonist were perfused using the Dynaflow Resolve System (Fluicell) and resulting currents were measured after equilibrium reached.

2.8.4.1 Problems with Whole Cell Recordings

In my hands, mechanosensitive TREK-2 channels were very unstable in whole cell configuration. The Dynaflow resolve system necessitates the need to pick the cells up during patching so that they can be manually moved to one of the 16 flow channels on the chip. Cells expressing TREK-2 were very fragile at this stage which remained a problem. Interestingly, I had relatively few problems with the non-mechanosensitive TASK-3 channel and untransfected cells, suggesting properties

of TREK-2 made it difficult to use in this system. In an attempt to increase stability, components of the solution were changed and expression was reduced (by buffering out with empty pFAW vector during transfection) but the problem still persisted.

2.8.4.2 Dose-Response Measurements

Dose-response measurements were performed using steady-state current-voltage (I-V) relationships. Currents were measured continuously during a 3000 ms ramp from a holding potential of -80 mV to +50 mV Figure 2.22. The voltage-protocol and resultant I-V curves are shown in Figure 2.22. I-V curves were normalised to the highest current in the absence of agonist. A summary value of modulation for each dose of agonist as calculated at +50 mV (dotted lines) and was used to generate dose-response curves. These were then fit as described previously to obtain an estimate for the EC50.

To remove the problem faced with fold change of VHH antibody activators within different cells (discussed in Section 2.8.3.2), an estimate for the maximal TREK-2 current was achieved by applying increasing doses of BL-1249 to HEK293 cells expressing TREK-2. Dose-response measurements on BL-1249 (top, Figure 2.22) confirmed that 100µM was saturating, which was therefore chosen to benchmark all VHH antibodies against.

For VHH antibody dose-response measurements, increasing doses of VHH antibody was perfused onto HEK293 cells expressing TREK-2. After application of the saturating dose of VHH antibody, 100 µM of BL-1249 was perfused to obtain an estimate for maximal activation. The effects of the VHH antibody were then normalised to the BL-1249 activated current which consistently was approximately

25% of maximal activation (bottom, Figure 2.22).

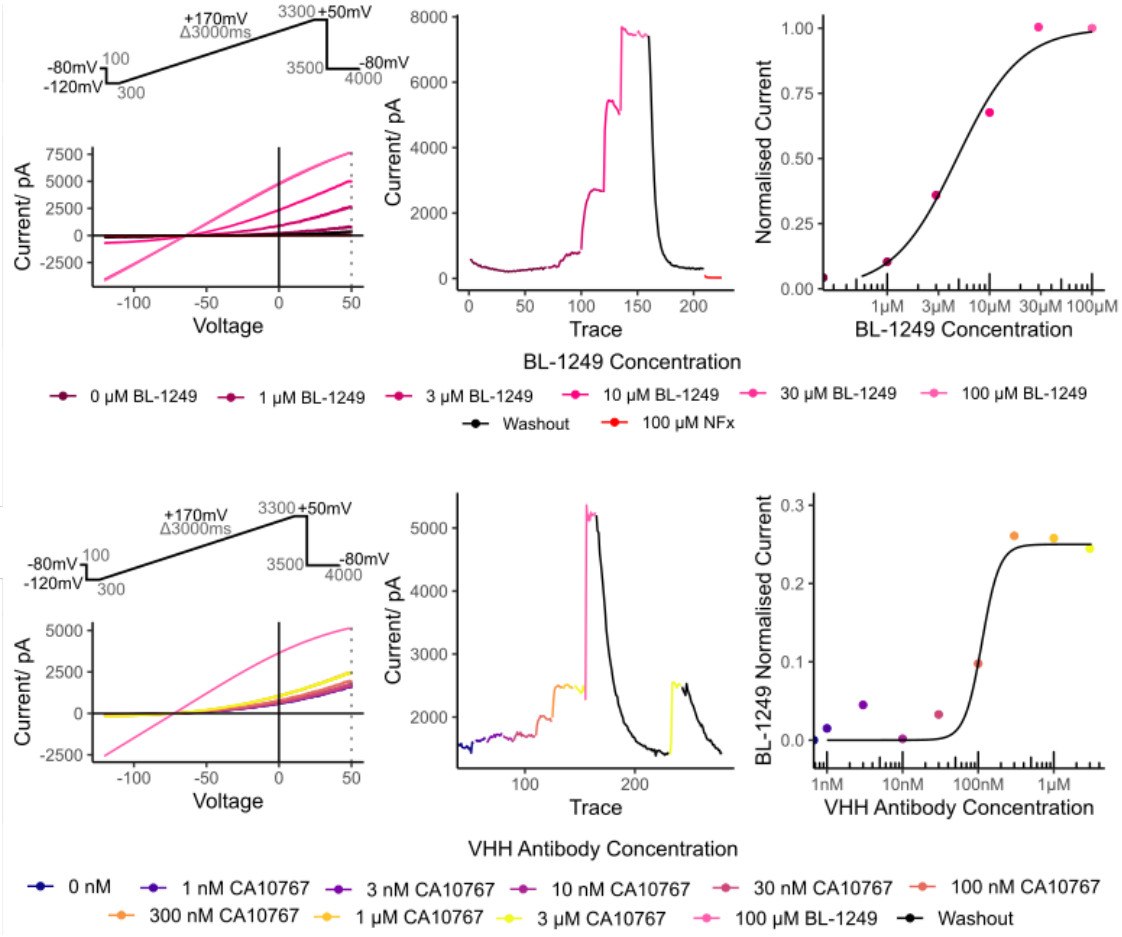


Figure 2.22: **Patch Clamp Dose-Response Measurements**

2.9 Figures in This Thesis

All numerical data were analysed and plotted using R (R Foundation for Statistical Computing) making use of the 'Tidyverse' package (Hadley Wickham).

Figures in this thesis were put together using inkscape.

For any figures that reproduce or are modified from published figures in articles, permission was obtained via the copyright clearance centre by RightsLink, and the original source and copyright information is verbosely labelled in the figure legend. For any figures that reproduce published figures from textbooks, permission was obtained via PLSclear.

All Structural figures were made in Pymol (Schrodinger) using custom written scripts.

All sequence alignments were made using MUSCLE (Edgar, 2004) in UGENE and alignments annotated with the TeXshade package (Beitz, 2000).

This thesis was written in Overleaf (LaTeX).

Bibliography

Aricescu, A., Lu, W., and Jones, E. (2006). A time- and cost-efficient system for high-level protein production in mammalian cells. *Acta Crystallogr D Biol Crystallogr*, 62(Pt 10):1243–50. 97

Beitz, E. (2000). Texshade: shading and labeling of multiple sequence alignments using latex2e. 16(2):135–139. 172

Chen, I., Dorr, B. M., and Liu, D. R. (2011). A general strategy for the evolution of bond-forming enzymes using yeast display. *Proc Natl Acad Sci U S A*, 108(28):11399–404. 144

Czirják, G. and Enyedi, P. (2006). Zinc and mercuric ions distinguish tresk from the other two-pore-domain k+ channels. *Mol Pharmacol*, 69(3):1024–32. 93

Edgar, R. C. (2004). Muscle: a multiple sequence alignment method with reduced time and space complexity. *BMC Bioinformatics*, 5:113. 172

Hermening, S., Kügler, S., Bähr, M., and Isenmann, S. (2004). *J Virol Methods*, 122(1):73–7. 97

Krieg, P. and Melton, D. (1984). Functional messenger rnas are produced by sp6 in vitro transcription of cloned cdnas. *Nucleic Acids Res*, 12(18):7057–70. 92, 93

Liman, E., Tytgat, J., and Hess, P. (1992). Subunit stoichiometry of a mammalian k+ channel determined by construction of multimeric cdnas. *Neuron*, 9(5):861–71. 92, 93

Massa, S., Vikani, N., Betti, C., Ballet, S., Vanderhaegen, S., Steyaert, J., Descamps, B., Vanhove, C., Bunschoten, A., van Leeuwen, F. W., Hernot, S., Caveliers, V., Lahoutte, T., Muyldermans, S., Xavier, C., and Devoogdt, N. (2016). Sortase a-mediated site-specific labeling of camelid single-domain antibody-fragments:

a versatile strategy for multiple molecular imaging modalities. *Contrast Media Mol Imaging*, 11(5):328–339. 146

Newnham, L. E., Wright, M. J., Holdsworth, G., Kostarelos, K., Robinson, M. K., Rabbitts, T. H., and Lawson, A. D. (2015). Functional inhibition of β-catenin-mediated wnt signaling by intracellular vhh antibodies. *MAbs*, 7(1):180–91. 98, 119

Norrander, J., Kempe, T., and Messing, J. (1983). Construction of improved m13 vectors using oligodeoxynucleotide-directed mutagenesis. *Gene*, 26(1):101–6. 92

Pardon, E., Laeremans, T., Triest, S., Rasmussen, S. G. G., Wohlkönig, A., Ruf, A., Muyldermans, S., Hol, W. G., Kobilka, B. K., and Steyaert, J. (2014). A general protocol for the generation of nanobodies for structural biology. *Nat Protoc*, 9(3):674–93. 137

Sélo, I., Négroni, L., Créminon, C., Grassi, J., and Wal, J. (1996). Preferential labeling of alpha-amino n-terminal groups in peptides by biotin: application to the detection of specific anti-peptide antibodies by enzyme immunoassays. *Journal Immunol Methods*, 199(2):127–38. 145

Shih, T., Smith, R., Toro, L., and Goldin, A. (1998). High-level expression and detection of ion channels in xenopus oocytes. *Methods Enzymol*, 293:529–56. 92, 93

Veggiani, G., Nakamura, T., Brenner, M. D., Gayet, R. V. V., Yan, J., Robinson, C. V., and Howarth, M. (2016). Programmable polyproteams built using twin peptide superglues. *Proc Natl Acad Sci U S A*, 113(5):1202–7. 139

Chapter 3

Scorpion Toxin Action on Nav Channels

3.1 Disclaimer

The work in this chapter was part of a highly collaborative project undertaken during my industrial internship at Genentech and most of the work presented in this chapter is published in Clairfeuille et al. (2019). As such, many other people's work is directly relevant to my experiments and discussions in this chapter and so here I attempt to clarify and acknowledge everyone's contributions to the project (in order of appearance in this chapter) and to highlight my own work in one place. I also attempt to make it clear within the text when work was not carried out by me and acknowledge the appropriate co-worker. In particular, the structural figures used in this chapter were made by Thomas Clairfeuille (TC) and are reproduced from (Clairfeuille et al., 2019) and reprinted with permission from AAAS. The τ data for the CTD mutants was recorded by me (AC) but the data was analysed by David Hackos (DH). I would also like to take the opportunity to thank my co-workers, particularly TC, Jian Payandeh (JP) and DH for their consistent support

and guidance throughout this project.

Purification of native AahII: Marie-France Martin-Eauclaire (MFME) and Pierre Bougis (PE)

Design, cloning and structural characterisation of Nav1.7-NavPas: JP, TC, Christopher P. Arthur (CPA), Claudio Ciferri (CC) and Alexis Rohou (AR)

Recombinant AahII Purification: AC

Channel Mutant Design: TC, JP, DH, **AC**

Channel Mutant cloning: DH, Yuwen Jian (YJ) and **AC**

Electrophysiology experimental design: JP, TC, DH and **AC**

Electrophysiology Recordings and data analysis of Nav1.7 and Nav1.2: AC* (except τ Data analysis performed by DH)

BgNav cloning, electrophysiology recordings and data analysis: José P. Llongueras (JL) and Frank Bosmans (FB)

Nav1.5 cloning, electrophysiology recordings and data analysis: Daniel Infield (DI) and Christopher Ahern (CA)

3.2 Introduction to Sodium Channels, Fast Inactivation and Toxins

3.2.1 Nav Channels iInitiate and Propagate APs

Upon changes in voltage, voltage gated sodium channels (Nav) rapidly activate within 1 ms and then rapidly inactivate within 5 ms. They produce a brief inward sodium current which is responsible for the rising phase of the AP and for its rapid conduction along nerve and muscle fibres (Ahern et al., 2016), as discussed in the Introduction. The intrinsic ability of sodium channels to inactivate is important to limit the frequency of firing APs and to ensure one-way transmission. As such Nav channels lie at the heart of electrical excitability (Ahern et al., 2016). There are 9 eukaryotic Nav channel subtypes, Nav1.1 to Nav1.9 which are expressed throughout the body and responsible for a wide range of channelopathies, thoroughly reviewed in (Erickson et al., 2018) and summarised in Table 3.1 below.

Subtype	Expression	Channelopathies
Nav1.1 *SCN1A*	CNS and DRG	General epilepsy with febrile seizure Dravet syndrome
Nav1.2 *SCN2A*	CNS and DRG	General epilepsy with febrile seizure Dravet syndrome Benign familial neonatal-infantile seizure
Nav1.3 *SCN3A*	Embryos and CNS	
Nav1.4 *SCN4A*	Skeletal Muscle	Potassium-aggravated myotonia Paramyotonia congenita Hyperkalemic periodic paralysis
Nav1.5 *SCN5A*	Heart, Embryos, DRG	Long QT syndrome Brugada Syndrome Conduction Dysfunction Sinus Node dysfunction Sudden infant death syndrome Atrial fibrillation
Nav1.6 *SCN8A*	DRG and CNS	Inherited cerebellar ataxias (mice)
Nav1.7 *SCN9A*	DRG and CNS	Primary erythermalgia Paroxysmal extreme pain disorder Chronic Insensitivity to Pain
Nav1.8 *SCN10A*	DRG	Neuropathic injury of DRG TGI model of neuropathic pain Radicular pain (humans)
Nav1.9 *SCN11A*	DRG and CNS	Neuropathic injury of DRG TGI model of neuropathic pain Radicular pain (humans) Congenital Insensitivity to Pain*

Table 3.1: **Sodium Channel Subtypes, Expression and Channelopathies Table simplified from (Erickson et al., 2018).**
*A *de novo* Nav1.9 GOF mutation in the IFM motif has been shown to display excessive activity at resting voltages, causing sustained depolarisation and neuronal hypoexcitability (Leipold et al., 2013)

3.2.2 Nav Channels are highly glycosylated tetrameric channels

In bacteria, Nav channels are formed as homotetramers, where four identical subunits come together to form a functional channel (e.g. NavAb, introduced in the

Introduction). By contrast, in higher organisms Nav channels are composed of a single heavily glycosylated polypeptide chain of 260 kDa required for function, the α- subunit, as shown in Figure 3.1A. Auxiliary β subunits of 20-40 kDa are involved in trafficking, increasing the level of cell-surface expression and modifying voltage-gating of the channel (Namadurai et al., 2015). The α subunits of eukaryotic channels are composed of four repeating domains, mirroring that of their prokaryotic counterparts, except they have much longer regulatory loops connecting the domains. Each repeating domain is composed of 6 transmembrane helices; helices S1-S4 make up the voltage-sensing domain (VSD) whilst helices S5 and S6 and the membrane re-entrant loop between them constitute the PD (PD, Figure 3.1B). The channel assembles as a tetramer exhibiting a domain-swapped orientation such that each VSD associates with the PD of the neighbouring subunit, most clearly seen in Figure 3.1D. Within each VSD, the S4 helix contains at least 4 conserved positively-charged residues, separated by two other amino acids which is involved in moving upon changes in voltage, as discussed in the Introduction (Ahern et al., 2016).

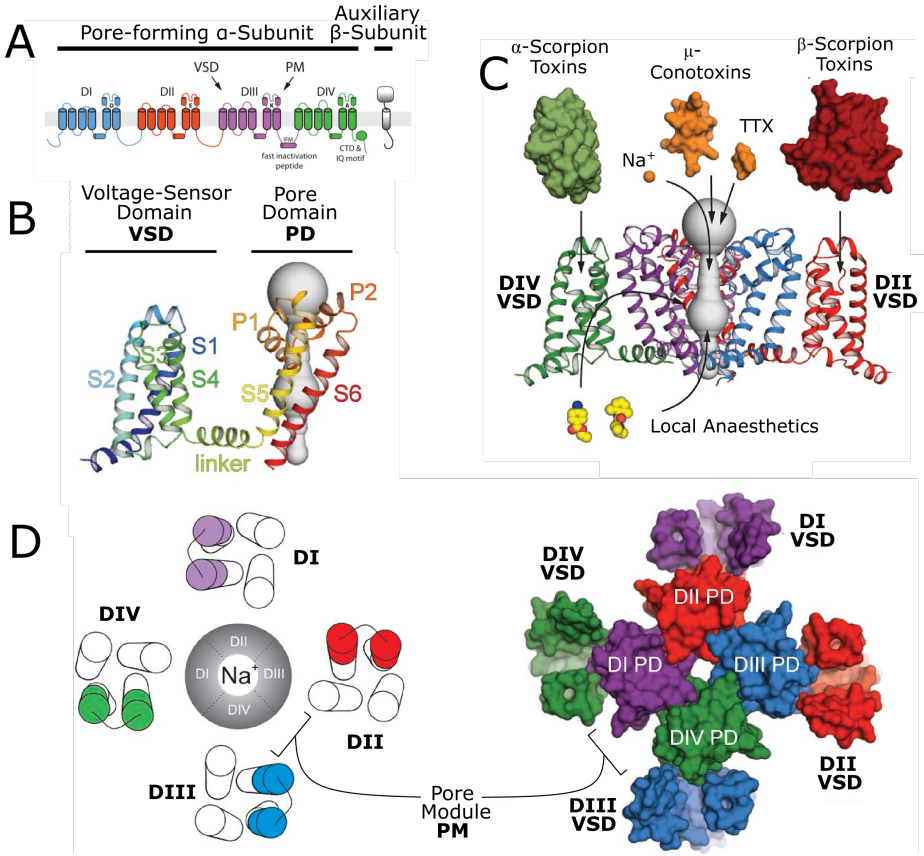


Figure 3.1: **Sodium Channels are the Target of Many Natural Toxins**
A: The pore forming α subunit consists of 4 repeating domains (DI to DIV, blue, red, purple, green), each composed of 6 transmembrane Within each domain, helices S1-S4 constitute the VSD while the S5 and S6 and the membrane re-entrant loop between them constitute the PD. The fast inactivation peptide resides in the DIII-DIV linker alongside a large cytoplasmic C-terminal domain (CTD). Auxiliary β subunits have the opposite topology, with an N-terminal Immunoglobulin (Ig) domain, followed by a single transmembrane helix (grey)
B: Structure of a single domain repeat showing helices S1-S4 forming a modular VSD domain (blue-green colours) connected via the S4-S5 linker to the PD (yellow-red colours) which consists of helices S5 and S6 connected by two pore helices P1 and P2.
C: Sodium channel structure as viewed from the membrane plane and coloured as in A. Nav channels are the target of many toxins including the α-scorpion toxins (green) which target the VSD of DIV, β-scorpion toxins (red) which target the VSD of DII, local anaesthetics (yellow) which bind to the inner mouth of the pore and pore blockers (orange) such as the μ- conotoxins and tetrodotoxin (TTX) which physically block Na^+ from permeating inwards through the channel.
D: Sodium channel structure as viewed from the extracellular side, coloured as in A, clearly showing the domain swapped orientation such that the PD of each subunit is most closely associated with the VSD of its neighbour.
Figure adapted from (Ahern et al., 2016). Reproduced and adapted within the remit of the creative commons public license.

3.2.3 Nav Channels are the target of natural toxins

Sodium channel directed neurotoxins have independently evolved in many walks of life as part of predator-prey interactions, demonstrating the pivotal importance of sodium channels and the catastrophic consequences of their dysregulation (Cardoso and Lewis, 2018). Interestingly, their ability to target human channels has recently been proposed as being an unfortunate side-effect of the necessity to protect themselves from natural predators (Herzig et al., 2020). Toxins have been exploited as molecular probes of channel structure/function relationships (Cardoso and Lewis, 2018). There is now a wealth of biophysical and pharmacological knowledge thanks to these naturally occurring toxins, but structural efforts had, until recently, trailed behind.

Toxins fall into two functional classes; pore blockers (orange, Figure 3.1C and Table 3.2) and gating modifiers (other colours, Figure 3.1C and Table 3.2). As the name suggests, pore blockers act by sterically or electrostatically preventing ion conduction through the channel whereas gating modifiers generally bind away from the pore and modify channel opening and closing, often having a profound physiological impact. Knowledge of how these toxins work opens up an avenue for rational drug design, as well as providing key contributions to mechanistic understanding of how these channels function (Cardoso and Lewis, 2018). It is worth noting that both pore blockers and gating modifiers can be small molecule or peptide toxins. A summary of the main classes of toxins acting on Nav channels are shown in Table 3.2 and their binding sites shown in Figure 3.1C.

Historically toxins were classified as acting on one of nine classical receptor sites, although the relevance of the classic nomenclature of these sites is being called into question by structural advances and knowledge of the molecular ar-

Toxin	Binding site		Functional Effect
	Classical	Structural	
Tetrodotoxin (TTX)	Site 1	Outer pore	Inhibits ion flow through channel
Saxitoxin (STX)	Site 1	Outer pore	Inhibits ion flow through channel
μ-Conotoxins	Site 1	Outer pore	Inhibits ion flow through channel
BTX	Site 2	Inner pore	Inhibits fast inactivation Shifts voltage-dependence of activation to more negative potentials
Veratridine	Site 2	Inner pore	Persistent channel opening
α-Scorpion toxins	Site 3	VSDIV (down)	Inhibits of fast inactivation
β-Scorpion toxins	Site 4	VSDII (Up)	Shifts voltage dependence of activation to more hyperpolarised potentials
Spider toxins	Site 3/4	One or more VSDs	One of: 1. Inhibits channel opening 2. Hinders Fast Inactivation 3. Shifts voltage dependence of activation to more hyperpolarised potentials
μO-conotoxin	Site 4	VSDII(Up)	Inhibits opening by preventing VSDII activation
δ-conotoxin	Site 3	VSDIV(Down)	Inhibits fast inactivation
Wasp toxins	Site 3	VSDIV(Down)	Slows fast inactivation

Table 3.2: **A summary of Toxins targeting Nav channels, their binding sites and their functional effects**

chitecture of the channels (for a description of the sites, see Cardoso and Lewis (2018)). Structures of the American cockroach NavPas channel in complex with the insect-specific desert bush spider toxin Dc1a (PDB: 6A90), a GMT which binds to VSDII, and additionally with the pore blockers TTX (PDB: 6A95) and STX (PDB: 6A91) have been solved (Shen et al., 2018). Structures of the tarantula toxin ProTX-II bound to VSDII of Nav1.7 grafted onto a NavAb scaffold have also been captured with the voltage-sensor in both the activated (PDB: 6NQ4) and deactivated states (PDB: 6N4R) by cryo-EM and the activated state also captured by X-ray crystallog-

raphy (PDB: 6N4I)(Xu et al., 2019).

Structural advances allowed structures of sodium channel-toxin complexes of Nav1.2 and Nav1.7 to be solved in quick succession, culminating in three structure-function studies (including this one) being published in the same issue of Science in early 2019.

Recombinant expression of Nav1.2 allowed the capture of the peptidic pore blocker μ- conotoxin KIIIA in the presence of the β2 subunit (PDB: 6JNE) (Pan et al., 2019). In the same issue, the recombinant expression of Nav1.7 allowed the capture of Nav1.7-β1-β2 complex bound to two combinations of pore blockers and GMTs; TTX and ProTX-II (PDB: 6J8I and 6J8J) and STX and huwentoxin-IV (PDB: 6J8G and 6J8H) (Shen et al., 2019). Also in the same issue was this study where we captured grafted VSDIV from Nav1.7 onto the NavPas channel and captured the structure in the presence (PDB: 6NT4) and absence (PDB: 6NT3) of the α-scorpion toxin AahII (Clairfeuille et al., 2019), which will be the focus of the rest of the chapter.

Since this chapter was written, a full length structure of the cardiac channel Nav1.5 was solved (Jiang et al., 2020) followed by a further Nav1.5 structure in complex with the α- scorpion toxin LqhIII (Jiang et al., 2021), thus allowing a direct comparison of apo- and toxin bound states, as well as the α scorpion toxin binding site. This will be discussed in detail in the 3.4.

3.2.4 α- scorpion toxins slow down fast inactivation

All but one species of lethal scorpion belong to the Buthidae family, which are characterised by their small triangular sternum, small claws and disproportion-

ately large stingers. A number of species from this family, whose toxins were used in this study, are shown in Figure 3.2C. Their venom consists of a highly complex mixture of enzymes, peptides and polypeptides, often containing multiple toxins, ensuring potent synergistic effects on the victim. The toxicity to humans is mainly attributed to the effects these toxins have on Nav channels (Bosmans and Tytgat, 2007) and can be split into two classes based on their binding site and pharmacological action.

α-scorpion toxins bind to VSDIV (classical site 3) and slow down fast inactivation, whilst β-scorpion toxins bind to VSDII (classical site 4) and shift the voltage-dependence of activation to more hyperpolarised potentials. Both classes are therefore gating modifier toxins. α-scorpion toxins can be further subdivided into three pharmacological classes, based on their preference for either mammalian channels (classical α), insect channels (insect α) or a mixture of both (α-like). The exquisite selectivity of these toxins to differentiate between mammalian and insect Na_Vs has attracted attention for the development of novel insecticides (Gordon, 1997; Silver et al., 2017). Meanwhile the β- family includes both mammalian and insect selective toxins, and will not be discussed further.

Native toxins can be purified from scorpion venom; the scorpion is immobilised on a surface and electrical stimulation of the stinger causes venom release which is collected. The venom can then be separated by High Pressure Liquid Chromatography (HPLC) and the highest molecular weight fraction is the species responsible for slowing down the fast inactivation process of sodium channels, the α-scorpion toxins. Following Size-Exclusion Chromatography (SEC), ion-exchange and reverse-phase columns are used to isolate pure toxin. The venom yield is very low compared to other venom producing animals, so recombinant expression and

chemical synthesis are often used to obtain pure toxin for experiments (Bosmans and Tytgat, 2007).

Mature α-scorpion toxins are single polypeptide chains of 60-64 amino acids (Rochat et al., 1972) cross-linked by four disulphide bonds (Kopeyan et al., 1974) to form a characteristic βαββ fold (Housset et al., 1994), as shown in Figure 3.2A,B. They bind to classical neurotoxin receptor site 3 and prevent outward gating charge movement of Domain IV S4, a conformational change necessary for fast inactivation (Sheets et al., 1999; Cestèle and Catterall, 2000). As such, they prolong APs of excitable cells and in their most extreme form can kill their prey by inducing paralysis and arrhythmia. In addition to their major effect of slowing down inactivation, they are reported to have a minor effect on channel activation by shifting the $V_{1/2}$ to more negative values (Chen et al., 2002, 2005). The binding to this site is reduced by membrane depolarisation (Gordon, 1997; Strichartz and Wang, 1986), increased by alkaloid binding at Site 2 e.g. veratridine (Gordon and Zlotkin, 1993) and altered allosterically by binding of site 5 and site 7 toxins e.g. brevetoxin and pyrethroids (Cestele et al., 1996; Gilles et al., 2003; Sharkey et al., 1987). There is evidence that suggests binding of even non-toxic ligands to site 4 induces a conformational change that does not alter channel gating but influences toxin binding at site 3 leading to enhanced toxicity (Cohen et al., 2006). This suggests that α- and β- scorpion toxins are synergistic not only with each other, but also with other non toxic components within the venom.

The second α-scorpion toxin purified from *Androcotonus australis* (named AahII), commonly known as the 'man killer scorpion' is a potent mammalian selective toxin and has been the workhorse for studies of the α-scorpion interaction with Nav channels. Early chemical modification experiments showed that disulphide

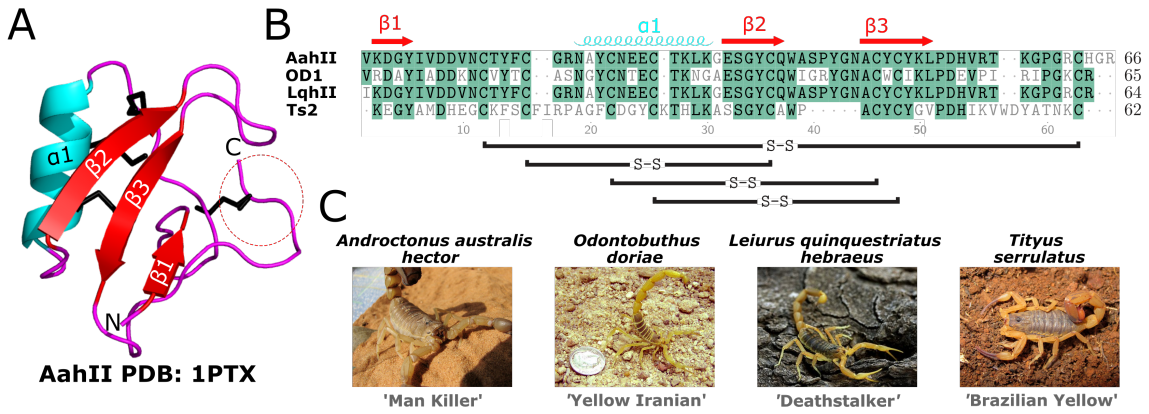


Figure 3.2: **AahII Sequence and Structure**
A: Structure of AahII (PDB: 1PTX) with α-helices coloured blue, β- sheets coloured red, loops coloured purple and disulphide bonds coloured black to show the classical βαββ fold. The NC-domain is circled, the conformation of which is different in insect-selective and mammalian-selective toxins.
B Annotated sequence alignment of a number of α-scorpions used in this study. The positions of the secondary structure are annotated above and the disulphide bonding cysteines annotated below.
C: Photos of the scorpions from which the toxins were isolated, along with their scientific Latin name (black, above) and their colloquial name (grey, below). The names of the toxins are numbered numerically upon discovery and correspond to the genus and species of the scorpion they were isolated from (AahII from *Androctonus australis hector*), OD1 from *Odonthobuthus doriae*, LqhII from *Leiurus quinquestriatus hebraeus* and Ts2 from *Tityus serrulatus*.

bonds are essential for bioactivity, modification of acid residues suppresses toxic activity and acetylation of lysine and tyrosine abolishes toxic activity (Habersetzer-Rochat and Sampieri, 1976). Antibody neutralisation studies revealed two sites required for toxin binding, including a site surrounding disulphide 12-63 and another site in the region 50-58 (El Ayeb et al., 1986).

These mapping studies were rationalised when the first AahII crystal structure was solved (PDB: 1PTX, Figure 3.2, Housset et al. (1994)) swiftly followed by a flurry of NMR structures of the classical α CsE-V (PDB: 1NRA, Jablonsky et al. (1995), insect α LqhaIT (PDB: 1LQH, Tugarinov et al. (1997)), and α-like LqqIII (PDB: 1LQQ, Landon et al. (1997)) and followed by a series of crystal structures of α-like toxins from *B. martensii Karch*, BmKM1, BmKM2, BmKM4, BmKM8 (PDB: 1SN1, 1CHZ, 1SN4 and 1SNB respectively, He et al. (1999, 2000); Li et al. (1996)). The structures revealed a conserved hydrophobic surface (CHS) which was confirmed by mutagenesis to be important for bioactivity (Zilberberg et al., 1996, 1997). Specifically, aromatic residues belonging to the CHS, the 37-44 loop and the C-terminus had previously been shown to be important for efficacy (Kharrat et al., 1989), along with charged residues in the N- and C-termini. Taken together, this was consistent with a multipoint interaction with the channel. The toxic region was further refined by modification of arginine residues and mapped to the CHS and C- and N-termini (Kharrat et al., 1990).

The cloning of toxins from other scorpion species confirmed the importance of these conserved regions. AahII affinity and toxicity could be conferred to the classical-α BotIII toxin by single mutation of the asparagine residue in BotIII to the Histidine at the equivalent position in AahII (N64H) (Benkhadir et al., 2004). Further probing of the C-terminus suggested that amidation of H64 does not affect

pharmacological activity of AahII (Legros et al., 2005) which had previously been reported (Benkhadir et al., 2004), and that replacement of K58 with hydrophobic or acidic residue resulted in an inactive toxin suggesting that this position is required for pharmacological function of α-scorpion toxins (Legros et al., 2005).

Interestingly, insect activity can be conferred onto classical α-toxins by movement of a 'core domain' involving residues on the loops between the conserved secondary structural elements and a five-residue turn with the C-terminal segment, a 'NC-domain' (Guan et al., 2004). This NC-domain can be observed on most known scorpion toxins with potency towards insect channels (Karbat et al., 2004; Guan et al., 2004) and involves a non-proline cis-peptide bond between residues 9 and 10 in the five-residue turn of these toxins. By contrast, this bond in classical α-scorpion toxins is in the trans conformation, circled in red in Figure 3.2A. The importance of this conformation was given further weight by a chimera structure where the NC-domain of the insect toxin Lqhα-IT was grafted onto the mammalian AahII ($AahII^{Lqh\alpha\text{-}IT(face)}$) revealed a protruding conformation of the NC domain with weak activity on mammalian Nav1.2 but high activity on insect Navs (Karbat et al., 2004). As such, the conformation of this NC domain appears to be critical for activity on insect channels.

3.2.5 α- scorpion toxins bind to Neurotoxin Receptor Site 3

In the late 1970s, it was shown that scorpion α-toxins and sea anemone toxins share a common receptor site on the sodium ionophore of the AP (green, Figure 3.1C) (Catterall and Beress, 1978), and shown to compete using radiolabelled AahII (Couraud et al., 1978). Follow up experiments using antibody neutralisation of toxin binding implicated the extracellular loops between S5 and S6 of DI

and DIV in the receptor site, from which they also suggested the domain swapped orientation of Nav channels (Thomsen and Catterall, 1989)

Mutagenesis of the extracellular acidic residues in Nav1.2 DI and DIV to neutral or basic residues revealed seven residues implicated in binding both the scorpion toxin LqTx and the sea anemone toxin ATXII. Substitution of S3 residues from Nav1.5 into Nav1.2 reduced LqTX affinity, a characteristic property of the cardiac subtype. Electrophysiology revealed that the charge reversal E1613R had 62-fold lower potency for LqTX (Rogers et al., 1996). Another study using mammalian Lqh-2 and insect Lqhα-IT toxins on chimeric channels, showed that mutation of K1432 (rNav1.4) to Threonine (as found in hNav1.7) strongly reduces toxin potency (Leipold et al., 2004). The S3-S4 linker of rNav1.2 was mutated to be identical to hNav1.2 by double mutation E1613D/K1617T, and did not confer human sensitivity to Lqh2 suggesting the involvement of other parts of the channel (Chen et al., 2000), as originally deduced by (Rogers et al., 1996).

Differences in binding of α, α-like and insect α- scorpion toxins were deduced by studying rNav1.4 which confers equal selectivity to all three toxins. Transfer of the S3-S4 linker from Nav1.2 and Nav1.3 onto Nav1.4 abolished sensitivity to the α-like Lqh3 and Insect LghαIT but not the classical mammalian selective Lqh2, while transfer from Nav1.6 had a minor effect on all three toxins, and transfer from Nav1.7 dramatically reduced LghαIT, slightly reduced LqH2 and had no effect on Lqh3. In the same study, D1428 (equivalent to E1613 in rNav1.2) was found to be critical (Leipold et al., 2004). Use of δ-conotoxins which compete with scorpion toxins highlighted the importance of the conserved S3-S4 loop hydrophobic residues Y1433, F1434, V1435 in rNAv1.4 for the activity of Lqh2 but not Lqh3 (Leipold et al., 2005).

3.2.6 Rationale

As explained in the Introduction, the necessity for voltage to operate these voltage sensors, and the lack of ability to control voltage during structure determination using cryo-EM results in the capture of voltage-gated channels in their resting state, at 0mV, i.e. the absence of an electric field. For the Nav channels, one would therefore expect to resolve four activated ('up') state voltage sensors per channel. In order to circumvent these shortcomings, we opted to use an α-scorpion toxin which is known to bind to VSDIV and slow down fast inactivation, and capture the structure of the channel in the presence and absence of this toxin, to capture VSDIV in both the deactivated ('down') and activated ('up') state respectively. Capture of a deactivated ('down') state voltage sensor could in turn give important structural insights into fast inactivation coupling in Nav channels, crucial for AP propagation. In addition, the structure would unambiguously identify the toxin-channel interaction putatively defined by the mutagenesis and labelling detailed above.

3.2.7 A humanised NavPas Chimera structure sets the scene

A protein engineering approach was used by TC and JP to graft the 4th human voltage-sensing domain (VSDIV) and the S5 helix of Domain I (D1-S5) onto the biochemically well-behaved NavPas Channel. A thermostabilisation assay was used to confirm that the construct was able to bind AahII and the small molecule GX-936 (Ahuja et al., 2015) was used to confirm the correct folding, functional and pharmacological relevance of this chimeric construct. For full details of rationale and optimisation, see Clairfeuille et al. (2019). Cryo-EM datasets of both AahII-bound NavPas-hNav1.7-VSDIV and the apo structure were collected and structures built by TC, CPA, and AR.

The importance of this structure cannot be understated; for the first time, the fourth voltage sensor (arguably the most important due its role in activation-inactivation coupling) was trapped in the deactivated state. This revealed novel interfaces between the gating charges on the voltage sensor and the ordered CTD, providing a framework for understanding this crucial coupling mechanism. In addition, it provides a snapshot of the VSDIV interaction site; how the toxin derives both its potency and its action, and the residues on the channel which it binds. Finally, it revealed an unexpected second toxin binding site on VSDI. These three parts of the structure will be discussed in detail in the following sections along with the experiments performed to help understand the gating and pharmacology of WT Nav1.7 stemming from this new structure.

3.3 Results

3.3.1 Native AahII is a potent modulator of Nav Channels

To assess the functional consequences of AahII purified from native venom, native AahII was applied to both Nav1.2 and Nav1.7 while holding the voltage at -100 mV to stabilise the closed state of the channel. The mean current during a 15 ms window after channel opening was used as a surrogate to quantify the slowing down of fast inactivation (for details, see Methods). AahII potently slowed down fast inactivation with an EC_{50} of 72pM ± 14pM and 55nm ± 5nM for Nav1.2 and Nav1.7 respectively.

Despite being potent on both channels, reflecting an ability of this toxin to inhibit many channel subtypes, the extent to which the channel slows down inactivation is markedly different. Upon toxin challenge, Nav1.2 produces a substantial residual current which is not seen in Nav1.7, where, even at high doses, it

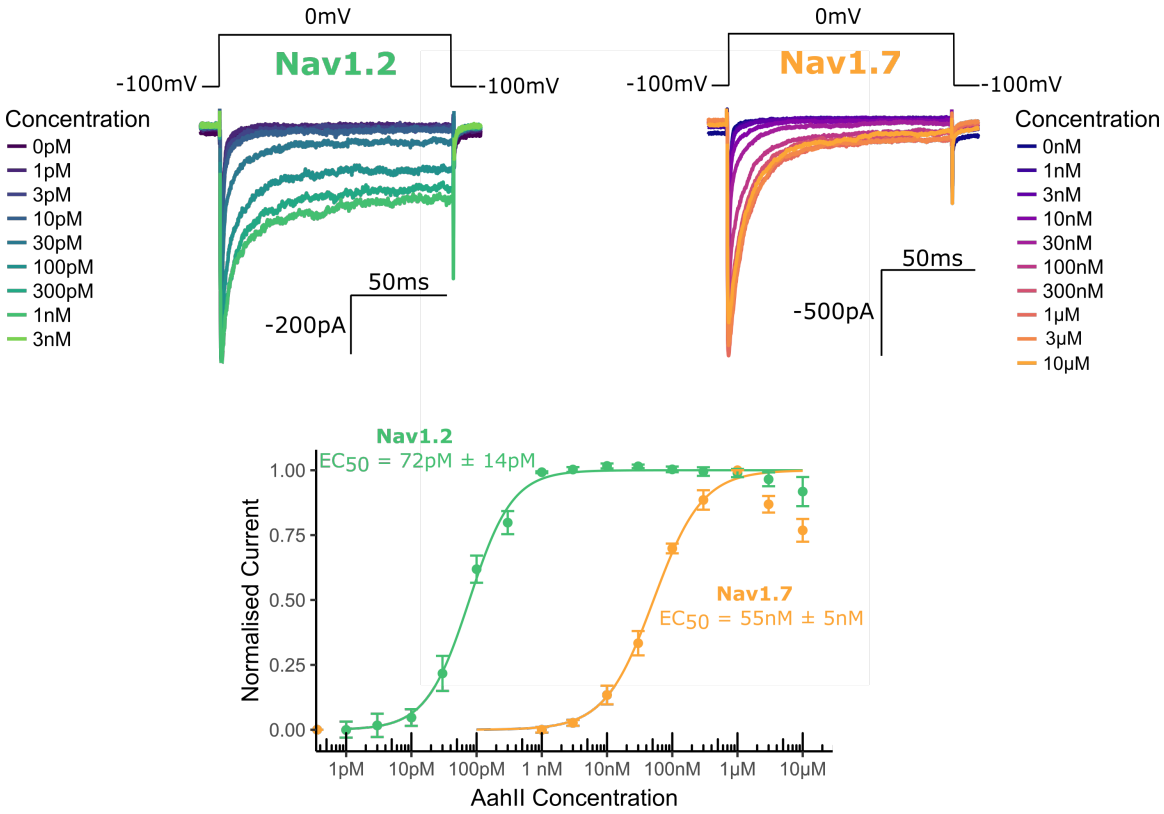


Figure 3.3: **AahII is a Potent α- Scorpion Toxin**
Top: Representative current traces elicited from Nav1.2 (blue/green colours) or Nav1.7 (purple/orange colours) challenged with increasing doses of native AahII in response to a voltage step to 0mV and holding at -100mV (pictured above).
Bottom: Dose-response curves generated from recordings such as above, by challenging both Nav1.2 (green) and Nav1.7 (orange) with increasing doses of AahII in response to a voltage step to 0 mV and holding at -100 mV. Lines represent fitted data from which the EC_{50} were estimated. Points represent mean normalised current and error bars represent the S.E.M.
Adapted from Clairfeuille et al. (2019). Reprinted with permission from AAAS

manages to inactivate almost fully (Top, Figure 3.3. This suggests that the fast-inactivation gating is inherently different between the two subtypes. Whether this is due to the toxin itself or difference in channel architecture was beyond the scope of this study; however the latter seems more likely as Nav channel subtypes show markedly different kinetics (Bennett et al., 2019). At higher concentrations (10µM), the toxin started to inhibit the peak currents, which is not typically reported. This observation is intriguing, as the structure revealed a second, lower

affinity binding site for AahII, and this is discussed further later.

3.3.2 AahII activity is state-dependent

In order to test the state-dependence of AahII binding to VSDIV, dose response measurements were carried out while holding the voltage at two different potentials and opening the channel at low frequency. Stabilising VSDIV in an active conformation by holding at -40 mV increased the potency roughly 15 fold when compared to the stabilised inactive conformation, achieved by holding at a voltage of -120 mV (Top, middle Figure 3.4) . Although this experiment is imperfect as it requires a short recovery pulse to -150 mV in order to record current (for details see Methods), it represents a lower limit for the potency decrease. This state-dependence of binding is typical for toxins that bind to voltage sensors.

This observation can be rationalised in light of the solved structures. Comparison of the AahII binding site between apo- and AahII-bound channel reveals that residues on AahII would sterically clash if the channel was in its up state (grey, Figure 3.4) but not the down state (green, Figure 3.4). In addition, the positively charged toxin interface (blue, Figure 3.4) displays electrostatic complementarity to the negatively charged VSDIV interface (red, Figure 3.4) only in the down state. These two observations are consistent with the toxin showing a higher potency on the voltage-sensor stabilised in its deactivated state.

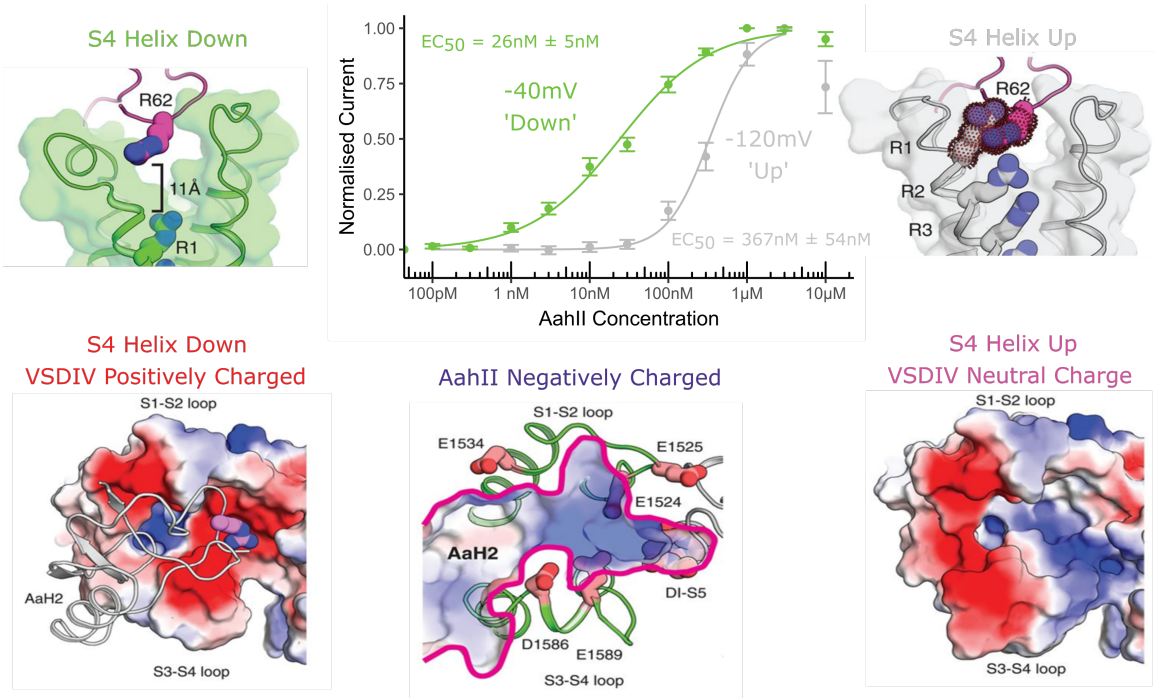


Figure 3.4: **AahII activity is State-Dependent**
Top: R62 from AahII can favourably interact with VSDIV when the S4 helix is in the down conformation (green, left). When the S4 helix is in the up conformation (grey, right) there is a steric clash between AahII and the uppermost gating charge. This is consistent with the dose-response measurements where the 'up' (grey) or 'down' (green) state voltage-sensors are stabilised by holding at -120mV or -40mV respectively and the current recorded from a pulse to 0mV after a short pre-pulse to -150mV challenged with increasing doses of native AahII. Lines represent fitted data from which the EC_{50} were estimated. Points represent mean normalised current and error bars represent the S.E.M.
Bottom: When the S4 helix is down, the VSDIV binding interface is predominantly positively charged (red, left), whereas when the S4 helix is up the VSDIV binding interface is neutral with both positive (red) and negatively-charged (blue) regions. By contrast, the AahII surface is negatively charged (blue, center) and therefore shows electrostatic complementarity to the down state voltage sensor.
Adapted from Clairfeuille et al. (2019). Reprinted with permission from AAAS

3.3.3 Interactions with Neurotoxin Receptor Site 3

The structure of the AahII-VSDIV-NavPas channel complex reveals the molecular details of α- scorpion toxin binding to Nav channels. AahII makes multipoint contacts across VSDIV and DI-PM burying 712Å^2 in interactions with four main regions on the channel D1-PM (Figure 3.5), a PM-glycan (Figure 3.5) , the S1-S2 loop (Figure 3.6) and the S3-S4 loop (Figure 3.7). AahII engages with the receptor site using both its rigid core scaffold and loop elaborations, deeply penetrating beneath the DI-pore turret loop to interact with the central PD. As such, AahII wedges itself into an extracellular cleft formed by VSDIV and DI-PM sterically preventing outward gating charge movement of the S4 voltage sensor.

To test the channel contributions to toxin potency, a series of mutants in WT Nav1.7 were made focusing on side chains that contact AahII directly in the structure. Efforts were also made to rationalise the importance of toxin side chains using toxin mutants.

3.3.4 Channel Determinants of Specificity

Mutant	Mean EC50 /nM	SEM /nM	t	Bonferroni Corrected p	Significance
WT	55	5			
N206R	54	7	0.09677	9.23925	ns
N270A	41	6	1.47983	1.545	ns
H273A	37	4	1.79503	0.88574	ns
F317N	50	8	-1.13797	2.67952	ns
K332A	77	4	-1.88744	0.75333	ns
Q1530A	67	5	-0.86388	3.99681	ns
Y1537A	36	8	1.79991	0.87775	ns
D1586A	**163**	**7**	**-10.12735**	**<0.0001**	***
D1586R	**228**	**16**	**-11.8004**	**<0.0001**	***
E1589A	37	8	1.54799	1.39026	ns

Table 3.3: Summary Table for AahII action on Nav1.7 Mutations made in this study. Two-tailed unpaired t-tests were used to compare the mean EC_{50} of WT Nav1.7 with the channel mutants and the p-value was adjustedusing the Bonferroni correction. Significance is indicated by *** p <0.001 , ** 0.001 <p <0.01, * 0.01 <p <0.05, ns non significant.

3.3.4.1 Summary

3.3.4.2 Glycan-PM and D1-PM

The structure revealed that residues on the reverse turn of AahII make multiple interactions with the glycan emanating from the NavPas scaffold (grey, Figure 3.5). To our knowledge, this is the first instance of a glycan being involved in a toxin binding site. The literature suggests that AahII is least potent on Nav1.7, Nav1.8 and Nav1.9 of all subtypes (Bosmans and Tytgat, 2007; Abbas et al., 2013), immediately suggesting that the glycan could aid tight interaction between toxin and channel based on the following observations. Nav1.7 and Nav1.9 do not have a glycosylatable Asparagine at this position, which may explain this low affinity. However, this fails to explain the low affinity for Nav1.8, which does have a Asparagine at this position. Other work has shown that no tested scorpion toxin has high affinity for Nav1.8 which has been rationalised to be because compared to all other subtypes, the S3-S4 loop is four amino acids longer in Nav1.8 and this prevents tight association of the channel and the toxin (Bosmans and Tytgat, 2007).

In order to rationalise the role of the glycan in toxin binding, point mutants were made in an attempt to either add a glycosylation site into Nav1.7 (F317N) or knock out the glycosylation site in Nav1.2 (N340A). The Nav1.7 F317N mutant responded identically to Wild Type when challenged with toxin with an EC_{50} of 50nM ± 8nM. However, it was not checked biochemically that this site was glycosylated, and as such no conclusions can be drawn from this result; either the glycan is not important, or this site was not glycosylated in the F317N point mutant. In addition, current could not be recorded from the Nav1.2 glycosylation knockout mutant N340A, however, it was not checked biochemically that it was expressed on the cell surface. Interestingly, an equivalent mutant on the *Blatella Germanica* (BgNav) channel, a close relation of the NavPas channel which is also glycosylated, failed to express in the hands of JP and FB (although again with the same caveat

that surface expression was not explicitly checked). Glycosylation is often part of a quality control procedure and so lack of glycosylation may lead to ER retention, which may explain why current could not be recorded from either the Nav1.2 or BgNav glycosylation knockout mutants.

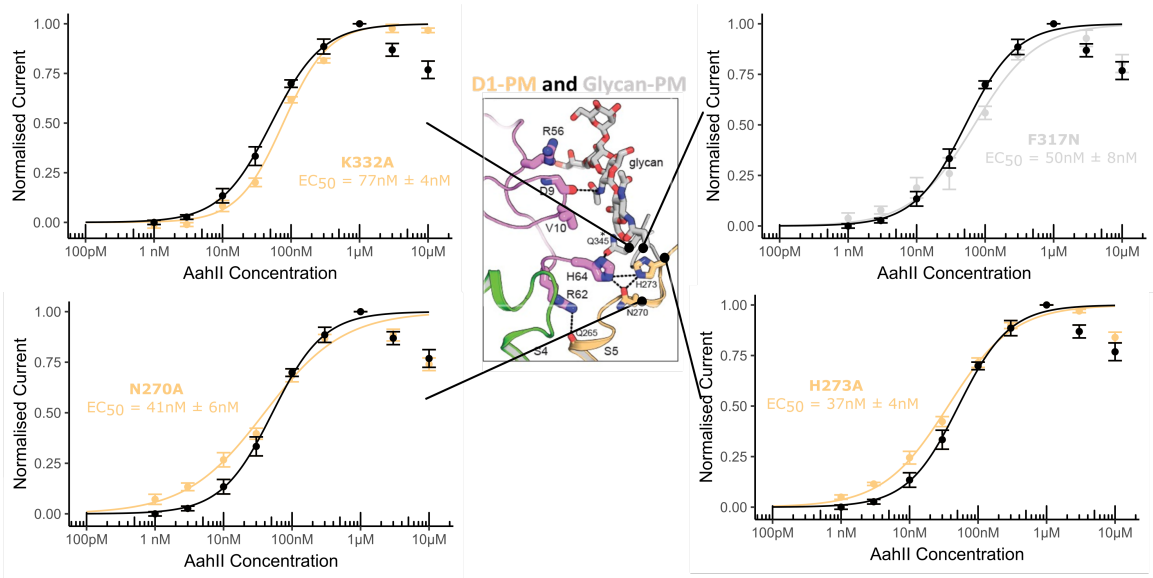


Figure 3.5: **Interactions with the Domain I Pore Module and Glycan Pore Module**
Center: AahII makes multiple interactions with the glycan emanating from the NavPas scaffold (grey) as well as side chains from the D1-PM (beige).
Surrounding: Dose-response measurements recorded by challenging Nav1.7 mutants with increasing doses of native AahII in response to a voltage step to 0 mV and holding at -100 mV. Wild type are shown in black and mutants are shown in grey and beige respectively. Lines represent fitted data from which the EC_{50} were estimated. Points represent mean normalised current and error bars represent the S.E.M.
Adapted from Clairfeuille et al. (2019). Reprinted with permission from AAAS

The C-terminal Segment (CTS) of the toxin dives deep into a cleft and directly contacts residues on the pore module of domain 1 (peach, Figure 3.5). In order to verify the interactions that the toxin makes with the Pore Module, mutants were made based on three residues which make a series of close interactions with H64 of the toxin in the hVSD4-NavPas structure. Two of these three residues (N270,

H273) belong to the humanised DI in the structure, whereas the N345 was a constituent of the NavPaS scaffold, and in hNav1.7 corresponds to K332.

To test the importance of the interactions with D1-PM, a series of alanine mutants focusing on these three residues were made which revealed EC_{50} measurements of 77nM ± 4nM for K332A, 41nM ± 6nM for N270A and 37nM ± 4nM for H273A. These non-significant effects on toxin potency likely suggest redundancy in this interaction network, although this network could potentially confer toxin selectivity towards channel subtypes as there are sequence differences in this region, but this was beyond the scope of this study.

3.3.4.3 S1-S2 Loop

The S1-S2 loop of VSDIV makes contacts with the CTS and β2- β3 loop of AahII. Q1530 of the S1-S2 loop contacts Y42 of the β2- β3 loop and G59 and P60 of the CTS. Meanwhile, Y1537 of S2 makes contacts with the backbone carbonyl of A39 of the β2- β3 loop. Interestingly, Y1537 is the target of the Nav1.7-selective small molecule antagonist GX-936 (Ahuja et al., 2015).

In order to appreciate the importance of this loop, alanine point mutations of side chains involved in this multipoint interaction were made. Mutation of both Q1530 of the S1-S2 loop and Y1537 on the S2 helix have non-significant effects on potency, with EC_{50} measurements of 67nM ± 5nM and 36nM ± 8nM respectively. The limited side chain engagement in this region and lack of importance of the Q1530 and Y1537 side chains is consistent with the ability of AahII to modulate multiple Nav channel subtypes.

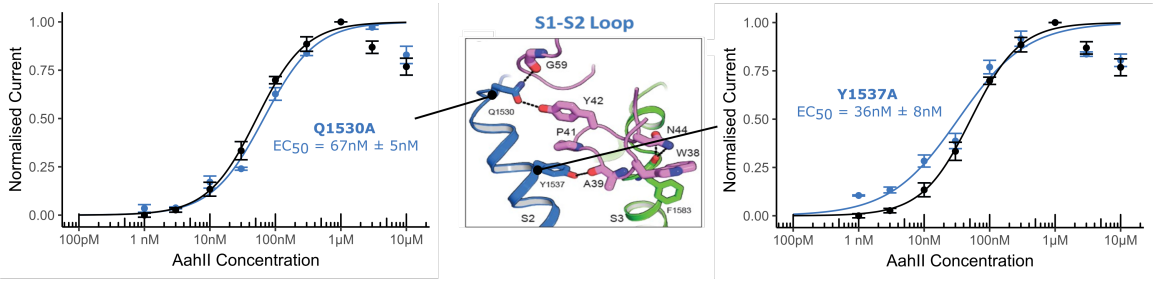


Figure 3.6: **Interactions with the S1-S2 Loop**
Center: AahII makes two interactions with side chains of the S1-S2 loop (blue), namely Q1530 and Y1537.
Left and Right: Dose-response measurements recorded by challenging Nav1.7 mutants with increasing doses of native AahII in response to a voltage step to 0 mV and holding at -100 mV. Wild type are shown in black and mutants are shown in blue. Lines represent fitted data from which the EC_{50} were estimated. Points represent mean normalised current and error bars represent the S.E.M.
Adapted from Clairfeuille et al. (2019). Reprinted with permission from AAAS

3.3.4.4 S3-S4 Loop

The S3-S4 loop forms a state-dependent interface that is engaged by the NC-domain and β2-β3 loop of AahII. D1586 coordinates T13 of AahII, while R62 and C63 of AahII form a hydrogen bonded network with E1589. The backbone carbonyl of F1583 additionally interacts with N44 of AahII.

In order to rationalise the effects of this interface, point mutants focusing on amino acids whose side chains interact with the toxin were made. Mutation of E1589A had a non-significant effect on potency with an EC_{50} of 37 nM ± 8 nM, however mutation of the D1586 to a neutral alanine significantly shifted the potency roughly 3-fold to 163 nM ± 7 nM. The potency could be further reduced by the charge reversal D1586R mutation for which we measured an EC_{50} of 226 nM ± 16 nM. Although this is less than the 62-fold reduction measured with LqhII and Nav1.5, this may be made accountable by the initial lower potency towards Nav1.7 and/ or the effects of different α- scorpion toxins. The fact that the S3-S4 loop moves upon changes in voltage, and that the toxin shows different potency

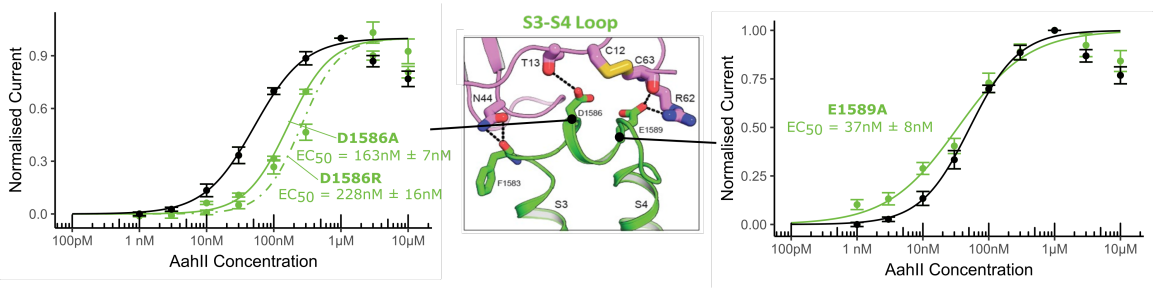


Figure 3.7: **Interactions with the S3-S4 Loop**
Center: AahII makes multiple state-dependent interactions with the S3-S4 loop (green), involving side chain interactions of D1586 and E1589.
Surrounding: Dose-response measurements recorded by challenging Nav1.7 mutants with increasing doses of native AahII in response to a voltage step to 0mV and holding at -100mV. Wild type are shown in black and mutants are shown in green. Lines represent fitted data from which the EC_{50} were estimated. Points represent mean normalised current and error bars represent the S.E.M. **Adapted from Clairfeuille et al. (2019). Reprinted with permission from AAAS**

towards the activated and deactivated states (Figure 3.4), rationalises the ability to affect potency by mutating this interface.

Mutant	Mean EC50 /nM	SEM /nM	t	Bonferroni Corrected p	Significance
WT	17	1			
R62nR	25	4	-1.85644	0.634578	ns
R62hR	48	11	-2.41013	0.28059	ns
R62Cit	**720**	**61**	**-11.43579**	**0.000162**	***
R62AgP	**51**	**6**	**-6.27155**	**0.009078**	**
R62A	**1300**	**300**	**-3.71057**	**0.045294**	**
H64A	**74**	**8**	**-6.37186**	**0.002262**	***

Table 3.4: Summary Table for Mutant AahII Toxins action on Nav1.7. Two-tailed unpaired t-tests were used to compare the mean EC50 of WT AahII with the toxin mutants and the p-value was adjusted using the Bonferroni correction. Significance is indicated by *** p <0.001 , ** 0.001 <p <0.01, * 0.01 <p <0.05, ns non significant

3.3.5 Toxin Determinants of Specificity

3.3.5.1 Summary

3.3.5.2 Recombinant AahII proves difficult to isolate

In order to test the contributions of side chains of AahII which make interactions with the toxin, a recombinant protein expression approach was adopted to generate AahII mutants. TC and JP designed a set of 11 mutants expected from the structure to make interactions with VSDIV. These constructs were cloned as His-tagged MBP fusions, expressed in Sf9 insect cells and protein was harvested from the media (detailed in Methods). The mutant proteins were purified by Immobilised Metal Affinity Chromatography (IMAC) using Ni-NTA, eluted from the resin with high imidazole and the MBP was removed by overnight cleavage with TEV protease. The following day the cleaved toxin was purified using SEC on a Superdex 200 (S200) column attached to an ÄKTA system and purity checked by SDS-PAGE (Figure 3.8A, B)

Elution from the S200 column yielded two species, the weights of which were determined by Mass Spectrometry (MS). The lighter band was the expected weight whilst the heavier band was 1185Da heavier than expected. This molecular weight is identical to that of tri-mannosyl-chitobiose (NAG(Fuc)-NAG-Man_3, Figure 3.8E), a common glycosylation adduct in insect cells. Indeed, in the natural AahII sequence, a putative insect glycosylation sequence NXT (where X is any amino acid except proline, red box, 3.8C) is present, which would not be glycosylated by the scorpion but could potentially be in our chosen expression strategy. To test this hypothesis, other α- scorpion toxins which had been previously purified as His-tagged conjugates (by TC) were TEV cleaved. Toxins containing this glycosylation sequence (e.g. AahII and LqhII) eluted from the S200 as two species, whereas those without it (e.g. Ts2) could be isolated as a single species (Figure 3.8D).

To test this glycosylation hypothesis, the eluted toxin was treated with two

different glycosylases. The higher molecular weight band was still present when treated with the amidase PNGase (which cuts the glycan between the innermost GlcNaC and the Asparagine, orange, Figure 3.8E,F) but was removed when treated with endoglycosidase Endo F3 (which cuts one sugar unit further up, between the two GlcNac residues within the diacetylchitobiose core, pink, Figure 3.8E,F.) The differential cutting is likely due to the enzyme being unable to access the first sugar site, but nonetheless confirmed that the higher molecular weight species was a glycosylated form of the desired toxin. It was not deemed feasible to isolate the unglycosylated toxin due to the very small size separation. This process would also be further complicated by the poor yield, presumably caused by this unnecessary post-translational modification by the insect cells.

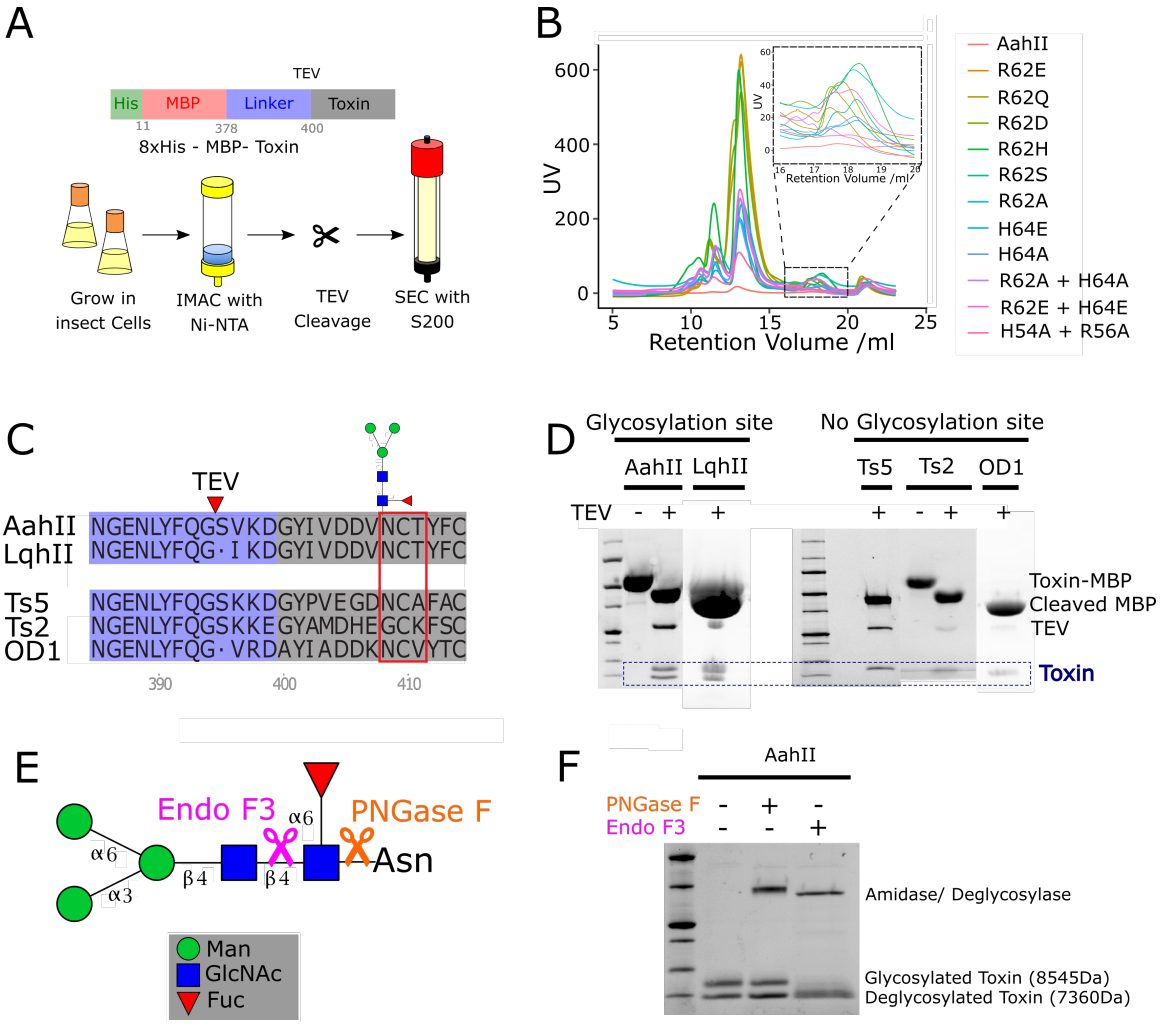


Figure 3.8: **Scorpion Toxin Biochemistry and Glycosylation**
A: Schematic of MBP linked constructs and purification strategy. The toxins were cloned with a N-terminal His_6-MBP fusion, grown up in insect cells and purified by IMAC with Ni-NTA. Toxins were isolated by SEC using an S200 column.
B: Resultant Elution profiles of toxin mutants from the S200.
C: Sequence alignments highlighting the putative NXT site (red box) for AahII and LqhII but not Ts5,Ts2 and OD1.
D: SDS-PAGE gels showing purification of toxins with and without the glycosylation sequence showing their isolation as two species or one species respectively (blue dashed box).
E: Structure of the putative glycosylation adduct and the cutting sites of PNGaseF (orange) and Endo F3 endoglycosidase (pink).
F: SDS-PAGE gel showing toxin treatment without (lane 1) or with PNGase F (lane 2) or with Endo F3 endoglycosidase (lane 3).

3.3.5.3 Recombinant OD1 proves unstable

Due to the shortcomings of isolating pure AahII mutants, a similar approach was adopted instead using the related α- scorpion toxin OD1, which had successfully been isolated previously within the department and did not contain the glycosylation sequence which had hampered our AahII efforts. OD1 shares 76% sequence similarity to AahII. A corresponding set of mutants was designed in OD1 and was purified using an identical strategy. This time, SDS-PAGE confirmed a single species and MS confirmed that the mass was as expected. Immediately after purification, the potency of the WT OD1 was tested using whole-cell patch clamp electrophysiology (green, Figure 3.8) and confirmed to be roughly equipotent to the synthetic toxin synthesised by Smartox (purple, Figure 3.8).

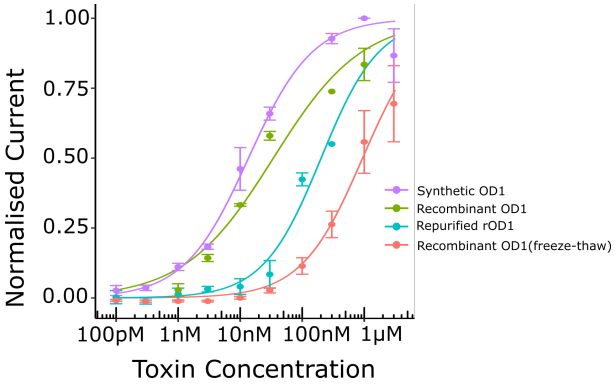


Figure 3.9: **Instability of OD1**
Dose-response measurements recorded by challenging Nav1.7 with with increasing doses of synthetic OD1 (Smartox, lilac), recombinant OD1 (green), recombinant OD1 after a single freeze thaw (blue) and after freeze-thaw and repurification using an S200 (red) in response to a voltage step to 0mV and holding at -100mV. Lines represent fitted data from which the EC_{50} were estimated. Points represent mean normalised current and error bars represent the S.E.M.

The remaining OD1 mutants were purified using an identical strategy, and a few were tested for potency. When the potency of the WT was re-tested, it appeared to be approximately 100-fold lower after a single freeze-thaw cycle (red,

Figure 3.8), despite being carefully flash frozen in liquid nitrogen. The WT protein was repurified using an S200 and the potency retested. The repurified protein was more potent than after the freeze-thaw cycle, but not back to the 'fresh' level (cyan, Figure 3.8). The instability of this toxin made us reluctant to use it to investigate the binding site.

3.3.5.4 Synthetic AahII mutants show the importance of charge in α- scorpion toxin action and explain the state-dependence

Due to the lack of success with the recombinant approach, AahII mutants were synthesied by a specialist peptide synthesis company (Smartox). The advantage of this approach, although financially steep, is that they can engineer mutants with non-natural amino acids, giving us an unlimited arsenal to probe side-chain chemistry. SDS-PAGE and MS confirmed that the AahII from both synthetic and native sources was identical (Figure 3.10). Owing to cost-restrictions, a more focused strategy was opted for and mutant toxins were designed to probe only the R62 and H6 residues. The relative importance of each of these residues as well as the effect of charge and side-chain length on potency was tested.

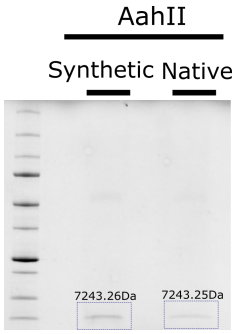


Figure 3.10: **Biochemical Identity of Synthetic and Native AahII**
SDS-PAGE gel showing biochemical identity of AahII either synthetically made by Smartox (left) or purified from native venom (right). Mass spectrometry confirmed the mass and identity of the two toxins.

In order to test the relative importance of the two residues R62 and H64 of

the CTS of AahII, the potency of the two alanine mutants was tested in a similar vein to the probing of the channel determinants of specificity. Both R62A and H64A significantly reduced potency (76-fold and 5-fold to EC_{50} values of 1.3 µM ± 0.3µM and 74 nM ± 8 nM respectively), highlighting the importance of both C-terminal residues. In order to test the importance of charge of R62, the neutrally charged Citrulline (R62Cit) was tested which again significantly shifted the potency 42-fold to an EC_{50} value 720 nM ± 61 nM showing that the positive charge on this arginine is important, potentially suggesting an electrostatic mechanism of gating charge movement inhibition (for more detailed discussion see 3.4.)

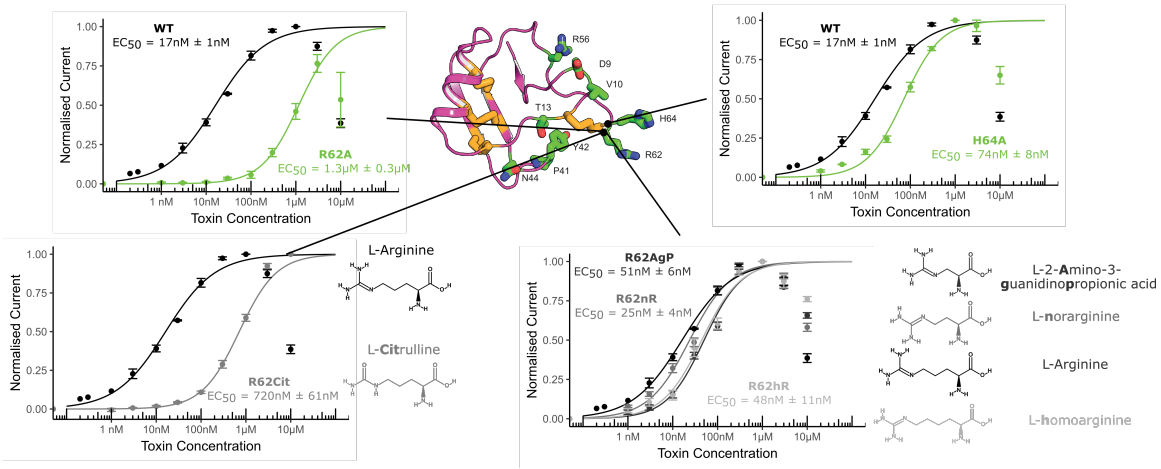


Figure 3.11: **Synthetic Toxin Mutants and their Potency on WT Nav1.7**
(Caption next page.)

Figure 3.11: (Previous page.) **Synthetic Toxin Mutants and their Potency on WT Nav1.7**
Center: AahII structure (purple) showing disulphide bonds (orange) and interacting side chains (green).
Top: Dose-response measurements recorded by challenging Nav1.7 with increasing doses of synthetic AahII alanine mutants in response to a voltage step to 0 mV and holding at -100 mV. Wild type are shown in black and mutants are shown in green. Lines represent fitted data from which the EC_{50} were estimated. Points represent mean normalised current and error bars represent the S.E.M.
Bottom: Dose-response measurements recorded by challenging Nav1.7 with increasing doses of synthetic AahII mutants with differential charge (left) or differential side-chain length (right) in response to a voltage step to 0 mV and holding at -100 mV. Wild type are shown in black and mutants are shown in shades of grey. Lines represent fitted data from which the EC_{50} were estimated. Points represent mean normalised current and error bars represent the S.E.M. **Adapted from Clairfeuille et al. (2019). Reprinted with permission from AAAS**

In addition, the importance of the side chain length of the arginine on toxin potency was tested using toxin mutants that differed in single methylene units of the side chain, but retained the positive charge. Removal of two methylene units (to form L-2-Amino guanidinopropionic acid, AgP), or one methylene unit (to form L-norarginine, nR) significantly reduced the potency 2-fold or had no effect, to EC_{50} values of 51 nM ± 6 nM and 25 nM ± 4 nM respectively, while addition of a single methylene unit (to form L-homoarginine, hR) did not significantly reduce the potency to an EC_{50} value of 48 nM ± 11 nM. Taken together, this suggests that the length of the side chain is important to allow optimal engagement of the sodium channel, and remarkably indicates that the positioning of this residue has been optimised through evolution to be better than non-natural amino acids.

3.3.6 VSDI interaction Site

Another key observation on the AahII-bound structure was that there was electron density on VSDI. The density is much more poorly defined than the corresponding VSDIV site, suggesting a lower affinity interaction, however a second AahII can be unambiguously docked into this site. Interestingly, this VSDI-AahII interface comes directly off the NavPas chassis, and so it seems that AahII has an inherent affinity for voltage sensors, and suggests a more universal interaction. AahII is a classical α-toxin so the NC-domain is in the trans configuration, unlike insect α-toxins. This interaction may have been picked up in fluorescence studies of the scorpion toxin Ts3 (Campos et al., 2008) but was attributed to allostery due to the proximity of VSDI and VSDIV. In the case of VSDI, this voltage sensor is activated unlike VSDIV which is deactivated, although it assumes a similar pose on both voltage sensors.

The high affinity blocking effect originally seen in the dose-response measure-

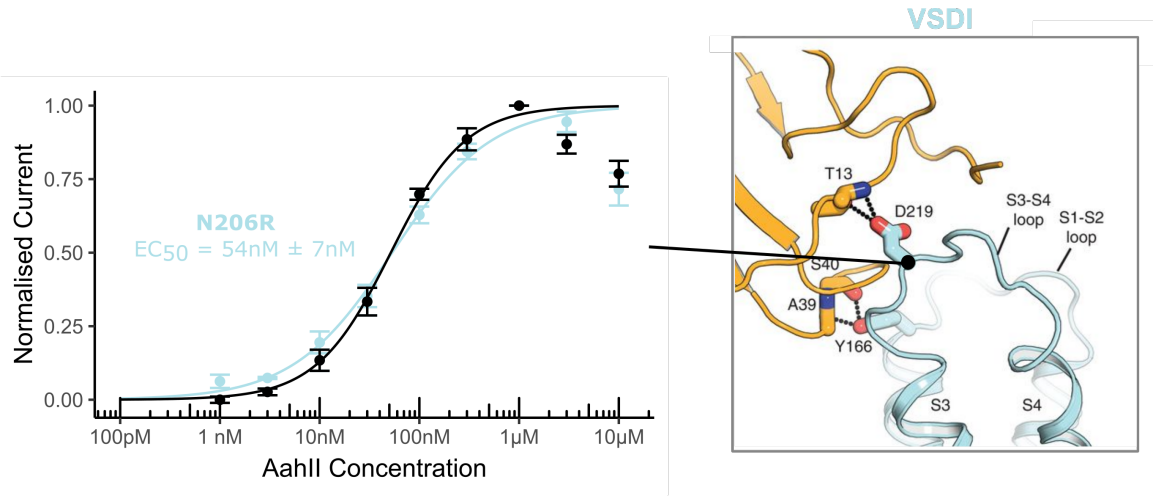


Figure 3.12: **AahII Interaction with VSDI**
Right: AahII makes a lower affinity interaction with VSDI emanating from the NavPas chassis involving D219 of the S3-S4 loop (light blue) which interacts with T13 on AahII (orange).
Left: Dose-response measurement recorded by challenging Nav1.7 N206R with increasing doses of native AahII in response to a voltage step to 0 mV and holding at -100 mV. Wild type are shown in black and Nav1.7 N206R is shown in light blue. Lines represent fitted data from which the EC_{50} were estimated. Points represent mean normalised current and error bars represent the S.E.M.
Adapted from Clairfeuille et al. (2019). Reprinted with permission from AAAS

ments of the slowing down of fast inactivation was intriguing and we wondered if this effect was mediated by the VSDI site. Another piece of data that pointed towards a putative VSDI site was the apparent state-dependence of the blocking effect (Figure 3.4), showing a preference for the up state, as seen in the structure; this would be typical of a voltage-sensor interaction. In addition, mutant toxins were also able to affect the extent of blocking, again suggesting the importance of charge and side chain length of R62, as well as the H64 (Figure 3.4). As the interaction is seen on the NavPas channel, which is non-functional, we approached some colleagues who work on the related German cockroach, *Blatella germanica* voltage-gated sodium channel (BgNav). JP and FB made a point mutant (D220R) in BgNav which abolished this high concentration blocking effect (Clairfeuille et al., 2019). The equivalent mutant was made in Nav1.7, N206R (D219 in NavPas) which, as

expected, was still able to slow down fast inactivation involving VSDIV (EC_{50} = 54 nM ± 7 nM) but also showed a similar blocking effect to wild type at 10 AahII. Application of higher doses of AahII above 10 µM was not possible as AahII becomes poorly soluble above this point.

In light of the VSDI mutant not significantly reducing the blocking effect, some kinetic measurements were attempted in order to get an estimate of affinity for the VSDI site, using the decrease in peak current upon application of 10 µM AahII as a readout. This would be performed at a number of different voltages in an attempt to further clarify the apparent voltage-dependence of the blocking effect. Whilst early data seemed promising, we soon came to the conclusion that the on and off rates were too fast to do this accurately and ultimately efforts on this front were side-lined in favour of characterising the VSDIV site more fully, and this data was instead obtained in the BgNav channel by JP and FB.

3.3.7 Mechanism of Fast Inactivation

In the AahII-VSDIV-NavPas structure, AahII has trapped VSDIV in a deactivated conformation. Comparison of this structure with the apo structure allowed testing of a potential electromechanical coupling mechanism of fast inactivation. In the AahII bound structure, the helical gating charge R5 combines with S4-S5 linker gating charges K7 and K8 to form an electrostatic bridge with conserved acidic residues on the α1 helix of the CTD (Figure 3.13). If this interaction is physiologically relevant then this interaction, here called 'Switch 1', may serve to slow down the upwards movement of VSDIV, and may explain two long-standing observations: the VSDIV contains more gating charges (Noda et al., 1984) and is intrinsically slower (Bosmans et al., 2008; Chanda and Bezanilla, 2002) than the other three domains. This interaction is likely to restrain the CTD and ultimately the

IFM motif via a second conserved electrostatic latch, here referred to as 'Switch 2'. Breaking of both of these interactions is likely necessary for the fast-inactivation particle (IFM) to bind to the pore module and terminate sodium conductance. This Switch 2 interaction will not be discussed further here, but details can be found in Clairfeuille et al. (2019).

However, two key factors should be noted; the CTD in the structure belongs to the NavPas chassis and so is likely different from the human channel. In addition, NavPas is recalcitrant to electrophysiological recordings so whether it undergoes fast-inactivation remains to be tested. It contains an ATD motif in place of the IFM motif; while BgNav has MFM and does fast-inactivate.

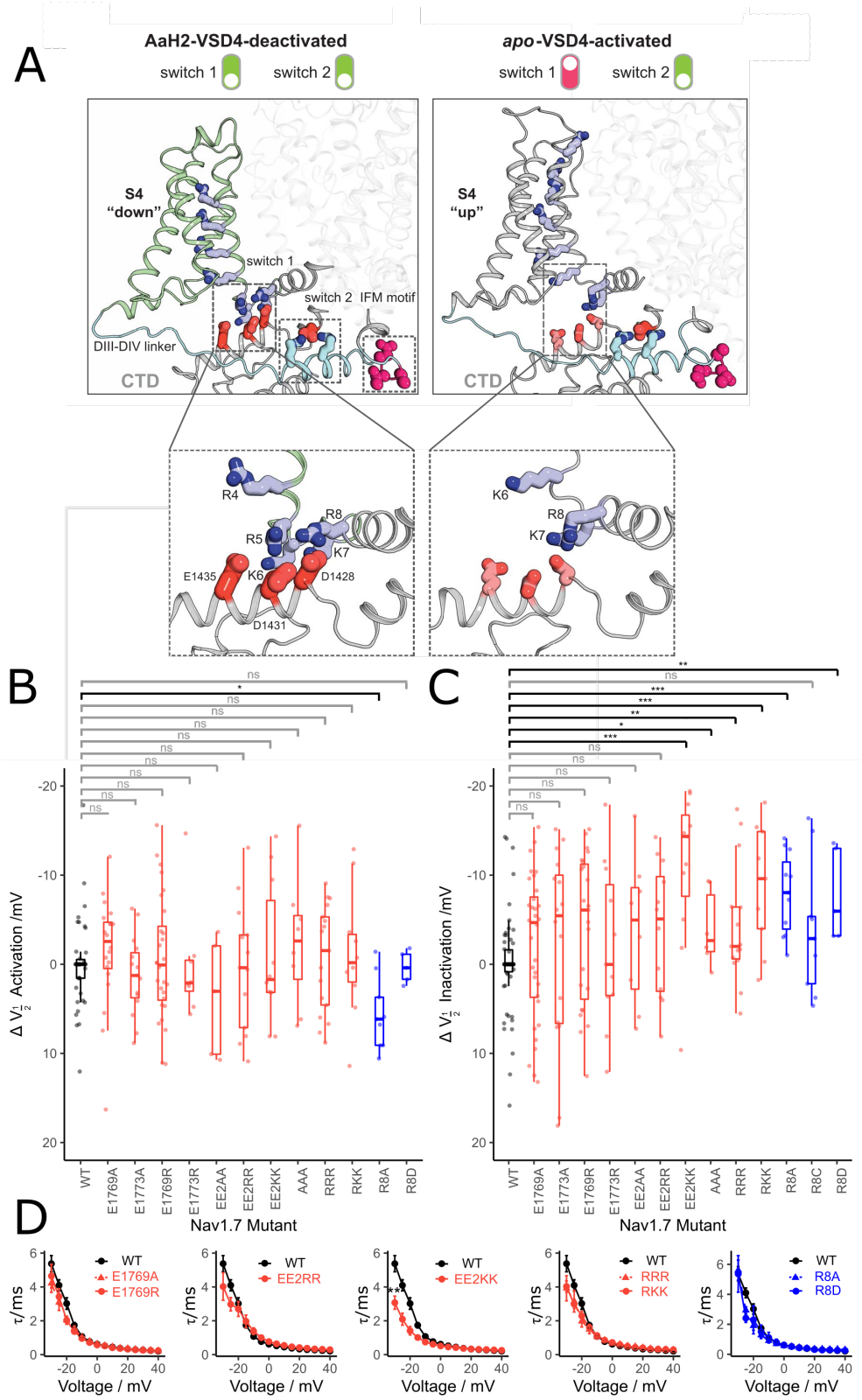


Figure 3.13: **Mutations Probing the 'Switch 1' Interface**
(Caption next page.)

Figure 3.13: (Previous page.) **Mutations Probing the 'Switch 1' Interface**
A: Structures showing the CTD interaction with the gating charges of VSDIV S4 ('Switch 1'). Positively charged residues from S4 (R5, K6, K7 and R8, blue) form ionic interactions with conserved negatively charged residues (E1435, D1431 and D1428, red) in the AahII-VSD4-deactivated state (left) which are subsequently broken in the apo-VSD4-activated state (right).
B,C: $\Delta V_{1/2}$ activation (B) or Inactivation(C) values from fitting individual activation curves for mutations made across the switch 1 interface. Data is presented as box plots representing the median, lower and upper quartiles, and all data points are shown. Each mutant was compared to wild-type and the significance was calculated using an unpaired two-tailed t-test. The p-value was corrected using the Bonferroni correction. The significance is based on the corrected p-value and is presented on horizontal bars at the top using the following key *** $p < 0.001$, ** $0.001 < p < 0.01$, * $0.01 < p < 0.05$, ns non significant. Coloured as in A
D: Time constants of inactivation (τ) as a function of test voltage recorded using the activation protocol for mutations made across the switch 1 interface. Each mutant was compared to wild-type at +30mV and the significance was calculated using a two-tailed unpaired t-test. The p-value was corrected using the Bonferoni correction and is presented above the data points using the following key *** $p < 0.001$, ** $0.001 < p < 0.01$, * $0.01 < p < 0.05$, ns non significant Coloured as in A
Adapted from Clairfeuille et al. (2019). Reprinted with permission from AAAS

In order to test the importance of Switch 1, a series of mutations in the CTD of Nav1.7 were made, focusing on the conserved acidic residues on α1 of the CTD (red, Figure 3.13) and the R8 gating charge that interacts with them (Figure 3.13). In the structure, E1435, D1431 and D1428 of NavPas correspond to E1769, E1773 and E1776 respectively of Nav1.7. The double mutants 'EE2AA' and 'EE2RR' correspond to E1769/E1773 in Nav1.7 while 'EE2KK' corresponds to E1773/E1776. The triple mutants 'AAA', 'RRR' and 'RKK' correspond to all three glutamates E1769/E1773/E1176 being mutated.

The steady-state activation and inactivation responses to voltage were measured to test the impact of this interaction. On each recording day, the $V_{1/2}$ values of both activation and inactivation of each mutant were compared to the WT to test the effect of the mutation (Figure 3.13B,C.) In our hands, mutants across this region appeared to significantly shift the voltage-dependence of inactivation to more depolarised voltages (Figure 3.13C), but have no significant effect on the voltage dependence of activation (Figure 3.13B), consistent with the role of switch 1 in affecting chanel inactivation but not activation. Additionally, the size of the shift seems to be dependent on the position and nature of the charge with lysine residues on the N-terminal end of the α1 helix of the CTD showing the greatest effect. However, relatively low n numbers and large variability in measured $V_{1/2}$ values prevented us from unambiguously highlighting the importance of individual components of this interface in Nav1.7.

Fitting the time course of inactivation for a subset of the mutations with a single exponential at each voltage (for details, see Methods) did not reveal a significant speeding up of inactivation with the exception of the EE2KK mutation (Figure 3.13D.) This interface was probed in a more targeted fashion by DI and CA on the

Nav1.5 channel in *Xenopus laevis* oocytes where they elegantly showed reversible charge-dependent shifts of $V_{1/2}$ by mutation of the Switch 1 interface (Clairfeuille et al., 2019), suggesting the importance of this interaction in the cardiac channel.

3.4 Discussion

In this study, we have used the workhorse α-scorpion toxin AahII (from *Androctonus australis hector*) to study the fast inactivation process in Nav channels. We have shown that AahII purified from native venom slows down the fast-inactivation process of both Nav1.2 and Nav1.7 showing its broad activity on different Nav channel subtypes.

In addition, we have probed the AahII interaction with Nav1.7 using structure-guided site-directed mutagenesis of residues in the toxin and the channel. The structure and the electrophysiological studies have shown the AahII interaction with VSDIV to involve multiple contacts across the S1-S2 loop, the DI-PM and the S3-S4 loop. Single point mutations within the channel mutants across this binding interface only appear to have a modest effect on toxin potency, consistent with a large binding interface. A highly conserved acidic residue (D1586) appears to make the largest contribution to toxin potency in this study, and potency can be further reduced by reversing the charge on this residue in close agreement with historical mapping studies. Importantly, our structure and electrophysiology data shows that binding of AahII to Nav1.7 involves more than just the proposed S3-S4 loop, but involves residues which are deeply encased within the channel pore.

The toxin engages mainly with two residues at its C-terminus, R62 and H64. Using synthetic toxins, we probed these two residues showing that the arginine

seems to have more effect on potency than does this histidine, but the histidine is still important. The side chain length of the arginine, which is highly conserved amongst α-scorpion toxins is important, as is the charge, and intriguingly the toxin appears to have optimised this residue for potency, even against side chains which do not naturally occur. Taken together, it rationalises the early chemical modification data suggesting that the overall βαββfold is important to perfectly place the arginine in a position to sterically prevent upward movement of S4. It is also interesting to think of the arginine acting as a gating charge mimetic, electrostatically influencing the electric field experienced by the gating charges, and explaining the state-dependence of the interaction. This type of mechanism is analogous to the proposed roles of β-subunits which are thought to influence voltage-sensor biophysics but instead through placing conserved negatively-charged sialic acid moieties emanating from their Ig domain to influence voltage-sensor function (Johnson et al., 2004; Namadurai et al., 2015).

The interaction captured here is important to the survival of the scorpion, whether it be protecting it against mammalian or insect predators or helping it to catch its prey in deserts where food and resources are scarce. From an evolutionary perspective, α-scorpion toxins are likely to have co-evolved with the channels they target. Given that their function is to bind to a plethora of different Nav channels, a multipoint interaction is favourable so that: 1) it is difficult for the channel to develop insensitivity to it and 2) it is able to target many channel subtypes offering broad protection. The result that no mutation made in this study abolishes efficacy is consistent with this hypothesis. Interestingly, D1586, the residue we found to have the most profound effect on toxin potency has been flagged as important for binding of many other α-scorpion toxins to different Nav channels (Rogers et al., 1996).

A large majority of the studies have focused on assessing the importance of the S3-S4 loop in toxin potency. Simply swapping this loop between different channels however, does not confer the potency of the donor channel, suggesting the involvement of other parts of the channel; potentially a glycan, DI-PM and S1-S2 loop. If this glycan is indeed important, which is not clear from the data presented here, this is the first instance of a toxin utilising a glycan in binding. The literature suggests that α- scorpion toxins generally show higher potency for subtypes with this glycan, showing lower potency against Nav1.7, Nav1.8 and Nav1.9, two of which (Nav1.7 and Nav1.9) have a glycan at this position but sadly our experiments to determine the importance of the glycan were without conclusion.

3.4.1 In Light of the Nav1.5-LqhIII structure

Since the publication of our NavPas-Nav1.7 chimera, structural advances have allowed the elucidation of the structure of the full length rat cardiac sodium channel Nav1.5 in the absence (PDB: 6UZ0, Jiang et al. (2020)) and presence of the Deathstalker Scorpion Toxin LqhIII (PDB: 7K18, Jiang et al. (2021)). Comparison of these two structures have obvious advantages compared to inferring structural details from a chimeric structure.

LqhIII showed high potency on the Nav1.5 channel (EC_{50} = 11.4 nM) where it anchors on top of VSDIV wedged between the S1-S2 and S3-S4 linkers, trapping the gating charges in a unique intermediate-activated state (Jiang et al., 2021). The interaction with the channel is overwhelmingly similar which is unsurprising given that this was the region of the channel which was humanised in our chimera.

3.4.1.1 Interactions with Neurotoxin Receptor Site 3

In our AahII-NavPas-hNav1.7 structure, AahII makes a multipoint interaction with a PM-glycan, DI-PM and S1-S2 loop as well as the state dependent S3-S4 loop. This interaction was very similar to the LqhIII-rNav1.5 structure showing a RMSD of 1.41 Åover 112 residues (Jiang et al., 2021). LqhIII engages primarily with K64 (analogous to R62 in AahII) and D1612 of the S3-S4 loop (equivalent to D1586 in Nav1.7) makes an interaction with the toxin. However these interactions were not probed experimentally in their study. One notable difference is that LqhIII is rotated 26° downwards pushing it further from the DI-glycan which is much smaller in rNav1.5 than in NavPas. As to whether this rotated binding pose is an artefact of the NavPas chimera or a unique feature of the placement and structure of the cardiac channel's glycan remains to be seen. Further structures of other Nav channel subtypes and scorpion toxins, paired with detailed biochemical experiments targeting the chemical nature of the glycan will be needed to unambiguously resolve these differences.

3.4.1.2 VSDI Interaction Site

In our AahII-NavPas-hNav1.7 structure, AahII bound in two positions; one in VSDI of the NavPas chassis and one on DIV contributed in part by Nav1.7. As NavPas is recalcitrant to electrophysiological recordings, it was impossible to test the functionality of the sites in the chimera. However, we did study them in the hNav1.7 channel and the German Cockroach BgNav channel which is closely related to the American Cockroach NavPas. We still saw the high affinity blocking effect in a mutant (N206R) which disrupted AahII binding to the BgNav channel, but were unable to ever conclusively show that the blocking effect we saw in Nav1.7 was due to binding at VSDI. fluorometry experiments on Nav1.5 with Ts3 during original mapping studies may have picked up a potential interaction with

VSDI which at the time was attributed to allostery owing to the domain swapped orientation (Campos et al., 2008).

By contrast LqhIII density was only found on LqhIII-rNav1.5 complex at a single binding site which was generally similar to our AahII binding site on VSDIV. As to whether the second binding site on our structure is physiologically relevant remains to be seen, however, the ability of AahII to bind to the NavPas VSDI in the down state suggests that AahII has an intrinsic affinity for voltage sensors which may or may not be a general feature of scorpion toxins, as LqhIII-rNav1.5 is the only other α- scorpion toxin-Nav channel complex currently available.

3.4.1.3 Mechanism of Fast Inactivation

In our AahII-NavPas-hNav1.7 structure, lower gating charges were stabilised by interaction with acidic residues emanating from the α1 helix of the CTD. By contrast the CTD in the LqhIII-rNav1.5 structure was disordered and not observed, as is the case in the Nav1.2 (Pan et al., 2019), Nav1.4 (Pan et al., 2018), Nav1.5 (Jiang et al., 2020) and Nav1.7 (Shen et al., 2019). As well as suggesting a large amount of disorder/mobility in this region, it also likely suggests a structural difference in the CTD of the cockroach and native mammalian channels.

However, given our electrophysiology was carried out in human Nav1.5 and hNav1.7 channels, and mutations in the 'Switch 1' and 'Switch 2' interface can affect fast inactivation, it suggests that this interaction is physiologically relevant, even if it is transient and/or secondary, consistent with the fairly modest effects of harsh triple mutations near the gating charges. Indeed, in most Nav subtypes, and particularly the well studied Nav1.5, this region is a disease mutation hotspot, which may be due to this interface or more generally the mobility of this region.

Bibliography

Abbas, N., Gaudioso-Tyzra, C., Bonnet, C., Gabriac, M., Amsalem, M., Lonigro, A., Padilla, F., Crest, M., Martin-Eauclaire, M.-F., and Delmas, P. (2013). The scorpion toxin amm viii induces pain hypersensitivity through gain-of-function of ttx-sensitive na+ channels. *PAIN®*, 154(8):1204–1215. 198

Ahern, C. A., Payandeh, J., Bosmans, F., and Chanda, B. (2016). The hitchhiker's guide to the voltage-gated sodium channel galaxy. *J Gen Physiol*, 147(1):1–24. 177, 179, 180

Ahuja, S., Mukund, S., Deng, L., Khakh, K., Chang, E., Ho, H., Shriver, S., Young, C., Lin, S., Johnson, J., Wu, P., Li, J., Coons, M., Tam, C., Brillantes, B., Sampang, H., Mortara, K., Bowman, K. K., Clark, K. R., Estevez, A., Xie, Z., Verschoof, H., Grimwood, M., Dehnhardt, C., Andrez, J.-C., Focken, T., Sutherlin, D. P., Safina, B. S., Starovasnik, M. A., Ortwine, D. F., Franke, Y., Cohen, C. J., Hackos, D. H., Koth, C. M., and Payandeh, J. (2015). Structural basis of nav1.7 inhibition by an isoform-selective small-molecule antagonist. *Science*, 350:aac5464. 190, 200

Benkhadir, K., Kharrat, R., Cestèle, S., Mosbah, A., Rochat, H., El Ayeb, M., and Karoui, H. (2004). Molecular cloning and functional expression of the alpha-scorpion toxin BotIII: pivotal role of the c-terminal region for its interaction with voltage-dependent sodium channels. *Peptides*, 25(2):151–61. 187, 188

Bennett, D. L., Clark, A. J., Huang, J., Waxman, S. G., and Dib-Hajj, S. D. (2019). The role of voltage-gated sodium channels in pain signaling. *Physiol Rev*, 99(2):1079–1151. 192

Bosmans, F., Martin-Eauclaire, M.-F., and Swartz, K. J. (2008). Deconstructing voltage sensor function and pharmacology in sodium channels. *Nature*, 456(7219):202–208. 213

Bosmans, F. and Tytgat, J. (2007). Voltage-gated sodium channel modulation by scorpion α-toxins. *Toxicon*, 49(2):142–158. 184, 185, 198

Campos, F. V., Chanda, B., Beirão, P. S., and Bezanilla, F. (2008). Alpha-scorpion toxin impairs a conformational change that leads to fast inactivation of muscle sodium channels. *J Gen Physiol*, 132(2):251–63. 211, 222

Cardoso, F. C. and Lewis, R. J. (2018). Sodium channels and pain: from toxins to therapies. *Br J Pharmacol*, 175(12):2138–2157. 181, 182

Catterall, W. and Beress, L. (1978). Sea anemone toxin and scorpion toxin share a common receptor site associated with the action potential sodium ionophore. *J Biol Chem*, 253(20):7393–6. 188

Cestèle, S. and Catterall, W. A. (2000). Molecular mechanisms of neurotoxin action on voltage-gated sodium channels. *Biochimie*, 82(9-10):883–892. 185

Cestele, S., Khalifa, R., Pelhate, M., Rochat, H., and Gordon, D. (1996). Alpha scorpion toxins binding on rat brain and insect sodium channels reveal divergent allosteric modulations by brevetoxin and veratridine. *Toxicon*, 3(34):303–304. 185

Chanda, B. and Bezanilla, F. (2002). Tracking voltage-dependent conformational changes in skeletal muscle sodium channel during activation. *The Journal of general physiology*, 120(5):629–645. 213

Chen, H., Gordon, D., and Heinemann, S. (2000). Modulation of cloned skeletal

muscle sodium channels by the scorpion toxins lqhii, lqh iii, and lqhalphait. *Pflugers Arch*, 439(4):423–32. 189

Chen, H., Lu, S., Leipold, E., Gordon, D., Hansel, A., and Heinemann, S. H. (2002). Differential sensitivity of sodium channels from the central and peripheral nervous system to the scorpion toxins lqh-2 and lqh-3. *European Journal of Neuroscience*, 16(4):767–770. 185

Chen, J., Tan, Z.-Y., Zhao, R., Feng, X.-H., Shi, J., and Ji, Y.-H. (2005). The modulation effects of bmk i, an α-like scorpion neurotoxin, on voltage-gated na+ currents in rat dorsal root ganglion neurons. *Neuroscience letters*, 390(2):66–71. 185

Clairfeuille, T., Cloake, A., Infield, D. T., Llongueras, J. P., Arthur, C. P., Li, Z. R., Jian, Y., Martin-Eauclaire, M.-F. F., Bougis, P. E., Ciferri, C., Ahern, C. A., Bosmans, F., Hackos, D. H., Rohou, A., and Payandeh, J. (2019). Structural basis of α-scorpion toxin action on nav channels. *Science*, 363(6433). 175, 183, 190, 192, 195, 199, 201, 202, 210, 212, 214, 216, 218

Cohen, L., Lipstein, N., Gordon, D., Cohen, L., Lipstein, N., and Gordon, D. (2006). Allosteric interactions between scorpion toxin receptor sites on voltage-gated na channels imply a novel role for weakly active components in arthropod venom. *The FASEB journal*, 20(11):1933–1935. 185

Couraud, F., Rochat, H., and Lissitzky, S. (1978). Binding of scorpion and sea anemone neurotoxins to a common site related to the action potential na+ ionophore in neuroblastoma cells. *Biochem Biophys Res Commun*, 83(4):1525–30. 188

El Ayeb, M., Bahraoui, E. M., Granier, C., and Rochat, H. (1986). Use of antibodies

specific to defined regions of scorpion. alpha.-toxin to study its interaction with its receptor site on the sodium channel. *Biochemistry*, 25(21):6671–6678. 187

Erickson, A., Deiteren, A., Harrington, A. M., Garcia-Caraballo, S., Castro, J., Caldwell, A., Grundy, L., and Brierley, S. M. (2018). Voltage-gated sodium channels: Navigating the field to determine their contribution to visceral nociception. *J Physiol*, 596(5):785–807. 177, 178

Gilles, N., Gurevitz, M., and Gordon, D. (2003). Allosteric interactions among pyrethroid, brevetoxin, and scorpion toxin receptors on insect sodium channels raise an alternative approach for insect control. *FEBS letters*, 540(1-3):81–85. 185

Gordon, D. (1997). A new approach to insect-pest control—combination of neurotoxins interacting with voltage sensitive sodium channels to increase selectivity and specificity. *Invertebrate Neuroscience*, 3(2-3):103–116. 184, 185

Gordon, D. and Zlotkin, E. (1993). Binding of an α scorpion toxin to insect sodium channels is not dependent on membrane potential. *FEBS letters*, 315(2):125–128. 185

Guan, R.-J. J., Xiang, Y., He, X.-L. L., Wang, Chun-Guang, G., Wang, M., Zhang, Y., Sundberg, E. J., and Wang, Da-Cheng, C. (2004). Structural mechanism governing cis and trans isomeric states and an intramolecular switch for cis/trans isomerization of a non-proline peptide bond observed in crystal structures of scorpion toxins. *J Mol Biol*, 341(5):1189–204. 188

Habersetzer-Rochat, C. and Sampieri, F. (1976). Structure-function relations of scorpion neurotoxins. *Biochemistry*, 15(11):2254–2261. 187

He, X., Deng, J., Wang, M., Zhang, Y., and Wang, D. (2000). Structure of a new

neurotoxin from the scorpion buthus martensii karsch at 1.76 å. *Acta Crystallogr D Biol Crystallogr*, 56(Pt 1):25–33. 187

He, X., Li, H., Zeng, Z., Liu, X., Wang, M., and Wang, D. (1999). Crystal structures of two alpha-like scorpion toxins: non-proline cis peptide bonds and implications for new binding site selectivity on the sodium channel. *J Mol Biol*, 292(1):125–35. 187

Herzig, V., Sunagar, K., Wilson, D. T. R. T., Pineda, S. S., Israel, M. R., Dutertre, S., McFarland, B. S., Undheim, E. A. B. A., Hodgson, W. C., Alewood, P. F., Lewis, R. J., Bosmans, F., Vetter, I., King, G. F., and Fry, B. G. (2020). Australian funnel-web spiders evolved human-lethal δ-hexatoxins for defense against vertebrate predators. *Proc Natl Acad Sci U S A*, 117(40):24920–24928. 181

Housset, D., Habersetzer-Rochat, C., Astier, J.-P., and Fontecilla-Camps, J. C. (1994). Crystal structure of toxin ii from the scorpion androctonus australis hector refined at 1· 3 å resolution. *Journal of molecular biology*, 238(1):88–103. 185, 187

Jablonsky, M., Watt, D., and Krishna, N. (1995). Solution structure of an old world-like neurotoxin from the venom of the new world scorpion centruroides sculpturatus ewing. *J Mol Biol*, 248(2):449–58. 187

Jiang, D., Shi, H., Tonggu, L., El-Din, T. M., Lenaeus, M. J., Zhao, Y., Yoshioka, C., Zheng, N., and Catterall, W. A. (2020). Structure of the cardiac sodium channel. *Cell*, pages 122–134.e10. 183, 220, 222

Jiang, D., Tonggu, L., El-Din, T. M. G., Banh, R., Pomès, R., Zheng, N., and Catterall, W. A. (2021). Structural basis for voltage-sensor trapping of the cardiac sodium channel by a deathstalker scorpion toxin. *Nature Communications*, 12(1):1–13. 183, 220, 221

Johnson, D., Montpetit, M. L., Stocker, P. J., and Bennett, E. S. (2004). The sialic acid component of the β1 subunit modulates voltage-gated sodium channel function. *Journal of Biological Chemistry*, 279(43):44303–44310. 219

Karbat, I., Frolow, F., Froy, O., Gilles, N., Cohen, L., Turkov, M., Gordon, D., and Gurevitz, M. (2004). Molecular basis of the high insecticidal potency of scorpion alpha-toxins. *J Biol Chem*, 279(30):31679–86. 188

Kharrat, R., Darbon, H., Granier, C., and Rochat, H. (1990). Structure-activity relationships of scorpion alpha-neurotoxins: contribution of arginine residues. *Toxicon*, 28(5):509–23. 187

Kharrat, R., Darbon, H., Rochat, H., and Granier, C. (1989). Structure/activity relationships of scorpion alpha-toxins. multiple residues contribute to the interaction with receptors. *Eur J Biochem*, 181(2):381–90. 187

Kopeyan, C., Martinez, G., Lissitzky, S., Miranda, F., and Rochat, H. (1974). Disulfide bonds of toxin ii of the scorpion androctonus australis hector. *Eur J Biochem*, 47(3):483–9. 185

Landon, C., Sodano, P., Cornet, B., Bonmatin, J., Kopeyan, C., Rochat, H., Vovelle, F., and Ptak, M. (1997). Refined solution structure of the anti-mammal and anti-insect lqqiii scorpion toxin: comparison with other scorpion toxins. *Proteins*, 28(3):360–74. 187

Legros, C., Céard, B., Vacher, H., Marchot, P., Bougis, P. E., and Martin-Eauclaire, Marie-France, F. (2005). Expression of the standard scorpion alpha-toxin aahii and aahii mutants leading to the identification of some key bioactive elements. *Biochim Biophys Acta*, 1723(1-3):91–9. 188

Leipold, E., Hansel, A., Olivera, B. M., Terlau, H., and Heinemann, S. H. (2005).

Molecular interaction of delta-conotoxins with voltage-gated sodium channels. *FEBS Letters*, 579(18):3881–4. 189

Leipold, E., Liebmann, L., Korenke, G. C., Heinrich, T., Gießelmann, S., Baets, J., Ebbinghaus, M., Goral, R. O., Stödberg, T., Hennings, J. C., et al. (2013). A de novo gain-of-function mutation in scn11a causes loss of pain perception. *Nature genetics*, 45(11):1399–1404. 178

Leipold, E., Lu, S., Gordon, D., Hansel, A., and Heinemann, S. H. (2004). Combinatorial interaction of scorpion toxins lqh-2, lqh-3, and lqhalphait with sodium channel receptor sites-3. *Mol Pharmacol*, 65(3):685–91. 189

Li, H., Wang, D., Zeng, Z., Jin, L., and Hu, R. (1996). Crystal structure of an acidic neurotoxin from scorpion buthus martensii karsch at 1.85 a resolution. *J Mol Biol*, 261(3):415–31. 187

Namadurai, S., Yereddi, N. R., Cusdin, F. S., Huang, C. L.-H., Chirgadze, D. Y., and Jackson, A. P. (2015). A new look at sodium channel β subunits. *Open biology*, 5(1):140192. 179, 219

Noda, M., Shimizu, S., Tanabe, T., Takai, T., Kayano, T., Ikeda, T., Takahashi, H., Nakayama, H., Kanaoka, Y., and Minamino, N. (1984). Primary structure of electrophorus electricus sodium channel deduced from cdna sequence. *Nature*, 312(5990):121–7. 213

Pan, X., Li, Z., Huang, X., Huang, G., Gao, S., Shen, H., Liu, L., Lei, J., and Yan, N. (2019). Molecular basis for pore blockade of human na+ channel nav1.2 by the μ-conotoxin kiiia. *Science*, 363(6433):1309–1313. 183, 222

Pan, X., Li, Z., Zhou, Q., Shen, H., Wu, K., Huang, X., Chen, J., Zhang, J., Zhu, X., Lei, J., Xiong, W., Gong, H., Xiao, B., and Yan, N. (2018). Structure of

the human voltage-gated sodium channel nav1.4 in complex with β1. *Science*, 362(6412):eaau2486. 222

Rochat, H., Rochat, C., Sampieri, F., Miranda, F., and Lissitzky, S. (1972). The amino-acid sequence of neurotoxin ii of androctonus australis hector. *Eur J Biochem*, 28(3):381–8. 185

Rogers, J., Qu, Y., Tanada, T., Scheuer, T., and Catterall, W. (1996). Molecular determinants of high affinity binding of alpha-scorpion toxin and sea anemone toxin in the s3-s4 extracellular loop in domain iv of the na+ channel alpha subunit. *J Biol Chem*, 271(27):15950–62. 189, 219

Sharkey, R. G., Jover, E., Couraud, F., Baden, D. G., and Catterall, W. A. (1987). Allosteric modulation of neurotoxin binding to voltage-sensitive sodium channels by ptychodiscus brevis toxin 2. *Molecular pharmacology*, 31(3):273–278. 185

Sheets, M. F., Kyle, J. W., Kallen, R. G., and Hanck, D. A. (1999). The na channel voltage sensor associated with inactivation is localized to the external charged residues of domain iv, s4. *Biophysical Journal*, 77(2):747–757. 185

Shen, H., Li, Z., Jiang, Y., Pan, X., Wu, J., Cristofori-Armstrong, B., Smith, J. J., Chin, Y. K., Lei, J., Zhou, Q., King, G. F., and Yan, N. (2018). Structural basis for the modulation of voltage-gated sodium channels by animal toxins. *Science*, 362(6412). 182

Shen, H., Liu, D., Wu, K., Lei, J., and Yan, N. (2019). Structures of human nav1.7 channel in complex with auxiliary subunits and animal toxins. *Science*, 363(6433):1303–1308. 183, 222

Silver, K., Dong, K., and S Zhorov, B. (2017). Molecular mechanism of action and selectivity of sodium ch annel blocker insecticides. *Current medicinal chemistry*, 24(27):2912–2924. 184

Strichartz, G. R. and Wang, G. (1986). Rapid voltage-dependent dissociation of scorpion alpha-toxins coupled to na channel inactivation in amphibian myelinated nerves. *The Journal of general physiology*, 88(3):413–435. 185

Thomsen, W. and Catterall, W. (1989). Localization of the receptor site for alpha-scorpion toxins by antibody mapping: implications for sodium channel topology. *Proc Natl Acad Sci U S A*, 86(24):10161–5. 189

Tugarinov, V., Kustanovich, I., Zilberberg, N., Gurevitz, M., and Anglister, J. (1997). Solution structures of a highly insecticidal recombinant scorpion alpha-toxin and a mutant with increased activity. *Biochemistry*, 36(9):2414–24. 187

Xu, H., Li, T., Rohou, A., Arthur, C. P., Tzakoniati, F., Wong, E., Estevez, A., Kugel, C., Franke, Y., Chen, J., Ciferri, C., Hackos, D. H., Koth, C. M., and Payandeh, J. (2019). Structural basis of nav1.7 inhibition by a gating-modifier spider toxin. *Cell*, 176(5):1238–1239. 183

Zilberberg, N., Froy, O., Loret, E., Cestele, S., Arad, D., Gordon, D., and Gurevitz, M. (1997). Identification of structural elements of a scorpion α-neurotoxin important for receptor site recognition. *Journal of Biological Chemistry*, 272(23):14810–14816. 187

Zilberberg, N., Gordon, D., Pelhate, M., Adams, M., Norris, T., Zlotkin, E., and Gurevitz, M. (1996). Functional expression and genetic alteration of an alpha scorpion neurotoxin. *Biochemistry*, 35(31):10215–22. 187

Chapter 4

VHH Antibody Action on K2P Channels

4.1 Disclaimer

In this chapter, the peak shift assay for assessing biochemical stability of VHH antibody-TREK-2 complexes was conducted by Karin Rödstrom.
Structures of VHH67-TREK-2 and VHH58-TREK-2 were crystallised and solved by Agenese Baronina, Karin Rödstrom, Ashley Pike and Elisabeth Carpenter. All other work is my own.

In the previous chapter we saw that α-scorpion toxins are capable of modulating Nav channels, and by using these toxins we were able to better understand structure-function relationships in Nav channels. In a similar vein, we sought to use a similar approach for K2P channels, although there are no known natural toxins that modulate K2P channels. We therefore raised a panel of VHH antibodies against two members of the K2P family; namely TREK-1 and TREK-2, and wanted to see if any of them were capable of modulating channel activity. We wished to

see if they could potentially be used as therapeutics as well as using them to better understand structure-function relationships in the K2P family, whose polymodal gating makes them structurally very interesting targets. In this chapter we show that some VHH antibodies are capable of modulating TREK-2, and they do so in a dose-dependent manner. We also attempt to elucidate their mechanism of action making use of known gating mutants and natural gating stimuli.

4.2 Introduction

4.2.1 Antibody Structure and Derivatives

Conventional antibodies assemble as tetramers, formed by the association of 2 Heavy (H) chains and 2 Light (L) chains . The two heavy chains are chemically linked to one another via two disulphide bonds, while one Light chain associates with each heavy chain via a dispulphide bond (Edelman, 1959) to form a characteristic Y-shaped molecule of 150kDa. Digestion with papain revealed two distinct products, which were called Fab (Fragment antigen binding) and Fc (Fragment crystallisable) based on their crude biochemical properties Figure 4.1; the Fab fragment is responsible for binding to an antigen (antibody generator) (Porter, 1959) and has incredible diversity, discussed later, while the Fc fragment crystallised and is much more highly conserved, although there are many isotypes with different effector functions. Alternative digestion with pepsin left a much larger fragment which still was capable of binding antigen and was hence called $(Fab')_2$, which could be further reduced with β-mercaptoethanol to form two identical fragments each retaining their antigen binding capabilities (Fab') Figure 4.1 (Nisonoff et al., 1960). Early work elucidating antibody structure by Rodney Porter and Gerald Edelman saw them awarded the Nobel Prize in 1972.

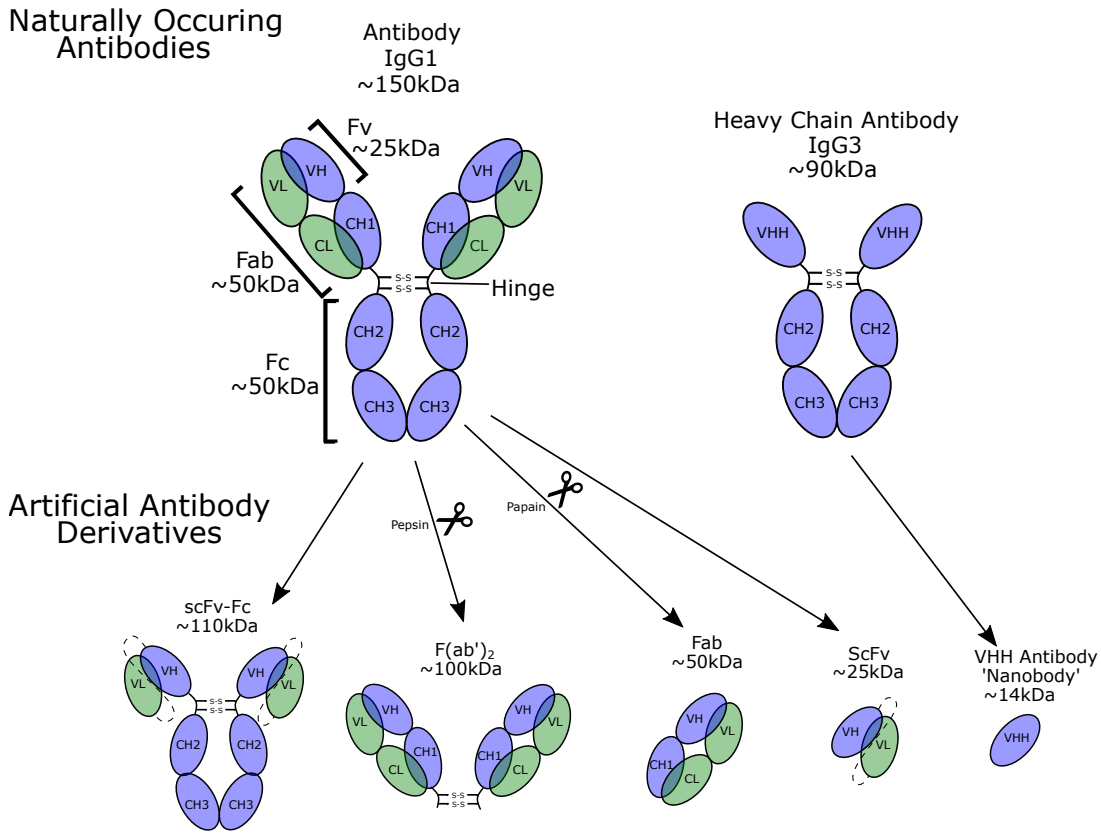


Figure 4.1: **Antibodies and Common Derivatives**
Left: Conventional Antibodies (e.g. IgG1) are 150 kDa tetrameric assemblies of two disulphide linked light chains (green) two heavy chains (blue). Functionally the antibody may be divided into constant domains and variable domains. Many derivatives are commonly used, but necessitates the need for contributions of both the heavy and light chain to bind antigen. The smallest fragment capable of this is the 25 kDa ScFc where the heavy and light variable domains are synthetically linked (dashed lines) to form a single chain.
Right: Heavy chain Antibodies (e.g. IgG3) are 90 kDa dimeric assemblies formed naturally by the deletion of the CH1 domain where association with the light chain usually occurs. As a result of this unique arrangement, only the heavy chain is required to bind antigen. The smallest fragment capable of this is the 14 kDa VHHantibody (trademarked nanobody^{TM} by Ablynx.)

The heavy chain (blue, Figure 4.1) typically consists of 4 distinct domains, one of which is variable and 3 of which are highly conserved hence named Variable region of Heavy chain (V_H) and Constant region of Heavy chain 1-3 (C_H1-3). The connection between C_H1 and C_H2 contains the conserved cysteines required for the association of the two heavy chains and is inherently flexible and thus called the hinge. In an analogous fashion, each light chain (green, Figure 4.1) has a single constant domain and a single variable domain (C_L and V_L respectively). The part of the antibody that actually engages the antigen is formed by the variable regions of both the Heavy and light chains (V_H and V_L respectively) and is known as the Fv (Fragment variable, Figure 4.1). Within each of these variable regions, there are 3 hypervariable loops named CDR1-3 (Complementarity Determining Region) because they are what give the antibody specificity towards its antigen. Ultimately, it is these 6 loops which are responsible for binding to the antigen, and as discussed previously, a huge protein scaffold is used to ensure these residues are placed optimally to bind to their antigen (Janeway Jr et al., 2001).

Since the functional role of an antibody is to bind to antigens, there is an inherent desire to form the smallest possible derivative which retains this function. From conventional antibodies, the smallest entity capable of binding to antigens is termed a ScFv, and is a synthetically linked V_H and V_L domain of 25 kDa (Figure 4.1, Glockshuber et al. (1990)). The discovery of Heavy Chain Antibodies (HCAbs) in the sera of camelids (Hamers-Casterman et al., 1993) and nurse sharks (Greenberg et al., 1995) however allowed further refinement in terms of size, and are the result of distinct genetic events.

HCAbs are formed naturally in camelids as a result of an independent gene deletion event by the deletion of the first constant domain (C_H1) of the heavy

chain where interaction with the L chain usually occurs. As such they are much smaller than conventional antibodies (90 kDa vs 150 kDa) and only have one variable domain (named VHH after Variable region of the heavy chain of heavy chain only antibodies) involved in antigen binding rather than the usual contribution of the heavy and light chains to the antigen binding region (Figure 4.1). VHH antibodies were protected by a series of patents in 2001 belonging to Vlaams Interuniversitair Instituut voor Biotechnologie (VIB), with their 2002 spin-out company Ablynx trademarking the term 'nanobody', although the terms are synonymous. Due to this unique arrangement, the VHH domain can be removed as a functional monomeric binder as it has the conventional CDR1-3 loops. For a review see Muyldermans (2013).

Meanwhile, HCAbs found in many cartilaginous fishes, known more commonly as the immunoglobulin new antigen receptor (IgNAR) are not the result of a gene deletion but instead the result of a uniquely long CDR3 loop which covers the light chain association site, thus preventing association. In an analogous fashion, the antigen binding region therefore consists of a monomeric binder containing only 2 loops (Feige et al., 2014) and are typically named VNAR antibodies as opposed to camelid VHH antibodies. IgNAR family proteins will not be discussed further but are reviewed in Zielonka et al. (2015).

Very recently, a new antibody derivative smaller than the VHH antibodies has been developed. Knob domain antibodies (known as knob-bodies) from bovine antibodies which contain ultralong CDR loops (Berens et al., 1997) have been developed to harness the unique binding capability of the ultralong CDR3 loop to bind targets. The resulting 4.2 kDa knob-body is the smallest known autonomous entity by binding antigen outside the confines of the antibody scaffold (Macpher-

son et al., 2020).

4.2.2 Introduction to the Adaptive Immune Response

In order to understand how antibodies are raised and what they do, it is important to review their role in the context of the immune response. A number of reviews and textbooks are available for this task, but here I will summarise the pertinent details; what they are for, how they come into contact with their antigen, how they develop affinity for their target, how such a staggering diversity of antibodies can be created and how the incredible low probability of an antibody coming into contact with what it binds. For full details, I would recommend Janeway Jr et al. (2001), which deals with everything summarised here, but in more detail.

Antibodies are one of the biochemical weapons of the adaptive immune system and are secreted by B-cells to neutralise potential threats, opsonise invading micro-organisms and activate the classical complement pathway. Through these three processes and binding to their cognate antigen, they render an organism or toxin inert by preventing receptor binding, interact with Fc receptors on phagocytic cells, enhancing their clearance by other players in the immune response and bind to the pathogen surface and trigger the complement cascade, ultimately culminating in the lysis of the organism via disruption of the ionic gradients across their membranes.

In order to understand what antibodies are raised against, it is first important to discuss how the B-cell first comes into contact with the antigen. Foreign bodies which are picked up exogenously, that is topologically outside of cells, must first be endocytosed or phagocytosed into the specialised cells of the immune system, known collectively as Antigen-Presenting Cells (APC's), comprising of Dendritic

Cells (DCs), macrophages (Mφ) as well as B-cells themselves. The endocytosed antigen accumulates in the early endosome which undergo a progressive process of maturation, forming late endosomes and ultimately lysosomes, during which the acidity increases and proteins are denatured and enzymatically degraded. It is here that peptides of 13-17 amino acids are loaded onto Major Histocompatibility Complex (MHC) Class II proteins whose biosynthetic pathway intersects the endocytic pathway in the late endosome. This MHC II-peptide complex is then trafficked to the membrane, and the APC is presenting the antigen.

The MHC II-peptide complex expressed on the surface of APC is recognised by either a T-cell receptor (TCR) or B-cell receptor (BCR) found on naïve (previously unexposed to antigen) T-lymphocytes and B-lymphocytes respectively. The TCR consists of an α- and β- chain non-covalently associated with a series of polypeptide chains, collectively called CD3 which transduce a signal to the T-cell to say that the TCR has been ligated, while the BCR is essentially a non-secreted antibody with an integral membrane domain associated with a signal transduction moiety termed collectively CD79. The membrane distal portion of the TCR or BCR interacts directly with the α- helices of the MHC binding groove and those residues of the peptide which make it unique. Binding of the TCR or BCR to the MHC II-peptide complex is however not sufficient to activate the naive T-cell or B-cell, and commit them to their cell fate; this is not a decision the cell takes lightly. Instead, activation requires co-stimulation which only occurs when there ae also signals of danger around. Binding of immature B/T- cells to self cell-surface antigens leads to clonal deletion thus allowing self-tolerance. The importance of this cannot be understated and the catastrophic dysregulation of this process is prevalent in autoimmune diseases.

In T-cells, co-stimulation generally occurs in the form of binding of CD28 on the T-cell to CD80/CD86 which are upregulated on activated APCs. Activation of the TCR and co-stimulation creates different responses in T-cells that are governed by the type of T-cell involved. Pertinent to this discussion, and in response to exogenous antigens, helper T-cell subset 2 (TH2) cells aid B-cells synthesise antibodies by providing activation signals such as Interleukin-4 (IL-4) and IL-10. In the case of B-cells co-stimulation involves binding of CD21 on the B-cell to C3d bound antigens as well as additional signalling through cytokines and CD40-CD40L interactions with T helper cells. It is in this way that B-cells can be activated either independently of T-cells or via T-cells. The activated B-cell can then commit to two fates, it can either become a plasma cell which secretes antibodies capable of binding to the peptide-fragment of the MHC or memory cells which provide immunological memory, allowing a faster and more rigorous response upon repeated exposure of the same antigen.

The above description of T/B-cell activation however poses two apparent problems; firstly, the TCR/BCR must be able to distinguish between a huge amount of different peptides bound to MHC molecules and secondly, the chance of the cognate MHC-peptide coming into contact with the TCR/BCR are exceedingly small. The solution to both of these problems will be discussed in turn.

To overcome this staggering diversity of ligands, each T/B-cell expresses a unique version of its TCR/BCR which differ in their membrane distal portion to create unique specificity for MHC-peptide complexes. In order to generate approximately 10^9 unique TCRs/ and 10^{13} BCRs, the one-gene one protein rule of genetics is crucially ignored. In the TCR, the and β chains are products of several gene segments V (red, Figure 4.2), D (green, Figure 4.2), J (yellow, Figure 4.2) and

C (blue, Figure 4.2) which are spliced together to form a functional gene. There are several copies of each segment within the genome, and each is selected at random and joined to the other segments by looping out the intervening DNA. This allows many combinations and permutations of the α and β chains to contribute to diversity. In an analogous way, diversity is created in each of the antibody heavy and light chains by V(D)J recombination, and further increased by the ability of any heavy chain to fold with either L chain (Figure 4.2). In addition, imprecise joining in the TCR and in the BCR results in random insertion of nucleotides into regions flanking the joining sites, a process known as N-region addition. The diversity genes (D) of both the TCR and the H chain of the BCR may be read in all three reading frames, further increasing the diversity.

The BCR (but not the TCR) can further increase its diversity through a process called somatic hypermutation. During clonal expansion of activated B-cells, regions of the V gene segment known as the complementarity determining regions (CDR) which interact with the antigen are mutated to fine-tune and change the overall affinity for the antigen. Over the course of an immune response, the strength of the interaction is refined in a process called affinity maturation.

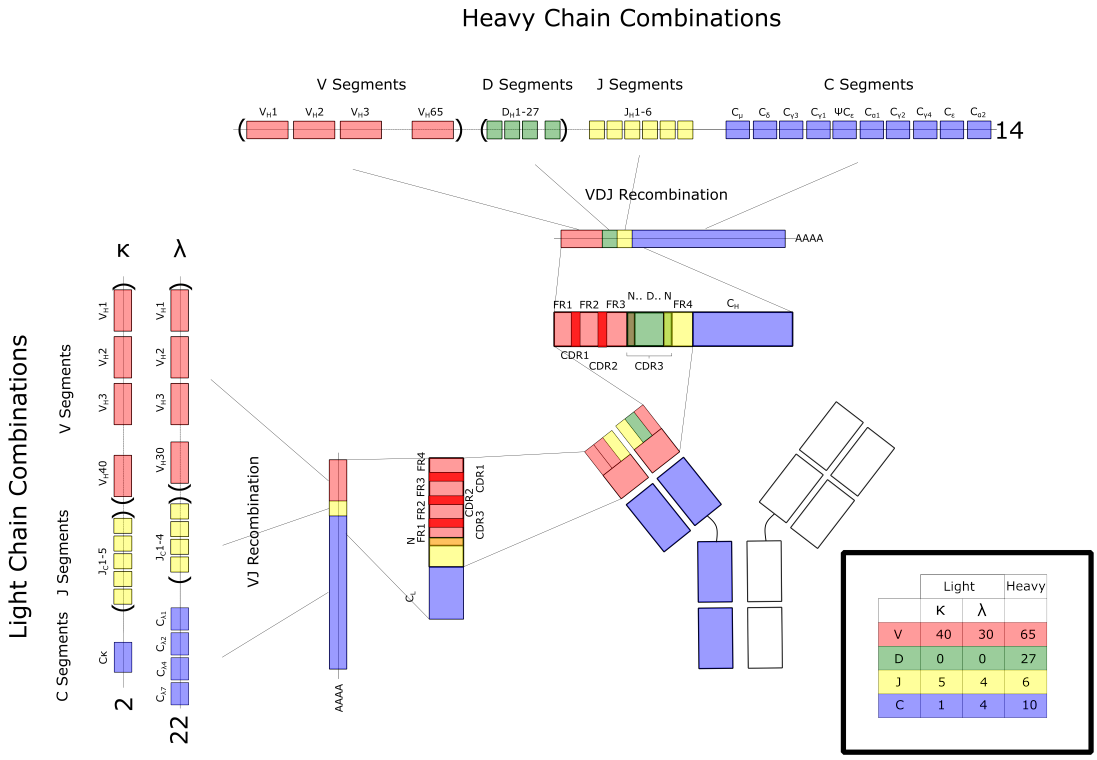


Figure 4.2: **V(D)J Recombination of Heavy and Light Chain Antibodies** Antibody diversity is created in each of the antibody heavy and light chains by V(D)J recombination. Heavy and light chains are the product of several gene segments V (red), D (green), J (yellow) and C (blue) which are spliced together to form a functional gene. Diversity is further increased by the ability of any heavy chain to fold with either Light chain. In addition, imprecise joining in the antibody results in random insertion of nucleotides into regions flanking the joining sites, a process known as N-region addition. The diversity genes (D) in the H chain of the antibody may be read in all three reading frames, further increasing the diversity. It is in this way that such a staggering number of antibodies may be formed from a limited genome.
Based on a figure in Janeway Jr et al. (2001)

To overcome the second problem of the incredibly low likelihood of the TCR/BCR binding to its cognate MHC-peptide complex, adaptive immune cells congregate in the lymphoid organs as well as circulating freely in the blood. Adaptive immune responses are initiated within secondary lymphoid organs e.g. spleen, lymph nodes and peyers patches which have naïve T and B-cells (which have not encountered antigen) and potent APCs including dendritic cells. As well as limiting the spread of infection during the induction of the adaptive response, the innate response transports foreign antigens from the site of infection to the lymphoid tissues for presentation to T and B-cells. Dendritic cells are often credited for the role of linking the innate and adaptive immune responses, and that is because of their role of acquiring antigens, processing them, presenting them onto MHC II. In response to inflammatory stimuli, DC lose their ability to phagocytose and downregulate their endocytic mechanism and migrate to the lymph node and upregulate co-stimulatory molecules such as CD40 and CD86, thus initiating the immune response.

The plasma cells themselves produce various isotypes of secreted antibody, (IgA, IgE, IgG and IgM) which differ in the nature of their Fc portion, and can be switched during an immune response in a process of class switching. This allows the changing of effector function throughout the immune response while maintaining the ability to bind the antigen. Conventionally, when people refer to antibodies, they generally mean secreted IgG.

4.2.3 Introduction to the K2P Channel Family

The mammalian two pore domain (K2P) family of K^+ channels consists of 15 genes, each encoding pore-forming subunits. Textbooks describe them as 'leak channels' as they contribute to the hyperpolarising background currents that main-

tain the resting membrane potential in almost all cells. In reality, almost all family members are finely regulated by a large number of stimuli (including voltage, Schewe et al. (2016)) and contribute to a range of pathophysiological mechanisms including pain and depression (Djillani et al., 2019). They form a structurally-related superfamily where two subunits come together to form a central tetrameric pore as discussed in the introduction.

Family members TREK-1 and TREK-2 are regulated by physical stimuli such as voltage (Schewe et al., 2016), heat (Maingret et al., 1999b; Alloui et al., 2006) and mechanical forces (Maingret et al., 1999a; Noël et al., 2009) as well as chemical stimuli such as intracellular pH (Maingret et al., 1999b; Honoré et al., 2002), extracellular pH (Cohen et al., 2008; Sandoz et al., 2009), (Heurteaux et al., 2004), phospholipids (Chemin et al., 2005), phosphorylation (Patel et al., 1999; Murbartián et al., 2005; Bockenhauer et al., 2001) and regulatory proteins (Sandoz et al., 2006, 2008). The K2P channels have a unique gating mechanism where their diverse sensory properties are achieved by coupling of different molecular sensors to a core gating apparatus at the selectivity filter (SF).

4.2.3.1 A Selectivity Filter Gate

Unlike many potassium channels, TREK channels do not have a lower gate. Instead, the primary activation mechanism was shown to reside close to or within the SF by the ability of quaternary ammonium ions (QA) to bind deep within the pore and freely access their binding site prior to channel activation by intracellular pH and pressure and that mutations in the SF and the nature of permeant ions profoundly influence gating (Piechotta et al., 2011). This type of gating has been termed selectivity filter gating or C-type gating owing to the similarity with

C-type inactivation in KcsA, introduced in the introduction.

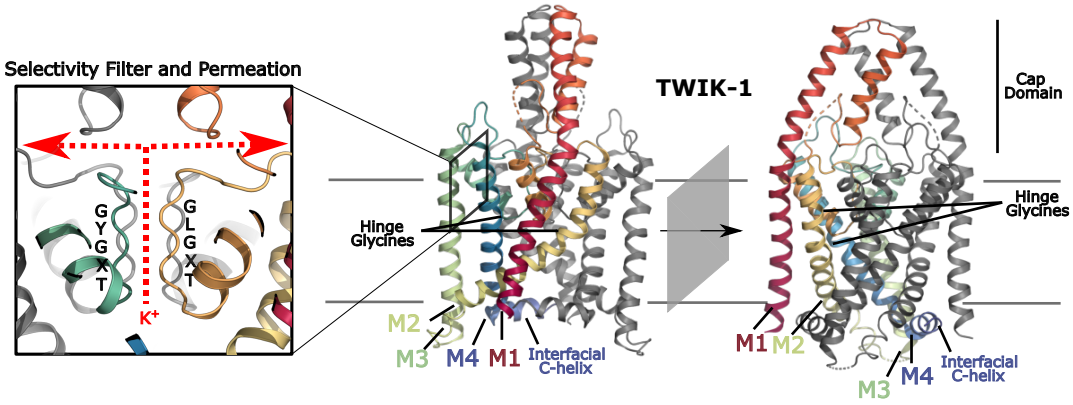


Figure 4.3: **TWIK-1 Structure Showing General K2P Architecture**
Centre: The TWIK-1 structure (PDB: 3UKM) with one subunit coloured grey and the other one is coloured continuously by TM helix (M1 red, M2 gold , M3 olive, M4 blue. Location of the hinge glycines in M2 and M4 and the interfacial C-helix are highlighted. Note the lack of domain-swap in helix assignment.
Right: 90° rotation of centre image, highlighting the large extracellular cap that protrudes from the membrane. Note the lack of domain-swap in helix assignment.
Left: Close up of the asymmetric Selectivity filter, and the bifurcated ion permeation pathway through the channel (red). Note the lack of domain-swap in helix assignment.

The structural resolution of human TWIK-1 (PDB: 3UKM, Miller and Long (2012)) and human TRAAK (PDB: 3UM7, Brohawn et al. (2012)) revealed the unique three dimensional structure of the K2P channels (Figure 4.3). The channels assemble as dimer, as expected by the topology, which is held together by a disulphide bond at the apex of a large 35Å helical cap that protrudes on the extracellular side, creating a bifurcated pore in which the ion pathway involves K^+flow through side portals (dotted arrows, left, Figure 4.3. It is worth noting that the tandem of pores makes the selectivity filter asymmetric, animportant consideration in SF gating (discssed later), although the principles of selectivity remain the same as KcsA as discussed in the introduction. Although the exact function of the cap is unknown, it is thought to render the channels insensitive to toxins. In both structures, lateral opening within the transmembrane helices suggested

that the channels were accessible to lipids, and an interfacial C-helix on the C-terminus of M4 appeared structurally poised to affect gating, lying laterally across the intracellular-membrane interface (Figure 4.3). The inner M2 and M4 helices were hinged at conserved glycines analogous to the glycine hinge in other K channels as discussed in the introduction (Figure 4.3).

A subsequent structure of TRAAK in complex with a Fab fragment unambiguously identified a domain swap of two helices across the channel which is not present in any other K channel structure (PDB: 4I9W, Brohawn et al. (2013)) Interestingly, in this structure, independently of the domain swap, one of the subunits had undergone a conformational change with respect to the other with two major structural consequences; in one subunit, the lateral membrane opening was closed and the interactions between PH1 and PH2 were lost. While not affecting the SF itself, however it appears to alter dynamics around the filter, corroborating the idea that structural changes from the C-terminus can be relayed to the SF without changing its structural integrity; a necessity for retention of potassium selectivity.

4.2.3.2 External pH Sensitivity

TREK-1 and TREK-2 are sensitive to external pH with a pK of 7.3 and independent of voltage, immediately suggesting a histidine outside of the electric field to be the primary pH Sensor (Sandoz et al., 2009). The external pH sensitivity was confirmed by scanning mutagenesis to be attributed to a conserved extracellular Histidine (H156 in hTREK-2b and H141 in hTREK-1c) and was independent of the state of the up/down transition (discussed more thoroughly in the next section) by use of mutagenesis (E306A) and binding of AKAP150 to stabilise the active conformation. However, TREK-1 and TREK-2 response to extracellular pH is opposite

in spite of the 78 % sequence homology, with TREK-1 channel activity being inhibited and TREK-2 activated by extracellular acidification. Making use of the opposite actions of external pH on TREK-1 and TREK-2, chimeric channels were used to show that it was the C-terminal portion of the loop connecting P2 and M4 which was responsible for the opposite effects.

Owing to the inherent flexibility of these loops, they are often poorly defined in structures and so how loop conformations are able to stablise the active or inactive SF remains enigmatic.

4.2.3.3 Mechanosensitivity, Temperature Gating and Intracellular pH gating via the TM helices (up/down transitions)

The M4 helix was implicated in both channel activation and inhibition in response to protons, heat and pressure via yeast potassium uptake screening to identify novel Gain of Function (GOF) mutations which were tested in response to a variety of stimuli (Bagriantsev et al., 2011). Additionally M4 was shown to be a sensor of metabolic and thermal stimuli which propagated signals to the SF gate (Bagriantsev et al., 2012). However, details of the role of the interfacial C-helix and by extension M4 remained controversial owing to two groups providing seemingly mutually exclusive roles of the M4 in activation based on different structural correlates.

One group solved structures of TRAAK in assumed conductive and non-conductive conformations based on the ion occupancy of the selectivity filter. The structure of Fab bound TRAAK 'down' structure (subunit A-up, subunit B-down, PDB: 4WFF (K^+), PDB: 4WFH (Tl^+)) was annotated as non-conductive, while a Fab-TRAAK-Trichloroethanol 'up' (subunit-A up, subunit B-up, PDB: 4WFE (K^+), PDB: 4WFG (Tl^+)) complex was annotated as conductive based on thallium anomalous difference peaks in the cavity (Brohawn et al., 2014). In the non-conductive state, a lipid-acyl chain accesses the cavity through one of the lateral openings and physically blocks ion passage. Meanwhile in the conductive state, rotation of M4 about a central hinge seals the opening, preventing lipid block and permitting ion entry (analogous to the previously published Fab-TRAAK dimer). Seemingly, their structures elegantly explained mechanosensitivity; a 2.7 nm^2 expansion of the cross-sectional area in the conductive state creates a membrane tension energy difference promoting force activation.

However, just two weeks later, a diametrically opposed model of force activation was proposed based on comparisons of structures of C-type gate activating mutations; G124I (PDB: 4RUE) and W262S (PDB: 4RUF) to their previously published domain swapped structure((Brohawn et al., 2013). Comparisons revealed a tilting and straightening of M4 and buckling of M2 upon channel activation (Lolicato et al., 2014). Here they annotated the down state as conductive and the up state as non-conductive. This model was also the opposite of KcsA where straight pore-lining helices are closed, but here they suggested that a straight M4 is activated.

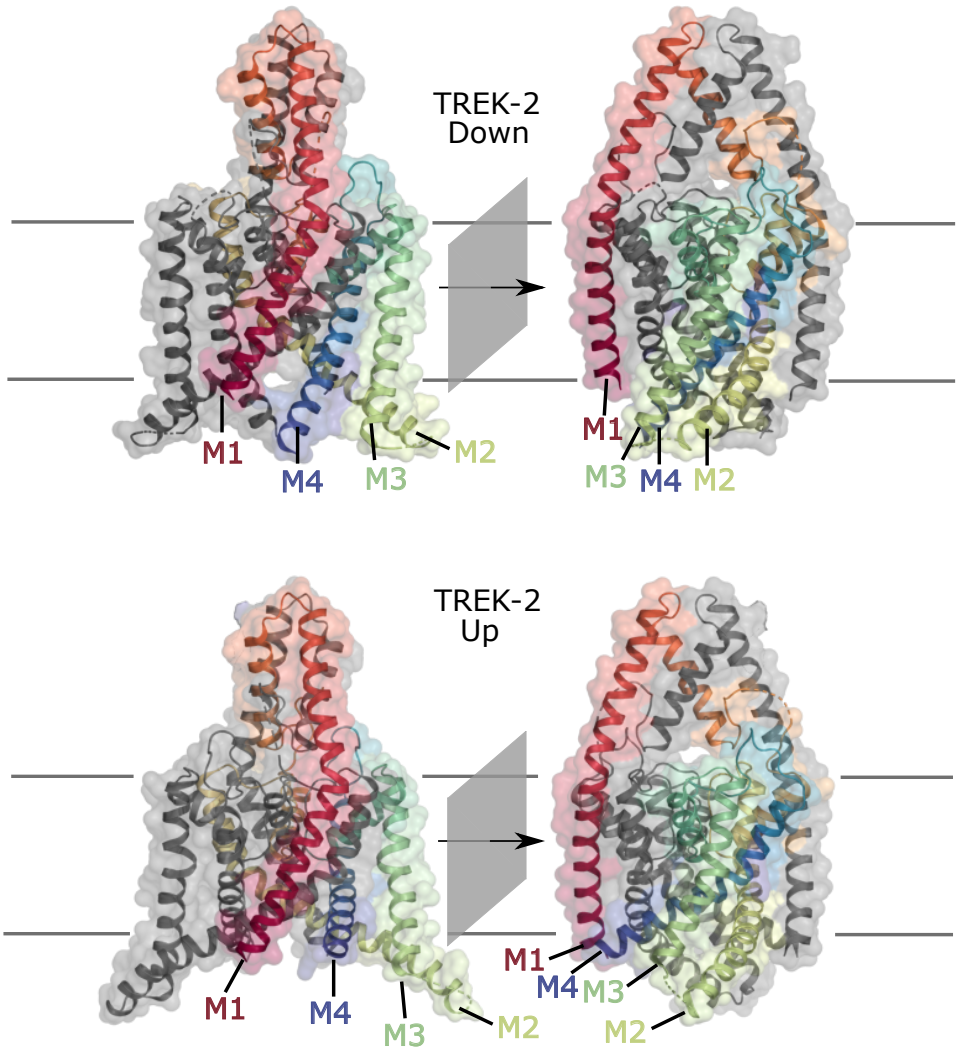


Figure 4.4: **TREK-2 Up and Down Structures Highlighting TM Transitions**
Top Left: The TREK-2 down structure (PDB: 4XDJ) with one subunit coloured grey and the other one is coloured continuously by transmembrane (TM) helix (M1 red, M2 gold , M3 olive, M4 blue. TIM helices M2,M3 and M4 are pointing downwards, perpendicular to the membrane plane.
Top Right: 90° rotation of the left image, highlighting the downwards facing transmembrane helices M2,M3 and M4 which are perpendicular to the membrane plane and the clear domain-swapped orientation which is typical of the family.
Bottom Left: The TREK-2 up structure (PDB: 4BW5) with one subunit coloured grey and the other one is coloured continuously by TM helix (M1 red, M2 gold , M3 olive, M4 blue). TM helices M2,M3 and M4 are pointing upwards, parallel to the membrane plane.
Top Right: 90° rotation of the left image, highlighting the upwards facing transmembrane helices M2,M3 and M4 which are parallel to the membrane plane and the clear domain-swapped orientation which is typical of the family.

These contradictory conclusions were reconciled by two structures of TREK in two conformations, (up, PDB: 4BW5, Figure 4.4 bottom and down, PDB: 4XDJ, Figure 4.4 top) and in complex with norfluoxetine (NFx) (down, PDB: 4XDK) and a brominated fluoxetine derivative (down, PDB: 4XDL), the active metabolite of Prozac which binds in a state-dependent way within a membrane fenestration found only in the down conformation (Dong et al., 2015). The NFx bound state was therefore in the down state, while the apo structure was captured in both conformations, which were both found to be conductive but with different activities, with the down state (NFx-sensitive) being lower activity than the up (NFx-insensitive) state (Dong et al., 2015). By using NFx, a follow up study demonstrated that activation by pressure, temperature, voltage and pH produce more than one structurally distinct open state, and channel activation does not simply involve the up-down transition (McClenaghan et al., 2016) .

Further credence to the unified theme of filter gating was provided by TREK-1 (PDB: 5VK5) and TREK-1 activator complexes with the N-aryl sulfonamide ML-355 (PDB: 5VKN) and the thiopene-carboxamide ML402 (PDB: 5VKP) which identified cation-π interactions within a cryptic binding pocket stabilising the C-type gate leak mode (Lolicato et al., 2017). This L-shaped pocket behind the SF formed by P1 and M4 inter-subunit interface, acting as molecular wedges which support the selectivity filter structure, and notably the binding pocket includes GOF mutation sites which had originally been picked up in yeast uptake screen (Bagriantsev et al., 2011) and crystallised in TRAAK (Lolicato et al., 2014). In addition to showing a druggable K2P pocket, the TREK-1 activator complexes also resolved extra turns of the C-helix in the 'up' conformation, although it is involved in lattice interactions so the physiological relevance remains to be seen.

4.2.3.4 Voltage-Gating

Voltage-sensing is common to all K2P channels except TWIK-1 however there is no canonical voltage sensor domain nor an obviously charged candidate capable of sensing the electric field across the channel. Instead, in K2P channels, voltage-sensitivity originates from the movement of 3-4 ions into the high electric field of an inactive SF, generating a 'one-way check valve' within the filter because outward movement of K^+ induces filter opening, whereas inward movement induces inactivation via filter collapse (Schewe et al., 2016). Consistent with the SF being responsible for voltage-gating, mutations affecting the S4 K site (**T**XGYG) abolish voltage-sensitivity and voltage-gating is dependent on the species of the permeant ion (Schewe et al., 2016). However, many physiological stimuli such as arachidonic acid, pressure, PIP_2 and acidic pH switch off this flux gating mode to convert K2P channels into a linear leak conductance (Schewe et al., 2016). Voltage-activation is tightly coupled to the electrochemical gradient ($V_m - E_{Rev}$) rather than the transmembrane voltage *per se* such that under physiological conditions, the voltage-dependent gating is evident due to a large negative driving force.

4.2.3.5 Structural Changes in the Gate

Despite decades of research implicating the SF as the primary gate in K2P channels, including structures of K2Ps in conformations that impact their activity (NFx, ML205, BL1249 etc), in all structures, the SF was in a single conformational state, owing to the high potassium concentration in all crystallisation conditions, which stabilised the filter gate, analogous to substrate-mediated catalysis in enzymes. Structures solved in varying $[K^+]$ showed that in low $[K^+]$ (e.g. 0mM K^+, PDB: 6W7B) conformational changes in SF1, SF2 and the SF2-M4 loop destroyed the S1 and S2 K^+binding sites, involving the carbonyl flip originally identified in KcsA. The S1 and S2 K^+binding sites were maintained in the presence of the activator

ML355 which stabilises the filter (0 mMK^+, ML-335, PDB: 6W8F, Lolicato et al. (2020). Disruption of loop mobility by either truncation or disruption of the conserved H bonding network blunts the response to a variety of C-type gating stimuli but can be restored upon channel activation with ML-335 (Lolicato et al., 2020).

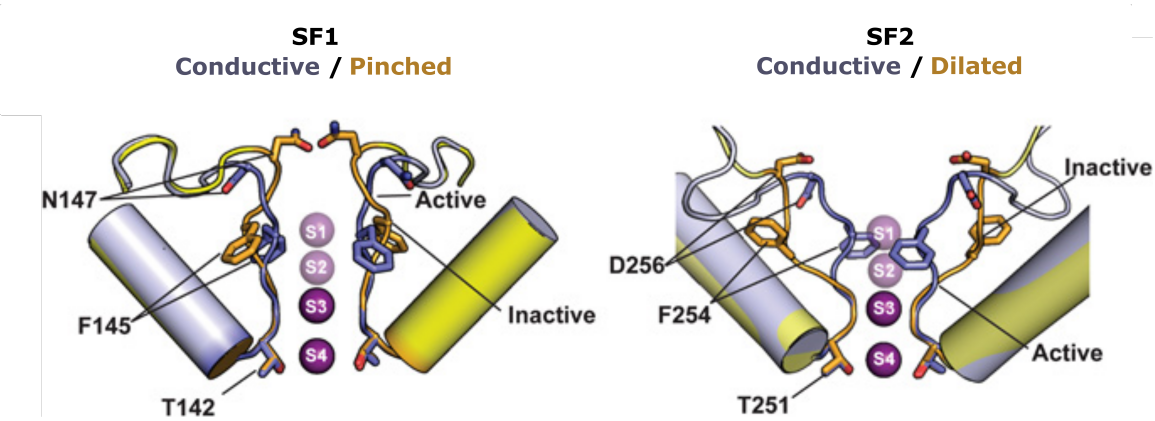


Figure 4.5: **Intrinsic Asymmetry of the Selectivity Filter Gate Showing Dynamics**
Left: Conformations of the SF1 from the low [K^+] and high [K^+] structures in the pinched (brown) and conductive (grey) conformations respectively.
Right: Conformations of the SF2 from the low [K^+] and high [K^+] structures in the dilated (brown) and conductive (grey) conformations respectively.
From Lolicato et al. (2020). Reprinted with permission from AAAS.

4.2.3.6 K2P Pharmacology

In addition to NFx and ML335 structures which have been useful to better understand K2P gating; two further molecules have been shown to modulate TREK-2 and helped understand channel function and their binding sites have been uncovered.

BL-1249 has been shown to activate not just TREK channels, but a number of K^+channels which also gate at the SF (e.g. hERG and BK_{Ca} families) but not channels which do not gate primarily at the SF (e.g. cyclic nucleotide–gated channel families, Schewe et al. (2019). While electron density has not been obtained for the Negatively Charged Activator (NCA) BL-1249, brominated derivatives and anomalous difference maps have unambiguously resolved the bromine peak, placing the BL-1249 beneath the SF and shown in combination with electrophysiology studies to overlap with THexA but not the smaller TEA. The negative charge on BL-1249 helps to stabilise the ion occupied (active) selectivity filter (Schewe et al., 2019).

In addition, the trinuclear ruthenium amine Ruthenium Red (RuR) has been shown to block TREK-2 but not TREK-1 owing to an acidic residue pair (recently coined the 'keystone inhibitor site') and sensitivity can be transferred to TREK-1 by introducing this negative charge into TREK-1. (Braun et al., 2015). Structures of a RuR-sensitive TREK-1 (I110D, PDB: 6V36) and in the presence of RuR (PDB: 6V3I) show RuR physically blocking the potassium the potassium efflux pathway by a 'finger in the dam' type inhibition mechanism physically occluding ion flux through the channel (Pope et al., 2020).

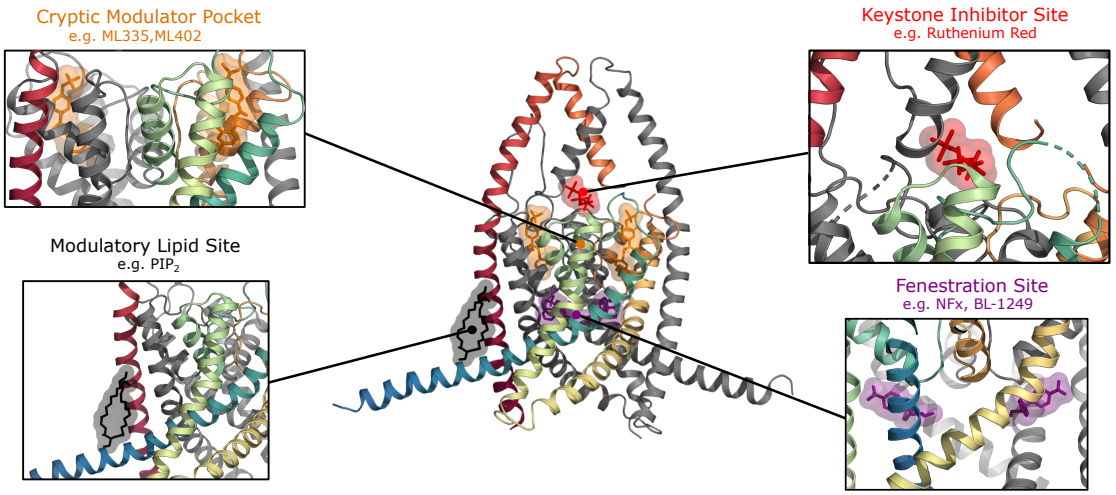


Figure 4.6: **K2P Pharmacology**
Centre: The TREK-1 up structure (PDB: 6CQ8) with one subunit coloured grey and the other coloured continuously by TM helix (M1 red, M2 gold, M3 olive, M4 blue. Transmembrane helices M2,M3 and M4 are pointing upwards, parallel with the membrane plane. Overlayed are small molecule modulators (coloured sticks and surfaces) which have been captured in complex with TREK-1 and TREK-2; ML335 (orange), Ruthenium Red (red), modulatory lipids (black) and Norfluoxetine (purple).
Surrounding: Close-ups of the Cryptic Modulator pocket, the keystone inhibitor site, the modulatory lipid site and the fenestration site.

4.2.4 Antibodies Targeting Ion Channels

In recent years, a number of commercial and academic efforts have aimed to target ion channels with antibodies and venom peptides. The potential specificity of the approach, combined with the convenient starting point of many naturally occurring toxins has attracted a great deal of interest. While a number of comprehensive reviews are available e.g. Wulff et al. (2019); Hutchings et al. (2019), the pertinent point remains that in spite of great progress in antibody based therapeutics in the oncology and autoinflammatory fields, to name but a few, there is only one antibody targeted against ion channels which has made it to human clinical trials (Carter and Lazar, 2018). Namely, a polyclonal sheep antibody against a nonfunctional form of P2X7 as a topical treatment for basal cell carcinoma (Gilbert et al., 2017). As for targeting the K2P channels, a monoclonal antibody against TASK-

3 has been shown to reduce metastatic breast cancer tumour progression in mice (Sun et al., 2016) but has yet to be put into clinical trials.

Nevertheless there are number of VHH antibodies capable of functional modulation of ion channels. Two VHH antibodies raised against the mouse ligand-gated P2X7 channel responsible for detecting damage through release of ATP and initiating a proinflammatory signalling cascade have been shown to both block (13A7) and potentiate (14D5) channel gating (Danquah et al., 2016). Further development of the inhibitory VHH antibody generated Dano1 which was able to specifically inhibit human P2X7 (Danquah et al., 2016).

Another VHH antibody (M2-7A) was capable of inhibiting proton influx through the influenza A M2 protein and through doing so inhibited replication of influenza A viruses *in vitro* and protected mice from a lethal influenza viral challenge (Wei et al., 2011)

A number of other VHH antibodies have recently been shown to have functional effects, as positive and negative allosteric inhibitors of pentameric ligand gated channels from the prokaryote *Erwinia* (ELIC, Brams et al. (2020), potent inhibitors of the mouse cys-loop receptor 5-HT_3 (Hassaine et al., 2014), phosphorylation inhibitors of the cardiac Ryanodine Receptor RyR2 and through attachment of an E3 ubiquitin ligase to an inert VHH antibody to inhibit auxiliary CaV β subunits (Li et al., 2019). These case studies offer exciting insights into specific functional modulation of channels with therapeutic potential.

In addition to antibodies and antibody derivatives, improved pharmacokinetics have been achieved by fusion of antibodies to cysteine knot rich scaffolds allow-

ing retention of binding specificity and affinity (Bell et al., 2018). The resulting 'knotbodies' platform was commercialised by Iontas Ltd which has since merged with FairJouney Biologics. Other engineering approaches involving VHH antibodies have involved grating them onto protein scaffolds to increase their molecular weight while retaining the full antigen binding specificity and affinity, which have been useful for cryo-EM efforts (Uchański et al., 2021). One such megabody is reported as a positive allosteric modulator of GABA receptors (Laverty et al., 2019).

4.2.5 Why Target K2P Channels with VHH Antibodies?

As discussed, the K2P channels appear to gate primarily at the SF, taking modular and diverse inputs and transducing them to signals in the form of a potassium-selective current flowing across the membrane. Large movements between 'up' and 'down propagate intracellular stimuli while extracellular stimuli are propagated via the loops connecting the membrane spanning or pore helices and the extracellular cap. It appears that changing the dynamics around the filter either by natural stimuli, mutation (e.g. G167I) or using drugs (e.g. BL1249, ML-335) is sufficient to drastically affect K2P channel activity. Better understanding of functionally relevant states in static crystal structures would help define the roles of the dynamics around the SF in channel activity, and functional modulators could allow the development of novel analgesics.

The large extracellular cap, a hallmark feature of K2P channels, renders them insensitive to many extracellular modulators, but offers a large antigenic surface that protrudes from the extracellular side of the membrane. This large cap, combined with the lack of natural toxins targeting the channels makes them attractive targets amenable to VHH antibody generation.

To this end, a panel of VHH antibodies were raised against the mechanosensitive TREK-2 and TREK-1 channels. The small size of VHH antibodies, combined with their ability to target epitopes which are inaccessible by larger molecules, their avidity and their selectivity towards their target made them attractive to use in order to better understand structure-function relationships in the K2P channel family.

4.3 Results and Discussion

4.3.1 Strategy

Purified truncated TREK-2 and TREK-1 proteins (G66-E340 10HF hTREK-2c and P26-S300 10HF hTREK-1a) were reconstituted into liposomes and injected into llamas to elicit an immune response. Details of this procedure along with the VHH antibody selection process are reviewed in detail in Pardon et al. (2014). Briefly, after llama immunisation, the immune repertoire is cloned and a library constructed. The antigen (here K2P channels) are immobilised and positive clones capable of binding to the antigen are selected by phage panning and screening.

This immunisation process results in channels which are randomly orientated within the liposomes, meaning that VHH antibodies could in theory be targeted to the extracellular or intracellular portion of the protein. However, VHH antibodies may be raised against epitopes that are not present in the full length protein due to the absence of the large C-terminus which has so far failed to be purified in substantial quantities. In addition, given the polymodal nature of gating in the K2P channel family, the VHH antibodies are likely to have been exposed to an array of different functional and structural states, particularly involving the flexible

extracellular loops around the SF which are known to be important for external pH sensitivity of the channels.

In total, 32 VHH antibodies were raised against TREK-2 while 18 VHH antibodies were raised against TREK-1. In spite of positive ELISA data provided by Nanobodies4Instruc, a number of the TREK-1 VHH antibodies were suggested to be wrong clones as their Open Reading Frame (ORF) did not match the protein sequences provided by Nanobodies4Instruc, and mass spectrometry of the purified protein matched the mass predicted by translation of the ORF. Efforts were therefore focused on the 32 VHH antibodies raised against TREK-2.

In order to assess the ability of VHH antibodies to form biochemically tight complexes Karin Rödstrom conducted a first pass screen for binding of to their purified target channel using a size-exclusion chromatography (SEC) peak shift assay. Binding of the VHH antibody to the channel increases the molecular weight and therefore causes it to elute earlier from the column. This crude binding assay revealed 14 binders for VHH antibodies raised against TREK-2 (blue, Figure 4.7) however none for TREK-1.

4.3.2 Screening for Extracellular Modulators of TREK-2

To examine if any VHH antibodies raised against TREK-2 exhibited functional effects on TREK-2 channel activity, macroscopic whole cell currents were recorded from *Xenopus laevis* oocytes injected with TREK-2 mRNA using the two electrode voltage clamp (TEVC) technique. Voltage ramps were applied both before and addition of 1 µg of VHH antibody to the bath (200µl containing high $[K^+]$) and the normalised current at +50 mV used to assess whether the VHH antibody resulted in a change in TREK-2 activity.

Of all screened VHH antibodies, only three VHH antibodies; CA10761, CA10767 and CA10776 (hereby shortened to VHH61, VHH67 and VHH76 respectively in text), showed clear functional modulation of TREK-2 activity (Figure 4.7A), and this was consistent with their ability to bind directly to the channel protein in the peak shift assay. VHH61 appeared to inhibit TREK-2 whilst both VHH67 and VHH76 appeared to activate TREK-2.

The normalised I-V curves for a subset of the VHH antibodies before and after VHH antibody application are shown in Figure 4.7B . They all reverse around +10 mV showing that the currents retain potassium selectivity upon VHH antibody-mediated modulation. In addition, the VHH-antibody mediated modulation was voltage-independent as modulation occurred across the tested voltage range Figure 4.7C), suggesting that the VHH antibodies do not bind within the electric field, and pertinently for the inhibitor VHH61, do not physically occlude the K^+efflux pathway.

As a negative control, the VHH antibodies were applied to uninjected oocytes which confirmed that the functional modulation (if any) was directed against TREK-2 not any endogenous channels Figure 4.7D).

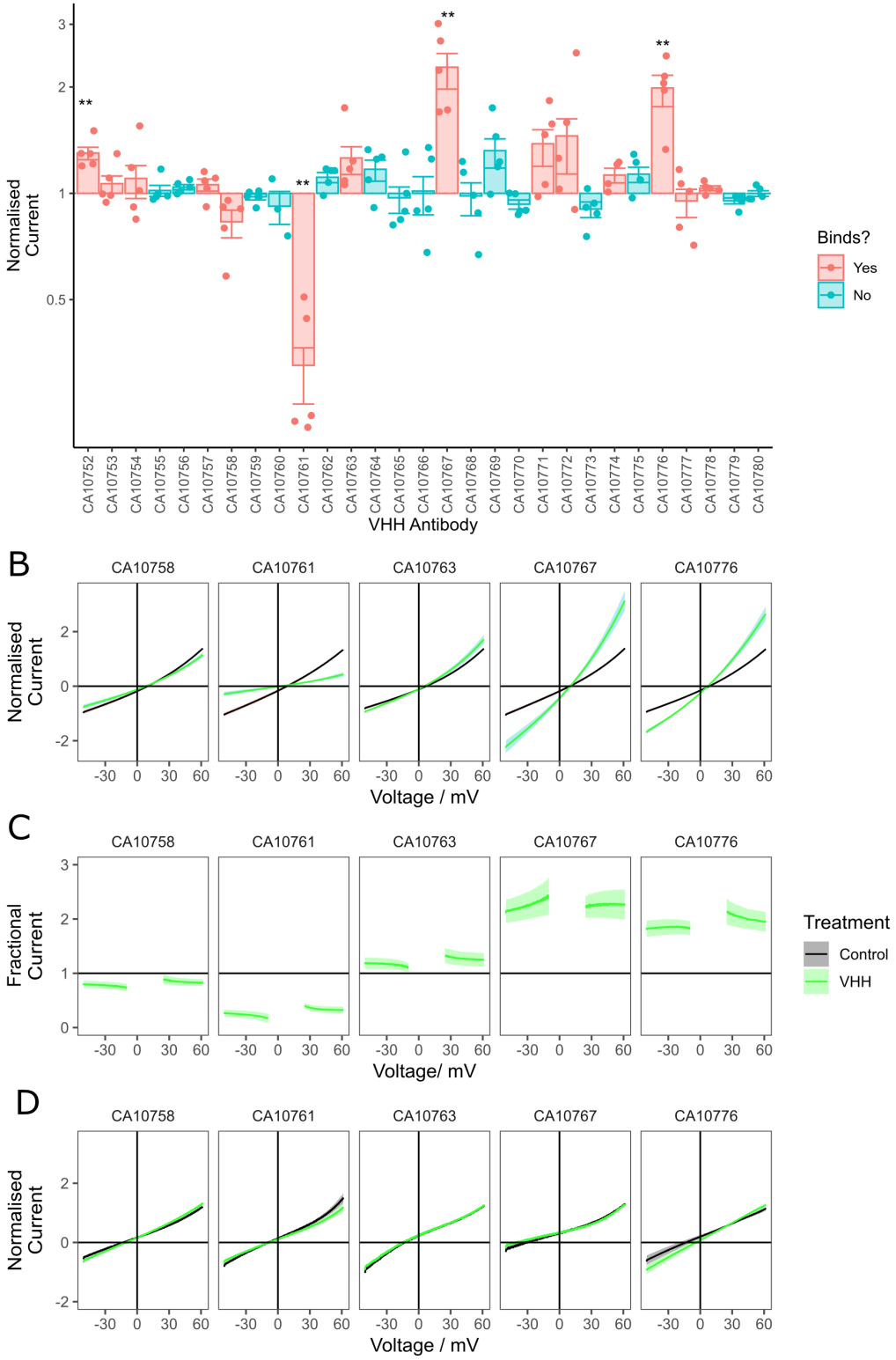


Figure 4.7: **Screening for Extracellular Modulators of TREK-2** (Caption next page.)

Figure 4.7: (Previous page.) **Screening for Extracellular Modulators of TREK-2**
A: Bar graph depicting mean current at +50mV after addition of VHH antibodies to *xenopus laevis* oocytes expressed relative to the maximal current prior to addition of VHH antibody depicted on a logarithmic axis. Cells are shown as individual points and error bars depicting S.E.M. VHH antibodies shown in red were predicted to bind in the SEC peak shift assay while those in blue were not predicted to bind. Current before and after VHH antibody addition were compared and the significance was calculated using a paired two-tailed t-test. For VHH antibodies that show significant modulation, significance is plotted above the data using the following key *** $p < 0.001$, ** $0.001 < p < 0.01$, * $0.01 < p < 0.05$.
Peak Shift assaay conducted by Karin Rödstrom.
B: Normalised I-V curves of a subset of VHH antibodies from the screen, showing the TREK-2 current response to voltage ramps ranging from -50 mV to +60 mV, normalised to the current at +60 mV prior to VHH antibody addition, both before (black) and after(green) VHH antibody application. Mean normalised current are depicted by lines and shaded ribbon represents the S.E.M.
C: State-dependence of a subset of VHH antibodies from the screen, showing the mean TREK-2 current at each voltage before (black) and after (green) VHH antibody application, normalised to the mean current at each voltage.
D: Normalised I-V curves of a subset of VHH antibodies from the screen, showing the endogenous current response to voltage ramps ranging from -50 mV to +60 mV, normalised to the current at +60mV prior to VHH antibody addition, both before (black) and after(green) VHH antibody application. Mean normalised current are depicted by lines and shaded ribbon represents the S.E.M.

4.3.3 Potency of modulation by VHH antibodies

In order to assess the potency of modulation by VHH antibodies, *Xenopus laevis* oocytes expressing human TREK-2 (hTREK-2) were challenged with increasing doses of the three VHH antibodies capable of functional modulation. Again the TEVC technique was utilised, however this time, increasing concentrations of VHH antibody were perfused over the oocyte in a bath containing a physiological K^+concentration. All three VHH antibodies showed concentration-dependent activity modulation of TREK-2 (Figure 4.8A). VHH61 inhibited TREK-2 with an IC_{50} value of 762 nM ± 193nM while VHH67 and VHH76 activated TREK-2 with EC_{50} values of 108nM ± 9nM and 419nM ± 52nM respectively. These dose-response measurements confirmed that the VHH antibody concentration used in the original screen was saturating.

Additionally, I-V curves confirmed that VHH antibody-mediated modulation of TREK-2 activity by all three VHH antibodies retained them in voltage-gated mode shown by clear outward rectification Figure 4.8B). This suggests that VHH antibody-mediated modulation does not convert them into leak mode, which was impossible to detect during the original screen where the high potassium concentration promoted leak-mode operation of the channel. This is consistent with their mechanism of action not being a result of binding in the cryptic site nor the fenestration site, consistent with steric and chemical considerations, and places them among the most potent modulators of known TREK-2 channels in the 100s of nM range.

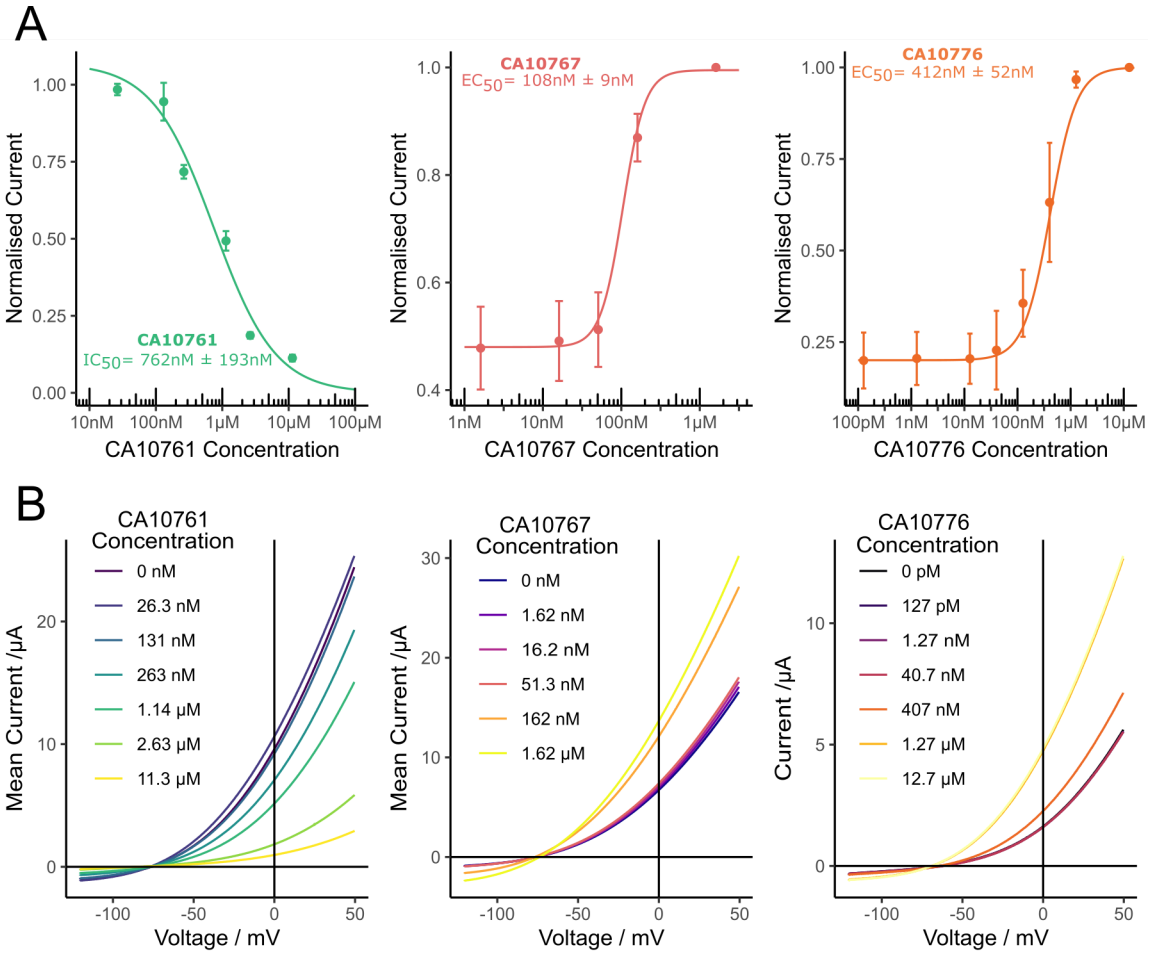


Figure 4.8: **Potency of VHH Antibody Modulators of TREK-2**
A: Normalised dose-response measurements of the three VHH antibody modulators of TREK-2 identified from the screen.The mean current at 0mV for each VHH antibody dose was normalised to unmodulated TREK-2, expressed as mean ± S.E.M
B: Mean I-V curves of each VHH antibody modulator used to generate the dose-response above.

4.3.4 Specificity of Functional Binders

In order to assess the specificity of the functional binders, VHH antibodies VHH61, VHH67 and VHH76 were tested to see whether they exhibited functional effects against other K2P family members. Given the impermeability of VHH antibodies to the plasma membrane, the binding site of the three VHH antibodies was deduced to be extracellular. The channel epitopes that may be targeted are shown in Figure 4.9, but namely include the two loops connecting M1 and SF1 and SF1 and M2 respectively (blue, Figure 4.9A) and the two loops connecting M3 and SF2 and SF2 and M4 respectively (red,Figure 4.9A). A full sequence alignment of these regions is also shown to highlight the conservation within this region.

The three VHH antibodies capable of human TREK-2b (hTREK-2) modulation were additionally tested on mouse TREK-2 (mTREK-2c) in order to assess the feasibility of their use in rodent pain models and immmunostaining of rodent tissues. Across the entire extracellular region the human and mouse isoforms share 96.5% identity and 98.8 % similarity, and mouse and rat isoforms are identical, hence only mouse TREK-2 was tested (Figure 4.9A). Additionally, the closely related human TREK-1 (hTREK-1c, 42.5% identity and 64.4% similarity) and the more distantly related human TASK-3 (hTASK-3, 22.47% identity and 46.07% identity) were also tested (Figure 4.9A).

Based on the EC_{50} concentrations determined from the dose-response measurements, 1µM of each VHH antibody was perfused over oocytes injected with the appropriate channel mRNA and voltage ramps recorded using the TEVC technique.

Consistent with previous experiments, all three VHH antibodies modulated hTREK-2 activity (Figure 4.9B, light blue), and unsurprisingly were capable of

modulating mTREK-2 activity in a similar manner (Figure 4.9B, lilac). Again unsurprisingly, none of the three modulators were capable of modulating TASK-3 (Figure 4.9B, red), which shows low sequence similarity in the extracellular portion of the channel Figure 4.9A. Although VHH antibodies VHH61 and VHH76 were unable to modulate TREK-1 activity, strikingly, VHH67 (a TREK-2 activator) appeared to be capable of inhibiting TREK-1 (Figure 4.9, green).

Once again, I-V curves showed that modulation of both hTREK-2 and mTREK-2 by all three VHH antibodies retains them in voltage-gated mode and does not modify the selectivity of the channel. Taken together, this data suggests that all three VHH antibodies should be suitable for immunostaining of rodent tissue and use in rodent pain models, whilst VHH antibody VHH61 and VHH76 show high specificity towards TREK-2.

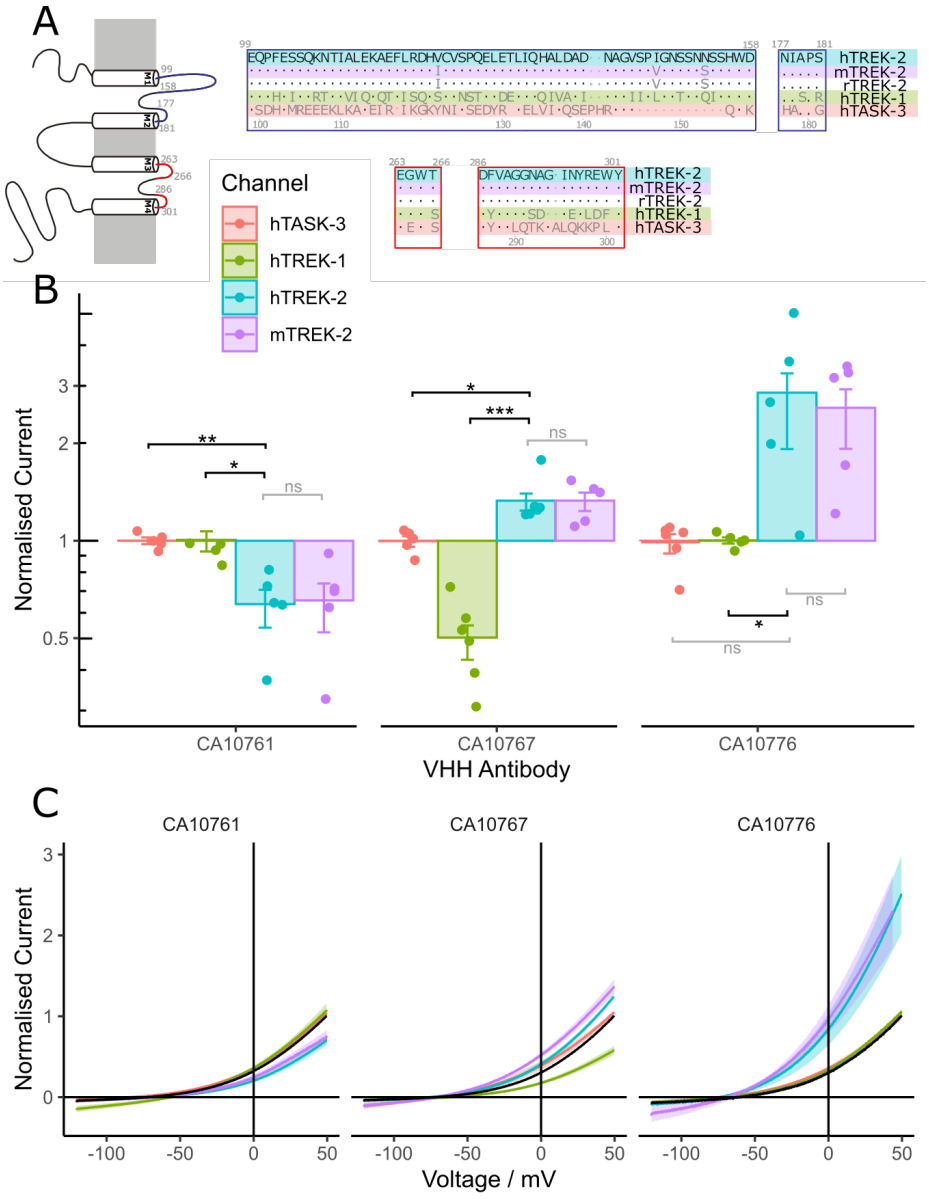


Figure 4.9: **Specificity of Functional Modulators of TREK-2**
(Caption next page.)

Figure 4.9: (Previous page.)**Specificity of Functional Modulators of TREK-2**
A: Left: Topology Diagram of the K2P family highlighting extracellular loops. **Right:** Alignment of human (blue), mouse (lilac) and rat (white) TREK-2, human TREK-1 (green) and hTASK-3 (red) in the extracellular region of the channel.
B: Bar graph depicting mean current at 0 mV after addition of VHH antibodies to *xenopus laevis* oocytes expressed relative to the maximal current prior to addition of VHH antibody depicted on a logarithmic axis. Cells are shown as individual points and error bars depicting S.E.M. Modulation by each VHH antibody on each channel was compared to TREK-2 and the significance was calculated using an unpaired two-tailed t-test. The p-values were corrected using the Bonferroni correction. Significance of the corrected p-values is plotted on the horizontal line above the bars using the following key *** $p < 0.001$, ** $0.001 < p < 0.01$, * $0.01 < p < 0.05$, ns non significant. Channels are coloured as in A.
C: Normalised mean I-V curves showing the TREK-2 current response to voltage ramps ranging from -120 mV to +50 mV, normalised to the current at +50 mV prior to VHH antibody addition, both before (black) and after VHH antibody application to hTREK-2 (blue), mTREK-2 (lilac), hTREK-1 (green) and hTASK-3 (red). Mean normalised current are depicted by lines and shaded ribbon represents the S.E.M.

4.3.5 Mechanism of Action

In order to probe the mechanism of action of the functional modulators, the activity of each VHH antibody was tested on a variety of TREK-2 gating mutants which disrupt channel gating by either decoupling known sensory inputs or affecting SF dynamics. The A179P mutant (P1-M1 linker, blue, Figure 4.10) is identical to WT TREK-2 (purple, Figure 4.10) except that it is insensitive to external pH fluctuations (Dong et al., 2015) and as identified in an internal yeast screen analogous to the one published in (Bagriantsev et al., 2011). The G167I mutant (Pore Helix 1, green, Figure 4.10) significantly increases TREK-2 currents putting the channel into leak mode by stabilising the active conformation of the SF (Bagriantsev et al., 2011), thought to be via a similar mechanism as the N-aryl sulfonamide ML-335 (Lolicato et al., 2017). Meanwhile E337 (distal C-terminus of M4, yellow, Figure 4.10) is the intracellular pH-sensor and mutation to Alanine locks the channel open by mimicking intracellular acidosis also converting it into leak mode (Maingret et al., 1999b).

Both G167I and E337A reduce channel regulation by intracellular and extracellular mediators and are often described as non-regulatable owing to their conversion of the channel to leak mode. The I-V curves of the wild type TREK-2 , A179P, G167I and E337A prior to modulation are shown as black lines in Figure 4.10C, where TREK-2 and A179P show voltage-dependent gating while G167I and E337A are in leak mode characterised by the ohmic voltage-dependence as previously reported (Bagriantsev et al. (2011); Maingret et al. (1999b),Figure 4.10C).

VHH61 was capable of modest inhibition of A179P and E337A compared to WT although was unable to drastically modulate the G167I mutant (Figure 4.10B,C). Taken together, this suggests that blunting the pH response is capable of signifi-

cantly reducing VHH61 modulation, suggesting that VHH61 inhibits at least in part through the external pH-sensing mechanism, consistent with the proposed extracellular binding site. In addition, the modest inhibition of the E337A mutant but not the G167I mutation is consistent with TM helix transitions being independent of destabilisation of the open filter, but stabilisation is the dominant effect.

Both VHH67 and VHH76 were able to activate A179P, however VHH67 was not able to activate to WT levels but VHH76 was. Neither VHH67 nor VHH76 were able to significantly activate the 'non-regulatable' G167I or E337A mutants (Figure 4.10B,C). Taken together, this suggests that blunting the pH-response does not affect the ability of VHH76 to activate TREK-2 but reduces VHH67-mediated modulation. This suggests that VHH76 activates through the external pH sensing mechanism while VHH67 activates at least in part through the external pH-sensing mechanism, again consistent with the proposed extracellular binding site.

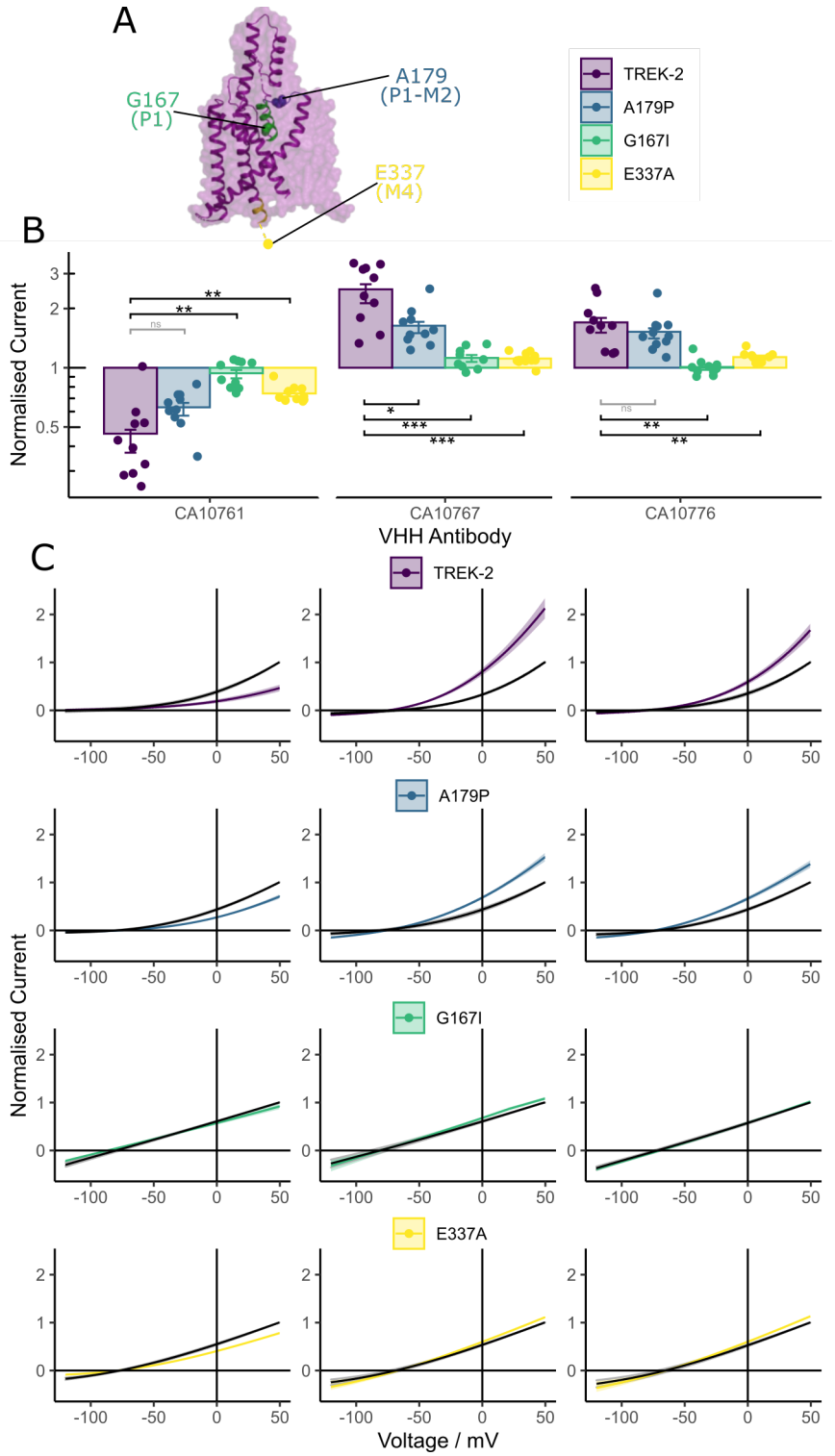


Figure 4.10: **VHH Antibody-Mediated Functional Modulation of TREK-2 Gating Mutants**
(Caption next page.)

Figure 4.10: (Previous page.) **VHH Antibody-Mediated Functional Modulation of TREK-2 Gating Mutants**
A: Structure of TREK-2 (PDB: 4XDJ), depicting the gating mutations. TREK-2 is coloured purple; one subunit is depicted as helices and the channel surface shown for the dimer. Mutations A179P, G167I and E337A are depicted as blue, green and yellow balls respectively and the secondary structure they reside in coloured to match the residue.
B: Bar graph depicting mean current at 0 mV after addition of VHH antibodies applied to *Xenopus laevis* oocytes expressing TREK-2 gating mutations expressed relative to the current at 0 mV prior to addition of VHH antibody depicted on a logarithmic axis. Cells are shown as individual points and error bars depicting S.E.M. Modulation by each VHH antibody on each mutant was compared to the wild type and the significance was calculated using an unpaired two-tailed t-test. The p-values were corrected using the Bonferroni correction. Significance of the corrected p-values is plotted on the horizontal line above the bars using the following key *** $p < 0.001$, ** $0.001 < p < 0.01$, * $0.01 < p < 0.05$, ns non significant. Colours matched to those in A.
C: Normalised mean I-V curves showing the TREK-2 current response to voltage ramps ranging from -120 mV to +50 mV, normalised to the current at +50 mV prior to VHH antibody addition, both before (black) and after VHH antibody application to wild type TREK-2 (purple), A179P (blue), G167I (green) and E337A (yellow). Mean normalised current are depicted by lines and shaded ribbons represent the S.E.M.

The data collected so far and theoretical considerations suggest that VHH antibodies VHH61, VHH67 and VHH76 may work by modulating the extracellular pH-gating (pH_{ext}) mechanism for a number or reasons. Firstly, the TEVC measurements involve extracellular pH application, VHH antibodies cannot cross the plasma membrane, and the only known extracellular modulation of TREK-2 is through the extracellular pH-sensing pathway. Secondly, VHH antibody VHH76 appears to activate TREK-2 but inhibit TREK-1, a response that could be achieved by shifting the external pH-sensitivity of these channels to more basic pHs, as TREK-1 and TREK-2 show opposite pH_{ext} sensitivity (Figure 4.9). Finally, VHH61 and VHH67 were unable to activate or inhibit respectively the pH_{ext}-insensitive A179P mutant to WT levels suggesting modulation through this mechanism (Figure 4.10).

In order to clarify the importance of the pH_{ext}-mechanism, pH dose-responses experiments were carried out by first perfusing ND96 at different pHs over oocytes and then returning to the initial pH and repeating the pH response but in the presence of VHH antibody. Dose-response measurements were carried out with increasing alkanisation (from pH 6.0 to pH 9.0) and acidification (from pH 9.0 to pH 6.0) to ensure VHH antibody mediated modulation was present in case pH altered binding. VHH antibody VHH76 was used as a control, as it was able to activate the A179P mutant to a comparable level to WT during the original gating experiments. The effect of the A179P mutation blunting the pH-response can be seen in Figure 4.11C.

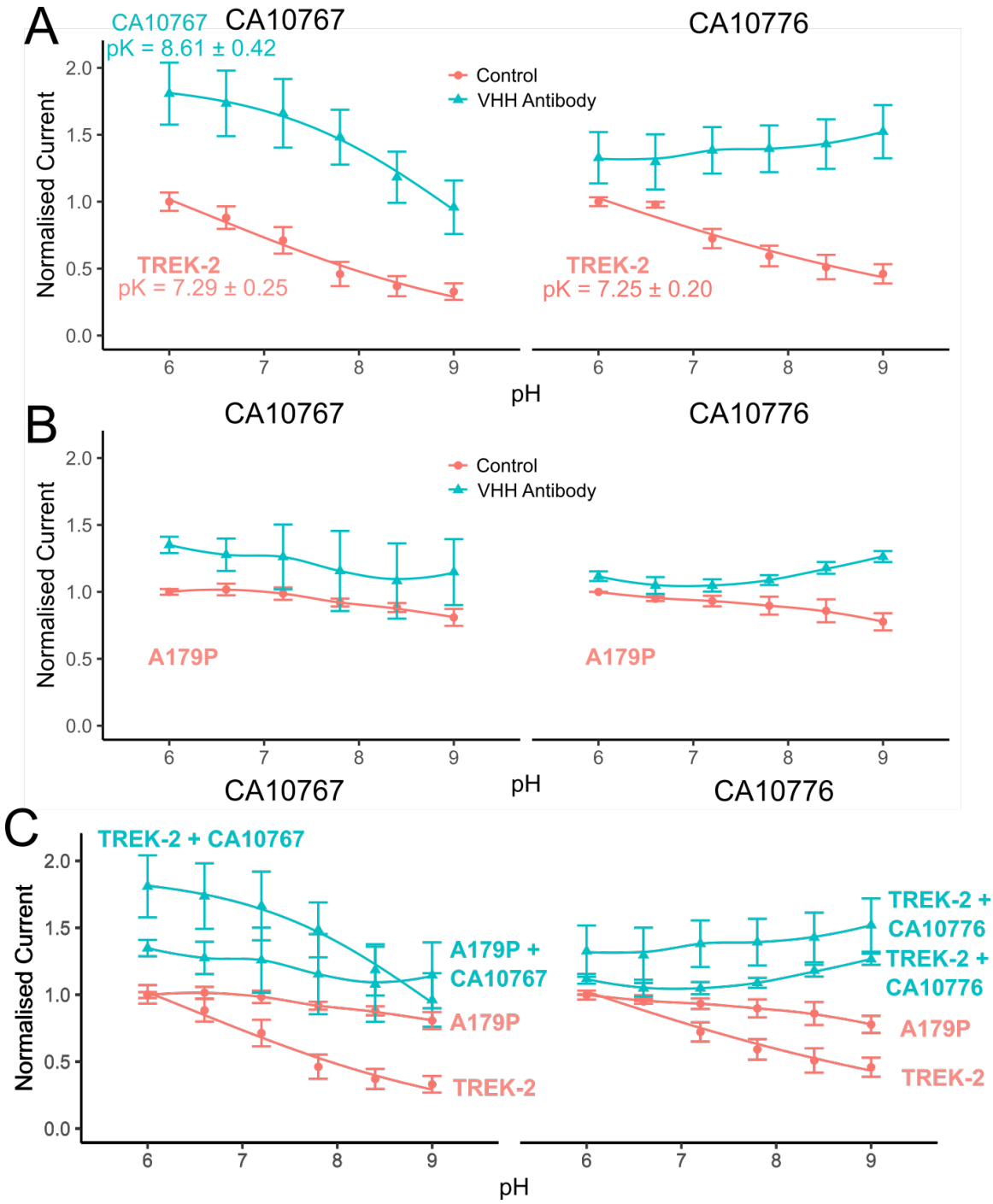


Figure 4.11: **VHH Antibody Modulation Response to External pH**
A: pH responses of TREK-2 without (red) and with (blue) VHH Antibody VHH67 (left) or VHH76 (right). The Current at 0mV was normalised to the TREK-2 current at pH 6.0 prior to VHH antibody application. Plotted as mean (points) ± S.E.M (error bars). **B:** pH responses of TREK-2 A179P without (red) and with (blue) VHH Antibody VHH67 (left) or VHH76 (right). The Current at 0mV is normalised to the TREK-2 A179P current at pH 6.0 prior to VHH antibody application. Plotted as mean (points) ± S.E.M (error bars). **C:** Overlay of A and B.

The pH_{ext}-response of TREK-2 in the absence of VHH antibody (Figure 4.11A,C red lines) gave a pK estimate of 7.29 ± 0.25 and 7.25 ± 0.20 respectively, consistent with published data (Sandoz et al., 2009). For both VHH antibody activators VHH67 and VHH76, pH dose-response measurements on TREK-2 were similar during both acidification and alkalinisation suggesting that both VHH-antibodies can modulate TREK-2 at both pH 6.0 and pH 9.0 (and by extension all pHs in this range). Interestingly, VHH67 activated TREK-2 (blue line, Figure 4.11) is still modulated by external pH sensitivity whereas VHH76 activated TREK-2 seems to be independent of external pH modulation (Figure 4.11A,C.) This result is consistent with the previous observation that VHH67 was unable to activate the pH_{ext}-insensitive A179P mutant to WT levels but VHH76 was. In addition, the crystal structure of a VHH76-TREK-2 complex has shown direct interaction of the VHH antibody with H156, the extracellular pH-sensor. This interaction was not seen in the VHH67-TREK-2 complex structure, directly consistent with these functional observations.

The pH_{ext}-response of the pH_{ext}-insensitive A179P mutant in the absence of VHH antibody (Figure 4.11B,C, red lines) was not significantly modulated across the tested pH range, consistent with the reported blunted pH-response of this mutation. Both VHH67 and VHH76 application to the A179P mutation failed to modulate to the WT levels, in contrast to the previously recorded result, but nevertheless, the pH-response was similar both with and without VHH antibody. The inherent flexibility of the pH-sensing loops may account for this decreased effect. Taken together, the data suggests that VHH67 activated TREK-2 is still subject to modulation by pH_{ext} whereas VHH76 activated TREK-2 is not, potentially implicating loop dynamics as key to VHH antibody-mediated modulation but also showing a difference between different modulators.

4.3.6 Determinants of Efficacy

In order to assess the determinants of efficacy, a series of point mutants were made across the VHH67-TREK-2 and VHH76-TREK-2 interfaces for which crystal structures had become available. Notably for VHH76 (structure not shown), a large number of residues in TREK-2 which were predicted to interact resided in the M1-P1 linker, the flexibility of which has been shown to be important in (de)stabilising the C-type gate (Lolicato et al., 2020). Simple mutation of these residues becomes difficult to interpret owing to the importance of these in general channel gating.

Efforts were therefore focused on the VHH67 interaction with TREK-2. The structure showed three VHH67 molecules (orange, Figure 4.12A) bound to each TREK-2 dimer (grey, Figure 4.12A); including two symmetry related extracellular binding sites involving the three CDR loops, and an unprecedented intracellular binding site, unlikely to be accessible in the full length channel. Dose-response measurements were carried out using patch clamp electrophysiology on HEK293 cells in the whole cell configuration making use of the microperusion Dynaflow Resolve Chip perfusion system (Fluicell) to avoid the problems associated with standard perfusion systems that were used for the TEVC experiments (large overall volume, large dead volume and slow fluid exchange, discussed further in methods.) The Dynaflow Resolve system had some extra problems in my hands while working with the mechanosensitive TREK channels which is discussed in Materials and Methods.

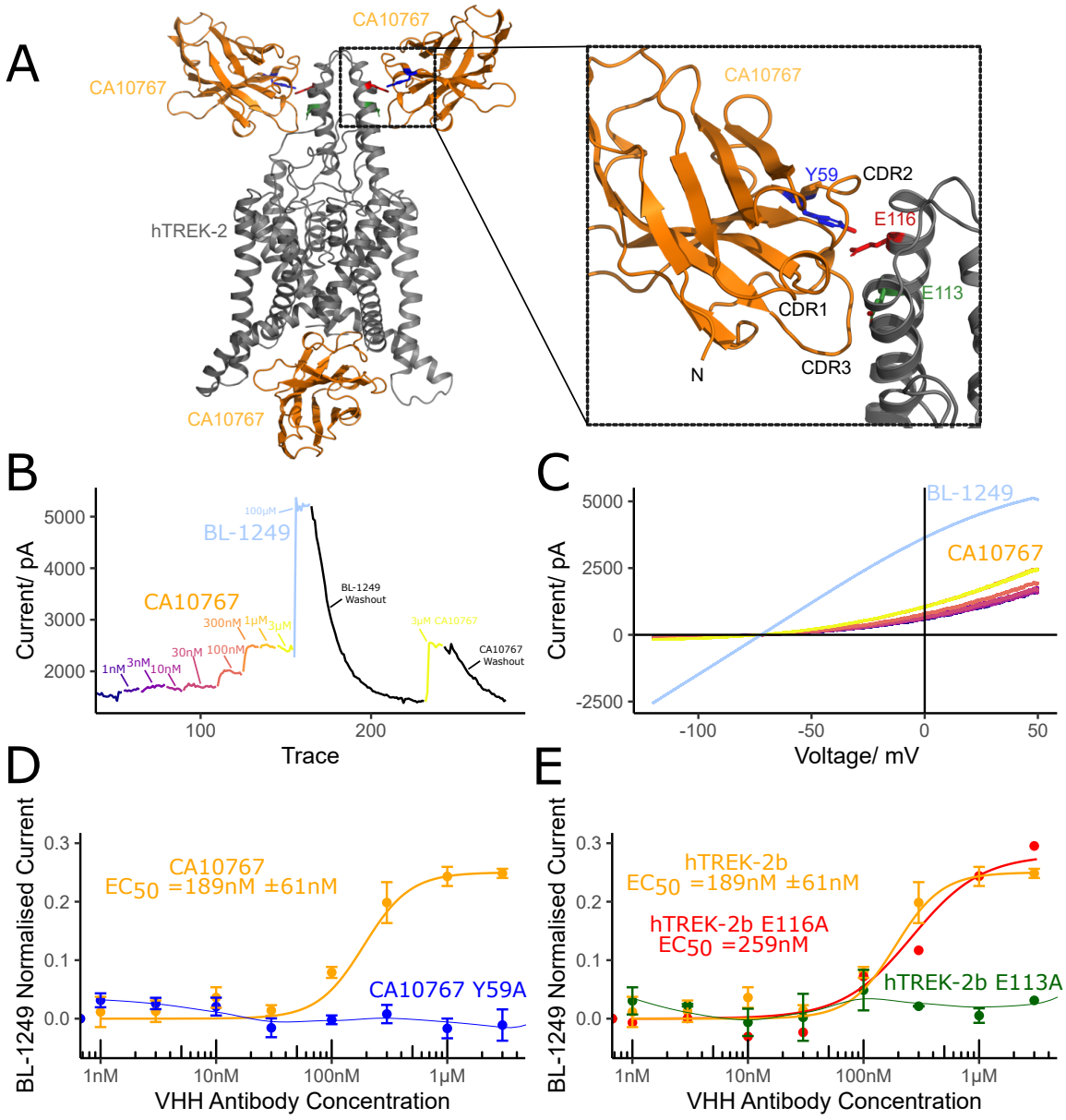


Figure 4.12: **VHH67 Determinants of Efficacy on TREK-2 in HEK293 Cells** (Caption next page.)

Figure 4.12: (Previous page.) **VHH67 Determinants of Efficacy on TREK-2 in HEK293 Cells**
A: Crystal structure of the VHH67 hTREK-2 complex. There are three VHH67 molecules (orange) bound to each channel dimer (grey). Inset box contains a close up of one of the extracellular interaction sites (rotated 180 ° compared to the full structure) with mutated residues shown as coloured sticks (E113, red, E116, dark green and Y59 blue). **Structure solved by Agenese Baronina, Ashley Pike, Karin Rödstrom and Elisabeth Carpenter**.
B: A typical Dose-response curve showing dose-dependent activation of TREK-2 by VHH67. The Current at +50 mV is plotted as a function of the sweep of I-V curve. The response was typically approximately 25% of the efficacy of BL-1249 (light blue). Following washout, a saturating dose of VHH67 elicits the same response (orange) and can be washed out (black line).
C: Representative I-V curves showing the TREK-2 current response to voltage ramps ranging from -120 mV to +50 mV, with increasing doses of VHH67. Colours matched to A.
D: Dose-response measurements of mutations made in VHH67. The mean BL-1249 normalised current is plotted as a function of VHH antibody concentration. VHH67 (orange) shows dose-dependent activation of TREK-2 while VHH67 Y59A (blue) shows no efficacy on TREK-2. Data plotted as mean ± S.E.M
E: Dose-response measurements of mutations made in hTREK-2b. The mean BL-1249 normalised current is plotted as a function of VHH antibody concentration. hTREK-2b (orange) and hTREK-2b E116A (red) show dose-dependent activation of TREK-2 while hTREK-2b E113A (dark green) shows no efficacy on TREK-2. Data plotted as mean ± S.E.M.

Dose-response measurements confirmed that in HEK293 cells as well as oocytes, VHH67 is capable of dose-dependent activation of hTREK-2 currents Figure 4.12B, with a similar EC_{50} of 189nM ± 61nM to that which was recorded from *Xenopus* oocytes. In these experiments, the activated current was normalised to a saturating dose (100 µM) of BL-1249 (which stabilises the leak mode of TREK-2) in order to get a estimate for the maximal activated current, a problem previously encountered with activator dose responses and discussed in methods. Using this readout, the efficacy of VHH67 consistently came out as roughly 25% of a maximally activated current evoked by a saturating dose (100 µM) BL-1249, (lightblue, Figure 4.12) suggesting a robust and large activation of TREK-2 current by VHH67.

In order to assess the effects of individual residues within the VHH67-TREK-2 interface, a point mutation in the VHH antibody β5 sheet, Y59A, was tested which was thought to interact with TREK-2 from low resolution structures. When TREK-2 was challenged with increasing dose of this mutant VHH antibody, there was no activity modulation (blue, Figure 4.12D) even at concentrations which were saturating with the wild type VHH antibody (orange, Figure 4.12D). This suggests that the Tyrosine is important for functional modulation of TREK-2 and that this interface is highly sensitive to perturbations, consistent with this region of the channel being important for C-type gate stabilisation.

In a similar manner a number of point mutants were made in the TREK-2 channel. Tested mutations were focused on residues protruding from the cap helices (E113A and E116A) which interact with non-charged residues in the CDR1 and CDR3 loops of VHH67. In a similar manner to the Y59A mutation in the VHH antibody, mutation of E113A was able to abolish VHH67-mediated activity of TREK-2 function (green, Figure 4.12E). However, VHH67 activity showed similar po-

tency to the wild type channel (orange, Figure 4.12E) on a TREK-2 mutation on the next solvent exposed residue (E116A, EC_{50} = 259nM(n =1), red, Figure 4.12E), one turn further up the cap helix. Taken together it suggests that some residues in the cap helix are critical for interaction while others are not. It is also interesting to note the closer proximity of E113A to the SF and loops surrounding it than E116, although because binding was not tested, it is impossible to tell whether VHH67 still binds to the channel from these experiments. The higher resolution structure (Figure 4.12A) clearly shows CDR3 interacting closer to the channel pore, however in the lower resolution structures available when these mutations were first made the CDR3 loop was poorly resolved.

These experiments help to validate the structural data which has since become available and is shown and discussed in the Discussion, and provide further credence to the idea that the VHH antibodies work through changing the pH_{ext}-gating pathway. The effects of the tested mutations appear to be all-or-nothing, suggesting the high sensitivity of this region to perturbation, and also potentially highlighting this region as an interesting pharmacological target.

4.4 Discussion

In this chapter, we have tested a panel of VHH antibodies raised against the hTREK-2 channel. We have shown that a subset are capable of functional modulation, and within our repertoire, there appears to be two VHH antibodies (VHH67 and VHH76) which are capable of activation and one (VHH61) which is capable of inhibition of TREK-2. All three VHH antibodies show dose-dependent activity modulation of TREK-2 with potency in the 100s of nM range; suggesting they are some of the most potent known K2P modulators. Generally, the VHH antibodies

show high functional selectivity towards the human and rodent isoforms. Selectivity is further probed in the next chapter to try and test selective- binding rather than selective- functional modulation.

Functional data using known gating mutants and pH-response curves and more recently, structural data is consistent with modulation occurring via the pH_{ext} pathway which modulates the filter gate, a naturally occurring modular input for the channel but one which has so far not been pharmacologically probed. Meanwhile, disruption of the VHH-antibody TREK-2 interface can abolish efficacy of the VHH antibody, validating the X-ray structures but critically suggesting the interface is highly sensitive to perturbations, consistent with this region of the channel being important for C-type gate stabilisation.

Further binding site interrogation could prove useful in elucidating exactly how VHH antibodies are capable of modulating TREK-2 function, but results will be difficult to interpret owing to the high flexibility of this region.

The electrophysiological experiments in this chapter were designed and performed in the absence of high resolution structures (which have since become available). The electrophysiology data has been elegantly explained by the structures; as an example, the VHH76-TREK-2 complex structure shows a direct interaction between the VHH antibody and the pH-sensing Histidine (H156), potentially explaining the pH-independence of modulation. In addition, generally VHH antibodies capable of functional modulation generally bind on the sides of the cap (e.g. VHH67, right Figure 4.13), while VHH antibodies which are functionally inert tend to bind to the top of the cap (e.g. VHH58, left Figure 4.13), consistent with existing knowledge about the SF gate.

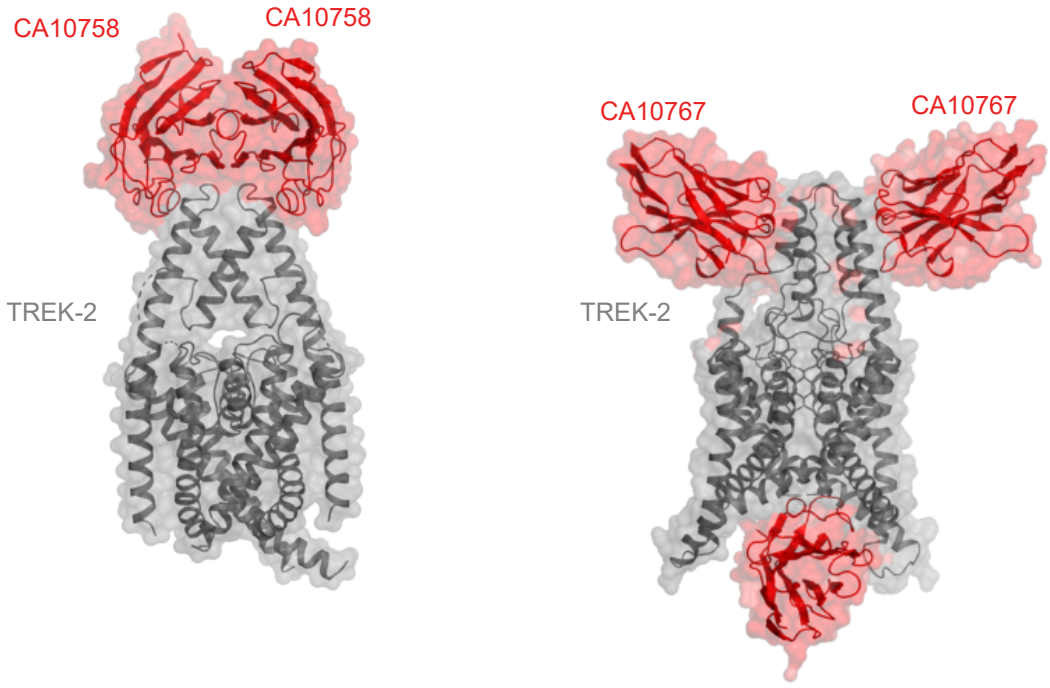


Figure 4.13: **Inert and Functional VHH Antibody Binders**
Generally functionally inert VHH antibodies (e.g. VHH58 bind to the apex of the cap) while functional modulatory VHH antibodies (e.g. VHH67 tend to bind to the sides of the cap,closer to the regulatory loops connecting the transmembrane helices.

Perhaps more interesting would be to test the VHH antibodies in potential pain models. We have shown that all three antibodies are capable of functional modulation of mouse TREK-2, which is identical to rat TREK-2 in the VHH antibody binding site. In particular, potent and selective activation of TREK-2 using either VHH67 or VHH76 could potentially be used to hyperpolarise the resting membrane potential of cells expressing TREK-2, thus decreasing the likelihood of action potential initiation by moving it further away from the threshold potential which could help to alleviate pain sensation.

Bibliography

Alloui, A., Zimmermann, K., Mamet, J., Duprat, F., Noëel, J., Chemin, J., Guy, N., Blondeau, N., Voilley, N., Rubat-Coudert, C., Borsotto, M., Romey, G., Heurteaux, C., Reeh, P., Eschalier, A., and Lazdunski, M. (2006). Trek-1, a k+ channel involved in polymodal pain perception. 25(11):2368–2376. 244

Bagriantsev, S. N., Clark, K. A., and Minor Jr, D. L. (2012). Metabolic and thermal stimuli control k2p2. 1 (trek-1) through modular sensory and gating domains. *The EMBO journal*, 31(15):3297–3308. 248

Bagriantsev, S. N., Peyronnet, R., Clark, K. A., Honoré, E., and Minor Jr, D. L. (2011). Multiple modalities converge on a common gate to control k2p channel function. *The EMBO journal*, 30(17):3594–3606. 248, 251, 269

Bell, D. C., Karratt-Vellatt, A., Surade, S., Luetkens, T., Masters, E. W., Sørensen, N. M., Butt, N., and McCafferty, J. (2018). Knotbodies: A new generation of ion channel therapeutic biologics created by fusing knottin toxins into antibodies. *Biophysical Journal*, 114(3):203a. 257

Berens, S., Wylie, D., and Lopez, O. (1997). Use of a single vh family and long cdr3s in the variable region of cattle ig heavy chains. *Int Immunol*, 9(1):189–99. 237

Bockenhauer, D., Zilberberg, N., and Goldstein, S. (2001). Kcnk2: reversible conversion of a hippocampal potassium leak into a voltage-dependent channel. *Nature neuroscience*, 4(5):486–491. 244

Brams, M., Govaerts, C., Kambara, K., Price, K. L., Spurny, R., Gharpure, A., Pardon, E., Evans, G. L., Bertrand, D., Lummis, S. C., et al. (2020). Modulation of the erwinia ligand-gated ion channel (elic) and the 5-ht3 receptor via a common vestibule site. *Elife*, 9:e51511. 256

Braun, G., Lengyel, M., Enyedi, P., and Czirják, G. (2015). Differential sensitivity of trek-1, trek-2 and traak background potassium channels to the polycationic dye ruthenium red. *British journal of pharmacology*, 172(7):1728–1738. 254

Brohawn, S. G., Campbell, E. B., and MacKinnon, R. (2013). Domain-swapped chain connectivity and gated membrane access in a fab-mediated crystal of the human traak k+ channel. *Proceedings of the National Academy of Sciences*, 110(6):2129–2134. 246, 249

Brohawn, S. G., Campbell, E. B., and MacKinnon, R. (2014). Physical mechanism for gating and mechanosensitivity of the human traak k+ channel. *Nature*, 516(7529):126–130. 248

Brohawn, S. G., Del Mármol, J., and MacKinnon, R. (2012). Crystal structure of the human k2p traak, a lipid-and mechano-sensitive k+ ion channel. *Science*, 335(6067):436–441. 245

Carter, P. J. and Lazar, G. A. (2018). Next generation antibody drugs: pursuit of the 'high-hanging fruit'. *Nat Rev Drug Discov*, 17(3):197–223. 255

Chemin, J., Patel, A. J., Duprat, F., Lauritzen, I., Lazdunski, M., and Honoré, E. (2005). A phospholipid sensor controls mechanogating of the k+ channel trek-1. *The EMBO journal*, 24(1):44–53. 244

Cohen, A., Ben-Abu, Y., Hen, S., and Zilberberg, N. (2008). *J Biol Chem*, 283(28):19448–55. 244

Danquah, W., Meyer-Schwesinger, C., Rissiek, B., Pinto, C., Serracant-Prat, A., Amadi, M., Iacenda, D., Knop, J.-H. H., Hammel, A., Bergmann, P., Schwarz, N., Assunção, J., Rotthier, W., Haag, F., Tolosa, E., Bannas, P., Boué-Grabot, E., Magnus, T., Laeremans, T., Stortelers, C., and Koch-Nolte, F. (2016). Nanobodies

that block gating of the p2x7 ion channel ameliorate inflammation. *Sci Transl Med*, 8(366):366ra162. 256

Djillani, A., Mazella, J., Heurteaux, C., and Borsotto, M. (2019). Role of trek-1 in health and disease, focus on the central nervous system. *Frontiers in pharmacology*, 10:379. 244

Dong, Y., Pike, A., Mackenzie, A., McClenaghan, C., Aryal, P., Dong, L., Quigley, A., Grieben, M., Goubin, S., Mukhopadhyay, S., Ruda, G., Clausen, M., Cao, L., Brennan, P., Burgess-Brown, N., Sansom, M., Tucker, S., and Carpenter, E. (2015). K2p channel gating mechanisms revealed by structures of trek-2 and a complex with prozac. *Science*, 347(6227):1256–1259. 251, 269

Edelman, G. M. (1959). Dissociation of γ-globulin. pages 3155–3156. 234

Feige, M. J., Gräawert, M. A., Marcinowski, M., Hennig, J., Behnke, J., Ausländer, D., Herold, E. M., Peschek, J., Castro, C. D., Flajnik, M., Hendershot, L. M., Sattler, M., Groll, M., and Buchner, J. (2014). The structural analysis of shark ignar antibodies reveals evolutionary principles of immunoglobulins. *Proc Natl Acad Sci U S A*, 111(22):8155–60. 237

Gilbert, S., Gidley Baird, A., Glazer, S., Barden, J., Glazer, A., Teh, L., and King, J. (2017). A phase i clinical trial demonstrates that nfp2x7 -targeted antibodies provide a novel, safe and tolerable topical therapy for basal cell carcinoma. *Br J Dermatol*, 177(1):117–124. 255

Glockshuber, R., Malia, M., Pfitzinger, I., and Plüuckthun, A. (1990). A comparison of strategies to stabilize immunoglobulin fv-fragments. *Biochemistry*, 29(6):1362–7. 236

Greenberg, A., Avila, D., Hughes, M., Hughes, A., McKinney, E., and Flajnik, M.

(1995). A new antigen receptor gene family that undergoes rearrangement and extensive somatic diversification in sharks. *Nature*, 374(6518):168–73. 236

Hamers-Casterman, C., Atarhouch, T., Muyldermans, S., Robinson, G., Hamers, C., Songa, E., Bendahman, N., and Hamers, R. (1993). Naturally occurring antibodies devoid of light chains. *Nature*, 363(6428):446–8. 236

Hassaine, G., Deluz, C., Grasso, L., Wyss, R., Tol, M. B., Hovius, R., Graff, A., Stahlberg, H., Tomizaki, T., Desmyter, A., Moreau, C., Li, X.-D. D., Poitevin, F., Vogel, H., and Nury, H. (2014). X-ray structure of the mouse serotonin 5-ht3 receptor. *Nature*, 512(7514):276–81. 256

Heurteaux, C., Guy, N., Laigle, C., Blondeau, N., Duprat, F., Mazzuca, M., Lang-Lazdunski, L., Widmann, C., Zanzouri, M., Romey, G., et al. (2004). Trek-1, a k+ channel involved in neuroprotection and general anesthesia. *The EMBO journal*, 23(13):2684–2695. 244

Honoré, E., Maingret, F., Lazdunski, M., and Patel, A. J. (2002). An intracellular proton sensor commands lipid-and mechano-gating of the k+ channel trek-1. *The EMBO journal*, 21(12):2968–2976. 244

Hutchings, C. J., Colussi, P., and Clark, T. G. (2019). Ion channels as therapeutic antibody targets. *MAbs*, 11(2):265–296. 255

Janeway Jr, C. A., Travers, P., Walport, M., and Chlomchik, M. (2001). *Immunobiology: The Immune System in Health and Disease*, volume 5th Edition. Garland Science. 236, 238, 242

Laverty, D., Desai, R., Uchański, T., Masiulis, S., Stec, W., Malinauskas, T., Zivanov, J., Parson, E., Steyaert, J., Miller, K., and Aricescu, R. (2019). Cryo-em structure of the human $\alpha 1 \beta 3 \gamma 2$ gaba a receptor in a lipid bilayer. *Nature*, 565(7740):516–520. 257

Li, T., Shen, Y., Lin, F., Fu, W., Liu, S., Wang, C., Liang, J., Fan, X., Ye, X., Tang, Y., Ding, M., Yang, Y., Lei, C., and Hu, S. (2019). Targeting ryr2 with a phosphorylation site–specific nanobody reverses dysfunction of failing cardiomyocytes in rats. *FASEB J*, 33(6):7467–7478. 256

Lolicato, M., Arrigoni, C., Mori, T., Sekioka, Y., Bryant, C., Clark, K. A., and Minor, D. L. (2017). K 2p 2.1 (trek-1)–activator complexes reveal a cryptic selectivity filter binding site. *Nature*, 547(7663):364–368. 251, 269

Lolicato, M., Natale, A. M., Abderemane-Ali, F., Crottès, D., Capponi, S., Duman, R., Wagner, A., Rosenberg, J. M., Grabe, M., and Minor, D. L. (2020). K2p channel c-type gating involves asymmetric selectivity filter order-disorder transitions. *Science advances*, 6(44):eabc9174. 253, 276

Lolicato, M., Riegelhaupt, P. M., Arrigoni, C., Clark, K. A., and Minor Jr, D. L. (2014). Transmembrane helix straightening and buckling underlies activation of mechanosensitive and thermosensitive k2p channels. *Neuron*, 84(6):1198–1212. 249, 251

Macpherson, A., Scott-Tucker, A., Spiliotopoulos, A., Simpson, C., Staniforth, J., Hold, A., Snowden, J., Manning, L., van den Elsen, J., and Lawson, A. D. G. D. (2020). Isolation of antigen-specific, disulphide-rich knob domain peptides from bovine antibodies. *PLoS Biol*, 18(9):e3000821. 237

Maingret, F., Fosset, M., Lesage, F., Lazdunski, M., and Honoré, E. (1999a). Traak is a mammalian neuronal mechano-gated k+ channel. *J Biol Chem*, 274(3):1381–7. 244

Maingret, F., Patel, A., Lesage, F., Lazdunski, M., and Honoré, E. (1999b). Mechano- or acid stimulation, two interactive modes of activation of the trek-1 potassium channel. *J Biol Chem*, 274(38):26691–6. 244, 269

McClenaghan, C., Schewe, M., Aryal, P., Carpenter, E. P., Baukrowitz, T., and Tucker, S. J. (2016). Polymodal activation of the trek-2 k2p channel produces structurally distinct open states. *J Gen Physiol*, 147(6):497–505. 251

Miller, A. N. and Long, S. B. (2012). Crystal structure of the human two–pore domain potassium channel k2p1. *Science*, 335(6067):432–436. 245

Murbartián, J., Lei, Q., Sando, J. J., and Bayliss, D. A. (2005). Sequential phosphorylation mediates receptor- and kinase-induced inhibition of trek-1 background potassium channels. *J Biol Chem*, 280(34):30175–84. 244

Muyldermans, S. (2013). Nanobodies: natural single-domain antibodies. *Annu Rev Biochem*, 82:775–97. 237

Nisonoff, A., Wissler, F., Lipman, L. c., and Woernley, D. (1960). Separation of univalent fragments from the bivalent rabbit antibody molecule by reduction of disulfide bonds. *Archives of Biochemistry and Biophysics*, 89(2):230–244. 234

Noël, J., Zimmermann, K., Busserolles, J., Deval, E., Alloui, A., Diochot, S., Guy, N., Borsotto, M., Reeh, P., Eschalier, A., and Lazdunski, M. (2009). The mechano-activated k+ channels traak and trek-1 control both warm and cold perception. *EMBO J.*, 28(9):1308–18. 244

Pardon, E., Laeremans, T., Triest, S., Rasmussen, S. G., Wohlkönig, A., Ruf, A., Muyldermans, S., Hol, W. G., Kobilka, B. K., and Steyaert, J. (2014). A general protocol for the generation of nanobodies for structural biology. *Nature protocols*, 9(3):674–693. 258

Patel, A., Honoré, E., Lesage, F., Fink, M., Romey, G., and Lazdunski, M. (1999). Inhalational anesthetics activate two-pore-domain background k+ channels. *Nat Neurosci*, 2(5):422–6. 244

Piechotta, P. L., Rapedius, M., Stansfeld, P. J., Bollepalli, M. K., Erhlich, G., Andres-Enguix, I., Fritzenschaft, H., Decher, N., Sansom, M. S., Tucker, S. J., et al. (2011). The pore structure and gating mechanism of k2p channels. *The EMBO journal*, 30(17):3607–3619. 244

Pope, L., Lolicato, M., and Minor Jr, D. L. (2020). Polynuclear ruthenium amines inhibit k2p channels via a "finger in the dam" mechanism. *Cell chemical biology*, 27(5):511–524. 254

Porter, R. (1959). The hydrolysis of rabbit y-globulin and antibodies with crystalline papain. *Biochem J*, 73:119–26. 234

Sandoz, G., Douguet, D., Chatelain, F., Lazdunski, M., and Lesage, F. (2009). Extracellular acidification exerts opposite actions on trek1 and trek2 potassium channels via a single conserved histidine residue. *Proceedings of the National Academy of Sciences*, 106(34):14628–14633. 244, 246, 275

Sandoz, G., Tardy, M. P., Thümmler, S., Feliciangeli, S., Lazdunski, M., and Lesage, F. (2008). Mtap2 is a constituent of the protein network that regulates twik-related k+ channel expression and trafficking. *Journal of Neuroscience*, 28(34):8545–8552. 244

Sandoz, G., Thümmler, S., Duprat, F., Feliciangeli, S., Vinh, J., Escoubas, P., Guy, N., Lazdunski, M., and Lesage, F. (2006). Akap150, a switch to convert mechano-, ph-and arachidonic acid-sensitive trek k+ channels into open leak channels. *The EMBO journal*, 25(24):5864–5872. 244

Schewe, M., Nematian-Ardestani, E., Sun, H., Musinszki, M., Cordeiro, S., Bucci, G., de Groot, B. L., Tucker, S. J., Rapedius, M., and Baukrowitz, T. (2016). A non-canonical voltage-sensing mechanism controls gating in k2p k+ channels. *Cell*, 164(5):937–949. 244, 252

Schewe, M., Sun, H., Mert, U., Mackenzie, A., Pike, A. C., Schulz, F., Constantin, C., Vowinkel, K. S., Conrad, L. J., Kiper, A. K., Gonzalez, W., Musinszki, M., Tegtmeier, M., Prydell, D., Belabed, H., Nazare, M., de Groot, B., Decher, N., Fakler, B., Carpenter, E., Tucker, S., and Baukrowitz, T. (2019). A pharmacological master key mechanism that unlocks the selectivity filter gate in k+ channels. *Science*, 363(6429):875–880. 254

Sun, H., Luo, L., Lal, B., Ma, X., Chen, L., Hann, C. L., Fulton, A. M., Leahy, D. J., Laterra, J., and Li, M. (2016). A monoclonal antibody against kcnk9 k+ channel extracellular domain inhibits tumour growth and metastasis. *Nature communications*, 7(1):1–12. 256

Uchański, T., Masiulis, S., Fischer, B., Kalichuk, V., López-Sánchez, U., Zarkadas, E., Weckener, M., Sente, A., Ward, P., Wohlkönig, A., Zögg, T., Remaut, H., Naismith, J. H., Nury, H., Vranken, W., Aricescu, A., Pardon, E., and Steyaert, J. (2021). Megabodies expand the nanobody toolkit for protein structure determination by single-particle cryo-em. *Nat Methods*, 18(1):60–68. 257

Wei, G., Meng, W., Guo, H., Pan, W., Liu, J., Peng, T., Chen, L., and Chen, C.-Y. (2011). Potent neutralization of influenza a virus by a single-domain antibody blocking m2 ion channel protein. *PloS one*, 6(12):e28309. 256

Wulff, H., Christophersen, P., Colussi, P., Chandy, K., and Yarov-Yarovoy, V. (2019). Antibodies and venom peptides: new modalities for ion channels. *Nat Rev Drug Discov*, 18(5):339–357. 255

Zielonka, S., Empting, M., Grzeschik, J., Könning, D., Barelle, C. J., and Kolmar, H. (2015). Structural insights and biomedical potential of ignar scaffolds from sharks. *MAbs*, 7(1):15–25. 237

Chapter 5

VHH antibodies as Tools

In the last chapter we saw that VHH antibodies were capable of functionally modulating TREK-2. A prerequisite for functional modulation is binding, and as such, VHH antibodies should be able to be used to detect channels in native tissues. In this chapter, we provide a proof of concept that nanobodies can be engineered in order to detect the presence of full length channels on the plasma membrane. We also show that they show high selectivity by not binding to closely related channels. In addition, we try to optimise expression of the VHH antibodies in order to produce more protein and minimise purification required for tissue staining and imaging, exploring options in both bacterial and mammalian expression systems.

5.1 Disclaimer

Some of the work presented in this chapter was carried out with a M.Phys Student working in the Tucker group, Jenna Elliot (JE) and an Oxion D.Phil Rotation Student, Kathryn Smith (KS) both of whom were day to day supervised by myself and I would like to clarify here the work that they contributed to this chapter in one place and thank them for their assistance with the project. Additionally I would like to thank Harvey Davis (HD) for providing rat Superior Cervical Ganglia tis-

sue slices and providing RNA-seq data to support the findings in this chapter. The work in this chapter was all designed by me (AC) and Stephen Tucker (SJT).

Experimental Strategy and Design: AC, SJT

Small scale expression trials of VHH antibodies in different *E. coli* strains: AC

Subcloning of VHH domain constructs into pET-22b, pET-28a, pHLSec: AC

Making Competent wk6, BL21(DE3) RIPL + ERv1p + DsbC cells: AC

Cloning Sorttag: AC

Expression and Purification of HRV3C, TEV, Sortase, Cytosolic VHH antibodies: AC and KS

C-terminal VHH domain tagging: AC

Sorttaging: AC and KS

Early VHH antibody expression and TREK-2 Expression: AC

TREK-2/TREK-1/TRAAK overlap extension PCR: AC

Other K2P-mCherry subcloning: AC and KS

VHH antibody fixing, permeabilisation, immunostaining, Imaging and Processing (includingFigure 5.9) JE with **troubleshooting by AC.**

VHH antibody fixing, permeabilisation, immunostaining, Imaging and Processing (including Figure 5.10 KS with **troubleshooting by AC.**

pScFcAc vector design and base vector creation: AC and SJT

VHH antibody cloning into pScFcAc and subsequent expression trials: KS

SCG immunostaining: AC

SCG preparation, RNA-seq data and plotting: Harvey Davis

5.2 Introduction

5.2.1 The need for tools for localisation

Immunohisto(cyto)chemistry (IHC) is an important method to visualise the distribution and amount of a certain molecule in a tissue using specific antibodies raised against the molecule of interest. Importantly, the technique is non-destructive and therefore allows the experimenter to see the expression pattern of a molecule in the context of a living tissue (Schacht and Kern, 2015). The steps in a simplified process can be summarised as follows:

(1) Tissue preparation

(2) Tissue Fixation, embedding, sectioning and hydration

(3) Blocking

(4) Antibody incubation

(5) Thorough Washing

(6) Detection

As one might expect, this process requires optimisation at every step, from ensuring the tissue is healthy and treated appropriately to selecting the correct antibody, concentration, blocking agent and detection means (O'Hurley et al., 2014). We sought to provide a proof of principle that we could detect VHH antibody

binding on cells which were expressing TREK-2 and show their selectivity towards TREK-2 over other closely related channels from the K2P family. Through doing so, we hoped to select candidates which in the future could be used as tools to detect TREK-2 expression and localisation in native tissues, and in this chapter we provide some very preliminary data that this soon could be realised with our panel of VHH antibodies by selectively staining neurons in a rat superior cervical ganglion (SCG).

5.2.2 Currently Available Antibodies

A huge problem with using commercially available antibodies is they are often polyclonal, expensive, un-engineerable and as to whether the antibodies are usable for a given application is very much in the hands of the company, where often limited information is available in order for the company to protect their products. While there are online databases which are curated for antibodies raised against a target and listing the citations available for it (e.g. CiteAb), most antibodies remain uncited making them unknown entities. As an example, of the 149 commercially available antibodies raised against TREK-2, only 19 of them are suitable for IHC, but only 2 of these have been cited. Furthermore 144 of all antibodies raised against TREK-2 have no citations available, while 4 out of the 5 with citations have all been cited less than 3 times.

The highest cited antibody against TREK-2 (11 citations) is commercially available from Alomone Labs. The antibody was raised against rat TREK-2 and shows specific staining for HEK293 cells expressing TREK-2 (Acosta et al., 2014). This antibody has been used to show TREK-2 expression in taste receptor cells (Lin et al., 2004) and when applied to DRGs and Dorsal roots, it was used to show TREK-2

expression in IB4–binding C-fibre nociceptors (Acosta et al., 2014). The Alomone labs antibody is reported to have been designed to recognise TREK-2 from mouse, rat and human samples for use in western blot and IHC applications and requires a fluorescent secondary antibody. However, the gold standard remains applying the antibody to a knockout mouse model, which has not been done for this antibody, or indeed any other antibody raised against TREK-2.

We have a library of approximately 50 VHH antibodies raised against TREK-1 and TREK-2 and we wanted to see if we could use them to selectively detect the target channel in cells expressing the channel. Ultimately, the aim would be to move these into native tissues, taking inspiration from an elegant study in which a Fab fragment raised against mouse TRAAK was used to show that TRAAK is expressed in the Node of Ranvier (Brohawn et al., 2019).

5.2.3 Advantages of VHH antibodies

The advantage of this approach is that monoclonal VHH antibodies can be produced by expression of a known DNA sequence, rather than the requirement for immunisation and sera for every experiment which produces different polyclonal antibodies each time. Not only does this allow unambiguous definition of the epitopes through detailed structural studies but also ensures that the same epitope is targeted every time, allowing reproducibility, and affords the opportunity to engineer the protein. By prioritising the engineering of VHH antibodies that bind extracellularly to reduce the need for permeabilisation as well as to ensure that the epitope recognised by the VHH antibody is present in native cells (protein used for immunisation is often truncated for expression purposes). The inherent small size of VHH antibodies allows them to diffuse more than four times better than larger

antibodies (Pizzo et al., 2018; Perruchini et al., 2009).

Ideally candidate VHH antibodies to be used in tissues should be: biochemically well behaved, bind tightly, bind extracellularly and bind specifically, all of which can be addressed in house. As well as producing detectable antibodies optimisation of VHH antibody expression is essential in order to make this process efficient not just for localisation studies, but also for detailed structural and functional studies.

5.3 Results

5.3.1 VHH antibody expression and purification in *E. coli*

As explained previously, VHH antibodies have disulphide bonds as an integral part of their structure. Disulphide bonds are unable to form inside cells which have a reducing environment, but can form via a catalysed reaction in the periplasm involving proteins of the disulphide bond forming family (DsbA-D), as seen in Figure 5.1. Producing protein in the periplasm has a number of other advantages for protein purification as well as being conducive to disulphide formation; there are fewer proteases than in the cytoplasm and many have their own substrates, there are fewer proteins in general and the periplasm can be selectively released by osmotic shock (Robbens et al., 1995; Wan and Baneyx, 1998; Singh et al., 2013).

VHH antibodies were produced in *E. coli* for the majority of this project. The purification protocol can be seen fully in Materials and Methods and is adapted from Pardon et al. (2014). The VHH antibodies received from Nanobodies4INSTRUCT had been cloned downstream of the PelB signal sequence, a 22 amino acid N-

terminal leader sequence which targets them to the Sec translocase for unfolded secretion into the periplasmic space (Lei et al., 1987) and contain a C-terminal hexa-his (His_6) tag for Immobilised Metal Affinity Chromatography (IMAC) and a Capture select^{TM} tag within the pMESy4 vector, shown in Figure 5.1. PelB is cleaved by a signal peptidase in the periplasm after secretion. VHH antibodies can then be purified out of the periplasmic space by osmotically shocking the outer membrane and removing cell debris. Subsequent purification using Cobalt (TALON) or Nickel (Ni-NTA) can isolate pure protein as verified by an SDS-PAGE gel.

The yields of this process in our hands were variable (0.1-5mg per litre culture) between different batches and even within batches (6 different VHH antibodies were often purified in parallel). We attributed this variability of yield to the efficiency of the osmotic shock process. Ensuring the osmotic shock buffer was made fresh and ice cold helped increase yield. The single largest consistent increase in yield came from using Ni-NTA over TALON, where yields were consistently a least 4-fold higher, although the variability still remained. A number of orthogonal approaches to optimise expression in *E. coli* were attempted before trying to make fluorescent-tagged VHH antibodies for use in IHC studies.

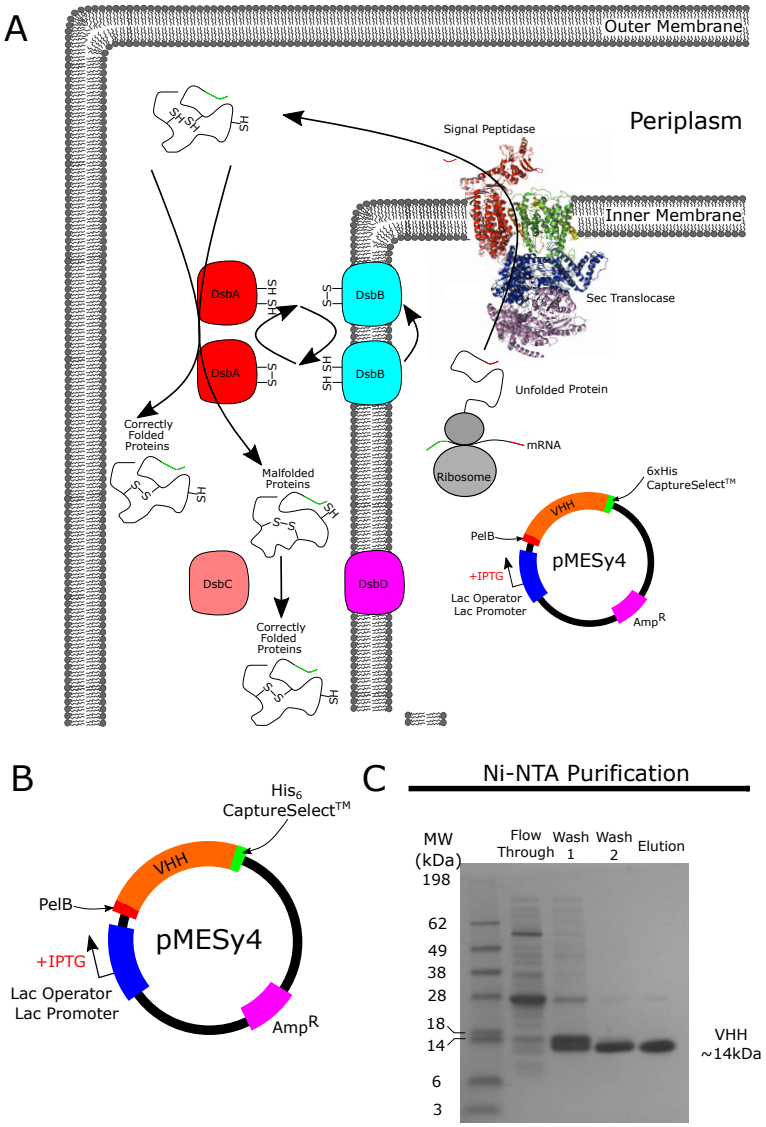


Figure 5.1: **Periplasmic Expression and Purification of VHH Antibodies**
A: Pictorial demonstration of the Expression Strategy. VHH antibodies in the pMESy4 plasmid were transformed into wk6 cells and residence maintained using ampicillin selection. VHH antibody expression was induced with IPTG. The PelB signal secretion sequence targets the unfolded protein for export via the Sec translocase and the signal peptide is cleaved by a signal peptidase after translocation. The VHH antibody folds in the periplasm, catalysed by proteins in the Dsb family. DsbA catalyses *de novo* disulphide bond formation which is itself regenerated using the DsbB redox partner. The disulphide bond isomerase DsbC corrects malfolded VHH antibodies and is itself regenerated using the DsbD redox partner. In this manner, correctly folded VHH antibodies are produced in the periplasm.
B: Plasmid map showing details of the pMESy4 vector.
C: SDS-PAGE gel to assess the purity of the VHH antibodies purified by Ni-NTA.

5.3.2 Optimisation of expression in *E. coli*

5.3.2.1 Expression in different strains and whole cell purification

In an attempt to test expression, small scale purification of four VHH antibodies raised against a number of different protein targets were expressed and purified from three *E. coli* strains in parallel. BL21(DE3)-R3-pRARE2 and BL21(DE3)pLysS were tested as they encode rare codon tRNA genes and reduce the basal expression of recombinant genes respectively and the yield from TALON purification of these strains was compared to the yield from wk6su- which is routinely used for VHH antibody expression (Pardon et al., 2014).

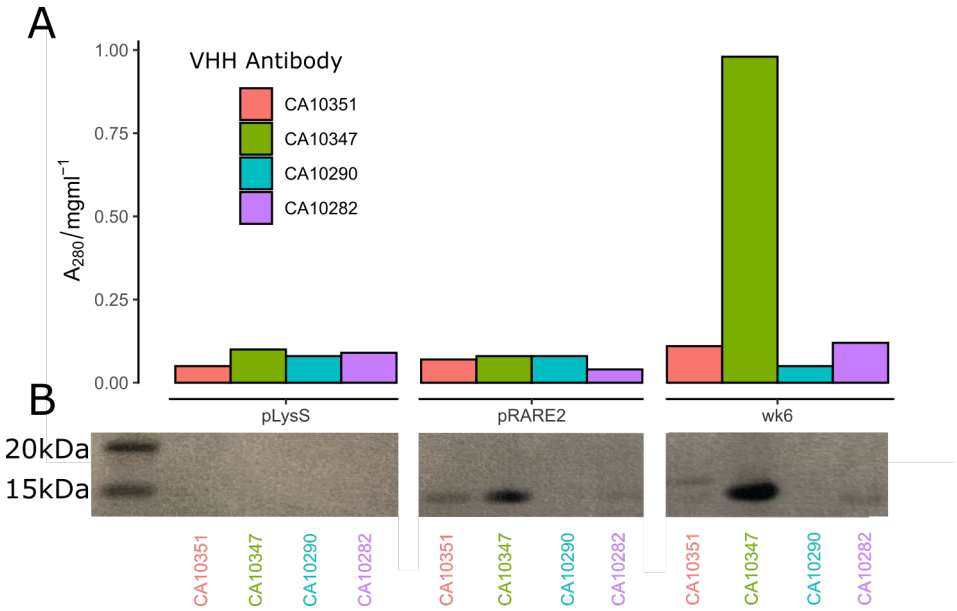


Figure 5.2: **VHH Antibody Expression in Different *E. coli* Strains**
A: A Bar graph quantifying the yield of a small scale VHH antibody grow up. The Absorbance values here are not corrected for the VHH antibody, instead they assume that 1Abs = 1mg/ml, and are hence overestimates of protein yield, however the relative yield between the different *E. coli* strains can be assessed.
B: A corresponding SDS-PAGE gel to assess the purity of the VHH antibodies. Some of the VHH antibodies could not be detected by Coomassie staining owing to their low concentration.

VHH antibody could be detected for all three *E. coli* strains. Yield from all of

the tested VHH antibodies expressed in BL21(DE3)-R3-pRARE2 and BL21(DE3)pLysS were low. Meanwhile yield of CA10347 in wk6 cells was high, however the differential yield between this VHH antibody and the other three also expressed in wk6 cells clearly shows the variability in VHH antibody recovery by this method. Taken together it suggests that expression is highest in the wk6su- strain, reconciling its use in routine VHH antibody expression (Pardon et al., 2014).

To remove the apparent variability in the osmotic shock process and in an attempt to increase the yield from VHH antibodies expressed in wk6su- *E. coli*, VHH antibodies were purified from the whole cell rather than just the periplasmic space. Rather than osmotically shocking the outer membrane, the whole cell was homogenised and lysed using a French press allowing purification of VHH antibodies from the whole cell rather than just the periplasmic space. Although a modest increase in yield was noted, the final preparation was less pure and required purification on a Sepharose 200 column which ultimately made the yield comparable with purification just from the periplasm (not shown).

5.3.2.2 Expression using a stronger Promoter

In an attempt to increase periplasmic expression of VHH antibodies, two VHH antibodies were subcloned into the pET-22b vector upstream of a PelB sequence and downstream of a T7 Promoter which is stronger than the Lac Promoter resident in the pMESy4 vector. By expression in any DE3 designated cells (encoding the T7 polymerase) the stronger promoter should in theory drive higher expression of the VHH antibodies.

Parallel expression and purification from BL21(DE3) cells with Ni-NTA showed an increased yield for one of the tested VHH antibodies (VHH61), but a decreased

yield for the other one (VHH67), suggesting that the stronger promoter does not obviously enhance VHH antibody yield. Again, this is consistent with the problem stemming from the variability in the osmotic shock rather than the expression *per se*.

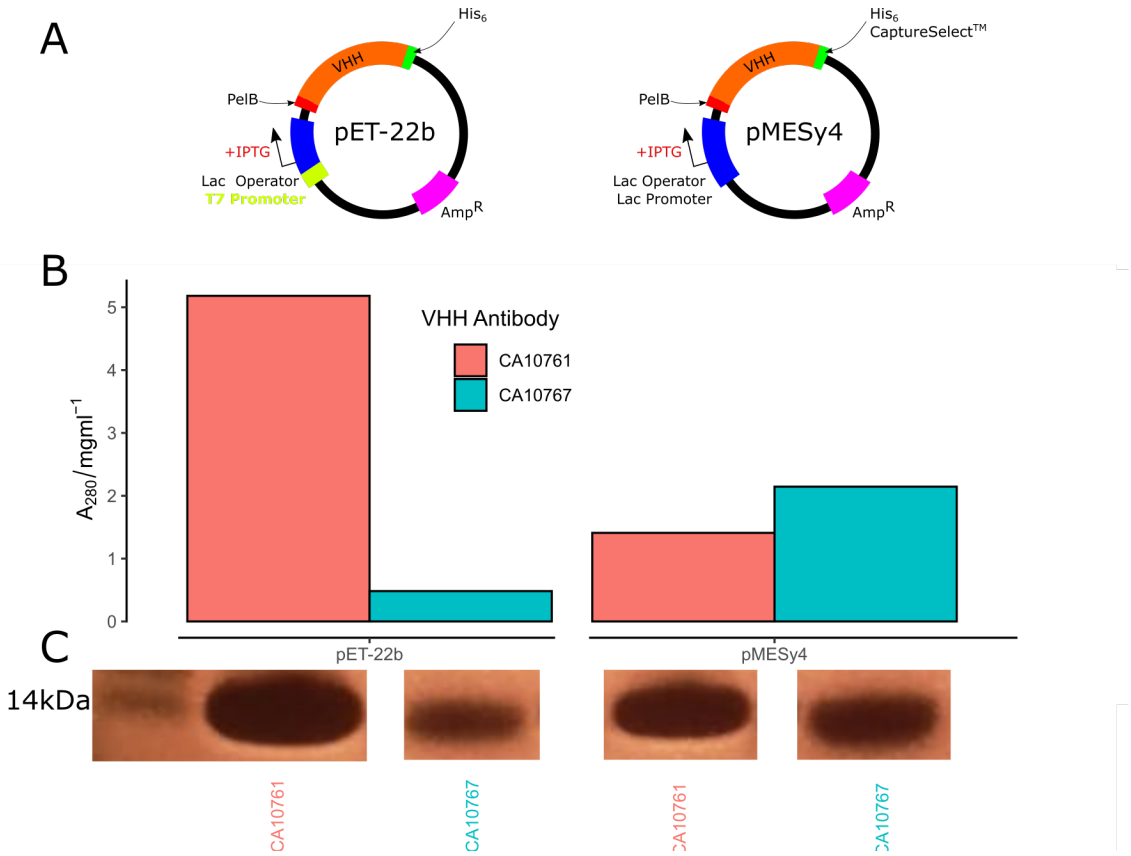


Figure 5.3: **VHH antibody Expression in Different Vectors**
A: Vector maps comparing the pET-22b and pMESy4 vectors showing main features.
B: A Bar graph quantifying the yield of a 1L VHH antibody grow up. The Absorbance values here are not corrected for the VHH antibody, instead they assume that 1Abs = 1mg/ml, and are hence overestimates of protein yield, however the relative yield between the different vectors can be assessed.
C: A corresponding SDS-PAGE gel to assess the purity of the VHH antibodies.

5.3.3 Immunohistocytochemistry on *Xenopus* Oocytes

In order to assess binding of unlabelled VHH antibodies, full length hTREK-2 was expressed in *Xenopus Laevis* oocytes and incubated with VHH antibodies. An anti-His_6 secondary antibody conjugated to Horseradish Peroxidase (HRP) was used to amplify the primary signal of the His_6-tag emanating from the VHH antibody. HRP catalyses the peroxidation of H_2O_2 and oxidises 3,3',5,5' Tetramethylbenzidine (TMB) to 3,3',5,5' Tetramethylbenzidine diimine (TMBDI), producing a blue solution that absorbs at 450nm. In this manner, successful binding of VHH antibody to TREK-2 on the oocyte surface should be detectable by the development of a blue signal after extensive washing as demonstrated pictorially in Figure 5.4.

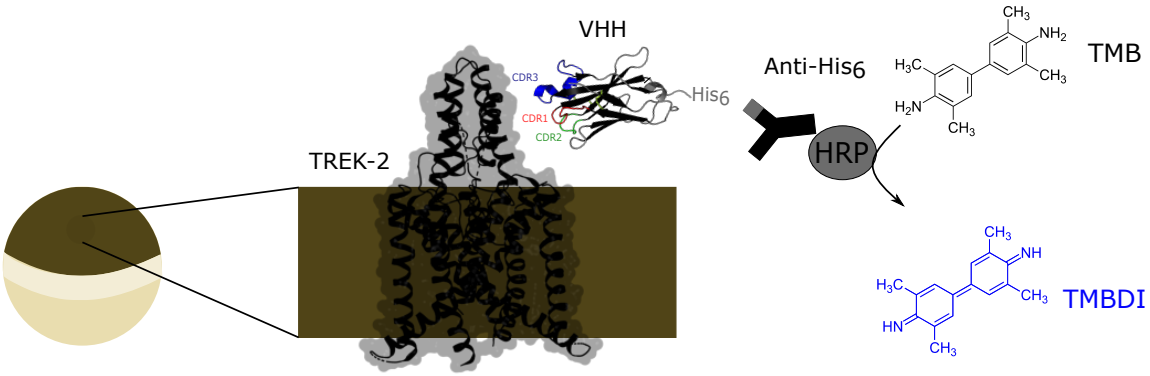


Figure 5.4: **Detection of VHH Antibody Binding to TREK-2 by IHC on *Xenopus* oocytes**
TREK-2 (black, PDB: 4XDJ) was expressed in *Xenopus* oocytes and detected by a VHH antibody. A secondary Anti-His_6 secondary antibody conjugated to Horse Radish Peroxidase was used to detect the presence of the His_6 tag present on the VHH antibody, and the presence indicated by a colour change to blue upon oxidation of TMB to TMBDI.

Whilst in principle this appeared to be a viable strategy for detecting VHH antibody binding, blue signal often appeared in negative control wells containing uninjected oocytes thus preventing unambiguous detection of binding. After many attempts to optimise this process, including increasing signal by channel expression, increased washing, altered VHH antibody incubation time, the presence of blue signal in the negative control persisted, preventing the development of this assay any further. After many attempts at troubleshooting, efforts were sidelined in favour of testing the unlabelled VHH antibodies for functional effects using the two electrode voltage clamp technique and producing fluorescent labelled VHH antibodies for unambiguous detection.

5.3.4 Expression of Fluorescent VHH antibodies in *E. coli*

In order to produce fluorescent VHH antibodies for potential use in IHC based assays and looking to the future, for immunostaining of native tissues, fluorescent VHH antibody production was attempted in *E. coli*. Many fluorescent proteins are unable to be translocated through the Sec translocase, meaning VHH antibody-fluorescent protein fusions are unsuitable for periplasmic expression, and even if they can be forced to translocate through sec (for example GFP can be translocated by fusion behind permaltose binding protein), then they often fail to fold correctly yielding inactive proteins (Feilmeier et al., 2000). GFP is reported to functionally fold if it is instead targeted to the Twin Arginine Translocase (Tat) System (Thomas et al., 2001), however this is paradoxical as it would prevent proper folding of the VHH antibody as the Tat system translocates folded protein and VHH antibodies are unable to fold owing to the reducing environment of the cellular interior.

In an attempt to produce C-terminal fluorescent conjugates from *E. coli* three orthogonal synthetic approaches were attempted. C-terminal labelling was cho-

sen to minimise disruption as the disulphide bonded β-sandwich framework of VHH antibodies places the C-terminus topologically on the other side to the three CDR loops. Either by expressing VHH antibodies in the cytoplasm (Veggiani and de Marco, 2011), C-terminally labelling the free carboxyl group on the C-terminus of unmodified purified VHH antibodies (Sélo et al., 1996) or by introducing a C-terminal sort-tag (Massa et al., 2016) for site specific labelling, we sought to produce fluorescent labelled VHH antibodies.

5.3.4.1 Cytosolic Expression and Purification of VHH antibodies

Although periplasmic expression and subsequent purification is attractive owing to the lower amount of impurities and the lack of decompartmentalisation of potentially disruptive proteases, being able to purify VHH antibodies from the cytosol could allow purification of VHH antibody fusions which are not tractable for periplasm extraction such as fluorescent labelled VHH antibodies. Integral to the structure of VHH domain antibodies are disulphide bonds which are needed for correct folding, so these need to be able to be formed wherever the VHH antibody is expressed. The cells therefore need to contain a cytoplasm with a reducing environment.

While commercial strains are available e.g. Origami/Rosetta-gami (Novagen) and SHuffle (NEB), in both strains the disulphide reducing pathways in the cytoplasm are disrupted (designated *Δgor ΔtrxB*) meaning the yields are typically low as there is no catalyst for *de novo* disulphide bond formation. To overcome this limitation disulphide bond containing proteins have been successfully produced in the cytoplasm of cells expressing the mitochondrial sulfhydryl oxidase Erv1p and the disulphide bond isomerase DsbC (Nguyen et al., 2011; Veggiani

and de Marco, 2011; Veggiani et al., 2016). Here catalysis of *de novo* disulphide bond formation is carried out by Erv1p.

In an attempt to express VHH antibodies in the cytoplasm, a selection of VHH antibodies were subcloned into the pET-28a(+) vector and transformed into BL21 (DE3) RIPL cells containing Erv1p and DsbC (kind gift of M. Howarth, (Veggiani et al., 2016)). Residence of both the Erv1p and DsbC and the VHH antibody was maintained by double antibiotic selection with chloramphenicol and kanamycin, and Erv1p and DsbC expression was induced by arabinose prior to induction of VHH antibody expression by IPTG, as demonstrated in Figure 5.5A.

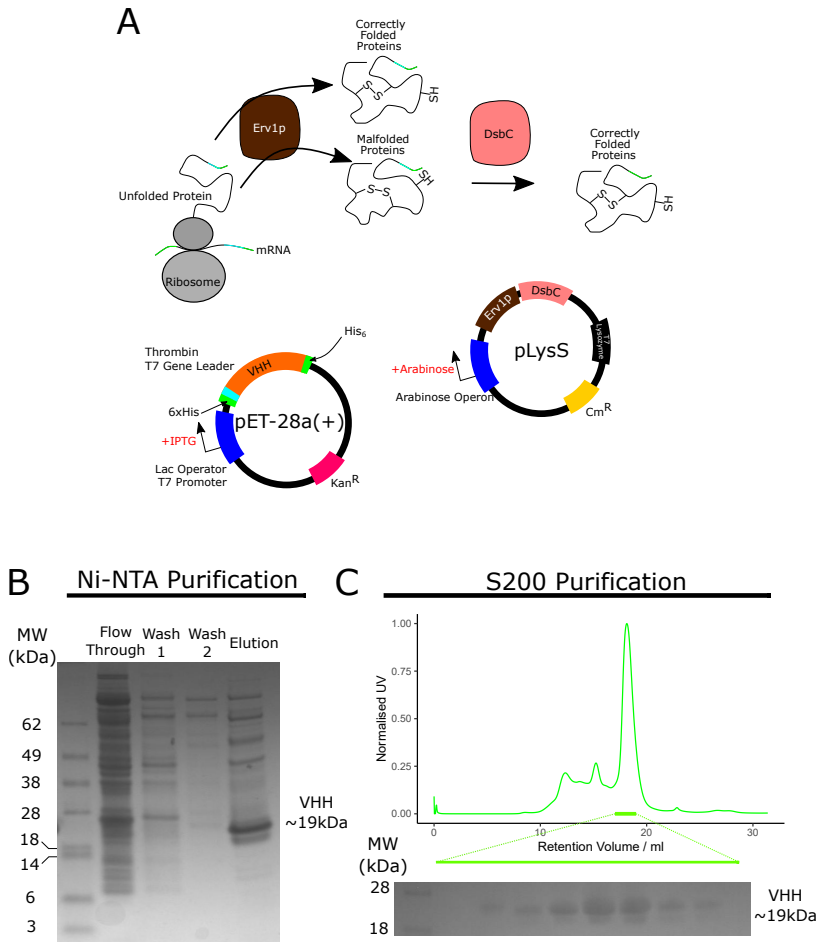


Figure 5.5: **Cytosolic Expression and Purification of VHH Antibodies**
A: Pictorial demonstration of the Expression Strategy. The Erv1p and DsbC genes were transformed into BL21(DE3) cells in the pLysS plasmid, and residence maintained using chloramphenicol selection. VHH antibodies were transformed into BL21(DE3) cells in the pET-28a plasmid and residence maintained using kanamycin selection. Dual Kanamycin and Chloramphenicol selection ensured maintenance of both plasmids. Erv1p and DsbC were induced by arabinose prior to induction of VHH antibody expression with IPTG. The mitochondrial sulfhydryl oxidase Erv1p catalyses *de novo* disulphide bond formation in the VHH antibody, while the disulphide bond isomerase DsbC corrects malfolded VHH antibodies. In this manner, correctly folded VHH antibodies are produced from the cytoplasm.
B: IMAC purification of VHH antibodies produced from the cytosol. Following cell harvesting, homogenisation and cell disruption, the soluble fraction is incubated with Ni-NTA. The flow through, two wash steps and elution are shown and over the course of the purification, an enrichment of VHH antibody can be seen.
C: SEC purification of VHH antibodies produced from the cytosol. The IMAC elution is injected onto a sepharose 200 column attached to an Akta purification system which separates proteins according to size. Through this method, relatively pure VHH antibody can be recovered.

Relatively pure protein was obtained by a combination of IMAC (Figure 5.5B) and size exclusion chromotography (Figure 5.5C), however, purity and homogeneity of the expressed protein should be further refined by washing Ni-NTA bound His_6-tagged VHH antibody with a higher background of imidazole before being suitable for functional studies. The protein expression was also lower than the reported 10s of milligrams (Veggiani and de Marco, 2011) but in line with yields obtained by periplasmic extraction (milligrams). Ultimately efforts on this front were sidelined in favour of attempting to generate fluorescent labelled VHH antibodies through other means. Nevertheless this result serves as a useful proof of principle that VHH antibodies raised against the K2P channels can be purified from the cytosol, thus in theory allowing fluorescent VHH antibody production via this route in the future.

5.3.4.2 C-terminal Tagging of VHH antibodies

Using purified unmodified protein, selective labelling of the free carboxyl group at the C-terminus of the VHH antibody was attempted by adapting a protocol for N-terminal labelling (Sélo et al., 1996). The pH was reduced to pH 6.5 to ensure that lysine ε-amino groups, side chain carboxyls of aspartate and glutamate are protonated but the carboxy terminus is deprotonated and the labelling reaction was extended to be overnight with a five time molar excess of Cy^{TM}3b mono NHS ester to promote inefficient labelling. Removal of the free dye was difficult, as free dye was eluted from Sephadex G-25 columns, and subsequent concentration was impossible as the dye stuck to the concentrator filters. Ideally all dye needs to be removed for downstream applications as it is very likely to non-specifically bind to cells and other hydrophobic surfaces. In addition, the inability to remove free dye made it impossible to quantify the amount of labelled protein and hence the labelling efficiency.

Based on the inability to C-terminally label at the free carboxyl group, focus was moved towards the use of sortase, a bacterial cell wall transpeptidase (Mazmanian et al., 1999) re-purposed for site-specific conjugation, which has been used successfully to conjugate fluorphores and other functionalities onto VHH antibodies (Massa et al., 2016). The sortase transpeptidation reaction (Figure 5.6A) involves the sortase recognising a LPETGG motif (Sortase tag, hereby named Sorttag) and cleaving upstream of the two glycines to form a VHH antibody acyl-sortase intermediate. The His_6-tagged sortase can then be regenerated by nucleophilic attack of a poly(glycine) synthetically linked to a fluorphore, (a number of which are commercially available), thus producing a site-specifically labelled VHH domain antibody. Subsequent purification relies on the untagged VHH antibody, the sortase and the VHH antibody acyl-sortase intermediate containing a His_6 tag, while the label and site-specific conjugated VHH antibody do not contain a his_6-tag, allowing purification by IMAC. Owing to the difference in size between the label and the site-specific conjugated VHH antibody, these can then be separated using a Superdex 75 column (Massa et al., 2016).

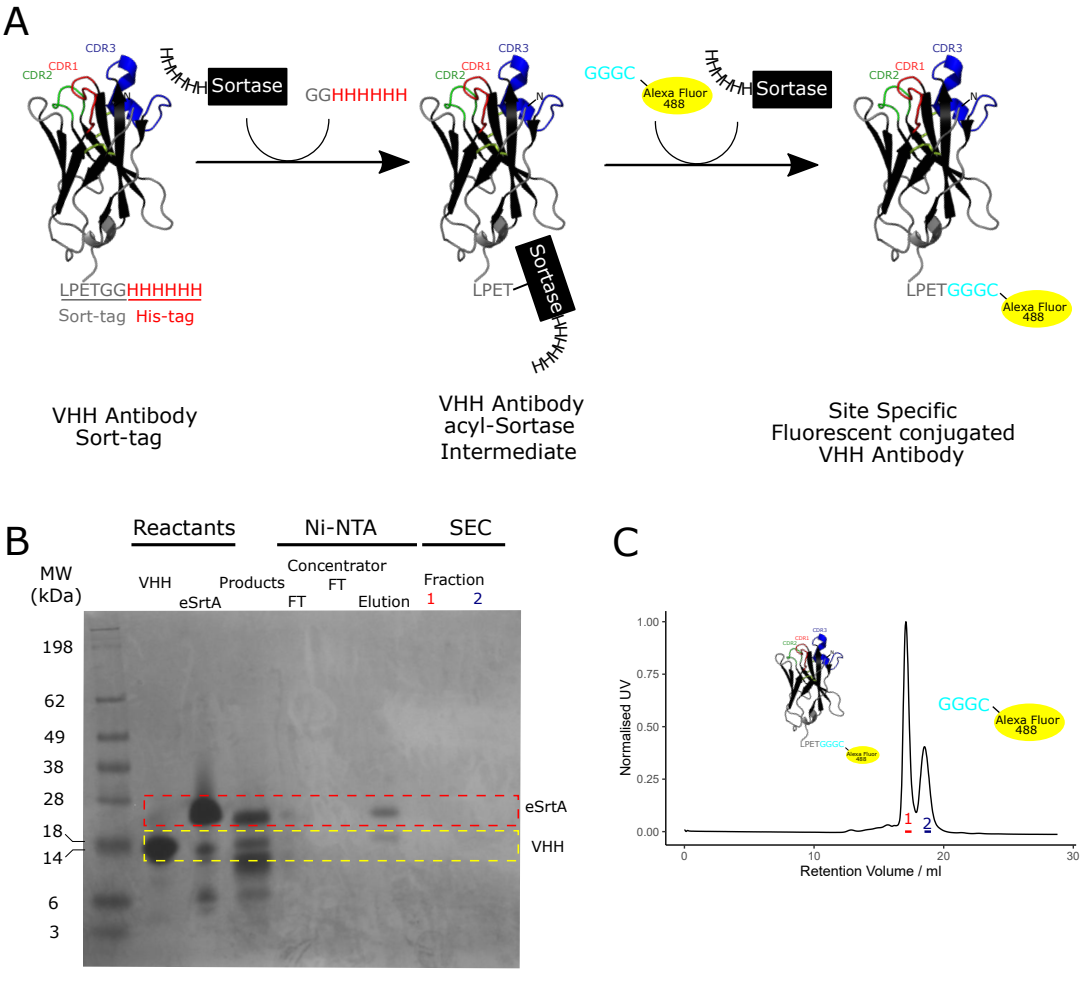


Figure 5.6: **Sorttagging of VHH Antibodies**
(Caption next page.)

Figure 5.6: (Previous page.)**Sorttagging of VHH Antibodies**
A: Schematic of the Sortase Reaction. A C-terminal sortase tag, 'Sorttag' (LPETGG, grey) is cloned upstream of the His_6-tag (red). The sortase recognises the LPETGG sequence and cleaves after the threonine, thus removing the His_6 tag and forming a VHH antibody acyl-sortase intermediate. The His_6-tagged sortase can then be re-generated by nucleophilic attack of the the GGGC-linked Alexa Fluor 488 which replaces the sortase in a site-sepcific manner. Importantly, this means that only the site-specific fluorescent conjugated VHH antibody and the free GCCC-Alexa Fluor 488 is not His_6 tagged, allowing subsequent purification using Ni-NTA. Based on a figure in (Massa et al., 2016).
B: Sortase Reaction Gel. Lane 1: Marker, Lanes 2-3: Reactants (VHH and eSrtA), lane 4: Products, lanes 5-7 Ni-NTA purification (Flow through, concentrator Flow through and elution), lanes 8-9 Size-Exclusion Chromatography purification (Fraction 1 (red) and Fraction 2(blue).
C: Size Exclusion Chromatography. The Flow through of the Ni-NTA was injected onto a Superdex 75 column attached to an Akta system and eluted as two fractions. The higher molecular weight fraction (Fraction 1, red) is thought to correspond to the Site-specific fluorescent conjugated VHH antibody while the lower molecular weight fraction (Fraction 2, blue) is thought to correspond to free dye.

In order to site-specifically label VHH antibodies, a Sorttag was cloned at the C-terminus of the VHH antibody using inverse PCR, upstream of the His_6 and CaptureSelect^{TM} C-terminal tags. The VHH domain-antibody-Sorttag-6H-CaptureSelect^{TM} was expressed in Wk6su- and purified by periplasmic extraction and the sortase was expressed and purified as detailed in (Chen et al., 2011). The sorttagging reaction was carried out based on the optimised protocol published in Massa et al. (2016) (VHH antibody: Sortase : label, 1:3:30), but the total reaction volume reduced five-fold to accommodate the small amount of fluorophore used in this pilot experiment.

The Sorttaging was carried out overnight followed by subsequent IMAC and SEC in an attempt to isolate pure site-specific conjugated VHH antibody. However, site-specifically labelled VHH antibody could not be seen in the IMAC flow through (Figure 5.6B, lane 5) owing to the small amount of protein, making it impossible to assess successful labelling at this point. As expected, the sortase and the untagged VHH antibody could both be eluted from the Ni-NTA column with high imidazole (Figure 5.6B, lane 7). The Ni-NTA flow through was applied to an S75 column and eluted as two peaks (Figure 5.6C), as described in (Massa et al., 2016). Both peaks absorbed at 488nm but only the larger peak (peak 1, Figure 5.6B) absorbed at 280nm consistent with the larger peak being Alexa488 conjugated VHH antibody and the smaller peak (peak 2, Figure 5.6B) being free Alexa488, and consistent with the result reported in Massa et al. (2016). However, once again, these two fractions were not visible on an SDS-PAGE gel (Figure 5.6B, lanes 8-9) owing to the small amount of labelled protein.

While this pilot experiment looks promising as a proof of concept, the labelling efficiency is poor, especially when it is considered that Alexa488 was in large molar excess for the sortagging reaction and not in line with the reported efficiency

(Massa et al., 2016). Scaling up the reaction and further refinement of sortase purity via purification by SEC may help to further increase the labelling efficiency, but time did not permit this to be carried out. Troubleshooting steps could also include a control reaction without the Alexa488 and detection of the VHH-antibody acyl-sortase intermediate either by SDS-PAGE and/or Western blot using an anti-His_6 primary antibody to check the functionality of the purified sortase. Nevertheless, this preliminary result may serve as an important framework for making bright conjugated VHH antibodies in the future as only very small quantities are needed for detection in immunohistocytochemistry.

5.3.5 Expression of VHH antibodies in Mammalian Cells

VHH antibodies are mammalian proteins and so it follows that expression in mammalian cells is a logical place to attempt larger scale production. In order to minimise the amount of purification required for downstream applications where blocking is typically required to remove non-specific binding, we opted to harvest VHH antibodies from the media. As such the VHH antibodies were secreted by mammalian cells as C-terminally linked fluorescent fusion proteins. A signal sequence upstream of the VHH antibody targets them for secretion into the Endoplasmic Reticulum (ER) where disulphides can form to allow correct folding. By simply harvesting serum, this would potentially prevent the need for the blocking step as the media is supplemented with 10% Fetal Bovine Serum (FBS). The major component of FBS is Bovine Serum Albumin, BSA, (reported to be at a concentration of 50mg/ml, Geyer et al. (2017)) which is traditionally used as a blocking agent in Western blots and immunohistocytochemistry.

99% of the protein content of serum is composed of albumin, total IgG, transferrin, fibronen, total IgA, α-2-microglobulin, total IgM, α-1-antitrypsin, C3 com-

plement, haptoglobin, α-1-acid glycoprotein, apolipoprotein-B, apolippoprotein-A1, lipoprotein(a), factor H, ceruloplasmin, C4 complement, complement factor B, pre-albumin, C9 complement, C1q complement and C8 complement whilst the final 1% is made up of hundreds of proteins (Issaq et al., 2007; Anderson and Anderson, 2002). Although the molecular identities are not overly important, it is worth noting that the serum contains IgA and IgM; that is bovine antibodies which will be important to consider for downstream applications involving secondary antibodies, and also makes the downstream purification more challenging as BSA and other components compete with the His_6-tag for binding of Ni-NTA during purification. If the protein is to be purified, the media should be replaced with media supplemented with 1% FBS rather than the usual 10% FBS immediately prior to transfection (Aricescu et al., 2006).

5.3.5.1 Expression of C-terminal mVenus tagged VHH antibodies

In order to produce fluorescent labelled VHH antibodies, a selection of VHH antibodies were subcloned into the pHLSec vector (Aricescu et al., 2006) downstream of the signal secretion sequence and upstream of a C-terminal mVenus (kind gift of Paul Miller) in order to produce VHH antibodies in media (Figure 5.7A.) VHH antibody-mVenus fusion proteins could be detected in media taken from transfected cells along with other media proteins by SDS-PAGE (Figure 5.7C, lanes 5-11) but not in an untransfected control (Figure 5.7C, Lane 3). Unambiguous detection of the His_6-tagged VHH antibody-mVenus fusions from transfected cells but not the untransfected control could be shown by Western blotting using an anti-His_6 antibody (Figure 5.7D) or by running the protein on a Native-PAGE gel and exciting at 488 nm (Figure 5.7E). The concentration of the fluorescent fusion was calculated by measuring the absorbance at 515 nm using a photospectrometer or plate reader, away from the other protein absorption peaks (Figure 5.7B) and

was typically in the µM to mM range.

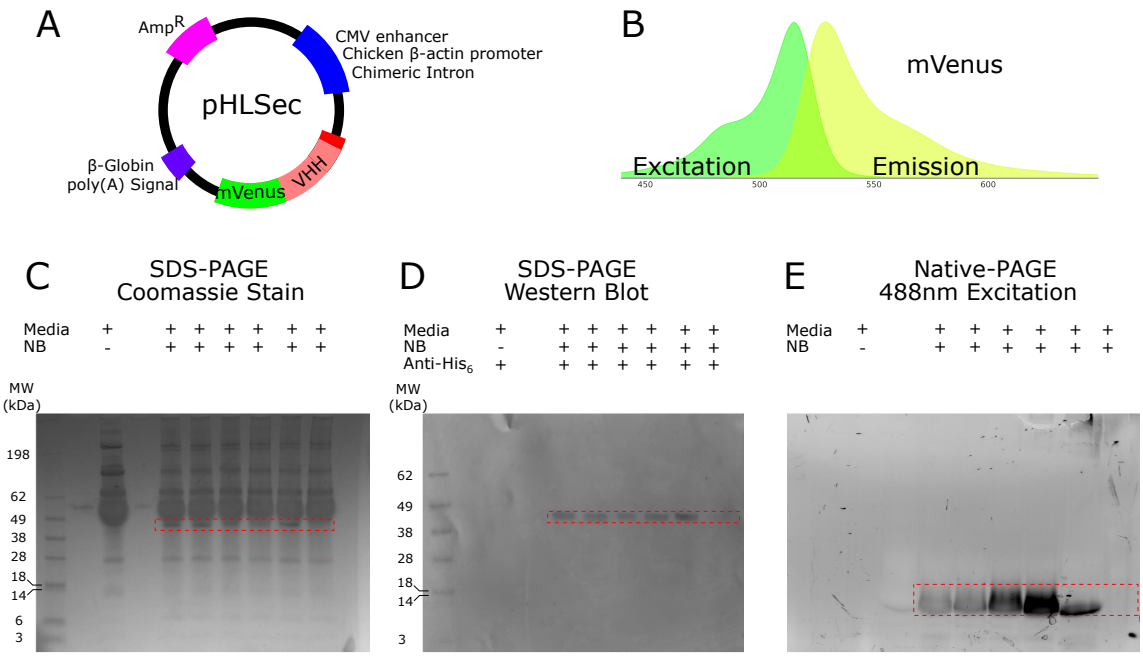


Figure 5.7: **Expression of C-terminal mVenus Tagged VHH Antibodies**
A: Plasmid map showing VHH antibody cloning downstream of the signal secretion sequence and upstream of mVenus.
B: Absorption and emission spectra of mVenus fluorophore.
C: SDS-PAGE of untransfected media (lane 3) and six expressed VHH antibodies (lanes 5-11).
D: Western blot of untransfected media (lane 3) and six expressed VHH antibodies (lanes 5-11) detected using a anti-His_6 primary antibody conjugated to HRP and detected using TMB substrate.
E: Native PAGE gel of untransfected media (lane 3) and six expressed VHH antibodies (lanes 5-11) detected by excitation at 488nm to show fluorescence of the mVenus fluorophore.

5.3.5.2 Creating a Modular Mammalian Expression System

Although the yield from the pHLSec vector was amenable to immunohistocytochemistry studies in mammalian cells (see IHC on Mammalian Cells), the literature suggested that increased expression could be obtained by placing the protein of interest upstream of a Single Chain Constant Fragment (ScFc). In this unique arrangement, which is reported to drive high levels of protein expression, a 59

amino acid linker connects the CH2 of one heavy chain to the CH3 domain of the other heavy chain together to form a single chain (Newnham et al., 2015), as shown in Figure 5.8B.

A new modular vector (pScFcAc) was therefore designed and cloned, based on a modified pLExm vector (Aricescu et al. (2006), for full details of modification, see Materials and Methods) to allow mammalian expression of VHH antibodies which could be cloned into this new vector upstream of a ScFc (Figure 5.8). The vector was designed to include two pairs of restriction sites (PstI and HindIII, and BamHI and Acc65I/KpnI) to allow restriction cloning of VHH antibodies and fluorescent proteins, separated by two protease sites (HRV3C and TEV) to allow subsequent production of both tagged and untagged VHH antibodies from a single vector.

Two base vectors containing GFP and mCherry between the HRV3C and TEV cleavage sites were made and six VHH domain antibodies cloned upstream of the HRV3C cleavage site of the GFP-containing vector. Expression trials are still underway for this vector, although it appears that this vector does not drive higher expression of GFP-linked VHH domain antibodies in our hands. GFP signal could be detected but the concentration is too low to be seen on an SDS-PAGE gel or Native-PAGE gel. Whether or not this is due to problems with the humanisation of the DNA sequence or a difference in IgG1 sequence will need to be addressed, however time did not permit troubleshooting.

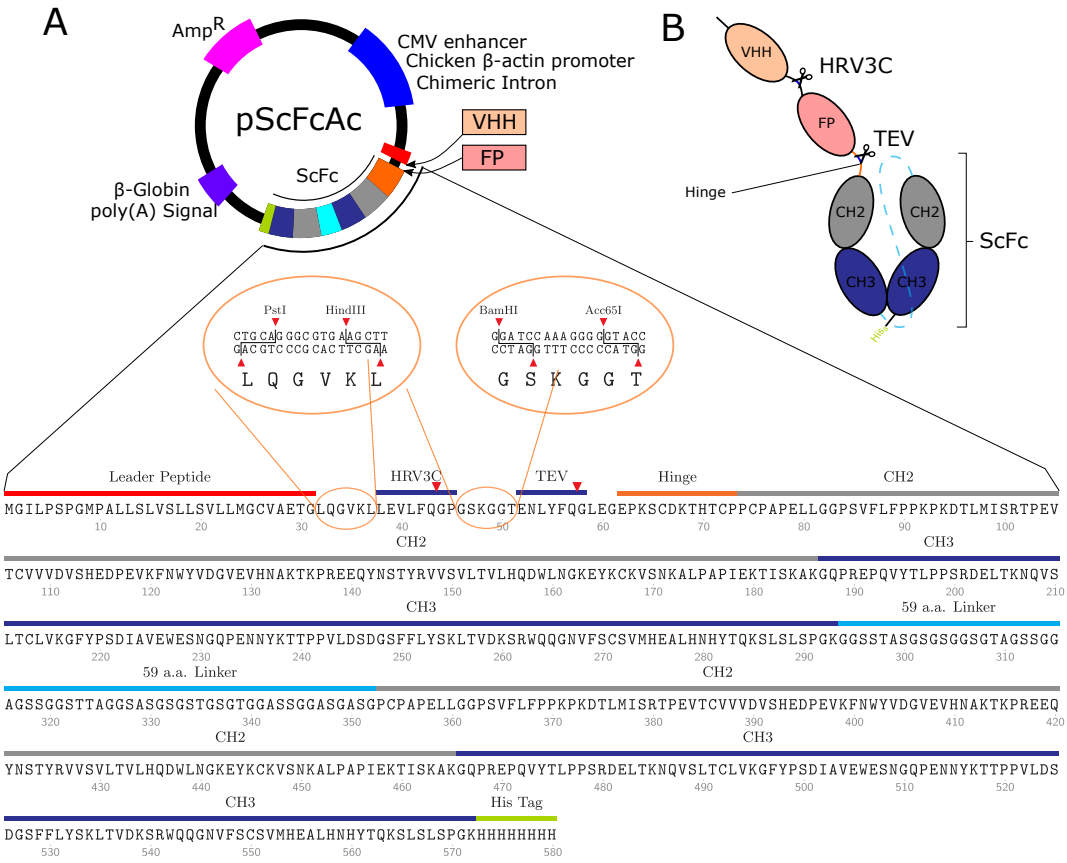


Figure 5.8: **Creation of and Expression from a Modular Mammalian Expression Vector**
A: Full Annotated Sequence of the pScFcAc vector, including the full protein sequence of the ScFc region.
B: Schematic of the final protein product of the ScFc region.

5.3.6 IHC on Mammalian Cells

5.3.6.1 Identification of VHH Domain Candidates for Use in Native Tissues

To test binding and select candidates for use on native tissues, VHH antibody-mVenus fusions were applied to both fixed, and fixed and permeabilised HEK293T cells expressing either mCherry alone or a hTREK-2-mCherry fusion. After one hour of incubation, the cells were washed and imaged using a Nikon Eclipse TE2000U inverted microscope containing TRITC and GFP filter cubes. mCherry and mVenus were selected as fluorescent fusions as they could be excited using the filter cubes available, and importantly, have little spectral overlap (for details of filter cubes, specifications and spectral overlap of the fluorophores see Methods).

After VHH antibody incubation and washing, cells were imaged during excitation with green light to detect mCherry/K2P-mCherry expression and during excitation with blue light to detect VHH antibody-mVenus fusions and images were overlaid to determine co-localisation. A pictorial representation of the experimental set up is shown in the bottom right inlay of Figure 5.9. This was carried out for a number of VHH antibody-mVenus fusions and required various rounds of optimisation including channel expression, cell preparation, VHH antibody incubation time and washing steps. Eventually after finding robust conditions, the assay could be carried out routinely.

Images were obtained using both the GFP and TRITC filter cubes and the pixel intensity for each cell in each channel (red and green) was plotted both with (blue triangles, Figure 5.9) and without (black circles, Figure 5.9) permeabilisation. While the values themselves are not informative owing to filter cubes in use, the trends are: points on the y-axis suggest binding independent of chan-

nel expression, i.e. non-specific binding, points on the x-axis suggest no binding independent of channel expression, while a positive linear relationship suggests dose-dependent binding.

Of the tested VHH antibody mVenus fusions, VHH54, VHH57, and VHH61 showed strong positive linear relationships with both fixed (R= 0.7996, R= 0.5949 and R= 0.9476 respectively), and fixed and permeabilised samples (R = 0.9572, R= 0.9577 and R= 0.7622 respectively), suggesting dose-dependent binding and clearly identifying themselves as candidates for native cell imaging. Binding of VHH58, VHH62, VHH63 and VHH67 could not be detected (low R values), which is noteworthy because both VHH58 and VHH63 are known from crystal structures to bind to the apex of the cap, while VHH67 is known from crystal structures and electrophysiology studies to bind on the side of the cap. Taken together, this suggests that the concentration of these VHH antibodies was not high enough to see binding, and shows the importance of developing a robust assay for screening. For all VHH antibodies tested on mCherry expressing cells, green pixel intensity was negligible independent of red pixel intensity suggesting that the interaction of those VHH antibodies are specific for the TREK-2 protein of the mCherry fusion not the mCherry itself, with all points lying along the x-axis (not shown).

Taken together, this data provides a proof of principle that VHH antibodies within our repertoire are capable of binding full length TREK-2 in a native membrane context, identifying candidates to take forward into further refinement through a specificity assay, and justifying a large cloning effort to create a number of negative control K2P-mCherry fusions.

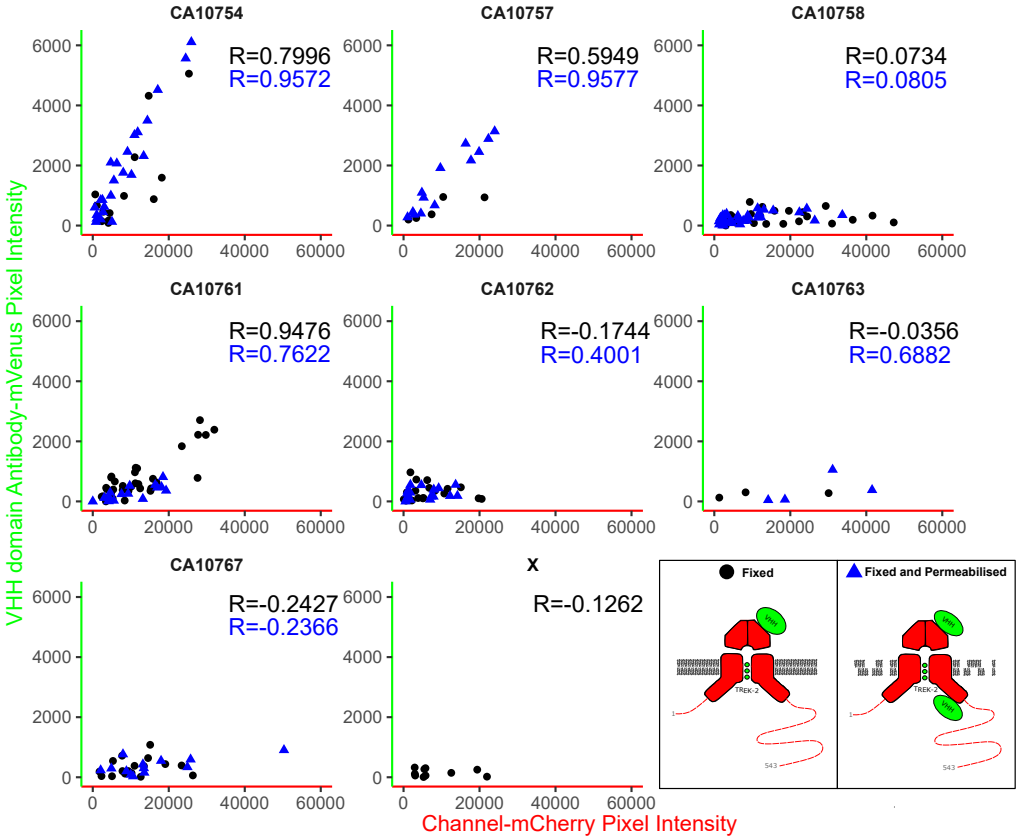


Figure 5.9: **Immunohistocytochemistry Using VHH antibody mVenus on HEK293T Cells Expressing hTREK-2**

The VHH-domain antibody-mVenus pixel intensity (green axis) is plotted against the channel-mCherry pixel intensity (red axis) for each VHH antibody. Each cell is represented as a single point and cells which have been fixed are shown as black circles while cells which have been fixed and permeabilised are shown as blue triangles. Correlation between the red and green pixel intensity was calculated using the Pearson Correlation Coefficient, and the R values are displayed in each case colour matched to the data. A pictorial representation of the experimental set up is shown as an inlay on the bottom right.

Images collected and processed by JE with assay design and troubleshooting, channel and VHH antibody cloning, VHH antibody production and data plotting with AC

5.3.6.2 Candidate Refinement for VHH Antibodies for Use in Native Tissues

To assess the specificity of binding of VHH antibodies, 11 other K2P-mCherry fusions were cloned to be used as negative controls for TREK-2 binding. HEK293T cells were again used to express K2P-mCherry fusions which were subsequently fixed and incubated with a panel of VHH antibodies in the low µM range. Images were obtained using a Nikon Eclipse TE2000U inverted microscope containing mCherry and GFP filter cubes: the new mCherry filter cube allowing channel expression to be visualised more clearly.

VHH antibody signal could be detected only for cells transfected with TREK-2 and co-localised with cells expressing TREK-2 (Figure 5.10A) suggesting that all tested VHH antibodies bind to their target, as suggested by the ELISA data provided by nanobodies4INSTRUCT. In addition, for all tested VHH antibodies, no VHH antibody signal was detected on cells transfected with other K2P channels including the closely related subfamily members TREK-1 and TRAAK as well as other more distantly related K2P channels of the TALK, TASK, TWIK, THIK and TRESK subfamilies (Figure 5.10B), suggesting exquisite selectivity of the VHH antibodies.

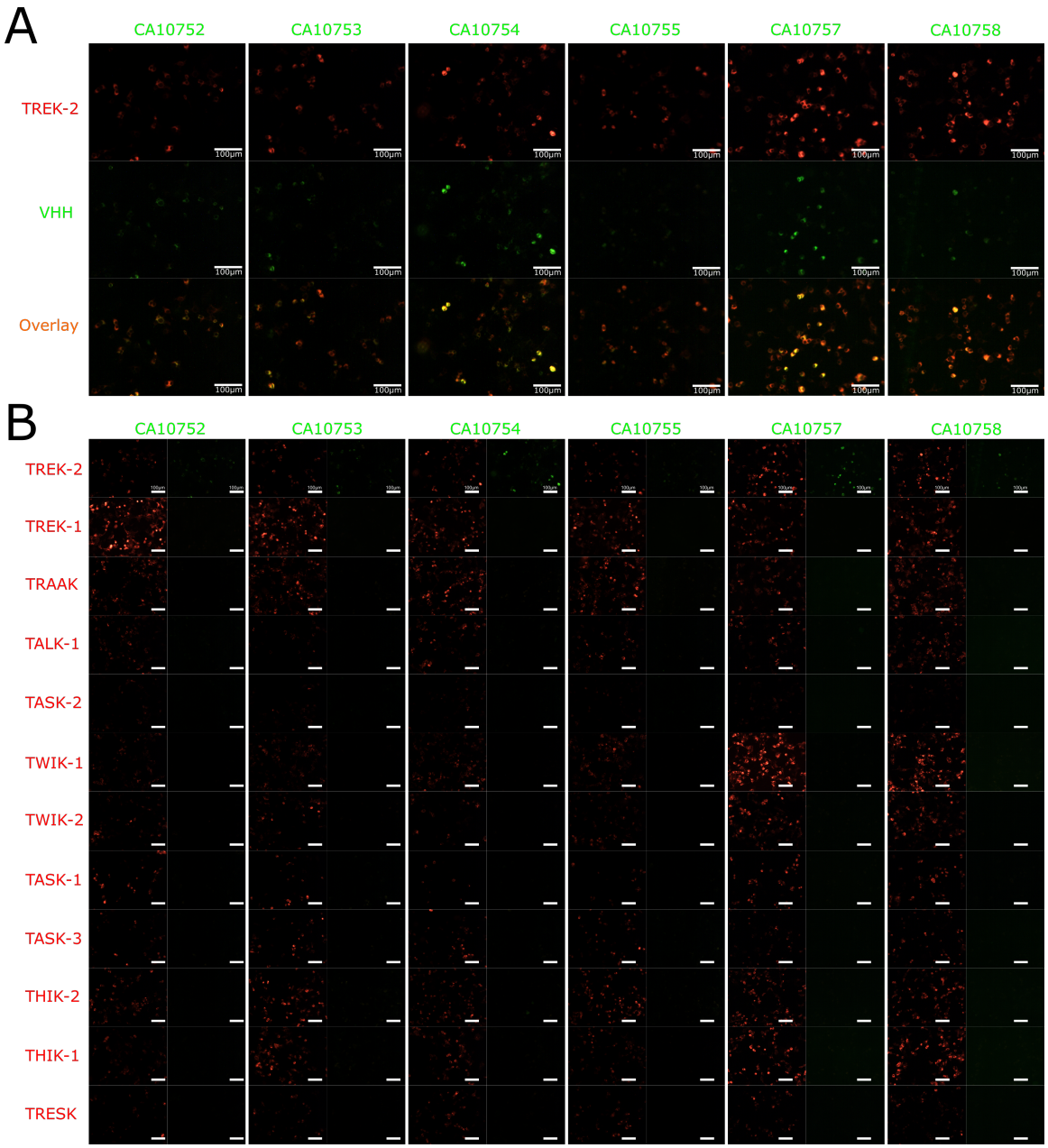


Figure 5.10: **Immunohistocytochemistry using VHH Antibody mVenus on HEK293T cells Expressing a Number of K2P Channels**
A: HEK293T expressing TREK-2-mCherry (top row, red cells), immunostained with VHH antibody (middle row, green) and overlaid images (bottom row, yellow). Scale bars represent 100µm.
B: HEK293T expressing a panel of K2P-mCherry fusions. Within each column of two images, left shows K2P-mcherry expression, right shows immunostaining with VHH antibody (green). Channels are ordered by decreasing sequence homology to TREK-2. Scale bars represent 100µm and are only labelled on TREK-2 images.
Data collection by Kathryn Smith with assay design and troubleshooting, channel and VHH antibody cloning and figure plotting with AC.

5.3.6.3 IHC on rat Superior Cervical Ganglion

Ultimately the end goal is to use VHH antibodies for imaging in native tissues to better understand K2P channel expression and localisation. To this end, two of the VHH antibodies, VHH52 and VHH57, which had emerged from the screening process as being selective for TREK-2 over all other K2Ps and expressing robustly, were applied along with the nuclear stain 4,6-diamidino-2-phenylindole (DAPI) to native tissues obtained from a 5 week old Rat Superior Cervial Ganglion (SCG, kind gift of HD), and imaged with a 405nm laser to detect DAPI and a 488nm laser to detect the VHH antibody-mVenus fusion. Whilst adequate controls were not carried out due in part to time constraints and in part to not having access to proper controls (VHH antibodies targeting different membrane proteins not expressed in the rat SCG), signal was detected after application of both VHH antibodies by excitation at 488nm. The signal was localised to neurons identified by their large round nuclei (blue, Figure 5.11A,B) rather than to glial cells (smaller, elongated nuclei), consistent with the expression of TREK-2 within the neuron but not the glial cells, as shown in the RNA-seq data from the rat stellate ganglion (HD, unpublished data, Figure 5.11C) and further reinforcing the suitability of our VHH antibody panel for immnunostaining of rodent tissues in spite of them being raised against human channels.

While the data presented here is heavily caveated owing to the lack of controls, these experiments may have important implications: VHH antibody-mVenus fusions may be able to detect rodent K2P channels localised in neurons without the need for a secondary antibody or other signal enhancer. This in turn, affords the ability to enhance the signal if needed, using anti-His_6, anti-mVenus or anti-camelid secondary antibodies.

.

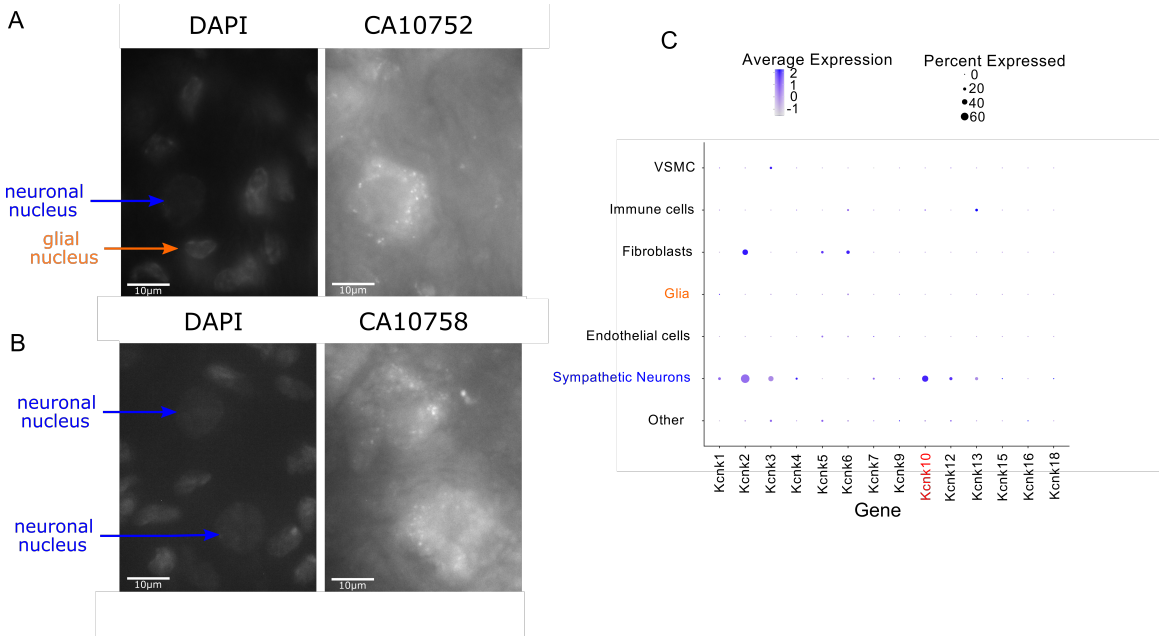


Figure 5.11: **Immunohistocytochemistry using VHH Antibody mVenus Fusions on Rat Superior Cervical Ganglia**

A: A population of cells within the rat Superior Cervical Ganglion stained with DAPI (left) which is used as a nuclear stain or VHH Antibody VHH52 (right) to specifically detect TREK-2. A neuron is shown by a blue arrow and a glial cell is shown with an orange arrow.

B A population of cells within a different rat Superior Cervical Ganglion stained with DAPI (left) which is used as a nuclear stain or VHH Antibody VHH58 (right) to specifically detect TREK-2.

C: RNA-seq data showing average expression level of all K2P genes (KCNK) detected in different cells of rat stellate ganglia. KCNK10 encodes TREK-2 (red) and glia are highlighted in orange and neurones are highlighted in blue.

RNA extraction and sequencing carried out by H. Davis, and data kindly provided to support this figure.

5.4 Discussion

In this chapter, we have attempted to optimise VHH antibody expression in both *E. coli* and HEK293T cells to increase their yield and as a toolkit to increase the engineering possibilities of VHH antibodies. The largest increase in yield we obtained was by swapping from TALON (Cobalt) to Ni-NTA. By expressing VHH antibodies in the cytoplasm of BL21(DE3) RIPL + Erv1p and DsbC and sorttagging we have provided a proof of principle that we can make fluorescent tagged VHH antibodies in *E. coli*, while expression in the pHLSec vector and the pScFcAc vector allows production of (impure) VHH antibodies from mammalian cells. Using the pHLsec vector we have shown that a subset of our mVenus-tagged VHH antibodies can bind to HEK293T cells expressing hTREK-2, and taken this further with promising candidates to show that they do not bind to other K2P channels. Finally, we provide some speculative data that suggests that some members of our VHH antibody library can bind to rat SCG neurons but not SCG glial cells.

Although the biochemistry described in this chapter is mostly attempting to replicate what others have done in the literature, undetailed protocols combined with lack of technical knowledge about what works for our panel of VHH antibodies has no doubt slowed progress. The lab has a new grant underway to raise VHH antibodies against other K2P family members such as the TASK-1/TASK-3 subfamily and synthetic heterodimeric K2P channels. When these arrive, there is now a working framework for binding and specificity assays which took months of cloning and optimisation. During all of our efforts in this chapter we have opted for modular design (such as subcloning, sorttaging, pScFcAc creation) for efficiency and futureproofing. Importantly, we now have a way to study VHH domain binding to K2P channels which do not modulate their function, which are in themselves important, something which when this project was in its infancy would

have drastically sped up progress. In addition, in this chapter we have opted for many orthogonal approaches due, in part, to not having a good understanding of what would or would not work, but these were important in informing us about VHH antibody biochemistry.

Additionally, by being able to produce tagged VHH antibodies, it opens up the possibility of tagging VHH antibodies which are known to functionally modulate TREK-2 and performing single molecule Förster Resonance Energy Transfer (smFRET) or patch clamp fluorometry which could be invaluable for correlating dynamics and function. However a large amount of work would need to be done in order to identify sites on TREK-2 where fluorophores could be inserted without compromising channel function.

Most importantly, we have started to identify candidate VHH antibodies (e.g. VHH52, VHH54 and VHH58) which we hope will be useful for other labs to study their chosen tissue and or (patho)physiological condition. As a result of a large amount of cloning and assay development, we have started to formulate what we hope will be a useful pipeline to screen and identify potential VHH antibody candidates which come through the lab. The screening is essential for any native studies and we look forward to working with other groups and are excited about the results which will come from these promising tools to better understand K2P channel localisation in both health and disease conditions.

Bibliography

Acosta, C., Djouhri, L., Watkins, R., Berry, C., Bromage, K., and Lawson, S. N. (2014). Trek2 expressed selectively in ib4-binding c-fiber nociceptors hyper-

polarizes their membrane potentials and limits spontaneous pain. *J Neurosci*, 34(4):1494–509. 294, 295

Anderson, N. and Anderson, N. G. (2002). The human plasma proteome: history, character, and diagnostic prospects. *Mol Cell Proteomics*, 1(11):845–67. 313

Aricescu, A., Lu, W., and Jones, E. (2006). A time- and cost-efficient system for high-level protein production in mammalian cells. *Acta Crystallogr D Biol Crystallogr*, 62(Pt 10):1243–50. 313, 315

Brohawn, S. G., Wang, W., Handler, A., Campbell, E. B., Schwarz, J. R., and MacKinnon, R. (2019). The mechanosensitive ion channel traak is localized to the mammalian node of ranvier. *Elife*, 8:e50403. 295

Chen, I., Dorr, B. M., and Liu, D. R. (2011). A general strategy for the evolution of bond-forming enzymes using yeast display. *Proc Natl Acad Sci U S A*, 108(28):11399–404. 311

Feilmeier, B., Iseminger, G., Schroeder, D., Webber, H., and Phillips, G. (2000). Green fluorescent protein functions as a reporter for protein localization in escherichia coli. *J Bacteriol*, 182(14):4068–76. 303

Geyer, P. E., Holdt, L. M., Teupser, D., and Mann, M. (2017). Revisiting biomarker discovery by plasma proteomics. *Mol Syst Biol*, 13(9):942. 312

Issaq, H. J., Xiao, Z., and Veenstra, T. D. (2007). Serum and plasma proteomics. *Chem Rev*, 107(8):3601–20. 313

Lei, S., Lin, H., Wang, S., Callaway, J., and Wilcox, G. (1987). Characterization of the erwinia carotovora pelb gene and its product pectate lyase. *J Bacteriol*, 169(9):4379–83. 297

Lin, W., Burks, C., Hansen, D., Kinnamon, S., and Gilbertson, T. (2004). Taste receptor cells express ph-sensitive leak k+ channels. *J Neurophysiol*, 92(5):2909–19. 294

Massa, S., Vikani, N., Betti, C., Ballet, S., Vanderhaegen, S., Steyaert, J., Descamps, B., Vanhove, C., Bunschoten, A., van Leeuwen, F. W., Hernot, S., Caveliers, V., Lahoutte, T., Muyldermans, S., Xavier, C., and Devoogdt, N. (2016). Sortase a-mediated site-specific labeling of camelid single-domain antibody-fragments: a versatile strategy for multiple molecular imaging modalities. *Contrast Media Mol Imaging*, 11(5):328–339. 304, 308, 310, 311, 312

Mazmanian, S., Liu, G., Ton-That, H., and Schneewind, O. (1999). Staphylococcus aureus sortase, an enzyme that anchors surface proteins to the cell wall. *Science*, 285(5428):760–3. 308

Newnham, L. E., Wright, M. J., Holdsworth, G., Kostarelos, K., Robinson, M. K., Rabbitts, T. H., and Lawson, A. D. (2015). Functional inhibition of β-catenin-mediated wnt signaling by intracellular vhh antibodies. *MAbs*, 7(1):180–91. 315

Nguyen, V. D., Hatahet, F., Salo, K. E., Enlund, E., Zhang, C., and Ruddock, L. W. (2011). Pre-expression of a sulfhydryl oxidase significantly increases the yields of eukaryotic disulfide bond containing proteins expressed in the cytoplasm of e. coli. *Microbial cell factories*, 10(1):1–13. 304

O'Hurley, G., Sjöstedt, E., Rahman, A., Li, B., Kampf, C., and Pontén, Fredrik and Gallagher, William M and Lindskog, Cecilia, t. (2014). *Mol Oncol*, 8(4):783–98. 293

Pardon, E., Laeremans, T., Triest, S., Rasmussen, S. G. G., Wohlkönig, A., Ruf, A., Muyldermans, S., Hol, W. G., Kobilka, B. K., and Steyaert, J. (2014). A general

protocol for the generation of nanobodies for structural biology. *Nat Protoc*, 9(3):674–93. 296, 299, 300

Perruchini, C., Pecorari, F., Bourgeois, J.-P. P., Duyckaerts, C., Rougeon, F., and Lafaye, P. (2009). Llama vhh antibody fragments against gfap: better diffusion in fixed tissues than classical monoclonal antibodies. *Acta Neuropathol*, 118(5):685–95. 296

Pizzo, M. E., Wolak, D. J., Kumar, N. N., Brunette, E., Brunnquell, C. L., Hannocks, M.-J. J., Abbott, N., Meyerand, M., Sorokin, L., Stanimirovic, D. B., and Thorne, R. G. (2018). Intrathecal antibody distribution in the rat brain: surface diffusion, perivascular transport and osmotic enhancement of delivery. *J Physiol*, 596(3):445–475. 296

Robbens, J., Raeymaekers, A., Steidler, L., Fiers, W., and Remaut, E. (1995). Production of soluble and active recombinant murine interleukin-2 in escherichia coli: high level expression, kil-induced release, and purification. *Protein Expr Purif*, 6(4):481–6. 296

Schacht, V. and Kern, J. S. (2015). Basics of immunohistochemistry. *J Invest Dermatol*, 135(3):1–4. 293

Sélo, I., Négroni, L., Créminon, C., Grassi, J., and Wal, J. (1996). Preferential labeling of alpha-amino n-terminal groups in peptides by biotin: application to the detection of specific anti-peptide antibodies by enzyme immunoassays. *J Immunol Methods*, 199(2):127–38. 304, 307

Singh, P., Sharma, L., Kulothungan, S., Adkar, B. V., Prajapati, R. S., Ali, P. S. S., Krishnan, B., and Varadarajan, R. (2013). Effect of signal peptide on stability and folding of escherichia coli thioredoxin. *PLoS One*, 8(5):e63442. 296

Thomas, J., Daniel, R., Errington, J., and Robinson, C. (2001). Export of active green fluorescent protein to the periplasm by the twin-arginine translocase (tat) pathway in escherichia coli. *Mol Microbiol*, 39(1):47–53. 303

Veggiani, G. and de Marco, A. (2011). Improved quantitative and qualitative production of single-domain intrabodies mediated by the co-expression of erv1p sulfhydryl oxidase. *Protein Expr Purif*, 79(1):111–4. 304, 307

Veggiani, G., Nakamura, T., Brenner, M. D., Gayet, R. V. V., Yan, J., Robinson, C. V., and Howarth, M. (2016). Programmable polyproteams built using twin peptide superglues. *Proc Natl Acad Sci U S A*, 113(5):1202–7. 305

Wan, E. and Baneyx, F. (1998). Tolaiii co-overexpression facilitates the recovery of periplasmic recombinant proteins into the growth medium of escherichia coli. *Protein Expr Purif*, 14(1):13–22. 296

Chapter 6

Discussion

6.1 Toxins and Antibodies Targeting Ion Channels

Throughout this thesis, we have attempted to make use of protein modulators of ion channels to better understand structure-function relationships. We are not alone in this pursuit, with lots of papers describing novel binding capabilities (e.g. knob domains of bovine antibodies Macpherson et al. (2020)), novel scaffolds (e.g. knot-bodies Bell et al. (2018)) as well as novel targets (e.g. SARS-CoV-2 3a Kern et al. (2020)).

Through use of α-scorpion toxins (Chapter 3) we were able to solve a structure of a down-state VSDIV, the first down state voltage sensor structure and probe the fast inactivation process in Nav1.7 through a novel interface picked up in the AahII-bound structure. This allowed us to answer some long-standing questions in the field such as: why do α-scorpion toxins show state-dependent toxicity, why does VSDIV have more gating charges than other VSDs, how might the IFM motif be restrained and how might activation-inactivation coupling occur in voltage-gated sodium channels. While our study was among the first, further structures

of intermediate states, proteins involving disease-associated mutations and more drugs will allow further questions to be answered. Among the most interesting, in my opinion, is how the fast inactivation process differs between the channels which is apparent by the differential kinetics between channel isoforms (Bennett et al., 2019), and differential structures captured between Nav1.7/NavPas-AahII (Clairfeuille et al., 2019) and Nav1.5-LqhIII (Jiang et al., 2021). Perhaps a universal inactivation mechanism, which is assumed when taking data from different systems and putting it together, is too simplistic an approach to fully understand this pivotal process which allows unidirectional firing of neurons and helps to regulate temporal firing patterns. From a physiological perspective, differential kinetics allows a much richer diversity of firing patterns, potentially justifying the evolution of channels with distinct kinetics.

On a perhaps more practical note, it would be interesting if it could be used to further develop a scorpion anti-venom, or if the currently available Anascorp^{TM}, an equine $(Fab')_2$ raised against the Bark scorpion (*Centroides*), a scorpion resident to Arizona, USA Krifi et al. (2005) neutralises the residues picked up in our study. Our work potentially suggests the basis for an antivenom might be targeting the prominent R62 residue which we have shown to drastically affect potency. Potentially raising antibodies against the C-terminus of the toxin could be sufficient to block AahII binding to Nav channels, and perhaps there is an unmet clinical need for this in subtropical countries. However this would require a lot of further work.

Even in the absence of a natural starting point, we were able to produce toxin-like VHH antibodies by injecting TREK-2 K2P channels into llamas, obtaining cDNA libraries and producing VHH antibodies. Using these VHH antibodies we were able to modulate K2P channel function from the extracellular side (Chapter

4), producing both activatory and inhibitory effects through very similar binding sites; a remarkable feature of SF gating in K2P channels. The VHH antibodies showed high selectivity towards their target and likely work through the external pH sensing pathway with high potency. While we were inconclusively able to show how they work, modulation of K2P function from the outside is a useful feature and it would be very interesting to put them into rodent pain models as we have shown they are capable of modulating mouse (and by extension rat) orthologs. The selectivity is worth mentioning owing to the promiscuity of all other K2P modulators and the need for selectivity for treatments for e.g. ischemia, epilepsy and pain (Gada and Plant, 2019). Modulation from the outside is particularly attractive as it does not require complex delivery and may be of use as novel therapeutics. The high selectivity exhibited may also be useful for deconstructing the role of individual K2P channels in the overall excitability of a neuron, offering a useful academic tool. While much work remains to be done on the therapeutic and academic potential of these VHH antibodies, a good starting point is now available.

Having access to a high throughput setup would undoubtedly facilitate and accelerate progress, but nevertheless we have used VHH antibodies to provide more evidence in favor of a single SF-gate in K2P channels, showing that (de)stabilisation of the gate though modulator binding to flexible loops around the SF can drastically alter channel activity. Our study highlights the modulatory potential of targeting the extracellular loops of K2P channels for which no known drug currently operates; further increasing the ever-growing rich poly-pharmacology of K2P channels.

Finally, we were able to develop an in house binding assay for VHH antibodies, which will be of immense use in the future for screening purposes to help

with the labour intensive process of screening libraries for useful VHH antibodies. Commercially available antibodies remain unknown entities which are unengineerable and expensive. The ability to transfer DNA sequences between laboratories and express and purify the VHH antibodies should ease the economic burden associated with antibody based experiments and we have provided detailed structural and functional studies of the VHH antibodies. The most obvious next experiment is to test them in TREK-2 Knock Out (KO) mice for off-target effects. Even if only a subset of our VHH antibody library do not bind to TREK-2 KO mice but bind to WT mice, then these VHH antibodies could prove to be of great value for better understanding TREK-2 expression at the protein level. In turn, this might unlock potential interactome studies of K2Ps allowing better understanding of how they integrate signals.

Into the future we envisage such experiments could be taken much further. K2P channels are known to form heterodimers and there is yet to be a direct detection method for these in native tissues. While this is not possible with our current VHH antibody library, a new one raised against synthetically linked heterodimers and use of the developed screening assay will help to show selectivity towards the heterodimer interface, which, in turn, could be used to try to provide direct evidence for heterodimers both in native tissues, but also allow unambiguous identification in heterologous expression systems. The lab in actively pursuing this avenue after a successful grant application to support VHH antibodies being raised against other family members and heterodimers.

6.2 Concluding Remarks

Protein modulation of ion channels remains to be a promising way of selectively modulating ion channel activity, but remains poorly represented in the clinic. As new technologies, scaffolds and high throughput techniques for screening and assessing efficacy and safety develop, we can expect a number of protein-based modulators making it through clinical trials in the future to combat a range of diseases. However, until then, proteins remain useful tools for the biophysicist, structural biologist and (electro)physiologist to better understand ion channels and the electrical excitability of membranes.

Bibliography

Bell, D. C., Karratt-Vellatt, A., Surade, S., Luetkens, T., Masters, E. W., Sørensen, N. M., Butt, N., and McCafferty, J. (2018). Knotbodies: A new generation of ion channel therapeutic biologics created by fusing knottin toxins into antibodies. *Biophysical Journal*, 114(3):203a. 330

Bennett, D. L., Clark, A. J., Huang, J., Waxman, S. G., and Dib-Hajj, S. D. (2019). The role of voltage-gated sodium channels in pain signaling. *Physiol Rev*, 99(2):1079–1151. 331

Clairfeuille, T., Cloake, A., Infield, D. T., Llongueras, J. P. P., Arthur, C. P., Li, Z. R., Jian, Y., Martin-Eauclaire, M.-F. F., Bougis, P. E., Ciferri, C., Ahern, C. A., Bosmans, F., Hackos, D. H., Rohou, A., and Payandeh, J. (2019). Structural basis of α-scorpion toxin action on nav channels. *Science*, 363(6433). 331

Gada, K. and Plant, L. D. (2019). Two-pore domain potassium channels: emerging targets for novel analgesic drugs: Iuphar review 26. *Br J Pharmacol*, 176(2):256–266. 332

Jiang, D., Tonggu, L., Gamal El-Din, T. M., Banh, R., Pomès, R., Zheng, N., and Catterall, W. A. (2021). Structural basis for voltage-sensor trapping of the cardiac sodium channel by a deathstalker scorpion toxin. *Nat Commun*, 12(1):128. 331

Kern, D. M., Sorum, B., Mali, S. S., Hoel, C. M., Sridharan, S., Remis, J. P., Toso, D. B., Kotecha, A., Bautista, D. M., and Brohawn, S. G. (2020). Cryo-em structure of the sars-cov-2 3a ion channel in lipid nanodiscs. *BioRxiv*. 330

Krifi, M. N., Savin, S., Debray, M., Bon, C., El Ayeb, M., and Choumet, V. (2005). Pharmacokinetic studies of scorpion venom before and after antivenom immunotherapy. *Toxicon*, 45(2):187–98. 331

Macpherson, A., Scott-Tucker, A., Spiliotopoulos, A., Simpson, C., Staniforth, J., Hold, A., Snowden, J., Manning, L., van den Elsen, J., and Lawson, A. D. (2020). Isolation of antigen-specific, disulphide-rich knob domain peptides from bovine antibodies. *PLoS Biol*, 18(9):e3000821. 330